UCGE Reports
Number 20290

Department of Geomatics Engineering

Contributions of Space Gravimetry to Postglacial Rebound Modeling with Different Rheologies

(URL: http://www.geomatics.ucalgary.ca/research/publications)

by

Wouter van der Wal

July 2009

UNIVERSITY OF CALGARY

Contributions of Space Gravimetry to Postglacial Rebound Modeling with Different Rheologies

by

Wouter van der Wal

A THESIS
SUBMITTED TO THE FACULTY OF GRADUATE STUDIES
IN PARTIAL FULFILMENT OF THE REQUIREMENTS FOR THE
DEGREE OF DOCTOR OF PHILOSOPHY

DEPARTMENT OF GEOMATICS ENGINEERING
CALGARY, ALBERTA
JULY, 2009

Abstract

The objective of this thesis is to study the contribution of the monthly satellite gravity data from the GRACE twin-satellite mission to the study of Glacial Isostatic Adjustment (GIA) in North America. The GRACE data set of monthly global gravity fields improves knowledge of this GIA especially in areas where terrestrial measurements are sparse, such as northern Canada.

Specifically, the following questions are researched for the study area of North America: (i) What is the uncertainty in long-term gravity rates estimated from GRACE data? (ii) Which of the global ice models fits best to the GRACE data? iii) Can a rheology which includes a non-linear flow law explain the GRACE observed maximum geoid rate?

It is found that straight forward filtering of the trend estimated from GRACE data removes more GIA signal than it removes errors, therefore recommendations are made for tuning an available filter. After filtering, measurement errors are small and can be represented by calibrated standard deviations or by residuals after estimation of a trend in the presence of annual and inter-annual signals. However, changes in continental water storage are a larger than expected error source that can not be mitigated. In addition, large unexplained inter-annual variability exists in the magnitude and in the patterns of the gravity rate estimated from up to 5 years of GRACE data.

The presence of two domes in the GRACE-derived gravity rate pattern as reported before occurs for a variety of processing techniques and is a stable result. However, the largest maximum gravity rate is found at the location of the Labrador ice dome instead of at the Keewatin ice dome. As a result, a better fit is obtained with the older ICE-3G and ICE-4G models than the more recent ICE-5Gv1.2 models for all reasonable viscosity profiles and for all amounts of smoothing applied to the GRACE data. This finding should motivate improvement or testing of a future ice model in North America using GRACE data.

Laboratory experiments show that linear and non-linear flow laws occur simultaneously in mantle rocks. GIA modelling in this thesis that incorporates this is found to explain historic sea level data almost as well as purely non-linear rheology, and is able to bring the maximum geoid rate in better agreement with the GRACE observed value than purely non-linear rheology. This is an important finding which can bring GIA modeling in better agreement with laboratory measurements for rock deformation. A small delay in the ICE-4G glaciation further improves the fit in geoid rate while keeping a good fit to global historic sea level data. Increasing ice thickness also improves the geoid rate fit, but worsens the fit with sea level data. Thus, it is better to delay the onset of melting than to increase ice thickness when modifying global ice models for an earth model with composite rheology.

Acknowledgements

I would like to thank my supervisors, Dr. Michael G. Sideris and Dr. Patrick Wu for their patience, understanding and guidance. I was fortunate to have shared an office with my friend and “third supervisor” Dr. Elena Rangelova. I am thankful for her contributions to all my work. I am grateful for Dr. John Wahr for hosting me and being on the defense committee. Thanks to Bryan Killett and Lin Liu for their help in Boulder. Dr. C.K. Shum is thanked for hosting me and for generating and discussing many ideas. Thanks also to Dr. Hyongki Lee and Tin Lian Abt for their help in Columbus. Dr. Hansheng Wang is thanked for sharing his sea level codes and for our cooperation. I am thankful to Dr. Doug Philips and the Westgrid team for their help with running computations on Westgrid. Many thanks to Dr. Holger Steffen for discussion and for commenting on a large part of this thesis. Dr. Alex Braun is thanked for all our discussions and being on the committee. I am grateful to Dr. Bert Vermeersen for allowing me to use his normal mode codes and to Dr. Nico Sneeuw for sharing his spherical harmonic bundle. Thanks to Dr. Hugo Schotman for our converstations in Delft. Thanks to Dr. Ed Krebes and Dr. Yang Gao for being on my candidacy and defense commmittee. Dr. John Ries and Dr. Srinivas Bettadpur are thanked for providing covariance matrices and for discussion, and Drs. Matt Rodell, Kristina Fiedler, Chris Milly and Huug van den Dool are thanked for making available hydrology model output.

Funding for my PhD studies was provided by NSERC and GEOIDE NCE grants to my supervisors and awards from the Department of Geomatics Engineering and the Schulich School of Engineering. I am grateful to Dr. Klaus-Peter Schwarz for installing graduate student awards.

Thank you Balaji, Meda and Matthias for your friendship and help in the beginning of my PhD. Thanks to all the others in the gravity group for the great time: Chen, Rossen, Bihter, Vidya, Sina, Alex, Martin, Mohammed, Sinem and Jin. Thank you Lorraine, John, Melanie, James, Stefan, Katrin, Ahmed and Ramon for being great friends. Thank you Fiona for being there for me at the end of my PhD. Niklas and Cecile, a special thank you for your friendship and our time together; it meant a lot to me. Thank you Myra, Mart, Papa.

There but for the grace of you go I

From: Kathy’s Song, written by: Paul Simon

in memory of my mother

Table of Contents

List of Tables

List of Figures and Illustrations

List of Symbols

Symbol	Definition
A	pre-stress exponent
a_e	mean radius of the Earth
$\mathbf{b}$	body force
b	inter-atomic spacing
C	ocean function
C_{lm}	Stokes coefficient
D	diffusion constant
d	grain size
e_{ij}	deviatoric strain rate
e	number of elements
E	Young’s modulus, activation enthalpy
$\mathbf{f}$	load matrix
fH_2O	water fugacity
GF	Greens Function
Δg	gravity anomaly
G	gravitational constant
$\mathcal{G}$	spatially varying part of the geoid
g	gravity
h_l	surface load Love number for radial displacement
h	water heights
k	Boltzmann constant
$\mathbf{K}$	vector residue
$\mathbf{K}_{ij}$	stiffness matrix
k_l	surface load Love number for the gravitational potential
$k_{l,e}$	elastic Love number for the potential
$k_{l,f}$	fluid Love number for the potential
l_l	surface load Loave number for tangential displacement
l	spherical harmonic degree
L	maximum spherical harmonic degree / surface load
M	number of modes
m	spherical harmonic order
N	number of time steps / number of months / geoid height
n	stress exponent, number of pixels
$\mathbf{N}$	shape matrix
o	observation
p	pressure / grain size exponent / prediction

$\tilde{P}_{lm}$	normalized Legendre polynomial
$\tilde{q}$	Mises equivalent stress
r	solid earth displacement, rank
$\mathbf{r}$	radius vector
$r_{j,l}$	modal strength
R	gas constant
$\boldsymbol{s}$	sea level
$\mathbb{S}\mathscr{L}_j$	spatially varying part of the sea-level
S	ocean heights/surface
S_{lm}	Stokes coefficient
$\boldsymbol{S}$	sample covariance matrix
$s_{j,l}$	relaxation mode
$\mathbf{S}_{ij}$	deviatoric stress
$\mathbf{t}$	surface tractions
t	time
T_l	factor that contains dimension in sea-level equation
$\mathbf{u}$	displacement
U_l	Legendre coefficient of radial displacement
V_l	Legendre coefficient of tangential displacement
$\underline{v}$	residuals
W	averaging function
$\mathbf{X}$	data matrix

List of Greek Symbols

Symbol	**Definition**
δ	increment / grain boundary width
$\delta(t)$	Delta function
δ_{ij}	Kronecker delta
Δ	Laplace operator or change
ε	strain rate tensor
$\tilde{\varepsilon}$	Mises equivalent strain rate
λ	Lame parameter / longitude
ρ	density
$\boldsymbol{\sigma}$	stress tensor
σ	surface load / standard deviation
σ_l	degree variance
θ	colatitude
∇	divergence
ϕ	gravitational potential/ melt fraction
ψ	spherical angle
η	viscosity
μ	rigidity
ν	Poisson’s ratio
χ^2	chi-squared or misfit
Ω	volume

List of Abbreviations

Abbreviation	**Definition**
BP	Before Present
CGSN	Canadian Gravity Standardization Network
CPC	Climate Prediction Centre
CSR	Centre for Space Research
FE	Finite Element
GFZ	GeoForschungsZentrum
GIA	Glacial Isostatic Adjustment
GLDAS	Global Land Data Assimilation System
GMT	Generic Mapping Tools
GRACE	Gravity Recovery And Climate Experiment
ITRF	International Terrestrial Reference Frame
LaD	Land Dynamics
LGM	Last Glacial Maximum
PCA	Principal Component Anslysis
PREM	Preliminary Reference Earth Model
RSL	Relative Sea Level
RMS	Root-Mean Square
SLR	Satellite Laser Ranging
SNR	Signal-to-Noise Ratio
VLBI	Very Long Baseline Interferometry
VCM	Variance Covariance Matrix
WGHM	WaterGAP Hydrology Model

Chapter One: Introduction

1.1 Background

Glacial Isostatic Adjustment (GIA) is the response of the solid Earth to the growing and melting of ice sheets. At the Last Glacial Maximum (LGM), approximately 21,000 years ago (Peltier, 2004), all of Canada was covered with a thick ice sheet, the weight of which caused subsidence of the Earth's crust. The removal of the ice sheets initiated relaxation that is still ongoing and measures over a centimetre per year in the Hudson Bay area.

The study of GIA has found many useful applications (e.g. in the fields of geodesy, geodynamics, solid Earth geophysics, glaciology, oceanography, climatology, astronomy, archaeology, geography, etc.) but historically it is used for the following purposes:

1) to provide predictions for removing the effect of GIA from observations so that other phenomena can be observed (e.g., correction of tide gauges to study the sea level change due to global warming; see Peltier and Tushingham, 1989; Davis and Mitrovica, 1996);
2) to study the rheology and flow properties in the Earth's mantle (e.g. Cathles, 1975; Karato and Wu, 1993) which can benefit the study of mantle convection and subduction; and
3) to provide information on past ice thicknesses and hence past climate (Peltier, 1998), which is important knowledge to put current climate changes in perspective.

This thesis aims to contribute to purposes 2 and 3, by investigating the contributions of the satellite gravity data set derived from the measurements of the Gravity Recovery and Climate Experiment (GRACE) twin-satellite mission, launched in March 2002. The study area is North America, but global historic sea level data are used as well. First, a short overview is given of the current knowledge and open problems related to purposes 2 (rheology) and 3 (Pleistocene ice sheets). Then, the GRACE data set and its use in GIA studies is discussed. Finally, the objectives of this thesis are presented and an outline of the thesis is given.

1.1.1 Rheology of the Earth's mantle

One of the objectives of GIA research is to constrain material properties in the mantle, albeit "the smoothest" version of the rheology that can explain GIA data (Ranalli, 2001). Early studies put a constraint on the average viscosity of the entire mantle, the so-called Haskell constraint (see Mitrovica, 1996, for discussion). Later studies try to constrain the average viscosity of different layers within the mantle (see Peltier, 1998, for review) but debate regarding the viscosity contrast between the upper and lower mantle is still ongoing (Kaufmann and Lambeck, 2002; Peltier, 2004; Wolf et al., 2006). Recently, it was shown that trade-off effects between viscosities of different layers prevent one from unambiguously inferring viscosity for three or more layers (Paulson et al., 2007a). GRACE data have already been used in an inversion with different data types for a two-layer viscosity profile in the mantle (Paulson et al., 2007b).

Most Glacial Isostatic Adjustment (GIA) models often employ a linear rheology in which the strain rate is linearly dependent on the stress through the Newtonian viscosity. However, laboratory experiments show that at least two different deformation mechanisms exist: diffusion creep, which leads to a linear stress-strain rate relationship, and dislocation creep (or power-law creep), which leads to a non-linear relation between stress and strain rate (Hirth and Kohlstedt, 2003; Ranalli, 1995; Karato, 2008). The type of deformation (diffusion vs. dislocation creep) can have a significant effect on mantle flow and hence the dynamics of the lithosphere and the asthenosphere and associated phenomena such as continental rifting and continental collision (Yuen and Schubert, 1976). Thus, determining the flow type is important to improve our understanding of these areas. More specifically, determining the type of mantle flow can open the door to the use of seismic anisotropy to constrain asthenospheric viscosity (Karato and Wu 1993, Podolefsky et al., 2004). A power-law relation between stress and strain rate has received some attention in GIA modelling (Sabadini et al., 1986; Wu, 1992; Gasperini et al., 1992; Karato and Wu, 1993; Wu, 1995, Wu, 1999; Wu 2001; Wu and Wang, 2008).

Because diffusion and dislocation creep operate at the same time, the total strain rate is the sum of the strain rates from both mechanisms. Such a composite rheology is a more realistic description of slow deformation in the Earth than a rheology with only one of the mechanisms. In this thesis it will be investigated whether a combined linear and non-linear rheology can also explain GRACE and historic sea level data. Previous studies of composite rheology made simplifying assumptions such as a flat Earth, and neglected self-gravitational effects, or used simplified ice loads (Gasperini et al. 1992; 2004; Giunchi and Spada, 2000; Dal Forno et al., 2005). To further assess the performance of composite rheology it is necessary to use more realistic spherical earth models with self-gravitation, in combination with realistic ice loads, and to compare predictions with more data sets. Specifically, the effect of composite rheology on gravity rate and uplift rate has not been studied, while a well known problem with a non-linear rheology is the small present-day uplift rate and gravity rate it predicts (Wu, 1999; Wu and Wang, 2008). Presently, it is not clear if the small uplift and gravity rates are biased by the fact that global ice loading histories are constructed by assuming linear rheology, or if they are the result of failure of non-linear or composite rheology to accurately describe mantle deformation.

1.1.2 Constraints of past ice thicknesses

Geological evidence in the form of (terminal) moraines can be used to reconstruct the extent of the past ice sheet (Dyke et al., 2002). To constrain the thickness of a past ice sheet, time series of historic sea level changes are most valuable (Peltier, 1998). Areas lacking such sea level data are the interior of North America. Inference of past ice sheet thicknesses is seriously hindered there (Tarasov and Peltier, 2004), although some information in pro-glacial lakes is available (Walcott, 1972). Global ice histories have been successfully reconstructed by combining the physics of the rebound process with relative sea level (RSL), land uplift and absolute gravity data (Peltier, 2004). However, due to the slow response of the Earth the ice sheet history constructed from RSL data cannot resolve rapid surges and retreats due to abrupt climate changes (Hughes, 1998).

GPS and absolute gravity data provide observations of the uplift process that could be used to constrain ice thicknesses. However, these data are also sparse in northern Canada. The appearance of two domes in gravity rate pattern derived from Gravity Recovery and Climate Experiment (GRACE) satellite data (Tamisiea et al.,

2007) supports a multi-dome Laurentide ice distribution as in, e.g., Dyke and Prest (1987). However, as argued in the next section, the accuracy of GRACE data makes it worthwhile to revisit the issue of the ice domes and the location of maximum ice heights.

Finally, ice models currently used by GIA researchers are all coupled to a linear Earth rheology despite the evidence for power-law creep; see the previous section 1.1.1. Non-linear rheology requires more ice or delayed melt (Wu and Wang, 2008), but currently it is not clear how the ice history should be modified for Earth models with composite rheology.

1.1.3 GRACE data

Geodetic data to constrain the GIA process in North-America are sparse and sensitive to local effects. Repeated absolute gravimetry measurements are only performed at a few selected sites (Lambert et al., 2001, 2006). Relative gravimetry measurements are more widespread and go back further in time, but clearly suffer from local non-GIA effects; see the figures in Pagiatakis and Salib (2003). Satellite Laser Ranging (SLR) measurements yield information on zonal components only, which means that the rebound process in North America and Fennoscandia and present-day ice melt in Greenland can not be separated (Velicogna and Wahr, 2002). Also, with a network of continuously operating GPS receivers supplemented with campaign measurements, pinpointing the exact center of maximum uplift is not possible due to the sparse network (Henton et al., 2006; Sella et al., 2007). Other present-day uplift rates are measured by satellite radar altimetry in an area close to Hudson Bay (Lee et al., 2008), and by combining tide-gauges and satellite altimetry in the Great Lakes area (Kuo et al., 2008). A combination of more terrestrial datasets can overcome some of the weaknesses in each of the individual data sets (Rangelova, 2007).

The launch of the GRACE satellites in March of 2002 revealed the time-variable gravity field of the Earth at monthly resolution with homogeneous coverage (Tapley et al., 2004). Prior to their launch, simulations showed that GRACE would be able to constrain upper mantle/transition zone and lower mantle viscosity within 30-40% (Velicogna and Wahr, 2002). However, the error level of GRACE satellites is higher than the target accuracy level (Wahr et al., 2004), and north-south stripe errors dominate unfiltered gravity field products (Chen et al., 2005b). Despite the larger than expected errors, GRACE data has been used successfully in a number of studies related to GIA. The contribution of GIA to static gravity anomalies over North America has been established (Tamisiea et al., 2007); a two-layer viscosity profile is inferred from GRACE data in combination with sea level data and C_{20} variations (Paulson et al., 2007b). GRACE data compared well with absolute gravity data in Fennoscandia (Steffen et al., 2009).

However, these studies either used a single standard processing technique (Paulson et al., 2007b), or did not give details of their processing (Tamisiea et al., 2007), or did not quantify the effect of post-processing techniques on signal and noise (Steffen et al., 2008a). With the abundance of post-processing methods presented in the GRACE literature (see Klees et al., 2008, for an overview) it is not clear what the effect of these post-processing techniques are, and how to apply them specifically for the purpose of GIA studies. Moreover, it was found that previous studies underestimated the effect of continental water storage variations (Van der Wal et al., 2008a). Some conclusions have been made in the literature about the ice loading histories to the GRACE data. Paulson et al. (2007b) used two different ice models and claimed that ICE-5G fits best. Tamisiea et al. (2007) concluded that ICE-5G provides a good fit. However, these findings can be undermined by the short time series used and the uncertainty in continental water storage variations.

In short, the uncertainty in the gravity rates extracted from GRACE for the purpose of constraining GIA models is currently not clear. For some purposes, such as the contribution of GRACE to the static gravity field (Tamisiea et al., 2007), the uncertainty is not critical for the conclusions reached, but the inference of the detailed ice loading history requires knowledge of the uncertainty in GRACE data when.

1.2 Thesis objectives

The purpose of this thesis is to study the contributions of GRACE data to GIA modeling. In particular, the following issues should be resolved with regards to using the GRACE data for GIA studies:

- How do various filters that can be applied to GRACE data affect the GIA signal in the GRACE data?
- Are there significant secular and inter-annual non-GIA effects that influence the secular gravity rate derived from GRACE?

With regard to the mantle rheology, this thesis focuses on a composite rheology which combines linear and non-linear flow laws. In particular the following questions are formulated:

- Can composite rheology explain RSL data and the GRACE-derived maximum geoid rate at the same time?
- What is the composite rheology that best fits RSL data and the GRACE-derived maximum geoid rate?

The homogeneous distribution of GRACE data makes GRACE data seem particularly useful for inferring the thickness of past ice sheets. This thesis aims to answer the following questions about such an inference:

- Can GRACE contribute information about past ice sheets?
- Can GRACE data resolve the difference between GIA models with two different ice models?
- Which ice model provides a best fit to the GRACE data?
- How should ice models be modified for composite rheology such that predictions agree with RSL observations and the GRACE-derived maximum geoid rate?

1.3 Thesis outline

Chapter 2 outlines the normal mode method that is used to compute the solid Earth response to surface loading and the sea-level equation that computes the water redistribution following build-up and melt of ice sheets. Global ice models ICE-3G, ICE-4G and ICE-5G, which are used as input for the simulations, are also discussed.

Predictions of the simulations in this chapter are used in simulations to support post-processing of the GRACE data and comparisons with the GRACE data.

Chapter 3 presents the equations and their boundary conditions for glacial loading that are solved using the finite element program ABAQUS. Evidence from laboratory and micro-physical studies on non-linear deformation mechanisms is reviewed and the implementation of composite rheology in ABAQUS is explained.

Chapter 4 presents the Level-2 GRACE data and the gravity field functionals that can be computed from it. Post-processing techniques and measurement errors are addressed in detail.

Chapter 5 is the first of the results chapters. Three important non-GIA effects are investigated: continental water storage, glacier melt, and lake level variations. Different methods are compared for estimating measurement errors in GRACE. The effect of filters is assessed, and one of the filters is tuned to improve the extraction of the GIA signal from GRACE. Finally, estimates of the GIA induced gravity and geoid rates are presented for use in inferences of the best-fitting composite rheology (Chapter 6) and the best-fitting ice model (Chapter 7).

Chapter 6 investigates composite rheology. The best fitting composite rheology parameters are found based on RSL misfit comparisons. Next, it is shown that composite rheology produces higher uplift and geoid rate than a purely non-linear rheology, which is more in agreement with observations. Finally, it is demonstrated that simple modifications to the ice history can improve RSL fit and geoid rates simultaneously.

Chapter 7 uses GRACE data to constrain the ice loading history. First, the sensitivity to gravity rate with respected to scaling of ice thicknesses in a small region is investigated. Simulations are performed to address the question whether uncertainty in hydrology effects can mask differences in ice loading histories. Finally, real GRACE data are used to find the location of maximum ice thicknesses and to find the best fitting ice model.

Chapter 8 summarizes the main findings of this thesis and gives recommendations on the use of GRACE data for GIA studies, and on the inference of ice models based on linear or composite rheology.

In Appendix A expressions are derived for the free-air gravity and sea level change as a function of an impulse and Heaviside surface load. In Appendix B predictions of sea-level codes used in this thesis are compared to published results from Spada and Stocchi (2005) and Paulson et al. (2007b). Appendix C derives the tensor form of power law creep. Appendix D discusses the implementation of time-dependent loading in relation to accuracy and computer time issues. Appendix E lists and plots the RSL sites used in Chapter 6.

Chapter Two: Normal Mode and Pseudo-Spectral Sea Level Method for Surface Loading Response

This chapter discusses the computation of the response of the Earth to loading by an ice sheet and complementary ocean by semi-analytical techniques. This computation can be divided into two parts: (i) computation of the solid Earth's response to a generic surface load; and (ii) computation of the self-consistent sea level response to the melting of the ice sheets and the solid Earth deformation.

The normal mode theory will be used for part (i) and is briefly described in section 2.1. The self-consistent sea level is obtained by iterative solution of the so-called sea level equation (Farrell and Clark, 1976). The sea level equation and the steps in the numerical algorithm to solve it are described in section 2.2. The global ice histories of Peltier and co-workers are used in this thesis, namely ICE-3G, ICE-4G and ICE-5G. A comparison of the uplift rates computed with the methods described in this chapter and published results from other groups is provided in Appendix B. Two models that will be used in the testing of post-processing filters on GRACE data are presented in section 2.4. A chapter summary is given in section 2.5.

2.1 Normal mode method for surface loading

The normal mode theory is developed by Peltier (1974), Wu (1978) and Wu and Peltier (1982), with important elements of the theory present in the works of Farrell (1972) and Longman (1962). Modifications of the method for multi-layer Earth models were made by Sabadini et al. (1982) and Vermeersen and Sabadini (1997). Here the implementation of the latter is used, with a code kindly provided by Dr. Bert Vermeersen of TU Delft.

The starting point is the linearized equation of momentum (Cathles, 1975; Wu, 2004; Sabadini and Vermeersen, 2004, eq. 1.10):

$$\nabla\cdot\boldsymbol{\sigma}-\nabla\left(\mathbf{u}\cdot\rho_0 g_0\mathbf{r}\right)-\rho_1 g_0\mathbf{r}-\rho_0\nabla\phi_1=0, \tag{2.1}$$

where $\boldsymbol{\sigma}$ is the stress tensor, $\mathbf{u}$ is displacement, ρ is the density, $\mathbf{r}$ is a unit vector in radial direction, g is the gravitational acceleration, and ϕ is the gravitational potential. Subscript 0 refers to the unperturbed state and subscript 1 refers to a perturbation from this state.

The first term in equation (3.10) is the divergence of stress; the second term is the advection of pre-stress; the third term represents the effects of compressibility, and the last term is the effect of the change in gravitational potential due to the perturbation. This term includes the effect of the load itself and mass redistribution of the load and all Earth masses. Inertial forces are neglected because of the slow movement of mantle material involved in GIA.

The effect of compressibility will be neglected from now on. The solution for a homogeneous compressible Earth in the Laplace domain is known (Wu and Peltier, 1982), but, for a multi-layered spherical Earth, computation is not trivial. Moreover, the semi-analytical normal mode theory yields only an approximation to a compressible Earth (Riva and Sabadini, 2009). The difference in uplift rate between elastically compressible and elastically incompressible rheology is small (Mitrovica et al. 1994, figure 2). In table 2 of Paulson et al. (2007b) it is shown that the inclusion of compressibility in a spectral model has a small effect (< 0.2) on the misfit values for gravity rates with respect to GRACE-derived gravity rates. Such effect is small compared to the differences in misfit that results from using different ice models, thus not including compressibility is not expected to have a large effect on the conclusions regarding different ice models.

The gravitational potential for an incompressible Earth model satisfies the Laplace equation:

$$\nabla^2 \phi_1 = 0 . \tag{2.2}$$

If no tangential stress is applied to the surface of the Earth, and if the Earth is laterally homogeneous, toroidal motions are zero. That means only spheroidal displacements are considered, which depend only on radial distance and spherical angle with respect to the load (Peltier, 1974; Wu and Peltier, 1982). Furthermore, isotropic material is assumed, for which the elastic parameters reduce to the two Lamé parameters μ and λ (or alternatively Young's modulus and Poisson's ratio). The stress-strain relation reads in index notation:

$$\sigma_{ij} = \lambda \delta_{ij} \sum_{k=1}^{3} \varepsilon_{kk} + 2\mu \varepsilon_{ij} , \tag{2.3}$$

where λ and μ are the Lamé parameters, and σ_{ij} and ε_{ij} are elements of the stress tensor and strain tensor. Not surprisingly, the solution only depends on one material parameter, μ, because only deviatoric stresses and strains are relevant. For the case of loading an incompressible material, hydrostatic pressure of arbitrary magnitude can be added to the solution (this leads to a problem in the FE solution, see section 3.4).

Until now, only elastic behaviour was considered by the stress-strain relation (2.3) , but for GIA we need time-dependent deformation. Different time-dependent behaviour can be distinguished (see Figure 2.1). After elastic deformation, the Earth's mantle will go through transient creep and steady-state creep.

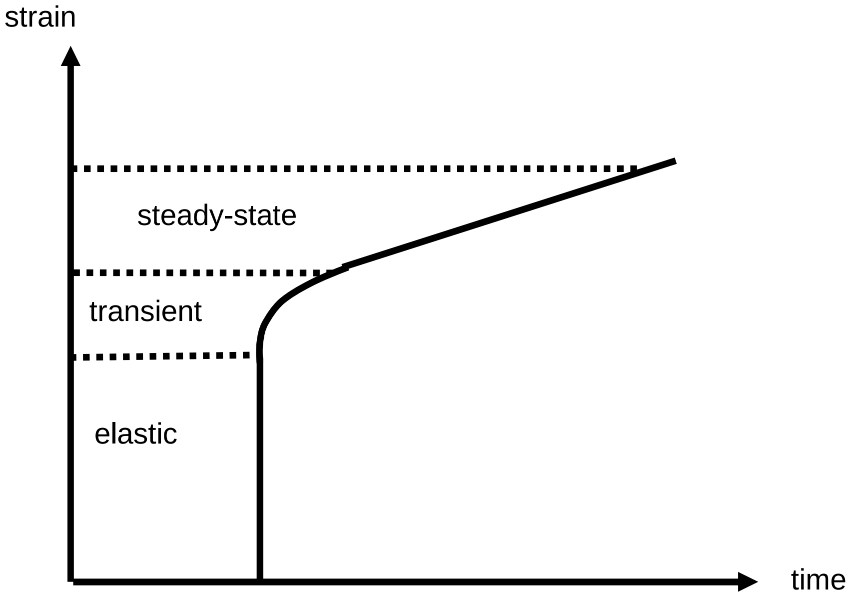

Figure 2.1: Schematic strain-time diagram denoting elastic, transient and steady-state creep regimes (after Ranalli 1995, Figure 4.5)

Elastic deformation is completely recoverable if the load is removed. The deformation in steady-state creep is permanent (Ranalli, 1995, p. 80) which means that after removal of the load there is no recovery of the steady state creep deformation. This should not be confused with the reversal of deformation that occurs after removal of the ice load. Buoyancy forces cause the reversal of deformation and not 'reversible' material behaviour such as occurs for an elastic material. Non-recoverable flow is called plastic flow, which occurs when the stress in the material exceeds the yield stress.

For high temperature and after a long time the steady-state part of the strain rate is much more important than the transient term (Ranalli 1995, p. 80). This is the assumption made in most GIA studies and also in this thesis. Justification of this assumption is indirect: there is some agreement between viscosity profiles constrained by static geoid anomalies cause by dynamic topography changes, and the profile derived from GIA studies. The agreement over such a long timescale shows that transient creep can not play an important role (Peltier et al., 1980; Ranalli, 2001). However, some results indicate that transient rheology can cause a difference in GIA inferred viscosity from the true steady state viscosity up to a factor of 10 (Karato, 2008, p. 330).

When neglecting transient creep, the material model in GIA modeling should describe both elastic and steady-state creep behaviour. This can be modeled by a so-called Maxwell element in which a purely elastic element is connected in series to a purely viscous element such that the strain rates are added. The viscous element in the Maxwell model represents steady state-creep which occurs below the yield strength. In tensor form the Maxwell element is (Peltier, 1974; Cathles 1975, p. 25):

$$\dot{\sigma}_{ij} + \frac{\mu}{\eta}\left(\sigma_{ij} - \frac{1}{3}\delta_{ij}\sum_{k=1}^{3}\sigma_{kk}\right) = 2\mu\dot{\varepsilon}_{ij} + \lambda\delta_{ij}\sum_{k=1}^{3}\dot{\varepsilon}_{kk}, \tag{2.4}$$

where δ_{ij} is the Kronecker delta and η is the dynamic viscosity. Laplace transforming this equation gives (Cathles 1975, p. 25):

$$\bar{\sigma}_{ij} = \lambda(s)\delta_{ij}\sum_{k=1}^{3}\bar{\varepsilon}_{kk} + 2\mu(s)\bar{\varepsilon}_{ij}, \tag{2.5}$$

where the overbar denotes the Laplace transform. The Laplace transformed Lamé parameters are given by:

$$\lambda(s) = \frac{\lambda s + \frac{\mu}{\eta}K}{s + \frac{\mu}{\eta}} \text{ and } \mu(s) = \frac{\mu s}{s + \frac{\mu}{\eta}}, \tag{2.6}$$

where $K = \lambda + \frac{2}{3}\mu$ is the bulk modulus. Noting that equation (2.5) is the same as the elastic constitutive equation in the time-domain (2.3), the solution to the viscoelastic problem can be obtained by solving the elastic problem in the Laplace domain (Peltier, 1974; Cathles, 1975, p. 25).

The momentum equation and the Laplace equation form a system of three partial differential equations of second order, which can be integrated numerically to obtain the required solution. However, in the normal mode method the equations are rewritten to a system of six first-order ordinary differential equations for which the solution can be obtained almost entirely analytically. The advantage of the numerical solution is that properties are allowed to vary continuously with depth, and compressibility can be included (Wu and Peltier, 1982). In the analytical normal mode method depth variations have to be approximated with a finite number of layers, and compressibility can only be approximated (Riva and Sabadini, 2009). On the other hand, an analytical solution offers additional insight and checks (Sabadini and Vermeersen, 2004, p. 8). Because of availability of computer codes for the semi-analytical normal mode codes of Vermeersen and Sabadini (1997) this method is used in this thesis.

After applying boundary conditions at the surface and at each interval (see Sabadini and Vermeersen, 2004, p. 18), the solution to the homogeneous problem consists of the roots of the so-called secular determinant (eq. 1.106, Sabadini and Vermeersen, 2004). These roots are inverse relaxation times, also called relaxation modes, and they arise from the discontinuities in the Earth model. Thus, characteristics of the relaxation process in terms of material properties can be deduced from them. There are modes for the Earth-surface transition, the mantle-lithosphere transition and the fluid core-mantle transition. Furthermore, each density contrast introduces a buoyancy mode and an interface between two layers of different η / μ introduces a pair of modes (Wu and Ni, 1996; Sabadini and Vermeersen, 2004, p. 22).

It is also necessary to find the relaxation models in order to transform the solution from the Laplace domain to the time domain. Finding the modes is usually done numerically. In the code of Vermeersen and Sabadini (1997) that is used in this thesis a bisection algorithm is used. A method to obtain the solution in the time domain was developed by Wu (1978). The form of the time domain solution is (Sabadini and Vermeersen, 2004, p. 34):

$$\left[U_l \quad V_l \quad -\phi_l\right]^T\Big|_{a_e,t} = \mathbf{K}_l^e\left(a_e\right)\delta\left(t\right)+\sum_{p=1}^{M}\mathbf{K}_{l,p}\left(a_e\right)e^{s_{l,p}t}\ , \tag{2.7}$$

where $\left[U_l \quad V_l \quad -\phi_l\right]^T$ are the Legendre coefficients of degree l of the radial and tangential displacement and the gravitational potential, respectively; a_e is the average radius of the Earth; $\delta\left(t\right)$ is the Dirac-delta function; M is the number of modes; $s_{p,l}$ is the p-th mode; and t is time. Furthermore, $\mathbf{K}_{l,p}$ are the vector residues at $s = s_p$, and $\mathbf{K}_l^e\left(a_e\right)$ denotes the elastic limit ($s \to \infty$); see Sabadini and Vermeersen, (2004) p. 34. The time domain solutions (2.7) are usually written in dimensionless form as follows (Wu and Peltier, 1982, equation 12):

$$\left[h_l \quad l_l \quad k_l\right]^T\Big|_{a_e,t} = \left[\frac{M_e}{a_e}U_l \quad \frac{M_e}{a_e}V_l \quad -\frac{M_e}{a_e g_0}\phi_l\right]^T\Bigg|_{a_e,t}\ , \tag{2.8}$$

where h_l, l_l and k_l are the surface load Love numbers for radial displacement, tangential displacement and gravitational potential perturbation, respectively, and M_e is the mass of the Earth. The Love numbers (the elastic as well as the viscous parts in (2.7)), and the modes s_l form the output of the normal mode codes used here. The time-domain form of the free-air gravity and the geoid, which are combinations of these, are derived in Appendix A.

2.1.1 Implementation issues and input

In the normal mode method, it is important that all M modes are found by the root-finding algorithm. A simple check whether all the modes are found for a particular degree is to plot the fluid k-Love number versus harmonic degree. The fluid Love number can be computed by setting $s = 0$ in equation (55) of Wu and Peltier (1982):

$$k_{l,f} = k_{l,e} + \sum_{j=1}^{M}\frac{r_{j,l}}{s_{j,l}}\ . \tag{2.9}$$

When important modes are missed in the root-finding, a discontinuity will appear in the plot and the root-finding should be repeated with a finer step size. All models used in this thesis have been checked accordingly.

The input required to compute the fundamental matrix **Y** are elastic material parameters for the Earth (density ρ and rigidity μ) and layer boundaries for each of the layers in the spherical Earth model (see Sabadini and Vermeersen, 2004). Most GIA models, e.g., Peltier (2004), Kaufmann and Lambeck (2002), Tamisiea et al. (2007), use elastic parameters taken from the Preliminary Reference Earth Model (PREM) (Dziewonski and Anderson, 1981).

In the semi-analytical normal mode method used in this thesis, an increase in the number of layers greatly increases the number of modes and consequently the chance that modes are missed in the root-finding procedure. Vermeersen and Sabadini (1997) showed that it is better to use an approximation to PREM and use all the modes than to use many layers and miss some important modes. Furthermore, they found that a 5-layer volume-average model is close to results with a model with many layers. Here, the major seismic discontinuities at the following depths are used (or close to these depths as the exact depth is debated and varies across the Earth): 400, 670 and 1180 km to arrive at a 6-layer model (see Table 2.1). The elastic parameters in Table 2.1 are obtained by volume-averaging from corresponding layers in PREM. The density profile was further modified to match a surface gravity of 9.81 m/s^2.

2.2 Sea level equation

The original complete formulation of the sea level equation is given in Farrell and Clark (1976). An efficient method to solve the equation is given by Mitrovica and Peltier (1991). Subsequent improvements include the implementation of time-dependent continent margins (Johnston, 1993) and rotational feedback (Milne and Mitrovica, 1998; Peltier, 1998). Here the description of Kendall et al. (2005) is followed closely, but rotational feedback is not implemented.

Table 2.1: Elastic parameters for the Earth model used with the normal mode method.

layer	depth [km]	density ρ [kg/m^3]	rigidity μ [x10^{11} Pa]
1	0-115	3192	0.60
2	115-400	3442	0.73
3	400-670	3882	1.10
4	670-1171	4527	1.81
5	1171-2891	5084	2.41
6	2891-6371	10925.0	0

Coding of the sea level equation started during the author's MSc thesis at the TU Delft. The self-consistent sea level and time-dependent ocean margins were implemented after that. The code makes use of a spherical harmonic transform by Dr. Pieter Visser, which uses a Fast Fourier Transform routine by Dr. Ernst Schrama, both of TU Delft.

This section reviews some of the concepts and equations needed to compute a self-consistent sea level, given the surface load prescribed by global ice histories and the solid Earth response computed with the normal mode theory. It is assumed that the reference Earth is a spherical Earth with radius a_e. The reference equipotential surface is the surface of this sphere. After loading and unloading, the geoidal and solid surface deviate from the spherical surface by an amount ΔG and ΔR, respectively. The sea level difference is defined as the difference between these amounts (Mitrovica and Peltier, 1991):

$$\Delta SL = \Delta G - \Delta R\,. \tag{2.10}$$

The Δ symbol denotes change, which is defined here as difference between the epoch under consideration ($t = t_j$) and the start of glaciation ($t = t_0$). δ denotes a difference between two quantities at subsequent time steps, which will be called 'increment'. The words 'sea level' are used in this section when the global field is meant, and 'ocean depth' when the change in water height over the world's oceans is meant, which is the projection of equation (2.10) on the ocean surface.

The continent-ocean margins are not constant throughout a glacial cycle but depend on the topography and the reference equipotential surface. Since topography before the ice age is not well known, one has to start with the present-day topography T_p and work backwards to find the initial topography T_0:

$$T_0 = T_p + \Delta SL_p \, . \tag{2.11}$$

Given initial topography, the topography at time t_j follows from the initial topography in combination with sea level from equation (2.10). Then, the ocean area at time t_j can be defined as areas of negative topography taking into account the presence of ice in ocean areas and checking whether the ice is grounded or not (Milne, 2002).

To avoid clutter, the latitude and longitude dependence of spatial quantities is not made explicit. Time steps are indicated by subscripts j, with j running from $j = 0$ (at the start of glaciation) to $j = N$ (at present). It is implicitly assumed that there is no remaining effect at the end of the glacial cycle that precedes the last one. This is clearly not true if one assumes that the preceding cycles are the same length as the last one, because otherwise there would be no gravity anomaly and solid Earth displacement remaining at present from the last ice sheet. However, for gravity rate the existence of glacial cycles before the last one are less relevant (Tamisiea et al., 2007).

It is useful to split the sea level change into a spatially varying part and a spatially uniform part:

$$\Delta SL_j = \Delta \mathscr{S}\mathscr{L}_j + \frac{\Delta\Phi_j}{g} , \tag{2.12}$$

where $\Delta\Phi_j$ is the average global shift (uniform) in potential that occurs when water is added to or removed from the oceans. The spherical harmonic coefficients of the spatially varying part of the sea level change are given by (from appendix A.2):

$$\Delta \mathscr{S}\mathscr{L}_{lm,j} = \Delta \mathscr{G}_{lm,j} - \Delta R_{lm,j} = T_l \left[L_{lm}^{j} E_l^{\Delta g} - \sum_{j=0}^{N-1} \delta L_{lm}^{j} \beta_l^{\Delta \mathscr{S}\mathscr{L}} \left(\Delta t \right) \right], \tag{2.13}$$

where $T_l = \dfrac{4\pi a_e^2}{2l+1} \dfrac{a_e}{M_e}$, and the surface load can be specified as the sum of ice and ocean height increments:

$L_{lm,j} = \rho_I \Delta I_{lm,j} + \rho_w \Delta S_{lm,j}$, and

(2.14)

$$\delta L_{lm,j} = \rho_I \delta I_{lm,j} + \rho_w \delta S_{lm,j} \, . \qquad (2.15)$$

A spectral form of the uniform shift in potential is (Kendall et al., 2005, equation 78)

$$\frac{\Delta\Phi_j}{g} = \frac{1}{\mathcal{C}_{00,j}} \left(-\frac{\rho_I}{\rho_w} \Delta I_{00,j} - \mathbb{S}\mathcal{L}_{00,j} \mathcal{C}_{00,j} + T_{00,0} \left(\mathcal{C}_{00,j} - \mathcal{C}_{00,0} \right) \right), \qquad (2.16)$$

It is clear that sea level itself is necessary to compute the terms in equation (2.12). Thus iteration is necessary. For that purpose, it is better to compute the sea level increment, for which can be derived in spectral form as (Kendall et al., 2005, equation 72)

$$\delta S_{lm,j} = -\Delta S_{lm,j} + \Delta\mathbb{S}\mathcal{L}_{lm,j} \mathcal{C}_{lm,j} + \frac{\Delta\Phi_j}{g} \mathcal{C}_{lm,j} - T_{lm,0} \left(\mathcal{C}_{lm,j} - \mathcal{C}_{lm,0} \right), \qquad (2.17)$$

where $\Delta S_{lm,j}$ is the change in ocean height from the start of loading until time t_j ; $\mathcal{C}_{lm,j}$ is 1 for ocean and floating ice and 0 for land or grounded ice, and $T_{lm,0}$ is the initial topography.

Iteration proceeds by computing a first guess for the sea level increment at t_j and then computing the quantities in equation (2.12) using equations (2.13) and (2.16). The next iteration of the sea level increment can be computed by equation (2.17). The initial topography is only known from equation (2.11) after the sea level is known at all time steps. Therefore, another iteration is needed over the entire glacial cycle. Convergence on the *i*-loop is defined by a test on the spherical harmonic coefficients of the ocean height increment. Convergence of the *k*-loop is governed by the sum of differences of spherical harmonic coefficients of the initial topography (Kendall et al., 2005, equations 83 and 86).

In section (2.4), the uniform ocean height approximation is used. In this case, the ocean height at each step is computed by equation (2.17) and (2.16) with $\Delta\mathbb{S}\mathcal{L}_{lm,j}$ and $\mathcal{C}_{lm,j} - \mathcal{C}_{lm,0}$ equal to zero:

$$\delta S_{lm,j} = \frac{\boldsymbol{\mathcal{C}}_{lm,j-1}}{\boldsymbol{\mathcal{C}}_{00,j-1}} \left(-\frac{\rho_I}{\rho_w} \delta I_{00,j} \right). \qquad (2.18)$$

2.2.1 Assumptions: rotation and geocenter motion

Rotational feedback can be included in the solution of the sea level equation (Milne and Mitrovica, 1998; Peltier, 1998), but this is not implemented here. Rotational feedback leads to a degree 2 order 1 pattern, which has the scale of the entire North America (Tamisiea et al., 2002). In terms of geoid rate, the magnitude of the signal in North America is less than 0.1 mm/year (Peltier, 1999, Figure 13). For testing post-processing filters on GIA simulations (section 5.3), the low degree parameters are not important, since they are not at all or hardly affected by the filter. For comparisons of the detailed shape of the gravity rate and inferences related to past ice sheets (section 7.5.2), the magnitude of the rotational pattern is likely also not important. In the viscosity inferences of section (7.6), the neglect of rotational feedback is probably absorbed by the lower mantle viscosity.

Finally, GRACE-derived values for C_{21} and S_{21} are found to be in reasonable agreement with values derived from other techniques, but the level of noise is still much larger than the formal error suggests. Thus, in comparisons with GRACE, the accurate treatment of rotational theory is rendered less important by the level of noise in the Stokes coefficients in which the rotational feedback manifests.

The center of mass of the Earth remains fixed in the orbit around the Sun unless external forces act on it. However, if a surface load is formed of which the center of mass does not coincide with the center of mass of the Earth, the center of mass of Earth plus load moves with respect to a coordinate system that is fixed to the Earth by geometrical means. Observations such as GPS are defined with respect to an Earth-fixed coordinate system, such as the International Terrestrial Reference Frame (ITRF). Thus, geocenter motion caused by GIA has to be accounted for by adding appropriate degree 1 coefficients (Farrell, 1972) when comparing results of surface load models to such observations. In the case of GIA, geocenter motion is induced by transport of mantle material from lower latitude to former glaciated areas at higher latitude. However, degree 1 coefficients are set to zero in GRACE processing (see section 4.1), so, in the comparison between GIA models and GRACE, the degree one coefficients should not be included in the model.

Moreover, the degree one coefficients are not part of the gravity anomaly because of the (l-1) term in equation (A.4). In the comparison between GIA models and GPS data in section (7.5.2), geocenter motion should be accounted for. This is not done in this thesis, thus lower mantle viscosity will probably be biased. By not including degree 1 terms in the computation, also the coupling between degree 1 terms and higher degree terms during the glaciation cycle (Paulson, 2006) is neglected.

2.2.2 Implementation issues

This section describes the spatial grid that is used in the implementation of the sea-level equation and the validation of the computer code. The time steps are determined by the global ice load histories which are described in the next section.

The maximum spherical harmonic degree L that is used is 256. Following Mitrovica and Peltier (1991), spherical harmonic transforms were implemented based on Gaussian quadrature. This leads to an exact spherical harmonic transform for maximum spherical harmonic degree L if the latitudinal nodes are determined by the zeros of a Legendre polynomial of degree $L + 1$. In that case the minimum number of parallels in the spatial field required to be able to obtain spherical harmonic coefficients up to degree L is $L + 1$ (Sneeuw, 1994). The longitudinal increments are: π / L. Thus, the advantage of the exactness of the SH transform comes at the price of having to interpolate all inputs on a Gaussian grid.

The implementation of the sea level equation for an axisymmetric model is compared with a FE model in Wu and Van der Wal (2003), where the excellent agreement between both methods was used as a benchmark for the FE model in that paper, but simultaneously serves as validation for the spectral sea level equation with uniform ocean height approximation. Partial validation of the 3D spectral model is offered by the good (but not perfect) agreement between the spectral method and the 3D FE model in section 3.5. Furthermore, spherical harmonic analysis and synthesis computer codes in FORTRAN are tested with routines in MATLAB. Results of the codes developed based on the algorithms in this chapter are used, amongst others, in Van der

Wal et al. (2004) and Braun et al. (2008). Note that the normal mode code is already validated (Vermeersen and Sabadini, 1997).

Small parts of the sea level equation, i.e., the implementation of the ice loading history and the implementation of the time-dependent continent margin, were not benchmarked before. Thus, a comparison is undertaken with results from other numerical codes presented in the literature; see Appendix B. Benchmarking with computer codes of other groups is hindered by the public availability of computer codes (currently only the code of Spada and Stocchi (2005) is made publicly available) and the differences in implementation of the sea level equation between different groups. Therefore, a comparison of results illuminates the differences in implementation as much as it does possible bugs in programming.

2.3 Global ice models

Details about implementation of the ice loading histories ICE-3G (Tushingham and Peltier, 1991), ICE-4G (Peltier, 1994) and ICE-5G (Peltier, 2004) are given in this section. The ICE-3G and ICE-4G models are shared among researchers. The ICE-5G version 1.2 model is available on the special bureau for loading website (http://www.sbl.statkart.no/projects/pgs/ice_models/Peltier_ICE-5G_v1.2/) and used here. ICE-5Gv1.2 is meant whenever ICE-5G is written in this thesis. Note that this version is different from the version for which results are presented in Peltier (2004); see discussion in section 7.7. For reading and interpolation of the ICE-5G model, use was made of Fortran routines from Dr. Hugo Schotman.

Ice-height increments for ICE-3G and ICE-4G are computed as the difference between ice thicknesses at the current step and the previous step. In the ICE-3G model the difference between ice thicknesses given at two consecutive heights is assumed to melt instantaneously at the beginning of the step. The glaciation of ICE-3G and ICE-4G is assumed to be the reverse of the deglaciation but with time steps of 7 ka. To obtain the total ice thickness used in equation (2.14) the ice thickness of the present day is removed. Even though ICE-3G was based on the non-calibrated C-14 time scale, the time steps are not calibrated in this thesis, to stay close to the original model used in many publications.

ICE-3G is a finite-disc model, i.e., the coordinates of the center of the disc and the radius are given. When the ice thicknesses are interpolated on a grid, holes appear in the ice heights. To remove these holes, an interpolation routine was written to fill the holes with the average of the ice thicknesses around the holes.

ICE-5G also prescribes glaciation. The ice thicknesses at the start of glaciation are subtracted from all ice thicknesses (Peltier, personal communication 2007) which means that it is assumed that the Earth with ice thicknesses at the start of glaciation is the reference state. Since a thick pack of ice is already present in Greenland and Antarctica at the start of glaciation, this reference state influences the comparison with ICE-3G and ICE-4G where ice thickness in those regions is growing linearly from zero. For checking for marine based ice (β in equation (52) of Kendall et al., 2005) the original ice thickness given in ICE-5G should be used, but for equations (2.16) and (2.13) the sum of the increments should be used.

2.4 Models used for testing GRACE filtering

In Chapter 4 GIA models are used to investigate the effect of post-processing filters on the GRACE-derived gravity data. The GIA models that are used for those simulations are discussed below. It was felt necessary to use two GIA models with distinct differences in gravity rate pattern but with a magnitude close to that found in GRACE data. ICE-3G and ICE-5G were used as loading history and the upper mantle and lower mantle viscosities were selected after trial and error to obtain a peak gravity rate in the models that is close to that of GRACE, which is found to be 1.59 µGal/year in Figure 5.28a:

- **i3_8_60**: ICE-3G history, upper mantle viscosity of 8 x 10^{20} Pas, Lower mantle viscosity of 6 x 10^{21} Pas, peak gravity rate 1.55 µGal/year;
- **i5_2_60**: ICE-5G history, upper mantle viscosity of 2 x 10^{20} Pas, Lower mantle viscosity of 6 x 10^{21} Pas, peak gravity rate 1.56 µGal/year;

The gravity rate for both models is shown in Figure 2.2, after smoothing with a Gaussian filter (see section 4.2.3.1) and cut-off at spherical harmonic degree 60. Note that the largest gravity rate for the model with the ICE-3G loading history is southwest of Hudson

Bay, while for the other model it is west of Hudson Bay. Furthermore, the smaller upper mantle viscosity in model i5_2_60 leads to less spatial detail in the gravity rate.

The gravity rate computed with solving the sea-level equation with fully time-dependent ocean margins is shown in Figure 2.3. The maximum gravity rate is 1.63 μGal/year, compared to 1.60 μGal/year in Figure 2.2. This difference is small compared to uncertainties in the model. Therefore, for misfit comparisons the uniform ocean height level approximation is used.

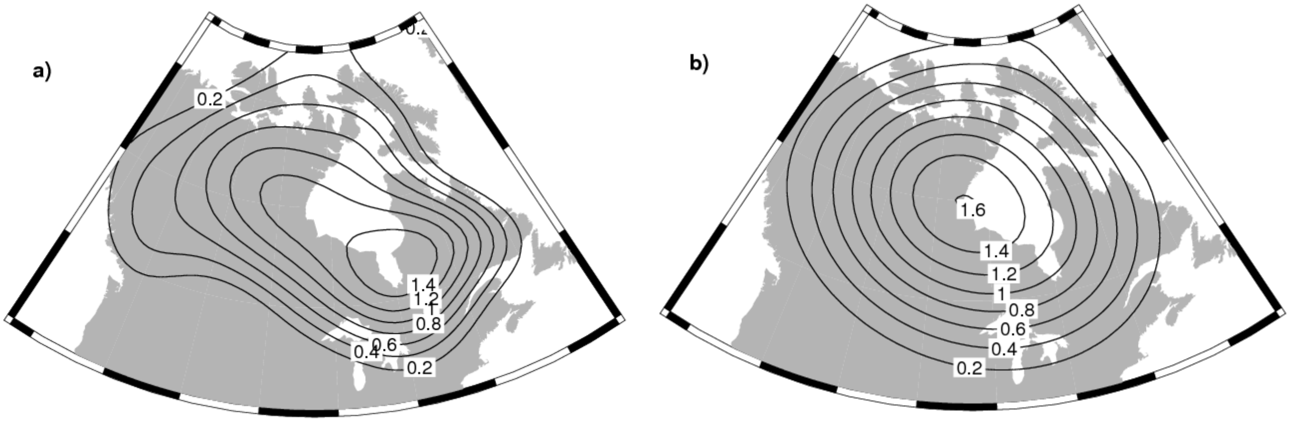

Figure 2.2: Gravity rate from two GIA models after Gaussian filtering with a 400 km halfwidth Gaussian filter (see section 4.2.3.1): (a) i3_8-60 and (b) i5_2-60.

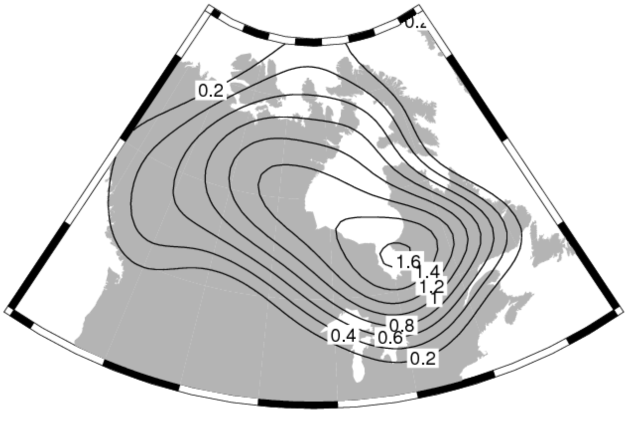

Figure 2.3: Gravity rate for model i3_8-60 with time-dependent ocean margins after Gaussian filtering with a 400 km halfwidth. Maximum gravity rate is 1.63 μGal/year.

2.5 Summary

A GIA model consists of a mathematical model for response of the solid Earth to surface loads and a theory for computing the ice-water redistribution on the deformable Earth as a function of a (global) ice load history. The theory for both components is briefly reviewed in this chapter. Compressibility, rotation and geocenter motion are not implemented, as explained in sections 2.1 and 2.2. The implementation of the theory summarized in this chapter is mainly validated by comparisons with an FE model, as discussed in section 3.5.

A time-dependent ocean-continent margin is implemented, but its effect on the gravity rate is shown to be small enough that time-dependent ocean margins can safely be neglected for misfit comparisons with GIA models with varying viscosity or ice models. Therefore, results in Chapter 5 and Chapter 7 use the uniform ocean height level approximation.

In the following, the term ‘GIA model’ refers to the combination of an ice loading history and viscosity profile. The results of such models are used extensively in Chapter 7 because the spectral methods with uniform ocean height approximation allow quick computation of GIA observables for a range of viscosities.

Chapter Three: Non-linear rheology in a finite element model of GIA

As stated in section 1.1.1 and in the objectives (section 1.2), the predictions of a GIA model with composite rheology is investigated in this thesis. In this chapter, the implementation of composite rheology in a finite element model is described. Results are presented in Chapter 6. A composite rheology consists of a flow law in which the strain rates of diffusion and dislocation creep are added. Thus, both a linear and non-linear flow law are part of such a composite rheology.

The super-position principle does not hold for a non-linear constitutive relation, as different modes are coupled (Wu, 2002b). Spectral methods rely on the superposition of different harmonics, therefore they generally do not work for problems with a non-linear rheology. However, perturbation solutions have been constructed based on spectral approaches to problems with a weakly non-linear medium (D'Agostino et al., 1997; Kaufmann and Wolf, 1999; Tromp and Mitrovica, 2000). In this thesis an existing Finite Element (FE) model of Wu (2004) is used, in which more complicated material behaviour can easily be implemented. However, realistic simulations require the use of large numbers of elements and several iterations which make computations slow.

Non-trivial problems in the implementation of GIA in the FE model are the implementation of buoyancy forces and the coupling of displacement and the gravitational potential in the boundary conditions. These problems and their solution by Wu (2004) are explained in section 3.1. Section 3.2 introduces diffusion and dislocation creep laws along with their numerical and experimental basis. Section 3.3 describes the implementation of composite rheology in the FE model. Section 3.4 lists input parameters used for the FE model. Section 3.5 presents a comparison between the FE and the spectral model of the previous chapter.

For most computations with ABAQUS the Lattice cluster on the Westgrid network (see: www.westgrid.ca) was used. At a later stage, a switch was made to the Terminus cluster at the High Performance Computing Centre of the University of Calgary. Parallel computation could potentially speedup ABAQUS computations, but the number of processing nodes is limited by the number of licenses available for ABAQUS users thus limited or no gain can be expected from parallel processing.

3.1 GIA modeling with the finite element method

A review of the use of the FE method for modeling lateral viscosity variations can be found in Steffen et al. (2006). The earliest use of finite element method in GIA appears to be Sabadini et al. (1986), who modified a code (TECTON) that was developed for subduction. An overview of studies that used the finite element method for visco-elastic relaxation is given in Table 3.1 along with some notable improvements in each of the studies. A more recently developed model is that of Spada et al. (2006). In addition to the FE method, there exist other numerical and perturbation methods for GIA computations with lateral variations in viscosity, see the list in Martinec (2000).

Table 3.1: FE modeling in GIA literature.

Sabadini et al. (1986)	axially symmetric cylindrical	uniform sea level	Wu (2002b, 2004)	3D spherical	self-gravitation
Gasperini & Sabadini (1990)	axially symmetric cylindrical	buoyancy using horizontal integration	Zhong et al. (2003)	3D spherical	built from mantle convection code
Wu (1992)	halfspace	commercial finite element package: ABAQUS	Latychev (2005)	finite volume	compressible (in the short-term limit)
Wu et al. (1998)	3D flat Earth		Paulson et al. (2005)		rotational feedback, but constant elastic properties
Martinec (2000)	3D spherical	FE-spectral			

3.1.1 Formulation of the elastic loading problem

The starting point for the elastic loading problem is the balance of forces, which states that the stresses acting on the surface of the body equal the forces acting on the inside of the body (e.g. Cathles, 1975):

$$\int_S \boldsymbol{\sigma} \cdot \mathbf{n} dS = \int_V \mathbf{b} dV , \tag{3.1}$$

where $\boldsymbol{\sigma}$ is the stress tensor, S is the surface of the body, $\mathbf{n}$ is the normal to the surface, $\mathbf{b}$ is a body force per unit volume, and V is the volume of the body. After applying the divergence theorem it follows that

$$\nabla \cdot \boldsymbol{\sigma} - \mathbf{b} = 0 . \tag{3.2}$$

Equation (3.1) represents force equilibrium, similar to equation (2.1) where the body forces are separated in different terms. Moment equilibrium is satisfied if the stress tensor is symmetric so that there are only 6 elements of the stress tensor at each point in the three-dimensional body. In FE programs, force equilibrium for every particle in the body is replaced by the requirement that force equilibrium holds for a finite number of subdivisions (the elements) of the structure.

A weak form of the differential equations can be derived by multiplying equation (3.2) with a test function $\delta \mathbf{u}^T = \left(\delta u \quad \delta v \quad \delta w \right)$ and integrating over the whole domain:

$$\int_V \delta \mathbf{u}^T \left(\nabla \cdot \boldsymbol{\sigma} + \mathbf{b} \right) = 0 . \tag{3.3}$$

After partial integration and rearranging this can be written as a scalar equation for the entire body. This is the so-called Virtual Work Principle which states that the work done by the internal stresses (or the internal potential energy) is equal to the work done by the surface and body forces. In ABAQUS and in FE methods in general, the Virtual Work Principle is used to find approximate solutions which satisfy equilibrium in some average sense:

$$\mathbf{K}_{ij} \tilde{\mathbf{u}}_j + \mathbf{f}_i = 0 . \tag{3.4}$$

The stiffness matrix $\mathbf{K}_{ij}$ is given by

$$\mathbf{K}_{ij} = \sum_{k=1}^{e} \int_{V_k} \mathbf{B}_i \mathbf{D} \mathbf{B}_j \tilde{\mathbf{u}}_j dV , \tag{3.5}$$

$\mathbf{D}$ contains the elastic moduli (here: Young's modulus E and Poisson's ratio ν):

$$\mathbf{D}=\frac{E}{(1+\nu)(1-2\nu)}\begin{bmatrix}(1-\nu) & 0 & 0 & 0 & 0 & 0\\ 0 & (1-\nu) & 0 & 0 & 0 & 0\\ 0 & 0 & (1-\nu) & 0 & 0 & 0\\ 0 & 0 & 0 & (1-2\nu)/2 & 0 & 0\\ 0 & 0 & 0 & 0 & (1-2\nu)/2 & 0\\ 0 & 0 & 0 & 0 & 0 & (1-2\nu)/2\end{bmatrix} \tag{3.6}$$

and $\mathbf{B}=\mathbf{SN}$, in which $\mathbf{S}$ contains partial derivatives with respect to the global coordinates:

$$\mathbf{S}^T=\begin{bmatrix}\frac{\partial}{\partial x} & 0 & 0 & \frac{\partial}{\partial y} & \frac{\partial}{\partial x} & 0\\ 0 & \frac{\partial}{\partial y} & 0 & \frac{\partial}{\partial x} & 0 & \frac{\partial}{\partial y}\\ 0 & 0 & \frac{\partial}{\partial z} & 0 & \frac{\partial}{\partial z} & \frac{\partial}{\partial z}\end{bmatrix}, \tag{3.7}$$

and $\mathbf{N}$ contains shape functions which approximate the displacement along an element:

$$\delta\mathbf{u}\approx\mathbf{N}\delta\tilde{\mathbf{u}}=\sum_{i=1}^{nn}\mathrm{N}_i\begin{pmatrix}u_i\\ v_i\\ w_i\end{pmatrix} \tag{3.8}$$

where $\delta\tilde{\mathbf{u}}$ is the virtual displacement at the nodes of the element; *nn* is the number of nodes in the element; and $\mathbf{N}$ are the so-called shape functions. A simple example of a linear shape function N_3 for a triangular element with *nn* = 3 is given in Figure 3.1.

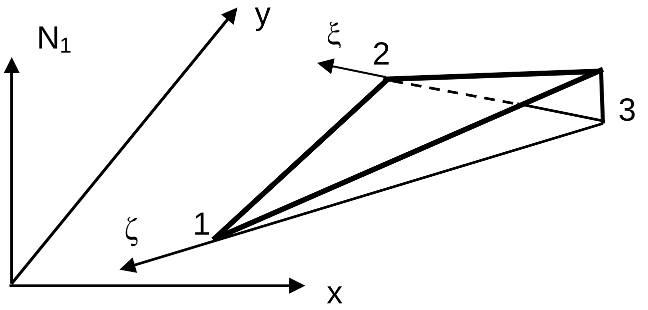

Figure 3.1: Linear shape function (thick solid lines) N_3 for the triangular element 123 (after Figure 2.2 of Zienkiewicz et al., 2005).

In equation (3.4), $\mathbf{f}$ is the load matrix:

$$\mathbf{f}_i = -\sum_{k=1}^{e} \int_{V_k} \mathbf{N}_i \mathbf{b} dV + \sum_{k=1}^{e} \int_{S_k} \mathbf{N}_i \mathbf{t} dS \ , \tag{3.9}$$

where $\mathbf{t}$ are surface tractions. The above formulation also holds if instead of virtual velocity field $\delta\tilde{\mathbf{v}}$ is introduced instead of virtual displacements $\delta\tilde{\mathbf{u}}$, in equation (3.8), and if stress and strain are to be replaced by stress rate and strain rate (ABAQUS Theory Manual, Section 2.1.1).

3.1.2 Equations of motion

Equation (3.2) is the form of the loading problem that is solved by FE methods. Thus, the equation of motion as it applies to geophysical problems has to be cast in the form of (3.4). From equation (2.1) is obtained for an incompressible model (Cathles, 1975; Wu, 2004):

$$\nabla \cdot \boldsymbol{\sigma} - \nabla\left(\mathbf{u} \cdot \rho_o g_0 \mathbf{r}\right) - \rho_0 \nabla \phi_1 = 0 \, , \tag{3.10}$$

The gravitational potential perturbation has to satisfy the Laplace equation, equation (2.2) Comparing equation (3.10) to equation (3.4) shows that the second and third term in equation (3.10) should be included either in the load matrix **f** or in the stiffness matrix **K**. Gasperini and Sabadini (1990) wrote the buoyancy force as a volume integral times displacement so that a term can be added to the stiffness matrix. Wu (2004) applied a stress transformation (his equation 11):

$$\mathbf{t} = \boldsymbol{\sigma} - \left(\rho_0 g_0 u_r + \rho_0 \phi_1\right) \mathbf{I} \, , \tag{3.11}$$

so that equation (3.10) reduces to

$$\nabla \cdot \mathbf{t} = 0 \, .$$

This is equivalent to equation (3.2) with body force zero. Thus, from the load matrix (3.9) the first term disappears, but the tractions remain and are to be introduced as boundary conditions; see the next section.

3.1.3 Boundary conditions

Traction, displacement and potential need to be prescribed on all boundaries (surface, Core-Mantle Boundary (CMB) and internal boundaries). After stress transformation (3.11), the traction boundary conditions are (Wu, 2004; Wu and Wang, 2006)

- Surface: $t_{rr} + \rho_0 g_0 u_r = -\sigma g_0 - \rho_0 \phi_1$; (3.12)
- Internal boundaries (continuity of stress): $\left[t_{rr}\right]_-^+ = \Delta\rho\left(g_0 u_r + \phi_1\right)$; (3.13)
- CMB: $\left[t_{rr}\right]^+ = \left(\rho_c - \rho_m\right) g_0 u_r - \left(\rho_c - \rho_m\right)\phi_1$; (3.14)

where $[\ ]_-^+$ denotes the quantity in square brackets above the boundary, minus the same quantity below the boundary. Terms with $\rho_0 g_0 u_r$ are equivalent to an elastic spring with spring constant $\rho_0 g_0$. Therefore, they can be inserted as Winkler foundation (Wu, 2004). In ABAQUS, the option FOUNDATION is available which requires as input the element number and the spring constant per unit area (ABAQUS analysis user manual sections 2.2.2 and 14.1.3). Gasperini and Sabadini (1990) use a horizontal integration over the elements instead of Winkler foundation, whereas Spada et al. (2006) also use a Winkler foundation. Other terms involving σ and ϕ_1 are inputted as distributed load in ABAQUS.

Displacement should be continuous at internal boundaries but is allowed to vary at the surface and the CMB, so that the boundary conditions are

- surface of the Earth: $u_r = \mathbf{u}\hat{\mathbf{r}}$;
- internal boundaries: $\left[\mathbf{u}\right]_-^+ = 0$; and
- CMB: $\left[\mathbf{u}\right]_-^+ = 0$.

The gravitational potential is continuous at all surfaces: $\phi_1\big|_-^+ = 0$. The potential gradient obeys (Cathles, 1975, p. 19) $\left[\nabla\phi_1 + 4\pi G\rho_0 u_r\right]_-^+ = 4\pi G\sigma$. Therefore, the following boundary conditions can be derived:

- Surface: $\left[\nabla\phi_1\right]_-^+ \cdot \hat{\mathbf{r}} + 4\pi G\left[\rho_0\right]^+ u_r = 4\pi G\sigma$.
- Internal boundaries: $\left[\nabla\phi_1 + 4\pi G\rho_0 u_r\right]_-^+ = 0$;

- CMB: $[\nabla\phi_1 + 4\pi G\rho_0 u_r]_-^+ = 0$.

To form boundary conditions (3.12) to (3.14), the potential perturbation must be known at each boundary. Thus, the Laplace equation is coupled to the FE program through the boundary conditions. First, ϕ_1 is transformed into spherical harmonics so that the radial dependence of the potential is separated from the part that depends on the latitude and longitude of the sphere. It is necessary to assume that the Earth model is made up of shells of constant density. Starting with the solutions at the CMB, one can propagate the solution upwards. The integration constants can be solved for because the surface boundary condition is known. Thus, the spherical harmonic coefficients of ϕ_1 are known at each interface, as required for the boundary conditions, equations (3.12) to (3.14). The steps are outlined in Figure 3.2, together with the steps required to solve the sea level equation; see next section.

3.1.4 Combination with the sea level equation

The sea level equation, given in spectral form in equation (2.17), is an integral equation that requires an iterative solution. Conveniently, iteration required to obtained the self-gravitation term and iteration required for the sea level equation can be performed together (Wu, 2004). The schematic computation is shown in Figure 3.2. As a first guess, the ice-equivalent sea level is computed, after which the displacement at all boundaries can be computed with the FE program. Using the matrix propagation method the potential perturbation can be computed at all interfaces. Then, the sea level change can be computed according to equation (2.12). The ocean function is taken to be time-dependent, as in section. However, for the FE program not the ‘full’ time-dependent continent margin is included, but only ocean inflow in Hudson Bay and the Gulf of Bothnia as ice leaves the ocean area is accounted for (Wang et al., 2006)

To save computation time, it is useful to see the maximum number of iterations that are needed. Wu (2004) found that 4 to 5 iterations are sufficient in general. Table 3.2 shows the misfit with respect to 30 RSL observations, for three different rheologies with the ICE-5G model. Misfit is the statistic used to compare models with data in this thesis, see section 6.4. It demonstrates that after iteration 2, differences with the final (iteration 4) number are small, so that when the best absolute misfit is not the goal, the computation can be stopped after the iteration 2. This is the case for the investigation of modifications in the ice thickness (section 6.6). Computation with 3D models with the original ICE-5G model are done with 4 iterations because a best fitting model is searched.

3.2 Constitutive relations

As stated in section 1.1.1, evidence for a non-linear rheology comes from micro-physical studies and laboratory studies experiments that observe dislocation creep in mantle materials under simulated mantle loading conditions. This section reviews some of that evidence and discusses how the creep laws are implemented in the FE model.

3.2.1 Steady-state creep from microphysics

This thesis assumes that GIA is governed by steady-state creep (section 2.1). However, within steady-state creep many creep mechanisms exist based on micro-physical theory (Ranallli, 1995, p. 314). For different reasons not all stresses are relevant for geodynamic processes and the most common and most relevant types of creep are diffusion and dislocation creep (Ranalli, 1995, p. 374).

The one-dimensional diffusion creep law can be written as (Ranalli, 1995, p. 321)

$$\dot{\varepsilon} = \alpha \frac{D_{diff}\,\mu\Omega_A}{kTd^2}\left(\frac{\sigma}{\mu}\right), \qquad (3.15)$$

where α is a proportionality constant; D_{diff} is the diffusion coefficient; μ is the rigidity; Ω_A is the atomic volume; k is Bolzmann’s constant; T is temperature; and d is the average grain size (diameter). The diffusion coefficient D_{diff} can be split in a part due to diffusion through the crystal lattice (Nabarro-Herring creep) and a part due to grain boundary diffusion (Coble creep).

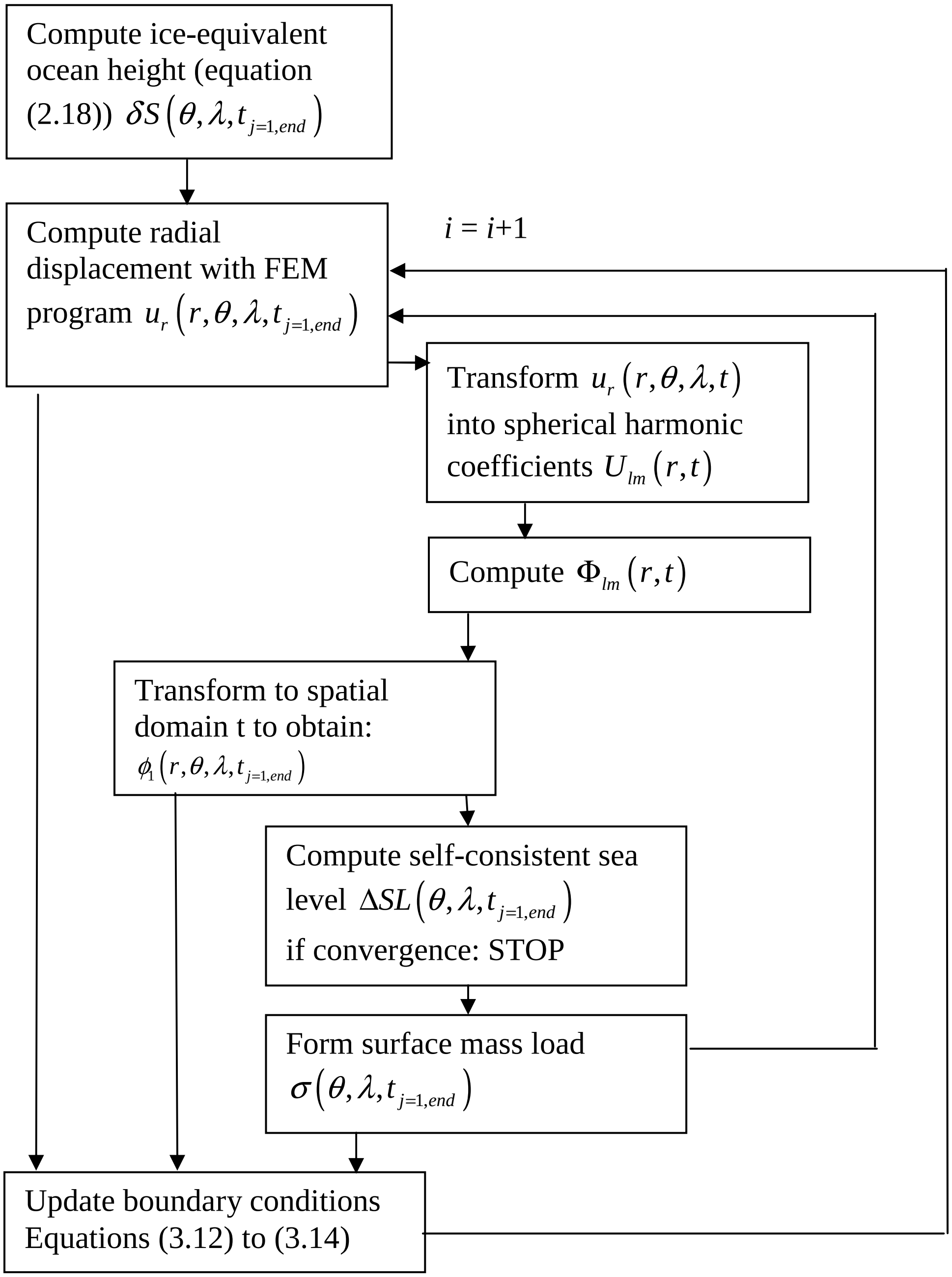

Figure 3.2: Flowchart of the steps required to compute GIA observables with the coupled Laplace FE method and the self-consistent sea level equation (Wu, 2004). Subscript *j* denotes the time-step, subscript p denotes the radial interface in the Earth model, and *i* is an iteration counter.

Table 3.2: Misfit between prediction and RLS observations at 30 sites, for different iterations of the coupled FEM-Laplace method.

iteration	1	2	3	4
n3A34s	47.70	47.61	47.55	47.55
n3A35s	52.46	53.81	53.84	53.80
n3A36s	57.84	59.73	59.70	59.61

If we assume that grain-boundary diffusion is dominant (which it likely is, see Hirth and Kohlstedt, 2003) the diffusion coefficient is

$$D_{diff} = \frac{\pi\delta}{d} D_{GB}\,, \tag{3.16}$$

where δ is the grain boundary width (more precisely the diffusion path, which can be larger than the average grain size *d*); and D_{GB} is the diffusion coefficient for grain boundary diffusion. Then equation (3.15) becomes

$$\dot{\varepsilon} = \alpha \frac{D_{GB}\mu\delta\Omega}{kTd^3}\left(\frac{\sigma}{\mu}\right). \tag{3.17}$$

The one-dimensional dislocation creep law can be written as

$$\dot{\varepsilon} = A_{dis}\frac{D_0\mu b}{kT}\left(\frac{\sigma}{\mu}\right)^n \exp\left(-\frac{E+pV}{RT}\right), \tag{3.18}$$

where A_{dis} is a proportionality constant; and *b* is the inter-atomic spacing. From equations (3.17) and (3.18) it is clear that dislocation creep dominates at high stress and coarse grain size, while diffusion creep dominates at low stress and small grain size.

3.2.2 Steady-state creep from experiments

Material tests are performed mostly in uni-axial compression, in which a stress σ_T is applied to a specimen (see Figure 3.3) and the corresponding strain rate in the horizontal direction is $\dot{\varepsilon}_T$ measured.

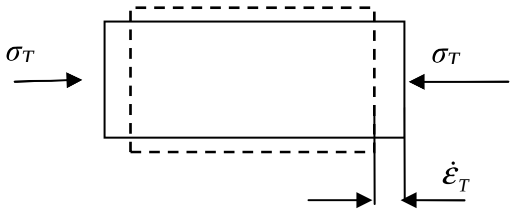

Figure 3.3: Uni-axial compression test on specimen with unit length.

If the load is held constant and deformation is measured, the test is a creep test (Ranalli, 1995, p. 306). Such tests find general stress-strain relations of the following form (Hirth and Kohlstedt, 2003):

$$\dot{\varepsilon} = A_D \sigma^n d^{-p} fH_2O^r \exp(\alpha\phi) \exp\left(-\frac{E+pV}{RT}\right), \tag{3.19}$$

where A_D is a dimensionality constant; n is the stress exponent; p is the grain size exponent; fH_2O is the water content; r is the water content exponent; α is a constant; and ϕ is the melt fraction. This equation is based on laboratory results, it does not address all sensitivities found in the real Earth such as lattice preferred orientation and phase transition.

3.2.3 Implementation

Following Gasperini and co-workers, only the stress-dependence of diffusion and dislocation creep is modelled, while it is assumed that all other material parameters are constant in the mantle. Thus, equation (3.19) is simplified to:

$$\dot{\varepsilon} = A\sigma^n . \tag{3.20}$$

All parameters in the creep rate equation (3.19) influence the final strain rate. However, from these parameters only stress and grain size influence the two deformation mechanisms in different ways. Diffusion creep is enhanced by low stress and small grain size (Karato and Wu, 1993). Since the grain size exponent is 2 or 3 (Ranalli 1995, p. 321) while the stress exponent can be 3 to 4, the stress is somewhat more important in deciding which of the two deformation mechanisms is dominant. Moreover, stress is derived from the glacial surface loading, which is already input to a GIA model. Therefore, it seems more natural to start by examining the stress-dependence of GIA relaxation rather than the grain-size dependence.

For a long time, the belief was held that in the presence of a large background stress the postglacial stress-strain rate relationship can be linear (Turcotte and Schubert, 2002 and Karato, 1998). However, such analysis is based on a simple scalar treatment of non-linear rheology. Schmeling (1987) already showed that in a tensor description glacial rebound sees an approximately linear rheology only when glacially induced stress is much smaller than tectonic stress, which is not the case in formally glaciated areas. Therefore, non-linear rheology is expected to markedly change the glacial isostatic response and has in fact been shown to do so (Wu, 1995, Wu, 2001). Moreover, the concentration of stress around the edges of the ice sheet causes a low effective viscosity which can affect the depth sensitivity of GIA observables compared to a purely linear rheology.

In the following, a short review will be given on some experimental results from which a value of A can be deduced. For all laboratory results it is important to realize that experiments do not take place under exact mantle conditions. Scaling relations have to be applied to transform the findings to realistic mantle conditions. The largest extrapolation is in stress conditions (Hirth and Kohlstedt, 2003), but also extrapolation to higher pressure conditions of the mantle (Karato and Wu, 1993) and the more diverse chemical environment in the mantle (Ranalli, 1995, p. 376) can cause differences between laboratory results and mantle rheology. Moreover, experimental results also have to account for the presence of water and single crystals versus polycrystals.

For the value of the stress exponent n Hirth and Kohlstedt (2003) conclude that 3.5 +/- 0.3 is a likely value for both wet and dry conditions. Ranalli (1995) p. 328 finds $n = 3.0 +/- 1.0$. For the model computations in Chapter 6, the stress exponent is taken to be $n = 3$ and is not varied, because RSL data cannot discern between $n = 3$ and $n = 4$ (Wu, 2002a; Wu and Wang, 2008).

Values for the remaining parameters of equation (3.19) for dislocation creep are given in table 1 of Hirth and Kohlstedt (2003). Pressures and temperatures at a depth of

200 and 400 km are read from Ranalli (1995) Figure 7.9. A typical grain size is a few mm; here a value of 1 cm is used, in agreement with Hirth and Kohlstedt (2003) table 1. With these assumptions, the values of *A* (for dislocation creep) and η (for diffusion creep) in

Table **3.3** are computed. It is clear from

Table **3.3** that the experimentally determined parameters in equation (3.19) can not pin down the pre-stress exponent to an order of magnitude. It is here that GIA studies can play a role to provide a constraint for a pre-stress exponent averaged over the mantle.

Wu and Wang (2008)'s computations lead to a value of A between 10^{-35} $Pa^{-3}s^{-1}$ and 10^{-36} $Pa^{-3}s^{-1}$. Moreover, values of A from 10^{-36} to 10^{-34} $Pa^{-3}s^{-1}$ agree with effective viscosities of 4 x 10^{18} to 4 x 10^{22} Pas if the stress is taken to be 3 to 30 MPa. These viscosity values are also found with linear rheology (see e.g. Mitrovica, 1996; Peltier, 1998; Kaufmann and Lambeck, 2002) and composite rheology (Gasperini et al., 2004; Dal Forno and Gasperini, 2007). Thus, in Chapter 6 *A* will be varied between four values: 3.3 x [10^{-33}, x 10^{-34}, x 10^{-35}, x 10^{-36}] $Pa^{-3}s^{-1}$ and the Newtonian viscosity will be varied from [1,3,9] x 10^{21} Pas.

Table 3.3: Values of the pre-stress exponent for dislocation creep and diffusion creep for two depths and a range of temperatures**.**

Depth	P	T	A [$Pa^{-3}s^{-1}$]		η [Pas]	
[km]	[GPa]	[K]	dry	wet	dry	wet
200	6	1200-1800	2 x 10^{-40} – 2 x 10^{-31}	2 x 10^{-40} – 8 x 10^{-31}	7 x 10^{22} Pas – 7 x 10^{16}	5 x 10^{26} – 2 x 10^{20}
400	13	1550-1800	1 x 10^{-37} – 2 x 10^{-34}	4 x 10^{-39} – 3 x 10^{-35}	2 x 10^{20} – 1 x 10^{18}	6 x 10^{24} – 3 x 10^{22}

3.2.4 Diffusion or dislocation creep in the mantle?

This section reports on evidence about the presence of diffusion and dislocation in the upper and lower mantle.

3.2.4.1 Upper mantle

Dislocation creep likely gives larger strain rates than diffusion creep at a depth starting below the lithosphere up to 200-300 km depth (Karato and Wu, 1993). The depth at which the transition for dislocation to diffusion creep occurs is most sensitive to values of the activation volume and grain size (Hirth and Kohlstedt, 2003). Grain size changes can be accomplished by different mechanisms, one of which is dynamic recrystallization. It is observed that dynamic recrystallization tends to act so that the strain rates of diffusion and dislocation creep approximately balance (de Bresser et al., 1998). Thus, grain size reduction might not be as important for stimulating diffusion creep, or an entirely different mechanism must be responsible for grain size changes, independent from the deformation mechanism. Ranalli (1995), p. 376 also observes that for stresses 1-10 MPa and grain size of 10-1000 µm, both creep mechanisms are competitive. Finally, a geodynamics study by Van Hunen et al. (2005) finds dislocation creep in the upper mantle below the Pacific up to a depth of 410 km.

3.2.4.2 Lower mantle

Literature cited by Ranalli (1995), p. 379, on micro-physical models favours non-Newtonian rheology in the lower mantle, although experiments on the most abundant lower mantle material (perovskite) show both diffusion and dislocation creep. Stresses below 1 MPa and grain size smaller than 1 mm should result in diffusion creep (Ranalli 1995, p. 380-381). Figure 3.4, copied from Ranalli (1995) Figure 12.7b, shows predominantly dislocation creep in the lower mantle.

3.2.5 Tensor form of dislocation creep

In order for equation (3.20) to be useful for a GIA model, it should be reworked into tensor form. Derivation of the tensor formulation following Ranalli (1995) is given in Appendix C from which the result is equation (C.8):

$$\dot{\tilde{\varepsilon}}_{ij} = \frac{3}{2} A\tilde{q}^{n-1} S_{ij}\,, \tag{3.21}$$

where $\dot{\tilde{\varepsilon}}_{ij}$ is an element of the deviatoric strain tensor that agrees with the definition of Mises equivalent stress (see equation (C.5)); S_{ij} is an element of the deviatoric stress tensor; and $\tilde{q}$ is the Mises equivalent stress (see equation (C.4)). Defining the viscosity as

$$\eta_{eff} = \frac{S_{ij}}{2\dot{\tilde{\varepsilon}}_{ij}} \tag{3.22}$$

it follows that the effective viscosity is equal to

$$\eta_{eff} = \frac{1}{3A\tilde{q}^{n-1}}\,. \tag{3.23}$$

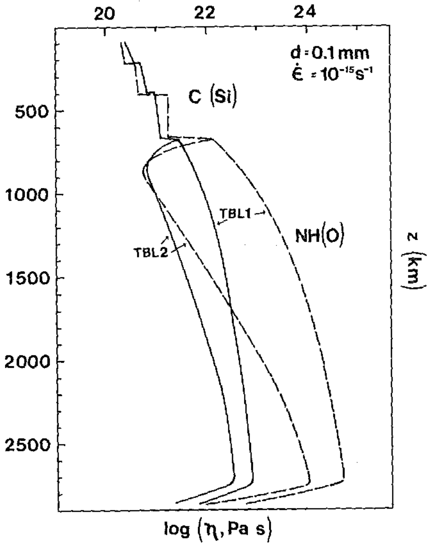

Figure 3.4 (Figure 12.7b from Ranalli (1995): Solid lines denote dislocation creep, dashed lines denote diffusion creep. TBL1 and BL2 are two different temperature profiles, C and NH denote two different diffusion mechanisms.

Note that the A used here is that used in ABAQUS, i.e. the pre-stress constant determined from a uni-axial stress experiment (Schotman, 2008). If A_{sh} from a shear stress experiment is available, the uni-axial A can be computed as

$$A = \frac{2}{3^{(n+1)/2}} A_{SH} . \qquad (3.24)$$

Previous studies have also used the uni-axial A (Wu, 1995; 2001; 2002; Wu and Wang, 2008).

Power-law creep can be implemented in a time hardening and stress hardening form as simple uni-axial law. Since hardening and softening are assumed to be in balance place for steady-state creep, the hardening functionality is not necessary and the simpler of the two (time-hardening) can be used:

$$\dot{\tilde{\varepsilon}} = A\tilde{q}^n t^m , \qquad (3.25)$$

where t is time. The accuracy of integration of the creep law (3.25) influences the computation time. This is explained in more detail in Appendix D.

3.3 Composite rheology in the finite element model

GIA Studies with power-law creep have mostly assumed power-law creep and diffusion creep to be mutually exclusive and restricted to certain layers (e.g. Wang and Wu, 2008). However, diffusion creep and dislocation creep are concurrent, and their strains are additive (Ranalli 1995, p. 326). Therefore, a composite rheology might be a better approximation of deformation in the real Earth (Ranalli, 2001; Korenaga and Karato, 2008). In this thesis a simple model of composite rheology is implemented in the GIA model discussed in the previous sections. The modeling aims to contribute to the following fundamental questions:

i) Can composite rheology better explain available GIA data? If so, predictions of existing GIA models based on linear rheology may need to be revised.

ii) What constraints does GIA modelling offer if the true rheology is of composite type?

A model in which creep rates from diffusion and dislocation creep are added can be found in Bird et al. (1960) where it is called the Ellis model. Parmentier et al. (1976) used this model in mantle convection and a similar model is used by Van den Berg et al. (1993). Gasperini et al. (1992) have introduced the first application of composite rheology in GIA modeling. This study is followed by Gasperini et al. (2004), Dal Forno et al. (2005), and Dal Forno and Gasperini (2007). Recent geodynamic studies not focused on GIA that use composite rheology include Podolefsky et al. (2004) and Becker (2006).

Composite rheology is defined as

$$\dot{\varepsilon}_{ij} = \frac{S_{ij}}{2\eta} + \frac{3}{2} A\tilde{q}^{n-1} S_{ij} = \left(\frac{3A_{n=1}}{2} + \frac{3}{2} A\tilde{q}^{n-1} \right) S_{ij}, \tag{3.26}$$

where equation (3.23) is used. η is the Newtonian viscosity which is related to $A_{n=1}$ by: $\eta = 1/(3A_{n=1})$, and other quantities are as defined before. The formulation is the same as Gasperini et al. (1992) and Giunchi and Spada (2000), except that here it is preferred to keep the creep parameter A as input parameter instead of the transition stress. The transition stress is the value of the effective stress where the strain rate from diffusion creep and dislocation creep are equal (Dal Forno et al., 2005):

$$A_{SH} = \frac{1}{2\eta * \sigma_T^{n-1}}, \tag{3.27}$$

and the uni-axial A can be computed with equation (3.24).

As stated in section 3.1.2, a transformation of stress, equation (3.11), is necessary to be able to treat the Earth loading problem in a commercial FE program. Thus, the stresses that are computed with ABAQUS are the transformed stresses, but the implementation of the uni-axial creep laws needs the true stresses. Therefore, we would need to take the stress computed in ABAQUS, transform with equation (3.11) and take the deviatoric part. However, since the second term in equation (3.11) contains only elements on the diagonal, they will not enter the deviatoric stress and the Mises stress computed by ABAQUS can be used directly in the creep law.

Power-law creep and linear creep law can be implemented using the standard CREEP command in the main ABAQUS input file. For a composite rheology, user-subroutine CREEP can be used to specify a stress-strain relationship other than the ones that are built in. Thus, the uni-axial composite rheology in the user subroutine is specified as follows:

$$\dot{\varepsilon} = A\tilde{q}^n + A_{n=1}\tilde{q}\,. \tag{3.28}$$

From equation (3.28) and equation (3.23) it can be shown that, for n =3, the transition stress at which the strain rate from linear and nonlinear rheology are equal, is

$$q_t = \frac{1}{\sqrt{3\eta A}} \tag{3.29}$$

The use of the subroutine is further tested by specifying a purely linear and purely non-linear law and compare the output with the standard implementation of power-law creep using the CREEP, LAW=TIME command. Figure 3.5 shows that they are almost identical.

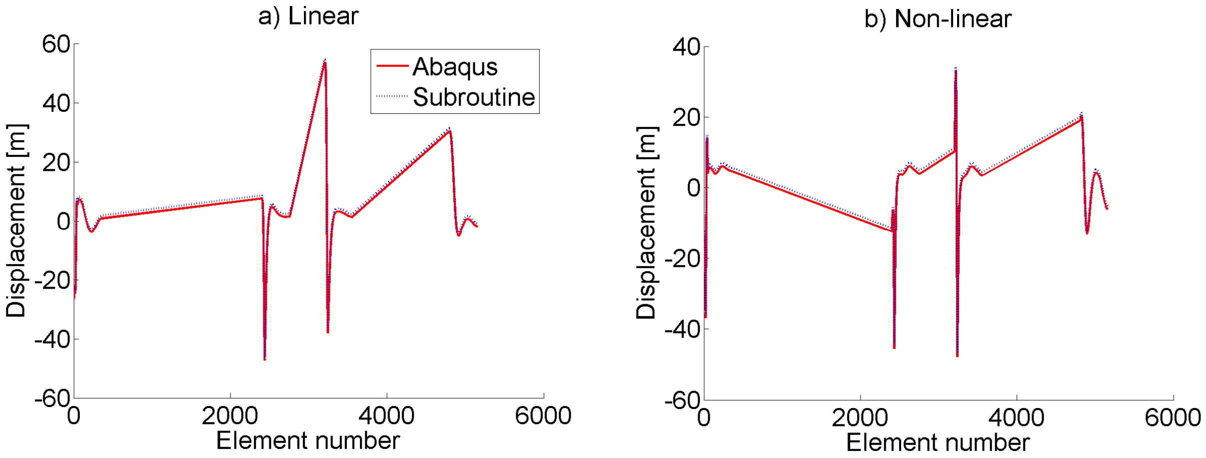

Figure 3.5: Comparison of displacement computed with subroutine and ABAQUS internal routine for (a) linear rheology (b) non-linear rheology. The blue line is shifted upward by 1 m to make it visible.

The subroutine is implemented in the 3-D self-gravitating spherical Earth (Wu, 2004; Wang and Wu, 2006; Wang et al., 2006). Because the large number of elements makes computation long and visualization cumbersome, the axisymmetric model of Wu and Van der Wal (2003) is also used for visualizing the stress distribution and for studying the effect of ambient stress.

3.3.1 Background stress

Gasperini et al. (1992), Giunchi and Spada (2000), Dal Forno et al. (2005) and Dal Forno and Gasperini (2007) include background stress as scalars. However, background stress is a tensor and can both increase and decrease the effective viscosity of power-law creep and hence the scalar sum of the background stress and the rebound stress only simulates the special case where the directions of the stress are parallel and of the same order of magnitude. Schmeling (1987) showed that the effect of background stress on rebound stress depends on direction. His argument will be repeated here, using Mises stress instead of the second invariant of the stress tensor, and with rebound stress being the primary (p) stress and convective stress being the secondary (s) stress.

Effective viscosity is given in equation (3.23) as

$$\eta_{eff} = \frac{1}{2A\sigma'^{\,n-1}_{E}} = \frac{1}{3Aq^{n-1}}\,. \tag{3.30}$$

Therefore, for constant *A*, the effective viscosity is proportional to q^{1-n}. When a primary and secondary stress co-exist, the Mises stress is computed as follows:

$$q = \sqrt{\frac{3}{2}\sum_{i,j}\left(\sigma_{ij}^{p} + \sigma_{ij}^{s}\right)^{2}}\;, \tag{3.31}$$

where superscript *p* denotes the primary and superscript *s* the secondary stress. Schmeling (1987) distinguishes three cases:

1). Stresses are parallel and have the same sign. For example: $\sigma_{11}^{s} = \sigma_{11}^{p}$. Substituting this in equation (3.31) yields

$$q = \sqrt{\frac{3}{2}\left(2\sigma_{11}^{p}\right)^{2}} = 2q_{p}\,. \tag{3.32}$$

It follows from equation (3.30) that the effective viscosity is reduced by a factor $2^{(1-n)}$ or ¼ for $n = 3$. Similarly, for orthogonal stresses, $q = \sqrt{2}q_{p}$, and for stresses parallel but with opposite sign: $q = \frac{1}{3}q_{p}$. Thus, a simplification as in Gasperini et al. (1992) where stress from rebound and convection are simply added only illuminates one of the possible scenarios where the primary and secondary stresses are in the same direction and approximately of equal magnitude.

3.4 Details of the model

The FE model consists of 12 layers, i.e., 2 layers for each layering in the Earth model. The grid is $2^o \times 2^o$, with mesh refinement under the ice sheet. For the elements at the north and south pole of the FE model a 6-node linear triangular prism (hybrid with constant pressure). All other elements are eight-node linear bricks. These elements are of second order, which means that the shape functions defined in equation (3.8) are of second order. Hybrid elements are used to remove a singularity that occurs because of the incompressibility of the material.

3.4.1 Elastic parameters

A 6-layer Earth model is used with elastic parameters given in Table 3.4. It is identical to the model used in Wu and Wang (2008) except that a 150 km thick lithosphere is used here instead of 115 km, and the model here is incompressible (see next section). Note that the density in the core and the lower part of the lower mantle differ from those in Table 2.1 but these differences are small.

3.4.2 Poisson ratio and compressibility

In the finite element model used in this thesis, the Poisson's ratio is taken to be 0.5, which corresponds to the theoretical limit of an incompressible fluid (Turcotte and Schubert, 2002, p. 107). Seismic wave velocities actually yield much lower Poisson ratios (0.28-0.50, see Turcotte and Schubert, 2002, Appendix F). However, these lower ratios imply a compressible material, which is harder to implement fully in the surface load theory (Wu, 2004). Compressibility consists of material compressibility and the effect of compressibility on internal buoyancy (Klemann et al., 2003). Although these effects can not be separated in the real world, one can employ a Poisson ratio smaller than 0.5 to include material compressibility, but neglect the effect of compressibility on buoyancy forces to avoid the instabilities associated with this effect (Klemann et al., 2003). This is indeed the approach followed by Wu and Wang (2008), who use a Poisson ratio in the order of 0.28, see their table 1. The instabilities are described in the ABAQUS Analysis User Manual as: "a very small change in displacement produces extremely large changes in pressure. Therefore, a purely displacement-based solution is too sensitive to be useful numerically". The selection of hybrid elements mitigates the sensitivity.

Table 3.4: Elastic constants used for ABAQUS 3D models.

Layer	r (km)	ρ (kg/m^3)	g_0 (m/s^2)	E (x10^{11}Pa)	μ (x10^{11}Pa)	ν
Lith	6371	3192	9.815	1.55	0.52	0.50
UM	6221	3442	9.866	1.89	0.63	0.50
TZ	5971	3882	9.969	2.83	0.94	0.50
LM1	5701	4527	10.014	4.60	1.53	0.50
LM2	5200	5074	9.947	6.24	2.08	0.50
Core	3480	10987	10.683	0	0	0

3.4.3 Ice models

The original ICE-4G model is used for deglaciation interpolated at the $2^o \times 2^o$ grid. Ice increase is modeled as a linear ramp. For ICE-5G, interpolation to the $2^o \times 2^o$ grid is performed by the *grdtrack* routine in GMT (Wessel and Smith, 1991). The ice thickness at present is removed from all ice heights. Glaciation is modeled as a linear ice increase up to the LGM at 26 ka BP. Increments are set at 26 ka, 22 ka and 18 ka BP, and from there on every 1 ka up to present. Smaller incrementation between 26 ka and 18 ka does not have a large impact on results.

3.5 Comparison with the spectral model

The axisymmetric FE model was benchmarked in Wu and Van der Wal (2003) where agreement was found to be excellent. In this section, the 3-D FE method of this chapter is compared with the spectral method of the previous chapter for the ICE-5G model.

Differences in the implementation of both methods are (except for different methods to solve the differential equations) are:

- Glaciation: In ABAQUS a ramp is assumed from the load at the beginning of the step to the end of the step. In the spectral code Heaviside increments are used.
- The ocean function is partly time-dependent in the FE method. In the spectral method the ocean function can be fully time-dependent or ice-equivalent meltwater can be used at all time steps.

The Earth model used is given in Table 3.4. The normal mode codes use the shear modulus, which can be calculated from Young's modulus and Poisson's ratio by

$$\mu = \frac{E}{2(1+\upsilon)} . \tag{3.33}$$

The spatial grid of the spectral sea level equation codes was changed to the $2^o \times 2^o$ polar grid that ABAQUS uses. The $2^o \times 2^o$ grid of the spectral method still starts at a latitude of 89 degree while the grid of ABAQUS starts at 90. Interpolation from one to the other grid was found to have negligible influence. The maximum degree in spherical harmonic expansions is 90. The difference between the full sea level equation and the melt water equivalent sea level is not important for the comparison (not shown). ICE-5G files are interpolated from the same ICE-5G files as the ice model used in ABAQUS, using the same interpolation method.

The differences in uplift rates between the FEM and spectral computation are shown in Figure 3.6. Interpolation is done by the *grdtrack* routine of GMT (Wessel and Smith, 1991), which uses bi-cubic interpolation. It can be seen that the differences are below 1 mm/year everywhere except for Baffin Island. These values are similar to the comparison in Wang et al. (2006).

Factors that could explain the difference could be the integration between ice increments in ABAQUS. ABAQUS applies a linear change from one increment to another, while in the spectral method a Heaviside load is assumed (Wang et al., 2006). It is also possible that increasing the number of elements in the 3-D model beneath the ice load decreases the difference. Relative sea level curves of the two methods match well; see Figure 4 of Wang et al. (2006).

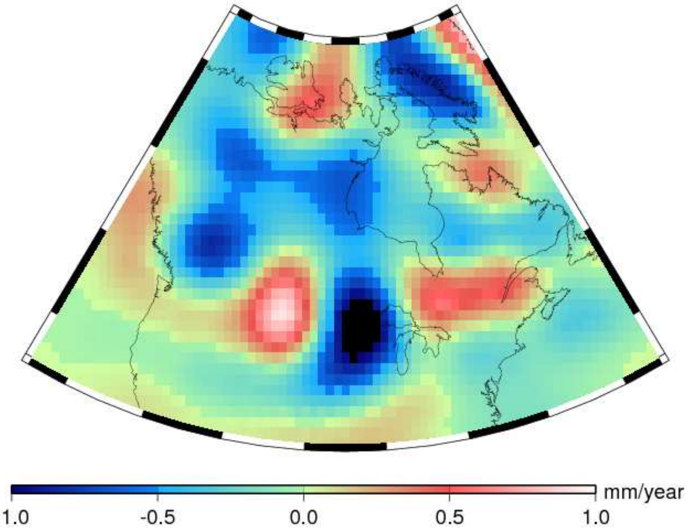

Figure 3.6: Uplift rate ABAQUS minus spectral with maximum spherical harmonic degree 90.

3.6 Summary

From microphysical studies and experiments, two main deformation mechanisms can be distinguished. In diffusion creep the viscosity is independent of stress, whereas for dislocation creep (power-law creep) the effective viscosity depends on stress. From earlier studies, dislocation creep is expected to occur in the upper part of the upper mantle, and a transition to diffusion creep is expected at depths of a few hundred km. In the lower mantle dislocation creep is expected to be dominant. For studying a rheology with power-law creep, the finite element (FE) method is used, because mode-coupling prevents the successful application of spectral methods. The commercial program ABAQUS is used with buoyancy forces, coupled Laplace equation and self-consistent sea level equation implemented as in Wu (2004). Compressibility and degree 1 are not implemented. The presence of background tectonic stress can both increase or decrease the effective viscosity, depending on the direction of the background stress, but is not included in the model. The model is shown to agree with a spectral model discussed in Chapter Two: to within 1 mm/year present day uplift rate.

The constitutive equation that is implemented consists of the summation of dislocation and diffusion creep rates, a so-called composite rheology. In a simplified form of the dislocation creep law, the strain rate depends on the stress exponent n and pre-stress exponent A. In Chapter 6 values of A between 3.3 x 10^{-33} and 3.3 x 10^{-36} $Pa^{-3}s^{-1}$ are used and a stress exponent of $n = 3$ to investigate whether composite rheology improves fit with GIA observations. These values are based on earlier studies with purely non-linear rheology which found reasonable sea level curves and uplift rates for these values of A. The Newtonian viscosity η will be varied between [1,3,9] x 10^{21} Pas.

Chapter Four: GRACE-derived gravity rate for GIA studies - Theory

This chapter deals with the gravity field functionals that are computed from the GRACE Level-2 products and their errors. In the first section, the Level-2 products provided by different processing centers are presented. The second section presents post-processing methods for the Level-2 products available from the GRACE literature and focuses on the methods that are used in this thesis. The third section discusses measurement errors and three different approaches to compute them that are used in this thesis. The final section addresses leakage, which is useful to understand the effect of upward continuation and filtering on the mass changes on the surface of the Earth and in the Earth's interior. In this chapter, MATLAB code from Dr. Nico Sneeuw and Dr. Matthias Weigelt is used with small modifications to do all spherical harmonic synthesis and analysis computations.

4.1 GRACE Level-2 Products

Level-2 products consist of coefficients (and their standard deviations) of a spherical harmonic expansion of a global gravity field at monthly or longer intervals. 'Official' GRACE solutions are provided by three processing centers:

- Center for Space Research (CSR), University of Texas (Bettadpur, 2007b);
- GeoForschungZentrum (GFZ), Potsdam (Flechtner, 2007);
- Jet Propulsion Laboratory, Pasadena (validation solutions) (Watkins, 2007).

More recently, several other groups have processed GRACE data and have come up with their own solutions:

- Centre Nationale d'Études Spatiales (http://bgi.cnes.fr:8110/geoid-variations/README.html);
- University of Bonn (Mayer-Gürr et al., 2007);
- Department of Earth Observation and Space Systems (Liu, 2008).

Results for the different official solutions are "highly comparable" (Schmidt et al., 2008) because background models are standardized in the latest release (4) compared to the first releases of Level-2 products. In this thesis, the CSR data with maximum spherical harmonic degree 60 is mostly used; comparing the different solutions and analyzing their differences is not a goal in this work. For a more detailed comparison of solutions from different processing centers in terms of secular gravity rates in Fennoscandia, see Steffen et al. (2008), who concluded that GFZ solutions produce the largest maximum secular gravity rate with location closest to that expected from uplift rate data in Fennoscandia.

The Level-2 solutions use an a-priori static gravity field in the processing, and it is in this field that there are important differences in solutions from different processing centers. CSR solutions use a combination of GRACE CSR release 2 solutions in combination with EGM96 for the higher degrees (Bettadpur, 2007a). GFZ release 4 solutions use the EIGEN_GL04C static gravity field (Flechtner, 2007). Dynamic parts of the a-priori gravity field include ocean tides, solid Earth tides and atmospheric and ocean variability.

In all solutions, linear trends in the following coefficients are removed: $C_{20}, C_{30}, C_{40}, C_{21}, S_{21}$. Since these coefficients partly contain GIA signal, the secular change has to be added back to the respective coefficients when studying GIA (or any other secular process). This can be done, e.g., for the C_{20} coefficient as follows:

$$C_{20,new}(t) = C_{20}(t) + \dot{C}_{20}(t - t_0), \tag{4.1}$$

where t is the epoch of interest; t_0 is an arbitrary reference epoch and $\dot{C}_{20}$ is the provided secular trend in the C_{20} coefficient. For time t, the midpoint of the data span (usually one month) can be used (Bettadpur, 2007b).

The final product provided by the data processing centers are spherical harmonic coefficients of the geopotential (Stokes coefficients) C_{lm}, S_{lm}, defined in the following expansion of the Earth's exterior geopotential (e.g., Bettadpur, 2007b) at point P:

$$V(r,\theta,\lambda,t) = \frac{\mu}{r} + \frac{\mu}{r}\sum_{l=2}^{L}\left(\frac{a_e}{r}\right)^{l}\sum_{m=0}^{l}\tilde{P}_{lm}(\cos\theta)\left(C_{lm}\cos m\lambda + S_{lm}\sin m\lambda\right), \tag{4.2}$$

where r is the radius of point P; θ is the colatitude of point P; λ is the longitude of point P; μ is the gravitational parameters of the Earth, 0.3986004415 10^{15} m^3s^{-2}; V is the gravitational potential; and a_e is the mean equatorial radius, which is selected to be the value of the Topex/Poseidon reference ellipsoid: 6.378136300 x 10^6 m (6.378136460 x 10^6 m for GFZ fields). For all applications this value can be assumed to correspond to the

Earth's surface. $\tilde{P}_{lm}$ = fully normalized associated Legendre polynomials. The normalization of the associated Legendre polynomials agrees with the usual geodetic definition (e.g., Heiskanen and Moritz, 1967)

$$N_{lm} = \sqrt{\frac{(2-\delta_{0m})(2l+1)(l-m)!}{(l+m)!}}\,, \tag{4.3}$$

where δ_{0m} is the Kronecker delta function.

The C_{20} coefficients derived from GRACE are still noisier than those derived from SLR (Bettadpur, 2008), therefore, in this thesis as in many other references, the C_{20} coefficient in GRACE solutions is replaced by the SLR-derived value. It is shown in Figure 5.27 that the effect of the C_{20} coefficient on the maximum gravity rate is small.

In GRACE data processing, the origin of the reference frame is selected to be at the instantaneous center of mass of the Earth (Bettadpur, 2007a). Therefore, the summation in equation (4.2) starts at degree 2; changes in the location of the center of mass of the Earth cannot be obtained from GRACE data. See Figure 11 of Van der Wal et al. (2008a) and Lee et al. (2008) to get an impression of the possible effect of shift in geocenter on the geoid rate derived from GRACE. It is likely that the neglect of such an effect in the geoid rate does not reduce the sensitivity of GRACE with respect to parameters in the GIA model such as the ice loading history. As can be seen from equation (4.8), degree 1 terms are zero in the gravity anomaly because of the (*l*-1) term.

4.1.1 Computation of gravity field functionals

From the Stokes coefficients, a gravity field functional *F* can be computed by:

$$F(r,\theta,\lambda,t) = X_0 + \sum_{l=2}^{L} X_l \sum_{m=0}^{l} \tilde{P}_{lm}(\cos\theta)\left(C_{lm}(t)\cos m\lambda + S_{lm}(t)\sin m\lambda\right), \tag{4.4}$$

where *L* is the maximum degree in the spherical harmonic expansion of the solution; and

$X_l = a_e$ for the geoid;

$X_l = \frac{(l-1)GM_e}{a_e^{\,2}}$ for free-air gravity anomaly;

$X_l = \frac{(l+1)GM_e}{a_e^{\ 2}}$ for free-air gravity disturbance.

(see e.g., Heiskanen and Moritz, 1967, p. 88/89). a_e is taken to be the Earth's surface. The degree zero term (X_0) is zero for GRACE data processing by convention.

Free-air gravity anomaly (rate) is what is meant when gravity (rate) is written in this thesis. There is no theoretical reason to use gravity anomaly as opposed to gravity disturbance. Gravity disturbance is the radial derivative of the disturbing potential (Heiskanen and Moritz, 1967, p. 85), but gravity anomaly is used here to be consistent with earlier GIA modelling in which gravity anomaly was used. Note that Paulson (2006) and Paulson et al. (2007b) use a definition for gravity rate that corresponds to gravity disturbance. In general, that definition results in enhanced spatial detail and noise, and a slightly higher maximum secular gravity rate.

For geophysical interpretation, only variations with respect to some mean field ($\overline{C}_{lm}$, $\overline{S}_{lm}$) are interesting, therefore, a mean of several years of monthly Stokes coefficients is removed from the coefficients provided in the data files:

$$\begin{aligned} C_{lm}(t) &= C_{lm} - \overline{C}_{lm} \\ S_{lm}(t) &= S_{lm} - \overline{S}_{lm} \end{aligned}, \tag{4.5}$$

to give the coefficients that can be used in equation (4.4).

It is useful to define the transformation between coefficients in a spherical harmonic expansion of a surface mass load (in equivalent water height with units of meter) to Stokes coefficients for simulations of present-day ice melt and continental water storage changes in 5.1.1. Water heights given on a grid can be expanded in terms of spherical harmonics as follows:

$$h(\theta,\lambda) = \sum_{l=0}^{\infty}\sum_{m=0}^{l} \tilde{P}_{lm}(\cos\theta)\left(\hat{C}_{lm}\cos(m\lambda) + \hat{S}_{lm}\sin(m\lambda)\right). \tag{4.6}$$

Note that the $\hat{C}_{lm}$ and $\hat{S}_{lm}$ have units of meters if the water height is given in meters. Here, C_{00} is assumed to be zero, or mass conservation can be enforced by adding a uniform layer to the ocean to make the C_{00} coefficient zero. Degree 1 coefficients are set to zero. The transformation of coefficients $\hat{C}_{lm}$ and $\hat{S}_{lm}$ to the coefficients of equation (4.4) is

$$C_{lm}\left(t\right)=\frac{3\rho_w}{a_e\rho_{ave}}\frac{1+k_{l,e}}{\left(2l+1\right)}\hat{C}_{lm}\left(t\right), \tag{4.7}$$

where ρ_w is the density of water 1000 kg/m^3 (the load is to be defined in 'equivalent water thickness'); ρ_{ave} is the average density of the Earth, 5517 kg/m^3; and $k_{l,e}$ is the elastic load Love number of degree l. Equation (4.7) accounts for the change in gravitational potential due to elastic displacement of the solid Earth. The elastic Love numbers used in this thesis are interpolated from those in Wahr et al. (1998). Equation (4.7) is the same as equation (12) in Wahr et al. (1998) except for a_e because surface mass density is used in that paper instead of equivalent water height. Implicit in this formula is the assumption that all mass changes occur in a thin layer at the Earth's surface. This is valid for continental water storage changes, glacier melting and sea level changes.

In computer code, equation (4.7) can simply be combined with the X_l of equation (4.4) so that the same spherical harmonic subroutine can be used to compute all gravity functionals as well as water height coefficients. The spherical harmonic synthesis will be explicitly given for gravity anomaly computed from spherical harmonic coefficients of a surface load in meter water height

$$\begin{aligned}\Delta g\left(\theta,\lambda\right)=-\frac{3\rho_w\mu}{a_e^{\,3}\rho_{ave}}+\frac{3\rho_w\mu}{a_e^{\,3}\rho_{ave}}\cdot\\ \cdot\sum_{l=2}^{L}\frac{1+k_l}{\left(2l+1\right)}\left(l-1\right)\sum_{m=0}^{l}\tilde{P}_{lm}\left(\cos\theta\right)\left(\hat{C}_{lm}\cos m\lambda+\hat{S}_{lm}\sin m\lambda\right)\end{aligned}. \tag{4.8}$$

For global spherical harmonic analysis, equation (4.6), visual inspection found that the 'approximate quadrature' method (Sneeuw, 1994) resulted in the smallest differences between a hydrology model on a grid, and the same model that is analyzed and synthesized subsequently. Thus, this method was selected to perform global spherical harmonic analysis.

4.1.2 Degree and order variances

For analysing the magnitude of GRACE data and their errors in the spectral domain it is useful to plot the 'information' per degree or order. The quantities that are used in the next chapter are the degree variances, defined as

$$\sigma_l^2 = \frac{1}{2l+1}\sum_{m=0}^{l}\left(C_{lm}^2 + S_{lm}^2\right). \qquad (4.9)$$

Note that this is different from e.g. equation (22) in Wahr et al. (1998), where the term *1/*(*2l*+1) is not included. The units of the degree variance σ_l^2 are the same as the units of the coefficients. Cumulative degree variances are defined as

$$\sigma_{l,cum}^2 = \sum_{k=0}^{l}\left(2k+1\right)\sigma_k^2 \ , \qquad (4.10)$$

where σ_k^2 are computed with equation (4.9). Finally, order variances are defined equivalently to degree variances:

$$\sigma_m^2 = \frac{1}{2\left(l+1-m\right)}\sum_{l=m}^{L}\left(C_{lm}^2 + S_{lm}^2\right), \qquad (4.11)$$

in which $S_{lm} = 0$ for $m = 0$.

4.2 Post-processing GRACE data

Gravity measurements contain a multitude of overlapping signals from mass change processes on or below the Earth's surface, at different length and time scales. Therefore, to isolate signals from GRACE data, inevitably, a-priori knowledge is used about the signals' location and temporal behaviour. For example, GIA behaves linearly over the GRACE time period. This knowledge leads to the application of least-squares estimation of a trend in the presences of seasonal signals, which is described in section 4.2.1.

It can be expected that after filtering the GRACE data, the signal explains most of the filtered data and that in particular GIA is one of the strongest signals in GRACE data. This leads to the technique of Principal Component Analysis (PCA), discussed in section 4.2.2, which looks for orthogonal spatial patterns that explain most of the variance of the signal (Jolliffe, 2002, Rangelova et al., 2007).

Other methods that rely more heavily on a-priori data could also be used, but such methods defy the idea of GRACE providing an independent data set for constraining GIA models. For the purpose of interpolating GIA uplifts stated in the introduction, such a hybrid approach would be acceptable, and indeed it has been developed by Davis et al. (2006). Based on the idea that neither data nor models are perfect, they developed a Kalman filter approach to combine data and models in a statistical optimal way. Rangelova (2007) combined GRACE with GPS and terrestrial gravity data using a least-squares collocation approach. This section discusses the least-squares approach to estimate a secular trend, followed by principal component analysis. The last section presents a classification of filtering techniques and discusses the three filters that are investigated in this thesis.

4.2.1 Least-squares estimation of trend

Since GIA is a secular process, it is sensible to estimate a linear trend in the coefficients and plot the magnitude of this trend on a spatial map. To avoid corruption of the trend by periodic signals, seasonal signals that dominate large scale mass transport should be estimated jointly (see e.g., Wahr et al., 2004). A semi-annual period can be included as well, so that the estimation for the gravity anomaly in each grid point of a spatial map becomes

$$\begin{aligned}\Delta g\left(t_j\right) = {} & k_1 t_j + k_2 \cos\left(\frac{2\pi}{T} t_j\right) + k_3 \sin\left(\frac{2\pi}{T} t_j\right) + \\ & k_4 \cos\left(\frac{2\pi}{T}\frac{t_j}{2}\right) + k_5 \sin\left(\frac{2\pi}{T}\frac{t_j}{2}\right) + v\left(t_j\right)\end{aligned} \tag{4.12}$$

where t_j is time epoch (unit of months); T is 12 months per year; k_1 is magnitude of the trend; k_2 and k_3 are the magnitude of the cosine and sine annual component, respectively; k_4 and k_5 are the magnitude of the cosine and sine semi-annual component, respectively; and $v(t_j)$ is the residuals (they may still contain geophysical signal).

For GRACE, the midpoint of the first and last day used for each monthly solution is used as the time of the *j*-th epoch. In some cases the 161 day tidal aliasing period of the S_2 tidal component is jointly estimated, however, this might no longer be necessary with the improvement of tidal models in Release 4 data, although C_{20} was found to contain significant energy at the 161 day frequency (Chen and Wilson, 2008). It was found here that estimation of signal at a 161 day frequency has a negligible effect on the maximum geoid rate (change of 1.2%).

Weighted least-squares can be used, where a weight matrix $\mathbf{P}$ is populated with the inverse of the variances for each coefficient on the diagonal. The variances are simply the squares of the calibrated standard deviations that are provided by the processing centers. The advantage of such an approach would be that it takes into account the change in accuracy from one month to another, e.g., caused by groundtrack changes, but this is not investigated.

4.2.2 Principal Component Analysis

Principal component analysis (PCA) is a technique to "reduce the dimensionality of a data set while retaining as much as possible of the variation present in the data set" (Jolliffe, 2002). The general idea of the method is given here, after which the implementation of PCA for GRACE data is discussed. For more details, refer to Rangelova (2007), whose software was used for PCA of GRACE data in this thesis. PCA has also been employed for GRACE data processing by Schrama et al. (2007) and Wouters and Schrama (2007) among others.

Assuming that a full signal covariance matrix $\boldsymbol{\Sigma}$ of the dataset $\mathbf{x}$ is known, the aim is to find a linear combination $\boldsymbol{\alpha}_1\mathbf{x}$ for which the quadratic form $\boldsymbol{\alpha}_1^{'}\boldsymbol{\Sigma}\boldsymbol{\alpha}_1$ is maximized with the length of $\boldsymbol{\alpha}_1$ equal to 1. It follows that $\boldsymbol{\alpha}_1$ is the eigenvector of $\boldsymbol{\Sigma}$ with eigenvalue λ_1. For GRACE, the population signal covariance matrix is not known and the sample covariance matrix $\mathbf{S}$ is used instead:

$$\mathbf{S} = \frac{1}{n-1}\mathbf{X}'\mathbf{X}, \tag{4.13}$$

where $\mathbf{X}$ is the data matrix ordered as n rows by p columns, where n is the number of observations (GRACE epochs) and p is the number of variables (the grid points).

A singular value decomposition of the data matrix X is useful for computation purposes and for visualizing the components:

$$\mathbf{X} = \mathbf{U}\mathbf{L}\mathbf{A}^T, \qquad (4.14)$$

where **U** is an n x r matrix that contains the time series; **A** is an r x p matrix that contains the spatial patterns, and **L** is an r x r diagonal matrix with eigenvalues on the diagonal. r = rank of **X**; in case of full rank this will be p, or the number of grid points for GRACE analysis. The columns of **UL** contain the time series, and the columns of **A** are the eigenvectors, which in GRACE data analysis are the spatial patterns of the signal of interest.

PCA uses a-priori information in that it searches for orthogonal spatial patterns and orders these according to their variance. Although there is no outright reason to believe that GIA and other processes and noise separate nicely in orthogonal modes, it is hoped that PCA can help in separating secular from inter-annual signals as PCA does not prescribe the time behaviour in contrast to least-squares. Moreover, 80% of the variance in a global hydrology model is the annual cycle, so that a spatial pattern with an annual or near-annual cycle will be likely found in the first few modes. A generalization of the method is multi-channel singular spectrum analysis investigated for GRACE by Rangelova et al. (2008).

4.2.3 Filtering of GRACE Level-2 products

GRACE data contain spurious north-south stripes (Chen et al. 2005b), which are an artefact of the measurements or the estimation of the gravity-field or the post-processing. The exact cause of the stripe errors is still unknown, although the north-south oriented orbit of GRACE definitely plays a role. Other possible partial causes for the stripes are aliasing (see Figure 2 in Han et al., 2004) and incorrect accelerometer scale and bias parameters needed in the orbit determination process (Schrama et al., 2007). With improved background models in the release 4 models, reduced magnitude stripes are observed. Post-processing is generally done by applying isotropic or non-isotropic filters to the Stokes coefficients before producing mass estimates.

Following Klees et al. (2008), filters can be divided in statistical and deterministic ones. Deterministic filters include Gaussian smoothing (Wahr et al., 1998), the non-isotropic Gaussian filter of Han et al. (2005), and the empirical filter designed by Swenson and Wahr (2006). Deterministic filters can be characterized according to their use of outside information. For example, Swenson and Wahr (2002) use the knowledge of the area of a river basin which is assumed to behave as one system to form an average mass change of the GRACE solutions over this river basin.

Statistical filters include using standard deviations of the coefficients as weights (Chen et al., 2006); filtering using empirical orthogonal functions (Rangelova et al. 2007, Wouters and Schrama 2007); Wiener filtering (Sasgen et al., 2007), and filtering based on statistical testing of the coefficients (Davis et al., 2008). Kusche (2007) and Klees et al. (2008) both relied on a synthetic error covariance matrix and a signal covariance matrix.

A deterministic filter can be easily applied to the spherical harmonic coefficients, and also to geophysical models to allow fair comparison between GRACE data and model results. At the time this work was conducted, the empirical Swenson and Wahr (2006) filter was the most widely used for removing the stripes. Synthetic noise covariance matrices needed for the Kusche (2007) and Klees et al. (2008) methods were not available during the course of this work. The full noise covariance matrix provided by CSR is shown to not describe the correlated errors well (see section 5.2.1). Therefore, this covariance matrix can not be used for the filtering methods of Kusche (2007) and Klees et al. (2008) and hence these filters are not applied in this work. The Swenson and Wahr (2006) filter is suitable for GIA because it can easily be applied to and tuned for GIA models. It is important to keep in mind that in this way the filter only influences the differences between competing GIA models. In other words, if the filter would affect all competing GIA models in the same way, the resolving power of the filtered GRACE data with respect to the GIA models is not reduced.

To counteract the effect of the increased noise with decreasing wavelengths in GRACE observations and to further reduce the stripes, smoothing is applied to equation (4.4). Smoothing can be written in a general form as (Han et al., 2005, equation 4):

$$\bar{F}(\theta,\lambda)=\iint_{\sigma'} F(\theta',\lambda')W(\theta,\lambda,\theta',\lambda')\,d\sigma', \tag{4.15}$$

where $W\left(\theta,\lambda,\theta',\lambda'\right)$ is an averaging function that depends on the locations of the two points with coordinates $\left(\theta,\lambda\right)$ and $\left(\theta',\lambda'\right)$. Decomposing F and W in spherical harmonics yields (Han et al., 2005, equation 5)

$$\bar{F}\left(\theta,\lambda\right)=\sum_{l=0}^{\infty}\sum_{m=0}^{l}\tilde{P}_{lm}\left(\cos\theta\right)\left\{\begin{matrix}\sum_{l'=0}^{\infty}\sum_{m'=0}^{l'}\left(W_{lmc}^{l'm'c}C_{l'm'}+W_{lmc}^{l'm's}S_{l'm'}\right)\cos m\lambda+\\ \sum_{l'=0}^{\infty}\sum_{m'=0}^{l'}\left(W_{lms}^{l'm'c}C_{l'm'}+W_{lms}^{l'm's}S_{l'm'}\right)\sin m\lambda\end{matrix}\right\}, \tag{4.16}$$

where $W_{lmc}^{l'm'c}$ is the coefficient corresponding to the $\cos m\lambda\cos m'\lambda'$ term, $W_{lms}^{l'm'c}$ the coefficient corresponding to the $\sin m\lambda\cos m'\lambda'$, etc. Equation (4.16) without simplification leads to filters based on a full covariance matrix (such as in Kusche, 2007 and Klees et al., 2008). Usually, simplifications such as isotropy are made about the properties of W, which leads to application of the Gaussian filter discussed in the next section.

4.2.3.1 Gaussian filter

The Gaussian filter was developed by Jekeli (1981) and introduced to GRACE data processing by Wahr et al. (1998). It is a simplification of equation (4.16) where the filter is assumed to depend only on the angular distance between the points $\left(\theta,\lambda\right)$ and $\left(\theta',\lambda'\right)$. In the spectral domain, the filter downweighs higher frequencies which are expected to be more corrupted by noise. In the spatial domain, the filter forms a spatial average by convolution with a Gaussian kernel. The weights (filter coefficients *W*) are given by the following recursion (Wahr et al., 1998):

$$\begin{aligned}W_0&=\frac{1}{2\pi}\\ W_1&=\frac{1}{2\pi}\left[\frac{1+e^{-2b}}{1-e^{-2b}}-\frac{1}{b}\right],\\ W_{l+1}&=-\frac{2l+1}{b}W_l+W_{l-1}\end{aligned} \tag{4.17}$$

where:

$$b = \frac{\ln 2}{1-\cos\frac{r_{\frac{1}{2}}}{R_E}} \tag{4.18}$$

$r_{\frac{1}{2}}$ is the halfwidth, or the spatial distance where the filter weight is reduced to one half. Directly programming this equation leads to instabilities, therefore small modifications have to be made to the recursion of (4.17). Here it is chosen to change the last line of the recursion to: $W_{l+1} = -\frac{2l-1}{b}W_l + W_{l-1}$.

4.2.3.2 Non-isotropic Gaussian filter

Han et al. (GJI, 2005) devised a filter where the filter weights depend on degree *l* and order *m*, but they are still independent of locations, such that *W* of equation (4.16) becomes

$$W_{lmc}^{l'm'c} = W_{lms}^{l'm's} = \begin{cases} \frac{W_{lm}}{4\pi} & l'=l, m'=m \\ 0 \end{cases}, \tag{4.19}$$

and all other coefficients are zero. In that case, equation (4.16) reduces to

$$\bar{F}(\theta,\lambda) = \sum_{l=0}^{\infty}\sum_{m=0}^{l} \tilde{P}_{lm}(\cos\theta) W_{lm}\left(C_{lm}\cos m\lambda + S_{lm}\sin m\lambda\right), \tag{4.20}$$

so that the filter can be implemented as element by element multiplication of matrix **W** with the coefficient matrix in the same format. The filter coefficients are computed as follows:

$$\begin{aligned} W_{lm} &= W_l\left(r_{1/2}(m)\right) \\ r_{1/2}(m) &= \frac{r_{EW}-r_{NS}}{m_1}m + r_{NS} \end{aligned}, \tag{4.21}$$

where W_l are the Gaussian filter weights of equation (4.17); r_{NS} is the smoothing radius for zonal components $m = 0$, and r_{EW} is the smoothing radius for $m = m_1$. r_{NS} determines the smoothing in latitude direction, and r_{EW} together with m_1 determines the amount of smoothing in longitude direction. Thus there are three parameters in total. Because of the decreased sensitivity of GRACE in east-west direction, r_{EW} is generally larger; Therefore, more smoothing is applied in the direction in which GRACE is least sensitive.

4.2.3.3 Destriping filter of Swenson and Wahr (2006)

Swenson and Wahr (2006) noted that the stripes observed in the GRACE maps correspond to a correlation in the spectral domain between even and odd degrees for Stokes coefficients of a particular order. They fitted a low order polynomial to a limited interval of coefficients of odd or even degree to describe this correlation. Since this correlation is not expected for natural phenomena, it should be removed from the Stokes coefficients by removing that part of the coefficients that is fit by the polynomial. Some variations to the method exist. For example, wavelet approximation can be used to describe the correlation (Rangelova et al., 2007). The window length and unchanged portion of the Stokes coefficients can be varied based on the order and on the error pattern (Duan et al., 2009). Here the unpublished result for window length of Dr. Sean Swenson and Dr. John Wahr is used, which was kindly provided for this research by Dr. John Wahr and for publication in Duan et al. (2009). Filtered coefficients were compared with filtered coefficients produced by Dr. John Wahr with the routine of Dr. Sean Swenson. Differences without any additional smoothing are small, see Figure 4.1, considering that the original amplitude of the stripes is in the order of centimetres.

In this thesis, the effect of the degree and order below which coefficients are unchanged (cut-off degree and order) is investigated. It should be stressed that for each combination of cut-off degree and order, the coefficients that are used for the polynomial fit can be different, because the window size varies with order, and because the window size might not be symmetric around the coefficient. For example, the $C_{12,12}$ coefficient might be filtered differently depending on whether the cut-off degree is 4 or 10.

4.3 Measurement errors

The term measurement errors as it is used in this thesis includes noise in the observations (accelerometers, star cameras, K-band ranging system), errors in processing and deficiencies in de-aliasing models (atmospheric pressure, ocean model), and omission errors (Gunter et al., 2006). Velicogna and Wahr (2002) investigated the de-aliasing error by using two difference atmospheric pressure fields. They found this error to be relatively small compared to other sources. Using simulations, Gunter et al. (2006) found that errors in the reference gravity field give noticeable errors, but they expect this error source to decrease with increasing GRACE data span. Han et al. (2004) showed that errors in some tidal components in the ocean tide dealiasing model can cause errors that are three times larger than the measurement error. All theses error sources can probably lead to errors that are random in time and space, errors that are confined to a specific location, or to the north-south stripes introduced in section 4.2.3.

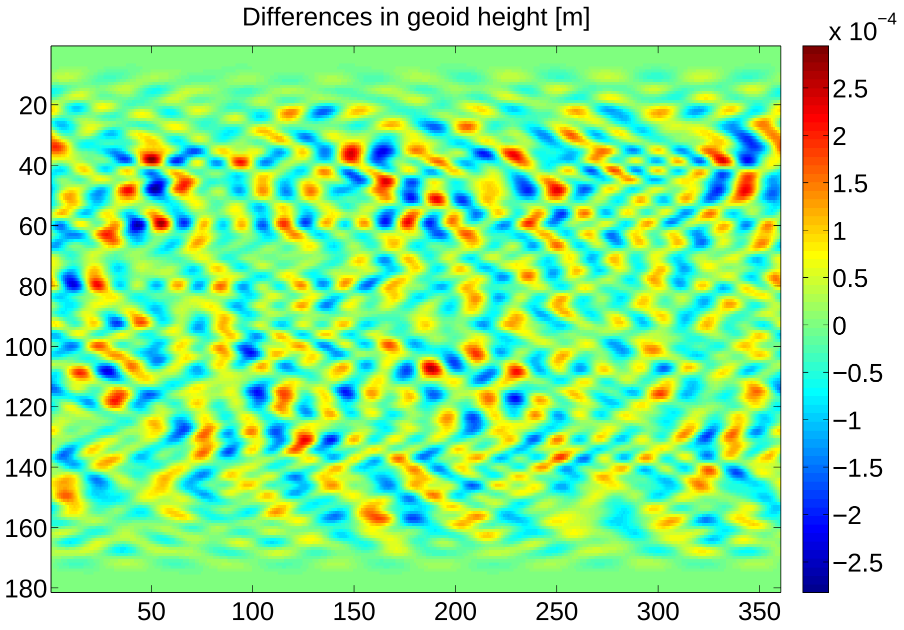

Figure 4.1: Differences in geoid height in [m] for a single month of GRACE data between Stokes coefficients filtered by Dr. John Wahr and after filtering with a MATLAB routine written by the author. No additional smoothing is applied.

Calibrated standard deviations for all coefficients are made available by the processing centers (see section 4.1). However, the errors that cause stripes arise from correlation between coefficients (Swenson and Wahr, 2006), which obviously can not be expressed by standard deviations alone. A full covariance matrix would ideally describe all such errors, but it is questionable whether full noise covariance matrices can describe the real causes for stripes because it takes into account white observation noise and the measurement geometry, at least the one produced by CSR Texas (Ries, pers. communication). It can be concluded that the simulated covariance matrices used by Kusche (2007) are able to describe the stripes, since the filter based on this covariance matrix seems to be successful in removing them.

Thus, since calibrated standard deviations and the noise covariance matrices have expected shortcomings, different methods to quantify errors have been applied in this thesis. Advantages and disadvantages of each method are discussed below.

Wahr et al. (2004) start from the assumption that the part of the Stokes coefficients which exhibits annual, semi-annual, or secular time behaviour is a physical signal. The remainder of the signal can then be assumed to be noise. In the extreme case where no filtering is applied, stripes with annual or semi-annual periods can be seen in estimated physical patterns. The method of Wahr et al. (2004) would incorrectly label these errors as signals. Conversely, a real geophysical signal can have inter-annual periods, and be classified as error. Wahr et al. (2006) elaborate on this method and scale the standard deviations to fit the magnitude of the residuals so that the error structure of the standard deviations is maintained, but the magnitude of residuals is obtained.

A similar idea is to use principal component analysis in the space domain (Rangelova et al., 2007) or frequency domain (Wouters et al., 2007) and reconstruct the signal with the significant modes only, because the higher modes in the spectrum of the signal covariance matrix are believed to represent noise. This suffers from the same drawbacks as the method of Wahr et al. (2004) because in the case of no filtering being applied, stripes are a part of, or dominate, the strongest modes.

Tamisiea et al. (2007) applied a method specifically for glacial isostatic adjustment studies, whereby they scaled standard deviations of the spherical harmonic coefficients by the reduction in misfit that is achieved after filtering. If filtering is successful, the GRACE estimate for the secular gravity rate is in theory closer to a GIA model so that a small misfit remains and the standard deviation for the coefficient is scaled by a small number. Possible criticism is twofold: the effect of the filter on both GIA and non-GIA signals can both increase or decrease the misfit, which does not indicate successful performance of the filter. Secondly, the success of the filter is based on a particular GIA model, which makes filter improvement biased.

Considering the above review, in this thesis a selection was made of three methods to quantify measurement errors in the space domain:

1) full noise covariance matrix;
2) calibrated standard deviations;
3) residuals after estimation of a trend, annual and semi-annual signal (Wahr et al., 2004).

These are discussed in the following section.

4.3.1 Full covariance matrix

In the following, the term Variance Covariance Matrix (VCM) will be used even though in some cases covariances may be assumed zero. The VCM is propagated for the selected filter by covariance propagation (Vaníček and Krakiwsky, 1986, p. 197):

$$\mathbf{C}' = \mathbf{M}\mathbf{C}\mathbf{M}^T \tag{4.22}$$

Where **C** denotes a VCM, **M** denotes a matrix that represents the filter, so that the filtered coefficients ordered in a vector, $\mathbf{K}'_{lm}$, are obtained from the original coefficients $\mathbf{K}_{lm}$ as

$$\mathbf{K}'_{lm} = \mathbf{M}\mathbf{K}_{lm} \,. \tag{4.23}$$

Haagmans and Van Gelderen (1991) give the error covariances between two points P and Q. Therefore, to obtain point error variances, their points P and Q are the same and their equation 1a becomes

$$Var(P)=\sum_{m=0}^{L}\sum_{k=0}^{L}\begin{array}{l}\left(\sum_{n=m}^{L}\sum_{l=k}^{L}Cov\left(\overline{C}_{nm},\overline{C}_{lk}\right)\overline{P}_{nm}(\cos\theta_P)\overline{P}_{lk}(\cos\theta_P)\right)\cos(m\lambda)\cos(k\lambda)+\\ \left(\sum_{n=m}^{L}\sum_{l=k}^{L}Cov\left(\overline{S}_{nm},\overline{C}_{lk}\right)\overline{P}_{nm}(\cos\theta_P)\overline{P}_{lk}(\cos\theta_P)\right)\sin(m\lambda)\cos(k\lambda)+\\ \left(\sum_{n=m}^{L}\sum_{l=k}^{L}Cov\left(\overline{C}_{nm},\overline{S}_{lk}\right)\overline{P}_{nm}(\cos\theta_P)\overline{P}_{lk}(\cos\theta_P)\right)\cos(m\lambda)\sin(k\lambda)+\\ \left(\sum_{n=m}^{L}\sum_{l=k}^{L}Cov\left(\overline{S}_{nm},\overline{S}_{lk}\right)\overline{P}_{nm}(\cos\theta_P)\overline{P}_{lk}(\cos\theta_P)\right)\sin(m\lambda)\sin(k\lambda)\end{array}$$

(4.24)

Coefficients $\overline{S}_{nm},\overline{S}_{lk}$ do not exist for $m = 0$.

4.3.2 Calibrated standard deviations

For calibrated standard deviations, the same equation (4.22) is used as for the full VCM but off-diagonal terms in the VCM are set to zero before propagating through the filter. Although the correlation between odd and even degrees that is related to the striping problem is obviously not described by the standard deviations alone, this case can still serve as a benchmark to compare the performance of the other methods against.

4.3.3 Residuals

Residuals are obtained after least-squares estimation of a trend, annual and semi-annual signal; see equation (4.12). Physical processes that are presumably annual, such as snow fall and melt in the mountains, typically do not have the same amplitude for every year and do not always have the same phase, therefore the annual cycle is estimated using a moving window of 2 years.

Even if the time series would consist purely of noise in the form of normally distributed random numbers, estimating a trend and annual cycle will remove some of this noise. This reduction of variance is computed by fitting a trend and annual cycle to a random time series of length equal to the GRACE time series. The thus obtained variance reduction for the number of epochs used in this thesis is typically 15%, and the GRACE residuals are multiplied by a factor approximately equal to 1.15. The root-mean-square of the errors in the spatial domain is computed from the residuals in the coefficients by (Wahr et al., 2006, equation 4)

$$\Delta = \sqrt{\sum_{l,m}\left({H_{lm}}^2 \left[\sum_{i=1}^{n} \frac{\delta C_{lm}^2}{n} \right] + {I_{lm}}^2 \left[\sum_{i=1}^{n} \frac{\delta S_{lm}^2}{n} \right] \right)}, \tag{4.25}$$

where Δ is the RMS of the errors; H_{lm} and I_{lm} are factors that relate the spherical harmonic coefficients to the spatially averaged mass change at a certain geographic location, as in equation (4.4) the combination of $\tilde{P}_{lm}$ and X_l; δC_{lm} and δS_{lm} are the residual coefficients, and *n* is the number of months.

In equation (4.25), it is assumed that errors are uncorrelated from one month to another so that the 1σ RMS errors for the geoid rate can be computed from the RMS of the mass errors computed in equation (4.25) by (Velicogna and Wahr, 2002)

$$\sigma_{\dot{N}_{GRACE,i}} = 12\sqrt{\frac{12}{(N-1)N(N+1)}}\sigma_{N_{GRACE,i}}, \tag{4.26}$$

where $\sigma_{N_{GRACE,i}}$ is the error in an individual month, and $\sigma_{\dot{N}_{GRACE,i}}$ is the error in the trend. For 59 months, the factor that multiplies the error in the individual month in equation (4.26) turns out to be approximately 0.09. In reality, errors can be time-dependent, such as tidal aliasing errors arising from mismodelling the S2 tide (Ray and Luthcke, 2006), but this is neglected here.

4.4 Leakage, signal mixing and resolution

Gravity data, either static or time-variable, suffer from non-uniqueness (e.g., Turcotte and Schubert, p. 195). The same gravity data set can be induced by different 3-D mass distributions. Before analyzing the GRACE data in terms of GIA in the following chapter, it is useful to review some issues related to non-uniqueness: (i) Non-uniqueness in vertical direction; (ii) Non-uniqueness in horizontal direction, and (iii) Leakage of signals from outside the area of interest due to smoothing.

The non-uniqueness in depth that exists for inversion of the static gravity field (e.g., in exploration geophysics) is removed in most GRACE studies by assuming that mass transport exists in a thin shell on the Earth’s surface. However, GIA takes place deep in the Earth’s interior, thus such approximation is not possible. GIA can be masked by water storage changes on the surface, and that turns out to be a problem for GIA inference from GRACE (see section 5.1.2).

For satellite gravity measurement, there is larger non-uniqueness in horizontal direction than for surface gravity measurements, because of the fact that the satellite is separated from the mass change processes by at least the flying altitude. This is illustrated by equation (1-88) in Heiskanen and Moritz, which computes the potential at satellite altitude V_{sat} from the potential known everywhere at the Earth’s ellipsoidal surface:

$$V_{sat}\left(r,\theta,\lambda\right)=\frac{1}{4\pi}\int_{\lambda'=0}^{2\pi}\int_{\theta'=0}^{\pi}V\left(a_e,\theta',\lambda'\right)\left[\sum_{l=0}^{\infty}\left(2n+1\right)\left(\frac{a_e}{r}\right)^{l+1}P_l\left(\cos\psi\right)\right]\sin\theta' d\theta' d\lambda', \quad (4.27)$$

It can be seen that the potential at satellite altitude is a weighted sum of potentials at the Earth’s surface. The factor between square brackets determines how much of the signal at θ',λ' is used for the potential at $\left(r,\theta,\lambda\right)$. Simons and Dahlen (2006) call this the ‘point spreading factor’. For increasing r this factor is increasingly globally supported, while for $r = a_e$ it becomes the delta function.

Since smoothing is an averaging operation in the spatial domain, the influence of mass changes far away from the point of interest increases. This is referred to by Swenson and Wahr (2002) as ‘leakage’ and can lead to increase or decrease of the signal of interest. Smoothing and the point spreading factor decrease the resolution, which leads to ambiguity between a narrow but strong mass change and a smaller mass change that exists over a wider area.

Item 3 receives the most attention in the literature, because the change in signal due to smoothing can be partly reversed. It is useful to keep in mind that resolution of satellite gravity data is inherently limited, and that influence of a strong signal (e.g., snow fall in the Rocky mountains) will overprint a neighbouring small signal (e.g., water level variations in river basins adjacent to the Rocky Mountains), irrespective of whether filtering is applied or not. In addition to these three items, signals are also averaged because the inter-satellite range results in a moving average over the distance between the satellites, approximately 200 km.

Items i) and ii) are studied in more detail in the sections 5.1.1 and 5.1.2. Item iii) also implicitly enters into those sections because the magnitude of the signal at a certain location is computed after filtering.

4.5 Summary

In this thesis the GRACE derived monthly gravity fields provided by CSR Texas are used in most cases, and in some cases those provided by GFZ Potsdam. Two techniques are explained for obtaining a secular signal from the spherical harmonic coefficients: (i) linear estimation of a trend in the presence of periodic signals, and (ii) principal component analysis (PCA). Of those, the trend estimation will be mainly used in the results of Chapter 5, and PCA will be used in section 5.4.1.2. Many filtering methods for GRACE data appear in the literature. In this chapter, the Gaussian filter (Wahr et al., 1998), the non-isotropic Gaussian filter (Han et al., 2005) and the destriping filter of Swenson and Wahr (2006) are introduced and they will be compared in section 5.3. Different methods exist to estimate measurement errors for GRACE. Because of disadvantages for each of the methods, several methods were discussed in more detail in this chapter: covariance propagation with a full matrix, and with calibrated standard deviations only, and residuals after estimating a trend, annual and semi-annual period simultaneously. These methods will be compared in section 5.2.

Chapter Five: GRACE-derived gravity rate for GIA studies - Results

The aim of this chapter is to study the uncertainty in the GRACE data, and to process the GRACE data for comparisons with GIA models. A choice was made to focus on analysis in the spatial domain, for the Laurentide glaciation only. Some previous studies performed a global inversion of GRACE data. For example, the simulation study of Velicogna and Wahr (2002) showed that retrieval of lower mantle viscosity to within 30-40% was possible. However, this could be too optimistic because measurement errors in GRACE turned out to be larger than expected (Wahr et al., 2006). Recently, Barletta et al. (2009) fitted localized mass sources to the secular signal in GRACE, and manually remove the sources that were believed not to represent GIA, to arrive at a GIA-only secular gravity. However, such a technique can not separate secular signals acting in the same area. The technique is also affected by the unknown ice history in places like Antarctica and Greenland.

The first sections investigate the secular gravity rate of continental water storage, present-day ice melt, and variations in open water and sea level changes. Following this, the magnitude of measurement errors is computed for the methods introduced in section 4.3. Some of the filters presented in section 4.2.3 are compared in terms of how much they reduce noise and affect the GIA signal. Finally, a gravity rate and a geoid rate pattern from GRACE are presented that can be used for GIA studies. This chapter mostly follows the results in Van der Wal et al. (2008a), but an additional filter is investigated, data and simulations are updated and lake level variations are included herein.

5.1 Non-GIA processes

5.1.1 Present-day ice melt

Rapid melting has been observed in areas in Alaska (Tamisiea et al., 2005; Luthcke et al., 2008) and Greenland (Velicogna and Wahr, 2006). In a map of the GRACE-derived secular gravity rate, the areas of ice melt are clearly separated from the GIA area. However, the point spreading factor (see section 4.4), aliasing and leakage due to smoothing can lead to gravity rates in the GIA area that are influenced by the ice mass loss outside this area, even though this can not directly be observed in the spatial domain. To investigate this, present-day ice melt will be simulated for the areas depicted in Figure 5.1. An estimate from Lutchke et al. (2008) of 84 Gt/year ice mass loss is assumed to occur in uniform melting in Alaska as in (Van der Wal, 2008b). The center of the ice sheet is selected to be 60º N and 140º W from visual inspection of the area in Figure 1 of Tamisiea et al. (2005). The peak gravity rate found with this simulation is -2.1 µGal/year (filtering described as in section 5.3.3), which is approximately the same as the peak found in GRACE-derived secular gravity rate over the same region.

For Greenland, estimates not based on GRACE data are available from, e.g., satellite altimetry, but they are hindered by poor coverage near the coast where most of the melting takes place and only give the geometry change of the ice sheet, which does not necessarily translate directly into mass loss because of snow compaction. The GRACE estimates for Greenland ice mass loss on the other hand still depend somewhat on the technique used. The average of the estimates from Luthcke (154 Gt/year), who used the mascon technique, and Velicogna (211 Gt/year), who used spherical harmonics and an averaging kernel, as reported in Witze (2008), is used here.

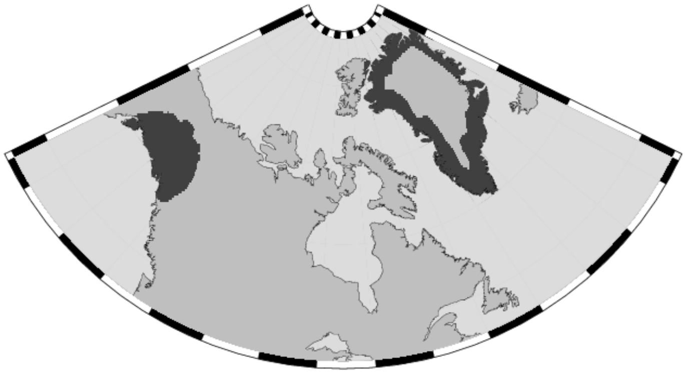

Figure 5.1: Area used for simulation of glacier melt in Alaska and Greenland. Ice is melting in the dark areas; inside the dark area in Greenland it is accumulating (from: Van der Wal et al., 2008).

Spherical harmonic analysis is performed up to degree and order 120. The gravity rate after synthesis up to degree 60 is shown in Figure 5.2 after smoothing with a 400 km

Gaussian filter. Small non-zero gravity rate extends across the northern hemisphere. Such long-wavelength signal likely does not change the gravity rate pattern in the Hudson Bay area much, but it could be argued that the ice melt should be removed from the GRACE data. However, the hydrology models discussed in the next section contain negative secular signal over Alaska and removal of glacier melt on top of removing hydrology distorts the gravity rate pattern over the GIA area as judged by visual inspection. Thus it is decided to not remove glacier melt simulations from the final gravity rate which is used in comparisons with GIA models. The glacier melt simulations are used to find the pixels where the GIA signal is much stronger than the glacier melt signal in section 5.3.

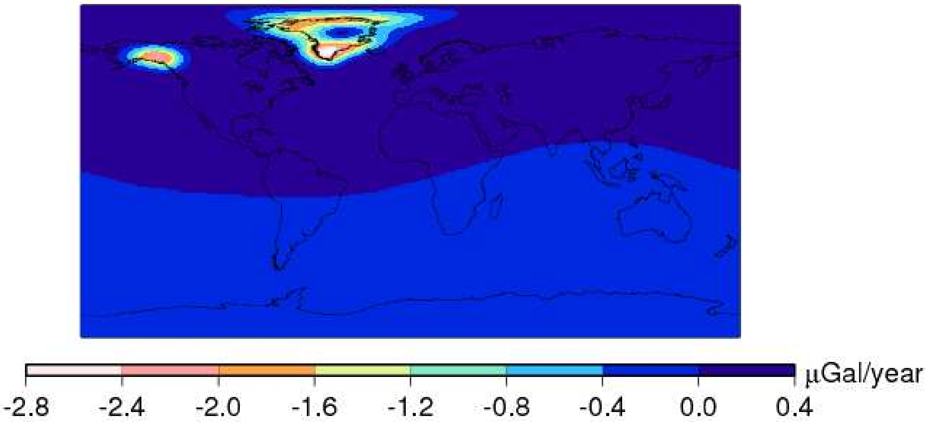

Figure 5.2: Gravity rate from ice melt simulations in Alaska and Greenland after smoothing with a 400 km halfwidth Gaussian filter.

5.1.2 Continental water storage variations

Water storage in the form of liquid water and snow varies mostly according to a seasonal cycle, but droughts or heavy rain in one or several years can result in inter-annual changes in water storage. In fact, areas in the interior of Canada and the U.S. are one of the few regions in the world singled out in Figure 6 of Döll et al. (2003) as having large inter-annual variations. Such variations when measured by GRACE can affect the estimated secular trend interpreted to be GIA. Due to lack of measurements of water

storage changes on a continental scale, a-priori information will have to come from global or continental scale hydrology models. Four global hydrology models that are available to the scientific community are investigated in this thesis. They are discussed briefly below, and some of their characteristics are summarized in
Table 5.1.

CPC

The CPC model of Fan and van den Dool (2004) uses the so-called ‘leaky bucket’ model: ground is modeled as a bucket which can hold a certain amount of water (76 cm) until it overflows. This depth and four other empirical parameters are tuned to streams in Oklahoma. Input for the model are monthly global precipitation data from the Climate Prediction Center (CPC) and the CDAS reanalysis of temperature data. Comparison with in-situ data shows that the model can accurately represent inter-annual variability (Fan and van den Dool, 2004). However, snow that lies on the ground is not explicitly accounted for in the model, which could lead to premature removal of snow in the model.

LaD

The Land Dynamics model of Milly and Shmakin (2002) takes input from near-surface state of the atmosphere and radiation fluxes from the International Satellite Land Surface Climatology Project on a global $1^{o} \times 1^{o}$ grid with 6-hour temporal resolution. The land surface is characterized by eight parameters which remain constant in time. Water balance and energy equations are solved to compute output in the form of snow, root-zone and groundwater. In comparisons with discharge observations, the model is found to explain 67% of the variance of annual runoff ratio anomalies. Here, the LadWorld-Gascoyne version, which is the latest one available, is used up to July 2007.

GLDAS

The Global Land Data Assimilation System (GLDAS) of Rodell et al. (2004) uses data from multiple sources in a data assimilation procedure. Compared to the other models, surface parameters such as vegetation classification are allowed to vary in time and are derived from higher resolution datasets. MODIS satellite data is used to correct snow cover in grid cells. Output is provided at: [ftp://agdisc.gsfc.nasa.gov/data/s4pa/GLDAS/GLDAS_NOAH10_M/2007] as soil moisture in kg/m^2 for four layers and snow. Here, the version with the Noah 2.7 land surface model (Chen et al., 1996) is used. Berg et al. (2005) found good correlation between the model and observations in Illinois and Iowa after a seasonal cycle was removed.

WGHM

The WaterGAP Global Hydrology Model (WGHM) of Döll et al. (2003) differs from previous models in two aspects that are not included in Table 5.1: (i) wetlands and lakes are part of the model and human water consumption is included; (ii) Compared to GLDAS, temporal resolution of the computations is lower (1 day vs. 6 hours) and spatial data is of lower resolution.

Table 5.1: Comparison of characteristics of versions of some global hydrology models.

	CPC	LaD	GLDAS	WGHM
input	CPC, CDAS Reanalysis	ISLSCP	ECMWF, NCAR,NOAA, AGRMET	Climatic Research Unit
land surface	5 parameters	8 parameters	NOAH	IMAGE 2.1
wetlands/lakes	no	no	no	yes
temporal resolution	daily	6 hours	6 hours$^{1)}$	1 day
snow on ground	no	yes	yes	yes
soil layers	1 layer	snow pack rootzone groundwater	snow pack 4 layers canopy	snow 1 layer canopy
resolution	$1^o \times 1^o$	$1^o \times 1^o$	$1^o \times 1^o$	$0.5^o \times 0.5^o$

Hydrology models do not give meaningful results over permanently glaciated grid cells, because glaciers simulations are not included. To mitigate the influence of glacier cell in the hydrology model grids, the glacier database of the National Snow and Ice Data Center (NSIDC, 1999) was used to locate center locations of glaciers that have an area greater than 25 km^2. Pixels that are within 0.7^o of the centers of these glaciers, see Figure 5.3, were masked out. Greenland was masked out entirely.

Figure 5.3: Locations of pixels within 0.7 degree of the center locations of glaciers with area larger than 25 km^2.

If hydrology models are to be used to ‘correct’ GRACE data for GIA studies, the question is how well hydrology model output simulates large scale interannual variations, considering that GRACE was meant to improve precisely those estimates. Regarding this question, the following defects in hydrology models can be identified:

1) Input forcing consists of fluxes (e.g., precipitation, river run-off) that can change quickly over time. A small bias in any of these fluxes or insufficient temporal sampling of the input forcing can result in a large bias or random error in the interannual variation (Shmakin et al., 2002). However, evapotransporation and river run-off are negative feedback terms, therefore, an error in these quantities can no cause a run-away bias in soil moisture.

2) Models are tuned, which “does not necessarily improve the dynamical behaviour of the Global Hydrology Model” (Döll et al., 2003). In particular, soil moisture is no longer consistent with (tuned) discharge. In many snow dominated regions in large parts of Canada, run-off is tuned and also discharge is corrected in WGHM, and as a result run-off is probably underestimated (Döll et al., 2003).
3) Input data area faulty. For example, snow fall is underestimated by precipitation gauges (Döll et al., 2003).
4) Modeling can be inadequate. An example is that river water which is diverted to other basins is not included in WGHM (Döll et al. 2003).
5) Due to the sampling of GRACE (when the satellites actually pass over the area) the satellites can sense continental water storage which is different from a simple average of daily or sub-daily output. According to Han et al. (2004), this systematic error can be as large as the GRACE measurement error.

This list does not exactly give confidence that the model output can be of any use. However, defects can be minor on the coarse temporal and spatial resolution of monthly gravity fields. For example, Van der Wal et al. (2008a) found that interannual changes between GRACE and three models agree quite well. Figure 5.4 and Figure 5.5 are figures taken from that paper. Figure 5.4 shows the second or third principal component, which show a positive water storage signal southwest of Hudson Bay. Figure 5.5 shows that the signal is a three year increase in water storage starting in the summer of 2003. The increase can be explained by abnormal dryness prior to the summer of 2003. The increase in water storage is then the return to a normal state of soil moisture content (M. Rodell, pers. comm., 2007). Some of the signal in GRACE data in Figure 5.4 could also be due to errors in the GIA model, e.g., the decrease west of Hudson Bay.

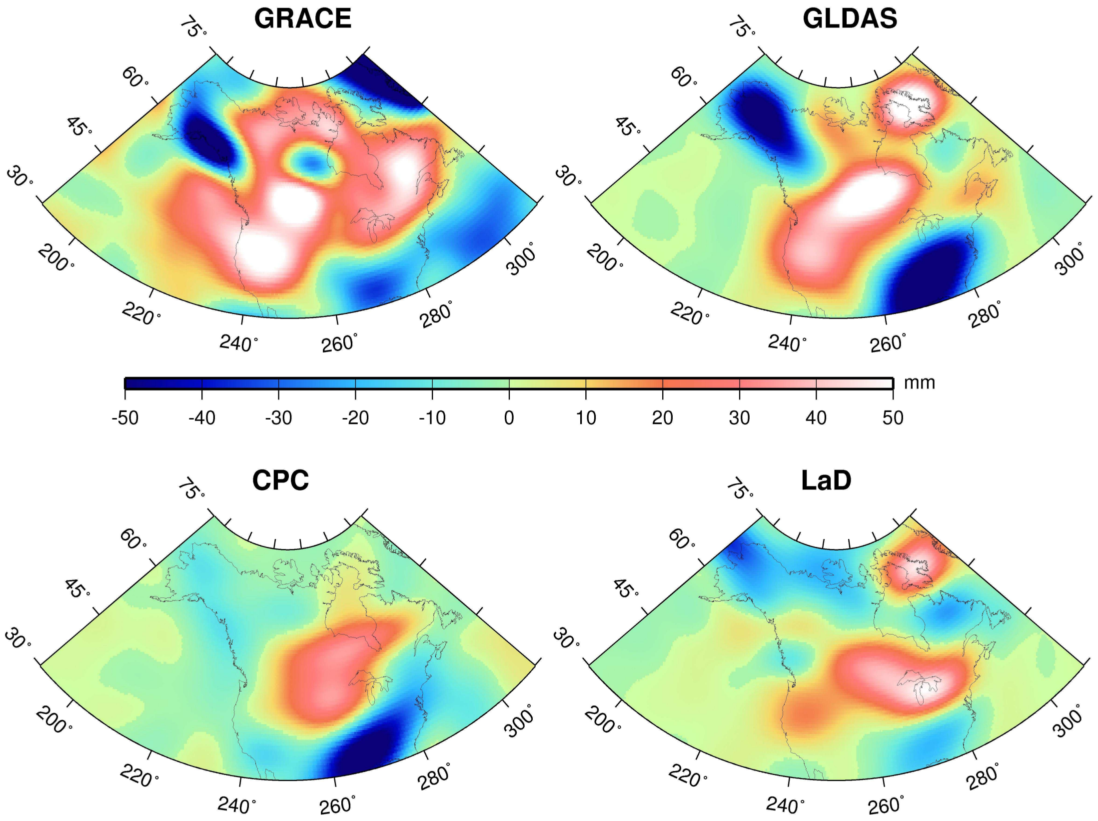

Figure 5.4: Spatial pattern of the second principal component for GRACE (after removal of ICE-5G/VM2 GIA model) and the hydrology models GLDAS and CPC, and the third principal component for LaD, for the period January 2003 - September 2006. The spatial pattern is to be multiplied with the time series in Figure 5.5 to get spatiotemporal patterns.

Finally, to asses the performance of the hydrology models on the scale of a mid-size river basin, the Nelson River basin (shown in Figure 5.6a in black) is selected for comparison between the hydrology models and GRACE. Model output in the form of spherical harmonic coefficients and GRACE data were filtered with a destriping filter applied at degree and order 5 and a Gaussian filter with 400 km halfwidth. Thus obtained water levels are averaged over the basin in the spatial domain and plotted in Figure 5.7. The analysis was performed in the frame of Valeo et al. (2007) and extended here to include recent data.

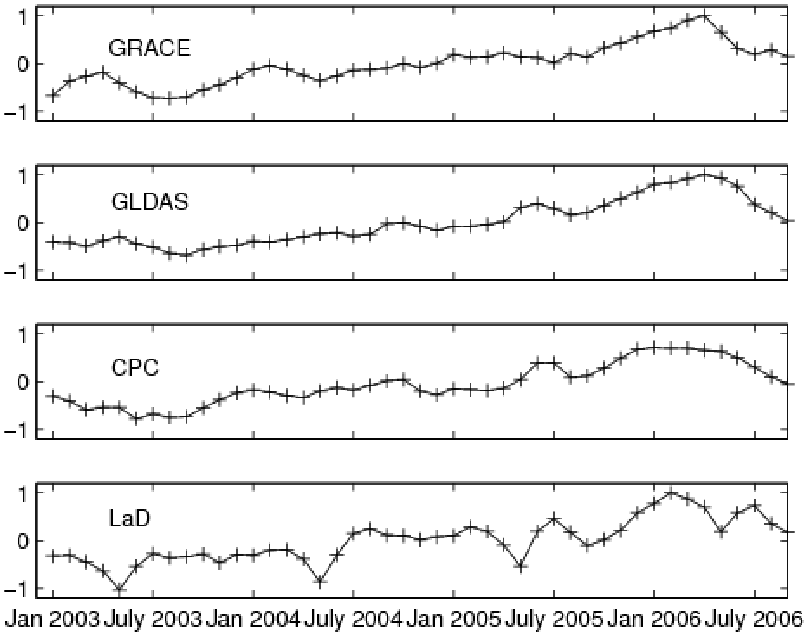

Figure 5.5: Time series corresponding to principal components in Figure 5.4. Increase in water storage starting in the summer of 2003 is visible in all hydrology models as well as in the GRACE data.

GRACE is corrected for GIA with the ICE-5G VM2 model (Peltier, 2004) which seems to overcorrect as there is a small positive trend in the hydrology models which is absent in the GIA-corrected GRACE results. It can be seen that the hydrology models GLDAS, WGHM and LaD compare well with GRACE, but CPC performs worse. Root mean square differences in Table 5.2 confirm this. GLDAS performs best in this area, which supports the use of this model as a correction for the continental water storage changes in GRACE in section 5.4. All models are generally one or two months ahead of GRACE, which is also observed elsewhere (e.g., Chen et al., 2005a).

Figure 5.6: Nelson River basin in black (from: Valeo et al., 2007).

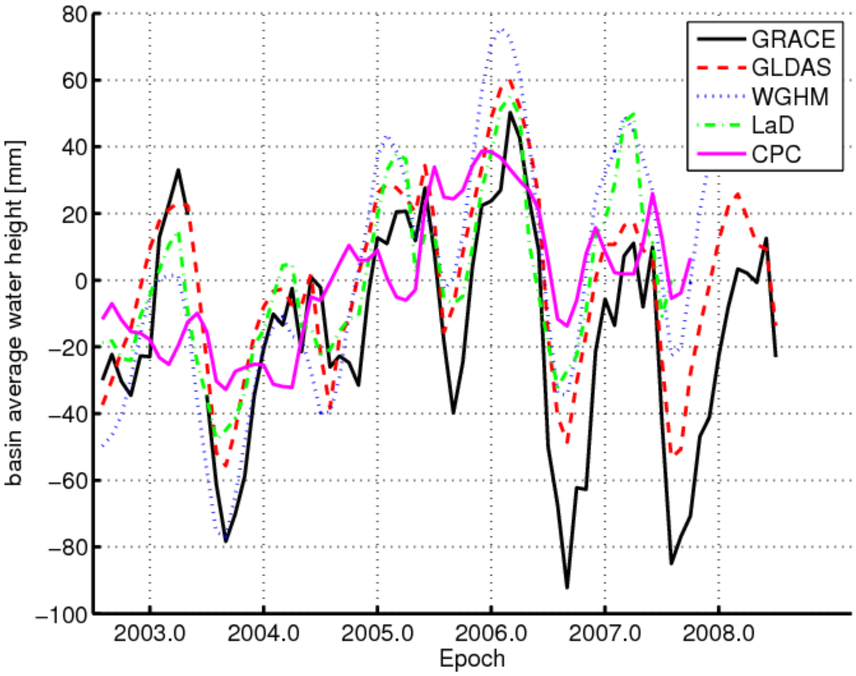

Figure 5.7: Basin averaged water levels for the Nelson River basin for GRACE and four hydrology models, after destriping filtering and smoothing with a 400 km Gaussian filter.

Table 5.2: Root mean square difference between hydrology model output and GRACE for the basin averages shown in Figure 5.7.

	GLDAS	**WGHM**	**LaD**	**CPC**
RMS [mm]	148	219	175	245

5.1.3 Lake level variations

Variations in large lakes such as the Great Lakes represent sizable mass variations that could distort the estimated GIA-induced secular gravity rate from GRACE. Fleitout (2007) suggested that declining lake levels in lakes Winnipeg and Winnipegosis from 2003 to 2005 had a significant influence on the gravity rate from GRACE, but did not quantify this in the abstract. Observations of water level variations in large lakes in North-America are available from tide gauges and satellite altimetry thus an attempt is made here to quantify the effect of water level variations on the GRACE-derived gravity rate. First, the different signals in the tide gauges measurement are discussed, and then the gravity rates.

Differences in water level between water levels observed simultaneously by tide gauges on one lake are small compared to the total mass variation of the lake as a whole, therefore it is not necessary to use satellite altimetry data to obtain water levels away from the coast (Van der Wal et al., 2006). Tide gauges measure the combined effect of water level changes that result from GIA, thermal effects, and in- and out-flow into the basin:

$$\dot{s}_{TG} = \dot{s}_{GIA} + \dot{s}_{th} + \dot{s}_{flow}\,, \tag{5.1}$$

where $\dot{s}$ denotes sea level rate, and subscripts denote GIA, thermal effects, and in- and out-flow of the lake, respectively. The in- and out-flow are assumed to also include precipitation and evaporation. Note that for the formulation of this equation it is irrelevant whether the in- and outflow is caused by natural variations or artificial regulation of the water level.

The sea level change caused by GIA at a tide gauge can be decomposed into a change in the solid Earth displacement $\dot{r}$ and a change in the geoid height $\dot{N}$ (Mitrovica and Peltier, 1991):

$$\dot{s}_{GIA,TG} = \dot{N}_{TG} - \dot{r}_{TG} \tag{5.2}$$

$\dot{r}_{TG}$ can be obtained from GPS stations collocated with tide gauges. The mass conservation term is neglected, which is allowed for the computation of present-day rates. Because the GPS heights refer to a fixed vertical datum, the rise of the datum at the tide gauge, $\dot{N}_{TG}$, should also be taken into account. $\dot{N}_{TG}$ can be estimated from terrestrial data (Rangelova, 2007).

Gravity changes measured by GRACE over the lake can be decomposed as follows:

$$\dot{g}_{GRACE} = \dot{g}_{GIA} + \dot{g}_{flow} + \dot{g}_{salinity} \tag{5.3}$$

Because we want to know $\dot{g}_{GIA}$, $\dot{g}_{flow}$ and $\dot{g}_{salinity}$ need to be removed from the GRACE data. $\dot{g}_{salinity}$ is neglected in the following because of lack of data, but $\dot{g}_{flow}$ can be quantified by isolating $\dot{s}_{flow}$ in equation (5.1) and converting it to gravity change by equation (4.8). Following this approach, equations (5.1) and (5.2) are combined to yield

$$\dot{s}_{flow} = \dot{s}_{TG} - \left(\dot{N}_{TG} - \dot{r}_{TG}\right) - \dot{s}_{th}\ , \tag{5.4}$$

after which equation (4.8) can be applied to give $\dot{g}_{flow}$, assuming $\dot{s}_{flow}$ to be constant over the lake area. GIA models predict water in- and out-flow due to solid Earth displacement and geoid height change. $\dot{r}_{TG}$ in equation (5.4) represents the extra water in the lake by a change in height of the lake bottom. $\dot{N}_{TG}$ represents the inflow or outflow that accompanies a change in the equipotential. Since both these terms are included in the most detailed treatment of the sea level equation in GIA models, they are rightfully included in (5.4). However, the uplift rates in the Great Lakes are within +5 mm/year and -5 mm/year (Braun et al., 2008, Figure 2) and uplift rates at Lakes Winnipeg, Winnipegosis and Great Slave Lake are in the order of 5 mm/year (not shown). The effect of a layer of water of 5 mm/year is negligible for the surface of the lakes considered here, except for the Hudson Bay. Thus, the terms $\dot{r}_{TG}$ and $\dot{N}_{TG}$ are neglected.

In the following, $\dot{s}_{th}$ will be computed from surface temperature data, to see if the effect should be included or can be neglected. Swenson and Wahr (2007) used surface temperature data for the lake and an averaged mixing depth to calculate thermal expansion using a constant thermal expansion factor. However, such approximation is likely not valid for the Great Lakes. From Figure 5.8, it is clear that the mixing depth, defined as the depth where a high temperature-depth gradient occurs, varies considerably from 10m to 35 m. Moreover, the temperature varies from just above 0 to close to 25 degrees. Over such a range, the thermal expansion coefficient is not constant, as can be seen in Figure 5.9. Thus, a different approach (Meredith, 1975) will be used herein to compute the increase or decrease in water level for a number of large lakes in North America.

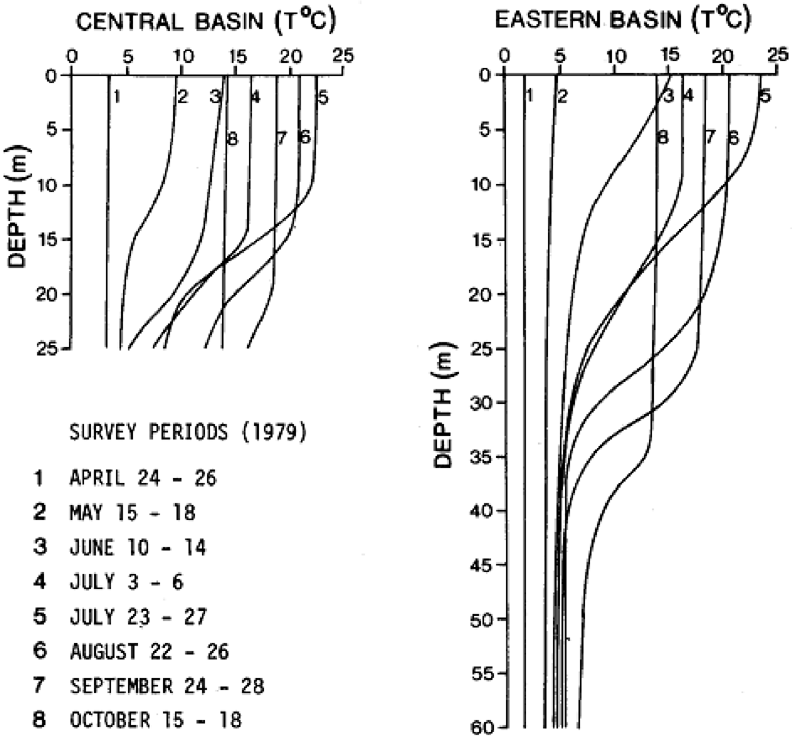

Figure 5.8 (fig. 7 of Schertzer et al., 1987): Temperature profiles at various dates in 1979, in the eastern and central part of Lake Erie.

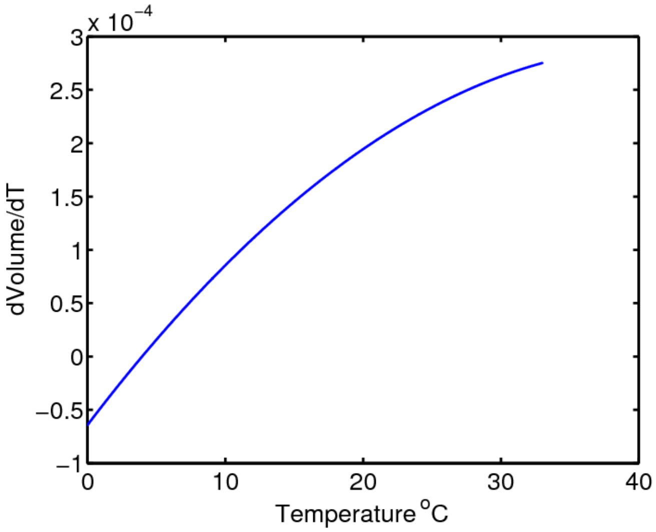

Figure 5.9: Thermal expansion for water as a function of temperature, derivative of equation (2) in Meredith (1975) with respect to temperature.

5.1.3.1 Great Lakes

The temperature profiles compiled by Meredith (1975) seem to be the most recent temperature profiles that area available for all of the Great Lakes. The profiles are made dimensionless by dividing the temperature at each layer by the surface temperature. ‘New’ temperature profiles are computed by multiplying the dimensionless profile with the actual measured surface temperature. Measured surface temperatures are obtained from the Great Lakes Surface Environmental Analysis (GLSEA, 2008). Temperature values at the beginning and middle of the month are obtained by averaging over one month of daily values. From the temperatures at the beginning of the month, a new volume is computed for each layer by means of the equation for water thermal expansion (Meredith 1975):

$$V^* = V_0\left(1 - 6.427\cdot 10^{-5}T + 8.5053\cdot 10^{-6}T^2 - 6.79\cdot 10^{-8}T^3\right), \quad (5.5)$$

where V^* is the new volume; V_0 is the reference volume, and T is the temperature of the volume of water in ºC. The change in volume is computed between the first days of two consecutive months. From these changes, cumulative volume changes are formed over the time period January 2002 - December 2007. It is found that the seasonal cycle has an amplitude of up to 2.5 km^3, but the trend is only 0.0044 km^3/year (0.075 mm/year water level change).

The water level changes for the Great Lakes computed with equation (5.4) are added in the space domain on a 0.1 x 0.1 degree grid and converted to gravity rates. The results are shown in Figure 5.10a. Thermal changes in water level, when converted to mass changes by multiplying with the density of water and converted to gravity rates as described above, are shown to be negligible in Figure 5.10b. Thus, most of the water level changes recorded by the tide gauges in the Great Lakes represent real mass changes (and uplift and geoid rates which were neglected above). The negative trend in Figure 5.10 mostly results from decrease in water level in Lake Superior from 2005 onwards. Mass changes in the Great Lakes water levels show a trend which is important for GIA studies due to the magnitude (maximum of 0.2 µGal/year) and the fact that they are on the edge of the former ice sheet.

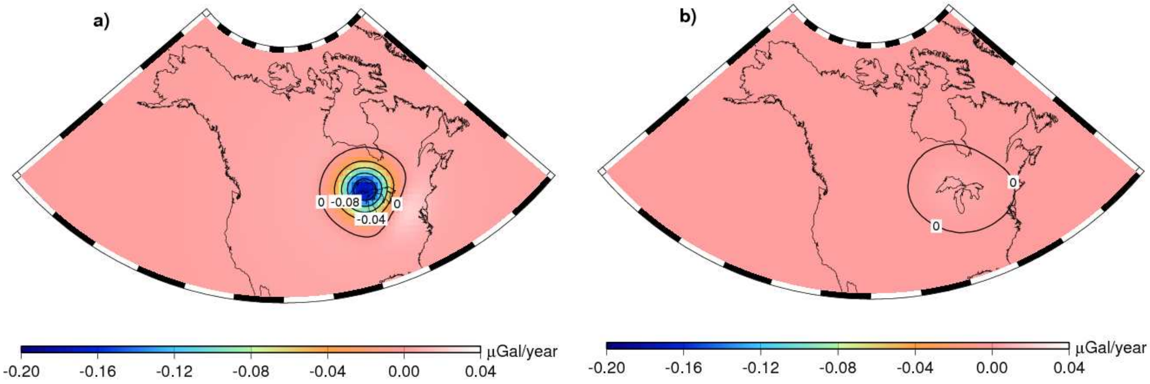

Figure 5.10: (a) Estimated gravity rate from water level change in the Great Lakes, from January 2002 – November 2007 after filtering with a 400 km halfwidth Gaussian filter. All volume change is assumed to be caused by mass changes. (b) Effect of thermal volume change converted to equivalent mass effect, expressed in µGal/year.

5.1.3.2 Lakes Winnipeg, Great Bear Lake and Great Slave Lake

Water levels for Lake Winnipeg are available from Environment Canada (http://www.wsc.ec.gc.ca/hydat/H2O/index_e.cfm?cname=main_e.cfm). Monthly water levels for all seven stations on Lake Winnipeg are averaged to obtain one value for the lake (the maximum standard deviation is 12 cm). The trend amounts to 7.5 mm water level change per year over a period from January 2002 to December 2007. The effect of GIA height changes in equation (5.1) is not taken into account. A plot of the gravity rate from water level variations in Lake Winnipeg is shown in Figure 5.11. Lake Winnipegosis is not considered here, as its area is one fifth of Lake Winnipeg's.

The Great Slave Lake has a considerable area: 28,400 km^2, but a small trend in water level: 0.136 km^3/year (0.04 mm/year water level change) from January 2002 to December 2007 and is therefore neglected. The tide gauge in the Great Bear Lake at the Hornby Bay station shows a trend of 0.64 km^3/year (1.7 cm/year). The maximum water temperature as measured in 1965 was 5.22 ºC (data compiled by International Lake Environment Committee, see http://www.ilec.or.jp/database/nam/nam-30.html and references therein), thus thermal expansion is not likely to play a major role. The trend in gravity turns out to be 0.015 µGal/year which is too small to consider. Thus from the other lakes only Lake Winnipeg has a trend large enough to consider.

WGHM models lakes by allowing precipitation and evaporation from lake grid cells, as well as in and out flow through the river routing network (Dr. Kristina Fiedler, pers. comm., 2008). GLDAS and CPC do not model open water variations. Therefore, the water level variations from the Great Lakes and Lake Winnipeg computed in the previous sections are incorporated into the spatial maps of water height variations of those models.

5.1.3.3 Hudson Bay

Hudson Bay is, by shoreline, the largest bay in the world but presently counts only one working tide gauge at Churchill. Monthly mean water levels at this tide gauge are provided by the Marine Environmental Data Service up to centimetre precision (http://www.meds-sdmm.dfo-mpo.gc.ca/meds/Databases/TWL/Products/Monthly_Means_b.htm). The one tide gauge at Churchill can not be expected to describe the entire water surface of the Hudson Bay as, for example, slow (5 cm/s) circulation patterns are in place that transport discharge from James Bay to western Hudson Bay (Gough et al., 2005). Preliminary analysis of satellite altimetry data in Hudson Bay was done for this thesis using altimetry data from the Jason satellite mission with standard corrections but the obtained trends were entirely dependent on the type of interpolation and the time period over which the data were average. Also, temperature profile studies in Hudson Bay are not available and further uncertainty is added by a reported decrease in discharge from North American rivers into Hudson Bay which leads to increasing salinity and hence increase in overall mass (Déry et al., 2005).

In view of the above mentioned uncertainties and effects, it is necessary to assume that the tide gauge at Churchill represents the entire water surface of Hudson Bay. Fitting a trend through the tide gauges times series in the presence of an annual cycle yields a 0.2 mm/year sea level drop for the period August 2002 – July 2007. However, the estimated trend in the tide gauges data in Churchill depends greatly on the time period over which the trend is estimated (not shown), even when an annual cycle is jointly estimated.

When the 11.4 mm/year land uplift of Churchill (Wolf et al., 2006) is subtracted from the measured 0.2 mm/year sea level drop according to equation (5.2), an 11.2 mm/year sea level rise remains, which seems an unrealistically high number. When the long-term tide gauge estimate of 9.65 mm/year (ibid) is assumed instead, sea level rise of 1.75 mm/year is found, which is close to the tide-gauge sole estimate for global sea level rise (Miller and Douglas, 2006). The effect in terms of gravity rate of 1.75 mm/year sea level rise in Hudson Bay is shown in Figure 5.11b. The maximum value is less than 3% of the maximum gravity rate estimated from GRACE in the same region (Figure 5.28), which agrees with prior findings (Dickey et al., 1997, p. 55).

In the following, this estimate will be used to represent mass changes from sea level changes in Hudson Bay. The trend estimated from the Churchill tide gauge from August 2002 – October 2008 (8.0 mm/year) is assumed to be the maximum value, so that the difference with respect to the long-term value of Wolf et al. (2006) (9.65 mm/year) is a measure for the error (1.65 mm/year).

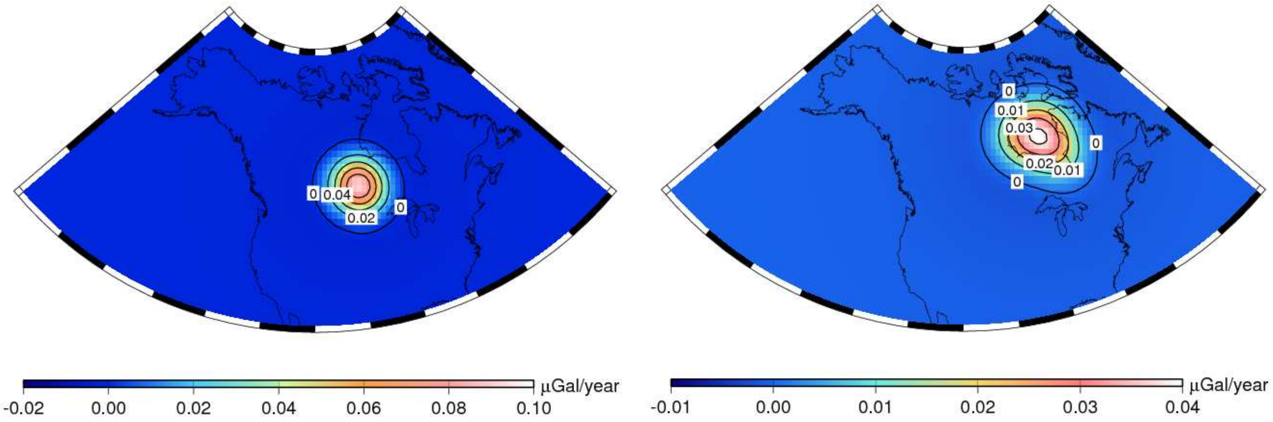

Figure 5.11: (a) Gravity rate estimated in Lake Winnipeg (Jan. 2002- Dec. 2007) based on tide gauge data, after smoothing with a 400 km Gaussian filter. (b) Same but for water level changes in Hudson Bay from a constant trend of 1.75 mm/year water level rise (Jan. 2002- Dec. 2007).

5.2 Measurement errors

The previous section investigated the secular trends resulting from non-GIA signals in North America. This section aims to shows the magnitude of measurement errors in GRACE data, computed with the methods presented in section 4.3. Of interest is the method that gives the largest and most conservative error estimates. Furthermore, it will be studied whether the fully-populated GRACE covariance matrix used in this research is representative of the stripe errors. The filter that is used in this section is the destriping filter of Swenson and Wahr (2006), the reason for which is explained in section 5.3.

5.2.1 Full covariance matrix

Full variance-covariance matrices (VCM) were kindly provided for the CSR release 4 solutions by Dr. Byron Tapley and Dr. John Ries. Liu (2008, p. 140) computed errors after destriping by rescaling the SH coefficients based on the power before and after destriping. Here the matrix with filter coefficients (**M**) will be computed for error propagation of the full VCM. Swenson and Wahr (2006) equation 4 gives the filter coefficients that make up **M**, however implementation is easier to understand using the schematic drawings in Figure 5.12. The coefficient to be filtered is of order 20 and degree

24. A window of 5 degrees is formed (black dots together with red dot) of coefficients of the same order and the same parity degree. A polynomial fit is produced (for example with the function *coeffun* in MATLAB) which gives the value denoted by the blue arrow, as a function of the value of the coefficients. The polynomial coefficients are to be entered in the 5 elements in the matrix **M**; see the drawing in Figure 5.13. The 5 coefficients are multiplied with the 5 elements in the vector $\mathbf{K}_{lm}$ to give the value of the coefficient obtained with the polynomial fit (blue arrow in Figure 5.12).

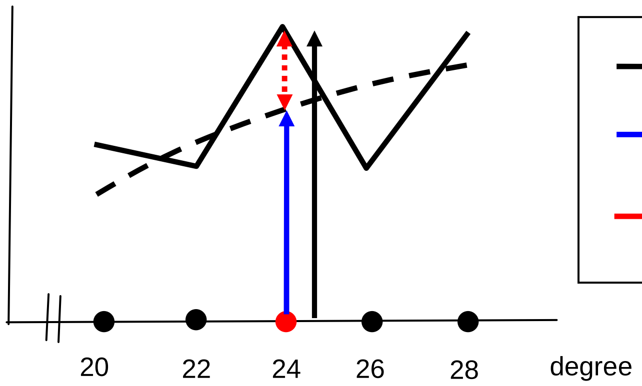

Figure 5.12: Schematic drawing of the principle of the Swenson and Wahr (2006) destriping filter for a fictitious coefficient of order 20 and degree 24.

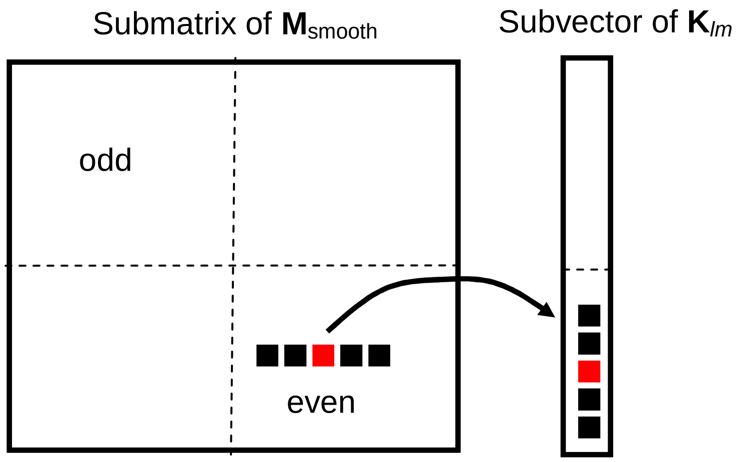

Figure 5.13: Schematic drawing of submatrix of the filter matrix M for order 20 and subvector of the element vector.

Because the filtered coefficient (red arrow) is the original coefficient (black arrow) minus the smoothed coefficient (blue arrow), the destriping filter matrix can be obtained by

$$\mathbf{M} = \mathbf{I} - \mathbf{M}_{\text{smooth}} \tag{5.6}$$

where $\mathbf{M}_{\text{smooth}}$ contains the polynomial coefficients.

The effect of the destriping filter on the standard deviations is shown in Figure 5.14. It is clear that the destriping filter does not simply downweight coefficients with higher degree. The peak at degree 15 (likely caused by stripes) is greatly reduced. A slight jump can be seen at degree 50. This is because the coefficients are not filtered for orders higher than 52 because a minimum window length of 5 coefficients is necessary to be able to reasonably fit a polynomial.

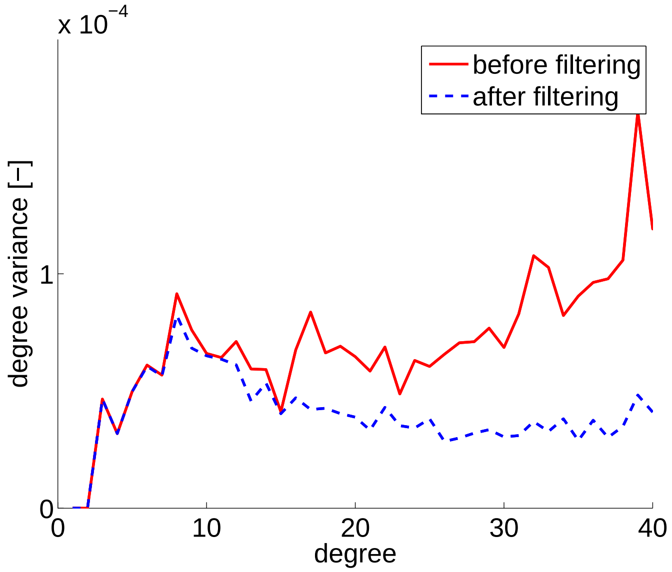

Figure 5.14: Degree variances, computed by equation (4.9), of the monthly gravity field for December 2006 before and after destriping filtering.

Point variances in the spatial domain are computed from the propagated covariance matrix, according to equation (4.24). Coding of this equation was based on MATLAB code of Balaji Devaraju, from the University of Stuttgart. According to Wahr et al. (2006), the inclusion of off-diagonal elements does not have much effect on the RMS of the mass error for GRACE gravity fields. Figure 5.15, which represents the gravity rate measurement error computed with a full and diagonal VC matrix, mostly confirms this: there is only slightly more variation in the longitudinal direction with errors being slightly smaller in Figure 5.15b. In the following, the VCM off-diagonal terms will be included; the extra computation time is not significant.

Omitted in the comparison are the standard deviations for the C_{20} coefficient. The standard deviations for degree 2 coefficients are an order of magnitude higher than other coefficients so that a plot of the errors in the spatial domain is dominated by the C_{20} pattern. Standard deviation from SLR-derived values is provided and can be used here, but the correlation with other coefficients is unknown, therefore degree 2 error coefficients are left out in the comparison.

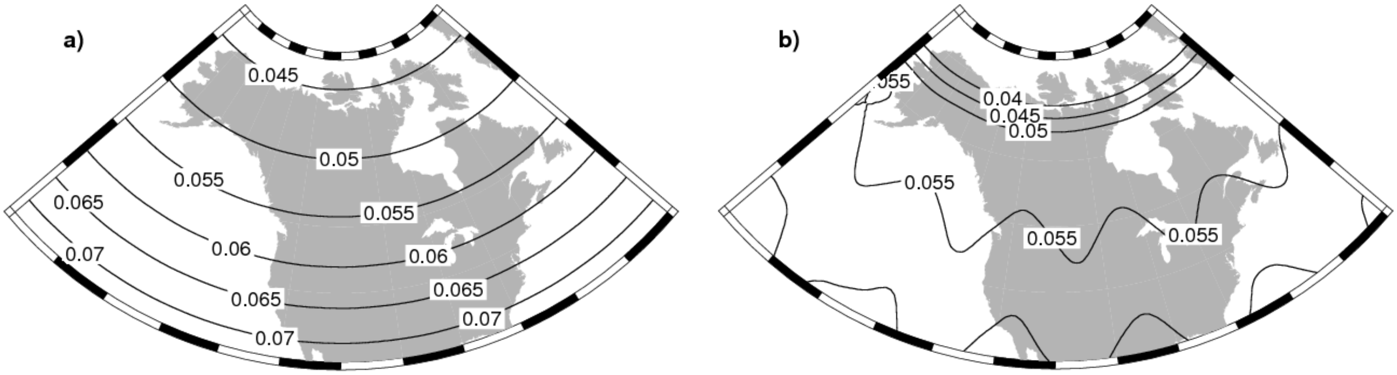

Figure 5.15: Gravity rate measurement error [µGal/year] for December 2006 computed with (a) off-diagonal in the covariance matrix terms zero (b) off-diagonal terms included.

5.2.2 Comparison of methods for determination of measurement errors

The three methods are compared in terms of cumulative degree variances (see equation (4.10) in Figure 5.16. Destriping filtering is applied on all coefficients with degree and order above 4. Interestingly, the full covariance matrix gives larger error estimates up to degree 15, but calibrated standard deviations show larger error estimates for the complete signal. This could be due to the fact that only the covariance matrix for December 2006 is used, while standard deviations are different for each month. Standard deviation is adversely affected by the decreased spatial coverage during the fall of 2004, when the repeat period was small and the distance between adjacent groundtracks large (Wagner et al., 2006). The GRACE errors can be seen to be well below the cumulative degree variance of the GIA model i3_8-60 (see section 2.4). That means that the measurement errors are not a limiting factor for extracting the GIA signal.

A comparison in the spatial domain is shown in Figure 5.17. The full covariance matrix shows more longitudinal variation (Figure 5.15b) and larger errors. Both increase southwards, as a result of the decreasing groundtrack density. The residuals show decreasing errors with latitude followed by an increase. The reason for this could be that the destriping filter performs better at higher latitudes above 45º (Swenson and Wahr, 2006). The method of residuals produces a slightly larger error estimates in the studied GIA-affected area and, therefore, this method is used to produce the final error estimate.

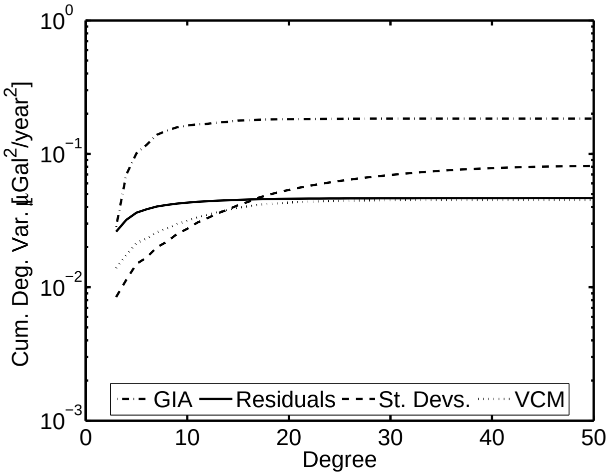

Figure 5.16: Cumulative degree variances (see equation (4.10)) for GIA model i3_8-60 and errors computed with residuals, calibrated standard deviations and a full covariance matrix.

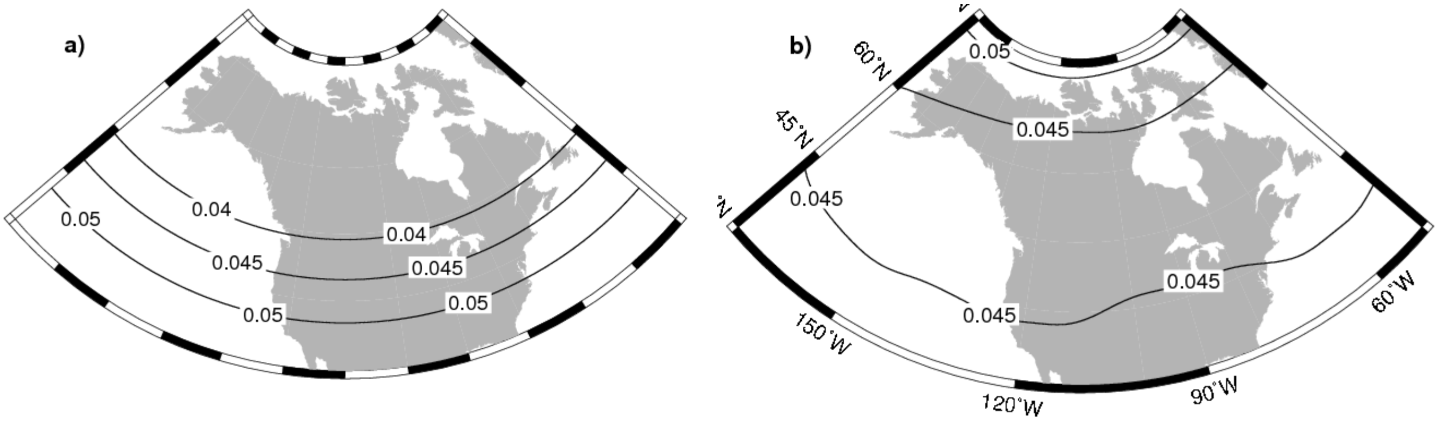

Figure 5.17: Measurement errors of the gravity rate [in μGal/year] computed with (a) calibrated standard deviations and (b) residuals.

5.3 Filters Performance Comparison

The filter performance should be assessed based on how much noise is removed and how much signal is retained. Ideally, the filter should not depend on any prior GIA information. Steffen et al. (2008) investigated the effect of the Han (2005) filter, the Swenson and Wahr (2006) filter, and the Gaussian filter on the estimated gravity rate in Fennoscandia. Based on a visual comparison, they concluded that the Gaussian filter gives a result that agrees best with the uplift pattern derived from GPS observations in Fennoscandia.

North America does not have dense GPS observations in the areas with the model GIA peaks (2007). Therefore, comparisons with GPS data may not lead to decisive results. In this chapter, an attempt is made to, for the first time, study the effect of different filters on synthetic gravity rate data set, where the ratio of signal and noise is to be maximized. The signal component is assumed to be the GIA models i3_8-60 or i5_2-60 of section (2.4). If no mention is made of the model, model i3_8-60 is used. The noise component is created using non-GIA signals represented by the continental water storage and glacier melting simulations summarized in Table 5.3. The time period is August 2002 – July 2007. It is assumed that the conclusions on the filters for a simulation over this period remain valid when the time period is extended.

The signal to noise ratio (SNR) is computed as

$$SNR = \frac{1}{n}\sum_{i=1}^{n}\frac{\dot{g}_{GIA,i}}{\sqrt{\left(\dot{g}_{WGHM,i}-\dot{g}_{GLDAS,i}\right)^{2}+\left(\sigma_{\dot{g}_{GRACE,i}}\right)^{2}}}, \tag{5.7}$$

where $\sigma_{\dot{g}_{GRACE,i}}$ is the measurement errors computed according to method 3 (equation (4.25) in section 4.3.3); $\dot{g}$ is the estimated secular gravity rate, and n is the number of points in the study area. The pixels in the coloured area of Figure 5.18 are used here.

The purpose of the SNR is to provide a single cost factor that takes into account both the removal of the signal and the reduction of noise by the filter. The SNR depends on the input models for GIA and continental water storage. Some results will be shown for alternative models (simulation 2 in Table 5.3).For a specific filter, the parameters that maximize the SNR provide the best filter performance. However, because measurement errors are small compared to the signal (see Figure 5.16), a small reduction in measurement errors can greatly increase the SNR. Therefore, the SNR is used only as a first step, to see if filter performance can be maximized by adjusting the parameters of a specific filter. In the next step, the reduction in signal amplitude is investigated.

Unlike Tamisiea et al. (2007) and Paulson et al. (2007b), the uncertainty in the hydrology models is taken into account in this thesis. Since the accuracy of the hydrology model is not provided with the model output, the difference between two models in equation (5.7) is one way to infer the uncertainty of the hydrology correction. Note that this uncertainty also takes into account the difference between open water variations modeled in WGHM and implemented in GLDAS and LaD according to section 5.1.3.

Figure 5.18 shows the gravity rate in pixels where the gravity rate mostly represents GIA. This is decided as follows. The secular gravity rate from GRACE was determined for the period August 2002 – July 2007 with the hydrology model GLDAS removed. Filtering was performed as described in section 5 of that paper. Pixels where the gravity rate from Alaska and Greenland ice melting is larger than 25% of the GRACE-derived gravity rate, or where the gravity rate is smaller than 0.5 μGal/year, are set to zero, leaving 554 pixels in the coloured area.

Table 5.3: Synthetic gravity models used to investigate filter performance.

	sim 1	**sim 2**	**errors 1**	**errors2**
Hydrology	WGHM	GLDAS/LaD[1]/CPC	$\sqrt{(sim1-sim2)^2}$	$\sqrt{(sim1-sim2)^2}$
Lake levels	included	based on tide gauges		
Alaska	84 Gt	102 Gt		
Greenland	183 Gt	211 Gt		
Hudson Bay	1.75 mm/year	3.4 mm/year		
Measurement errors			Residuals	calibrated standard deviations

[1] whenever LaD is used, the time period is Aug 2002 – July 2007.

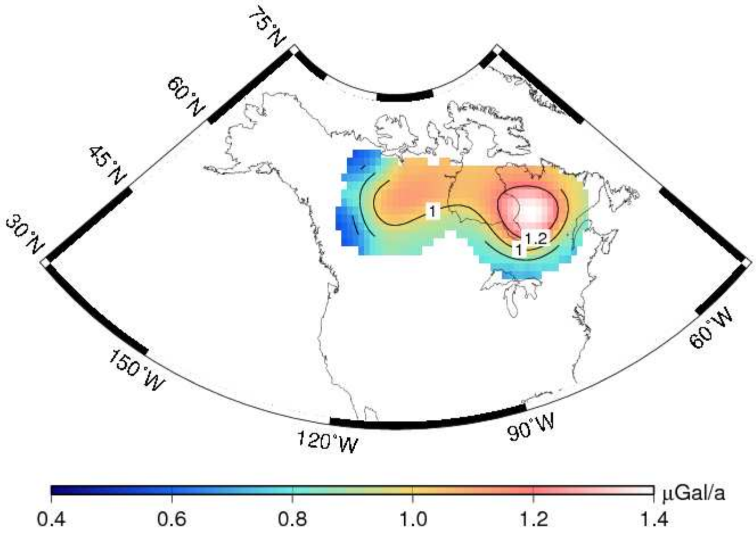

Figure 5.18: Figure 7a from Van der Wal et al. (2008a); see description in text.

5.3.1 Gaussian filter

Gaussian smoothing has become a standard against which more sophisticated methods of filtering are compared. Some filtering methods still require smoothing in a second step, such as the destriping filter. Paulson (2006); Tamisiea et al. (2007), and Paulson et al. (2007b) also applied Gaussian filtering after destriping to GRACE data to extract the

GIA signal over North America but they did not investigate the effect of different halfwidths in a systematic way.

The effect of the Gaussian filter on the SNR in equation (5.7) is shown in Figure 5.19. SNR increases slightly for halfwidths between 50 and 200 km; then it increases sharply until 1000 km when the SNR reaches a maximum. Closer inspection of the magnitude of the terms in equation (5.7) reveals that between 200 and 900 km the increase in SNR results from a decrease in the difference in the hydrology models.

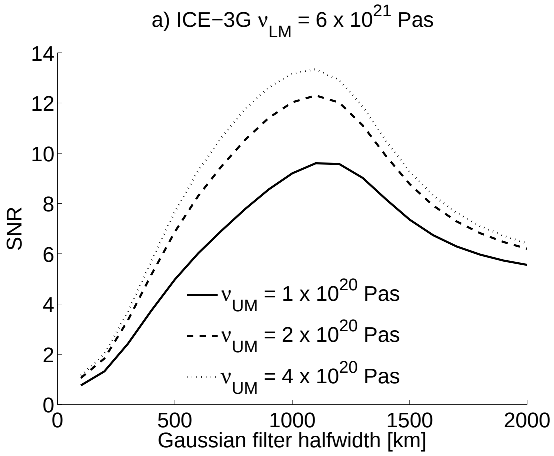

Figure 5.19: Simulated signal-to-noise ratio as a function of Gaussian smoothing radius for different GIA models: (a) ICE-3G with a lower mantle viscosity of 6 x 10^{21} Pas; (b) ICE-5G with a lower mantle viscosity of 6 x 10^{21} Pas.

As smoothing increases beyond 1000 km halfwidth, SNR decreases. This can be explained by the large power that GIA displays in the low degrees. When the halfwidth is increased so that even the low degrees are smoothed, the SNR is reduced while the errors are already small. The maximum SNR is obtained for a 1200 km halfwidth for the models with the ICE-3G history or 1000 km for the ICE-5G history. Figure 5.20 shows the maximum gravity rate for GIA models with varying upper mantle viscosity. It is clear that for a 1000 km halfwidth the gravity rates are greatly reduced. Thus, at maximum SNR the data can not distinguish well between variations of different GIA models. The

SNR and reduction in gravity rate are therefore not sufficient to determine the optimal Gaussian filter halfwidth.

It can be expected that different amounts of smoothing result in different sensitivity of the model with respect to ice sheet history and mantle viscosity. Therefore, for simulations in section 7.4.3 and misfit comparisons in section 7.5.2, the Gaussian filter halfwidth is varied. When only one gravity rate is discussed, 400 km Gaussian filter halfwidth is used as is common in the literature (e.g. Steffen et al., 2008, and Swenson and Wahr, 2008) and because it gives a strip-free gravity rate pattern while still showing two domes.

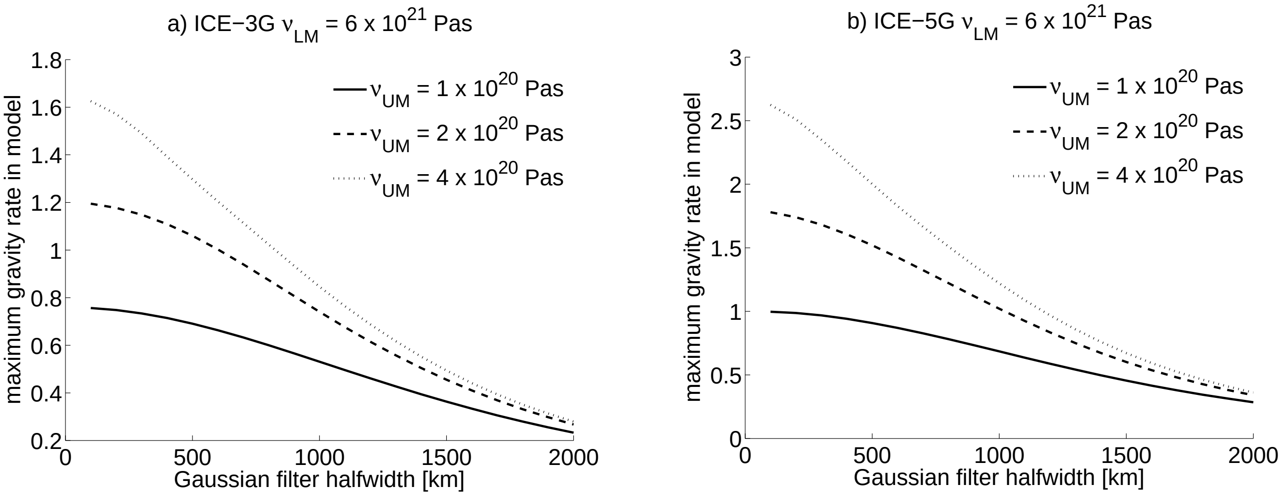

Figure 5.20: Maximum gravity rate as a function of the Gaussian smoothing radius for different GIA models: (a) ICE-3G with a lower mantle viscosity of 6 x 10^{21} Pas; (b) ICE-5G with a lower mantle viscosity of 6 x 10^{21} Pas.

5.3.2 Non-isotropic Gaussian filter

MATLAB code to compute the filter weights for the filter of Han et al. (2005) from Dr. Holger Steffen was used. The non-isotropic Gaussian filter of Han et a. (2005) contains three filter parameters (see equation (4.21)): (i) a radius for zonal components (r_{NS}), (ii) the order m_1 for which the second radius holds, and (iii) the second filter radius (r_{EW}). Filter radii in north-south and east-west direction are varied between 100 and 2000 km and the SNR is plotted in Figure 5.19 for two different choices of m_1 and GIA model i3_8-60. m_1 = 15 is preferred by Han et al. (2005). The choice of m_1 is seen to have a small influence on the pattern of the maximum signal to noise: SNR generally reduces for an increase in m_1. The filter halfwidths where SNR is maximum are 400 and 1800 km for r_{NS} and r_{EW} respectively. Interestingly, the 400 km is what is commonly used as halfwidth for the Gaussian filter (see e.g. Steffen et al., 2008, and Swenson and Wahr, 2008).

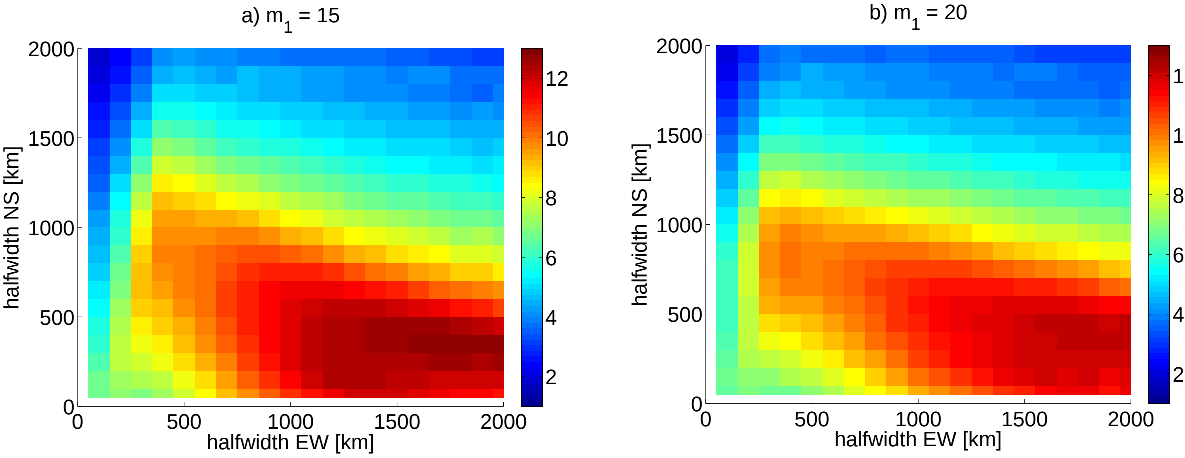

Figure 5.21: SNR of Han et al. (2005) filter vs. halfwidths in north-south and east-west direction., for (a) m_1 of equation (4.21) equal to 15, and (b) m_1 = 20.

The effect of the filtering on the maximum gravity rate is shown in Figure 5.22 for the two different GIA models i3_8-60 and i5_2-60. As expected the maximum gravity rate decreases with increasing halfwidth. However, the figure shows that the decrease is sharper with increased smoothing in north-south direction than in east-west direction. This is probably due to the shape of the GIA uplift pattern which is more east-west oriented. Thus, a larger smoothing radius in north-south direction includes more grid cells with zero or small gravity rate values. In Figure 5.22b, it can be seen that the model with ICE-5G shows that the maximum is reduced more with increasing smoothing radius in east-west direction, compared to ICE-3G. This is likely due to the particular shape of the pattern; the conclusion might not hold true for all viscosity profiles of ICE-5G.

5.3.3 Destriping filter

Here a modification is investigated for the choice of parameters for the 'original' destriping filter of Swenson and Wahr (2006). The window size and the order of the polynomial can be adjusted as in Chambers (2006). New in this research is the investigation of the effect of the spherical harmonic degree and order above which coefficients are filtered with the destriping filter (cut-off degree and cut-off order) on the SNR and on the maximum gravity rate. Tamisiea et al. (2007) specified which degree and order they used as cut-off but did not show a trade-off. SNR was used by Van der Wal (2008a) who found a maximum SNR for degree 19 and order 8. The analysis therein is repeated here with the datasets described in the previous sections.

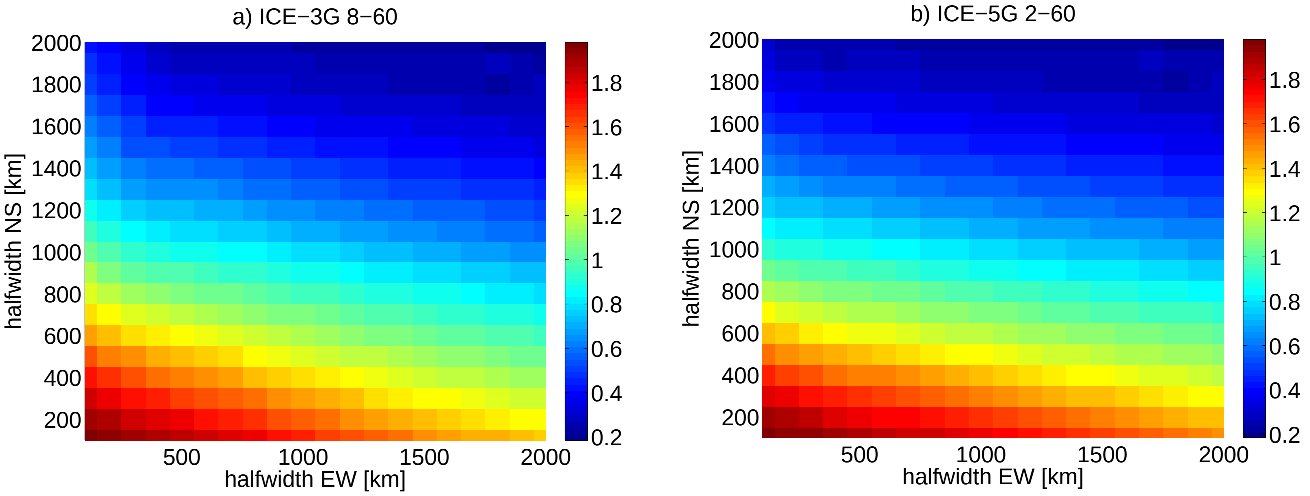

Figure 5.22: Maximum gravity rate of two GIA models filtered with the Han et al. (2005) filter. (a) i3_8-60, (b) i5_2-60.

Figure 5.23 shows that the SNR for the same two GIA models as used in the previous sections peaks at degree 10 and order 2. However, at those cut-offs, the part of the GIA signal that is filtered out is quite large, as can be seen in Figure 5.24, which shows the RMS difference between two models before and after filtering. It is noteworthy that the RMS does not decrease monotonically when cut-off degree and order are increased, i.e., filtering more coefficients of the model can result in a smaller RMS. This can be the result of the location of the stripes that are artificially induced by the filter with respect to the 554 pixels.

To ensure that the GIA signal is not too much affected by the destriping filter, it is required that the RMS difference be not too large. For visual aid a black box is drawn in both Figure 5.23 and Figure 5.24, which roughly contains the orders for which RMS is up to 0.05 μGal/year for the ICE-3G 8-6 model. The ICE-5G 2-6 model has smaller differences.

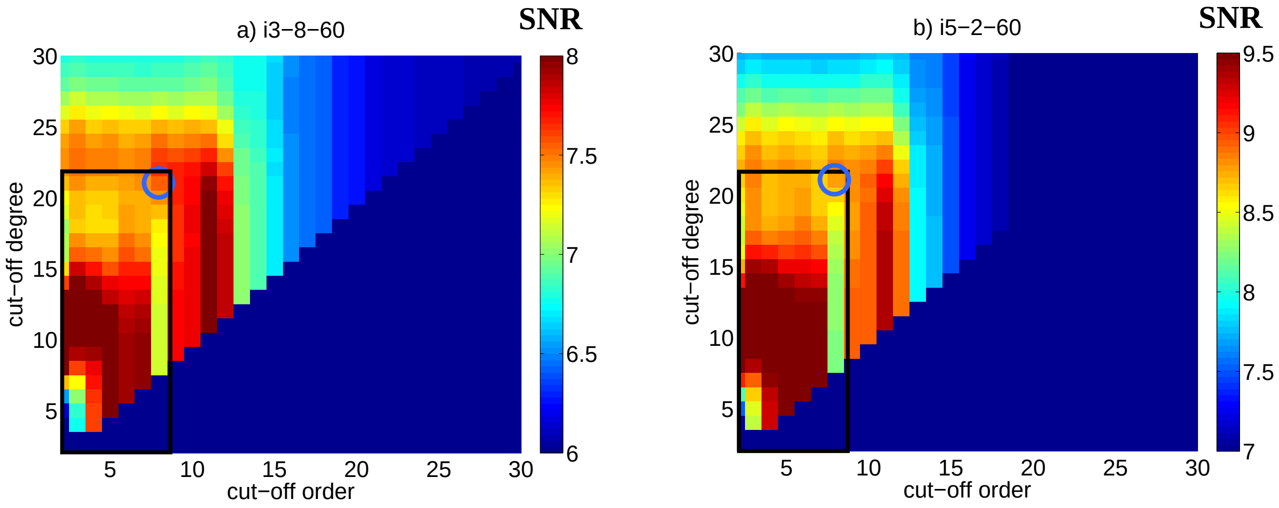

Figure 5.23: SNR ratio for two GIA models, i3_8-60 and i5_2-60 for varying cut-off degree and cut-off order.

To investigate the sensitivity with respect to the particular choices in the simulation, the order of the polynomial used to fit the correlation between coefficients (see Figure 5.12) was increased to 3 (results not shown). As expected, the destriping filter affects the signal slightly more. The 2nd order polynomial provides higher SNR which makes it a better choice. The SNR is plotted once more in Figure 5.25, but now with LaD and CPC models instead of GLDAS. The high SNR to the right of the black box is shifted in comparison with Figure 5.23, which indicates that these high values are due to the choice of hydrology models.

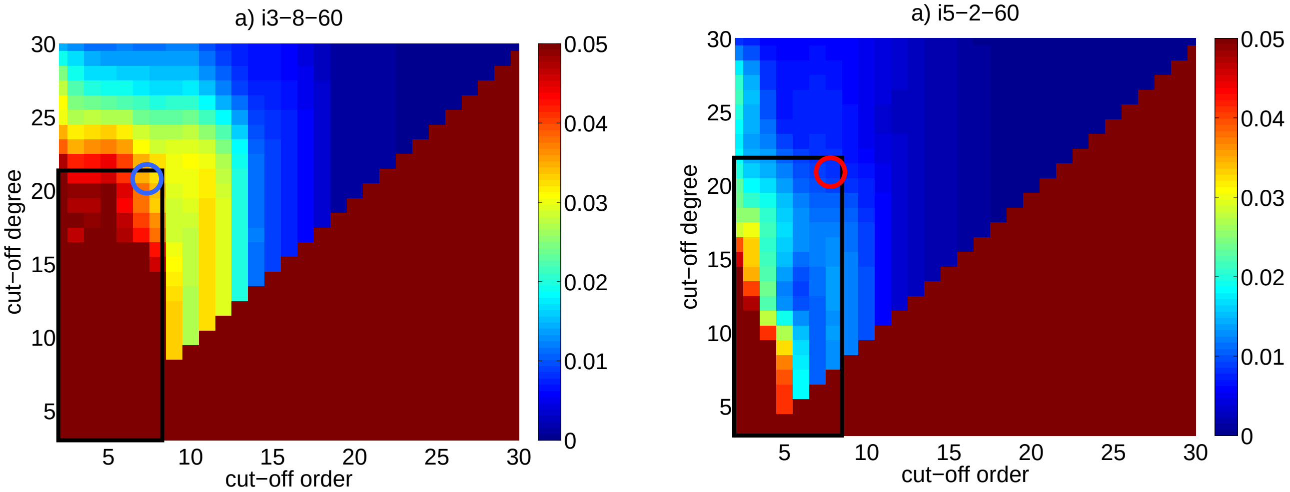

Figure 5.24: RMS difference between two GIA models before and after destriping: (a) i3_8-60; (b) i5_2-60.

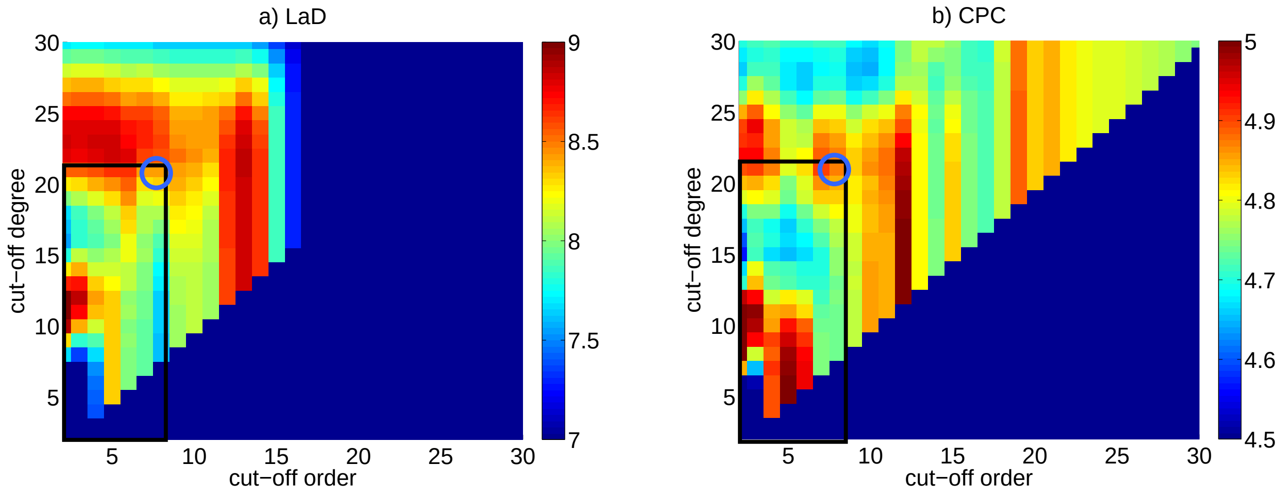

Figure 5.25: SNR vs cut-off degree and order in the destriping filter. (a) LaD hydrology model; (b) CPC hydrology model in simulation 2 (see Table 5.3).

Figure 5.26 plots the SNR with measurement errors the only error sources. We can now look for a combination of cut-off parameters for which RMS is low in Figure 5.24, and SNR is high in Figure 5.23 and Figure 5.25. Cut-off order 8 and cut-off degree 21 seems to fulfill these requirements and is denoted with a blue circle in all these figures. Visual inspection of the effect of destriping filter with these parameters on the model, as well as the effect on the estimated trend from GRACE data shows this indeed to be a good compromise.

The sharp changes in RMS with increasing cut-off order seem odd for a phenomenon as smooth as GIA. Inspecting the order variance, computed with equation (4.11), in Figure 5.26b confirms the presence of small jumps in the orders 6, 8 and 10. A cut-off at degree 8 or below results in significant modification of the model, as shown by the green dashed line. A cut-off at order 8 and degree 21 results in minor decay of the signal at orders 10 and 15 (red dotted line).

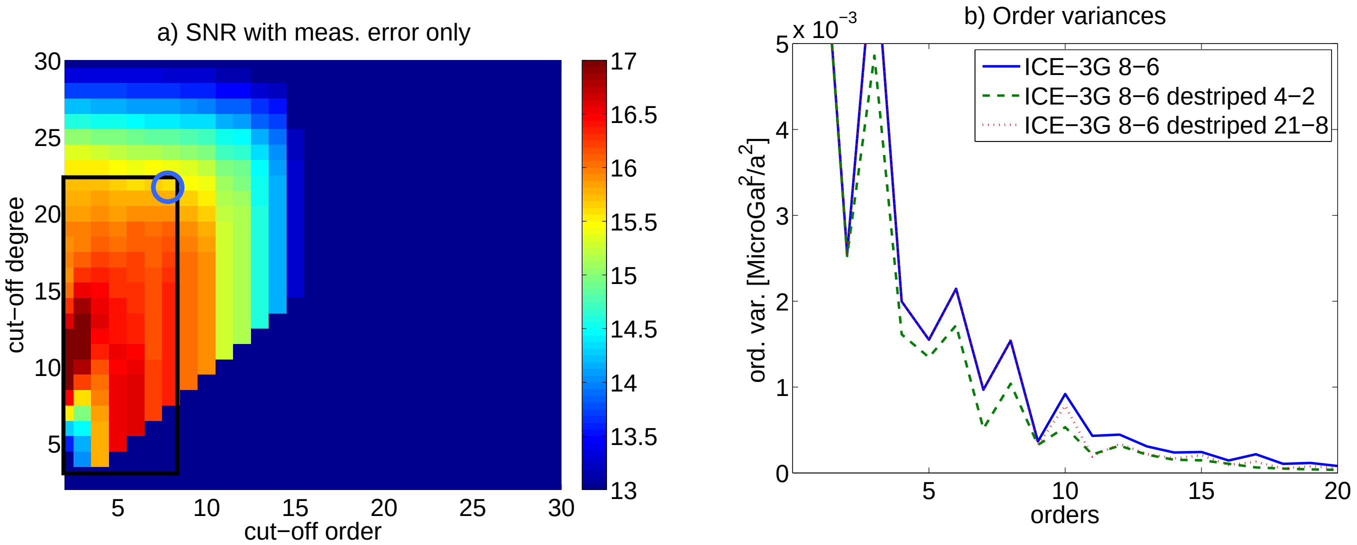

Figure 5.26 (a): SNR with measurement errors only. (b) Order variance for GIA models before destriping filtering is applied (black solid line), after destriping filtering is applied with cut-off degree 4 and order 2 (green dashed line), and cut-off degree 21 and order 8 (red dotted line).

5.3.4 Summary

Performance of the Gaussian filter (Wahr et al., 1998), non-isotropic Gaussian filter (Han et al., 2005) and Swenson and Wahr (2006) filters is compared for two different GIA models and three different combinations of hydrology models. New in this research is that the filters are compared in terms of performance parameters such as the SNR and RMS in signal reduction. It is shown that the maximum SNR for the first two filters is reached for large smoothing radii, which is not desirable because the maximum gravity rate is greatly reduced in that case. Since the Swenson and Wahr (2006) filter acts mostly to remove stripes, the effect of the filter on GIA models is limited and this effect does not monotonically increase with filtering more coefficients (Figure 5.23).

Thus, it is possible to find a cut-off degree and order where the SNR is high and the maximum gravity rate is not too much affected. The compromise was found to be cut-off degree 21 and cut-off order 8 based on visual inspection of plots of SNR, RMS reduction and order variance. The RMS reduction for these parameters is 0.028 μGal/year. The fact that such a compromise is possible makes the destriping filter suitable for extracting GIA signal from GRACE. After destriping filtering, isotropic Gaussian filtering should still be applied but a smaller radius can be used than without the destriping filter (Swenson and Wahr, 2006).

Other filters are available (Chen et al., 2006; Sasgen et al., 2007; Kusche, 2007; Klees et al., 2008), see section 4.2.3, whose performance for GIA is not investigated here. Out of those, the Chen et al. (2006) filter was found to artificially enhance east-west features (Rangelova 2007, p. 131).

5.4 GRACE estimated gravity rate

This section investigates the influence of the length of the GRACE time series on the maximum gravity rate estimated from the same time series. After that, gravity rates are presented for least-squares estimation of a trend, with the destriping filter parameters selected in section 5.3.3. Gravity rates are also shown for a least-squares estimate with GFZ data even though the effect of filtering on these data is not investigated. However, the gravity rate derived from the GFZ solutions can strengthen the conclusion of the location and of the maximum gravity rate. For the same reason a PCA based estimate is presented in section 5.4.1.2.

The gravity rate patterns presented in this section are used in Chapter 7 to constrain the mantle viscosity and to infer the location of maximum ice thickness. Because geoid rates were computed with GIA models with composite rheology, the geoid rate pattern is presented in section 5.5 and used as a constraint for composite rheology in section 6.5.

5.4.1.1 Least-squares

In Van der Wal et al. (2008a), it was shown that a gravity trend estimated from three or four years of GRACE data depends strongly on the time-series segment chosen. Figure 5.27 shows that even the maximum of a gravity rate trend estimated from five years of data (squares) varies between 1.35 and 1.52 μGal/year. Note that this difference is larger than the effect of the GRACE measurement errors in Figure 5.17. The variation can be due to interannual changes in continental water storage. However, removing GLDAS (circles) or WGHM (triangles) results in the same variation therefore the interannual variation has another cause, unless the true interannual water storage signal is not captured by both hydrology models. The interannual changes could be due to aliasing of K1 and K2 tidal signal. Particularly the degree 2 coefficients in GRACE solutions are of low quality. However, removing low degree coefficients C_{20}, C_{21}, S_{21} does not have an effect on the variation in the maximum gravity rate in the figure, thus errors in these coefficients are also not causing the variation in maximum gravity rate.

Figure 5.27 shows that the estimated secular gravity rate that starts at April or May of 2002 results in the lowest maximum trend. Those two months will be excluded from the final estimate, also because data was not collected during the complete month.

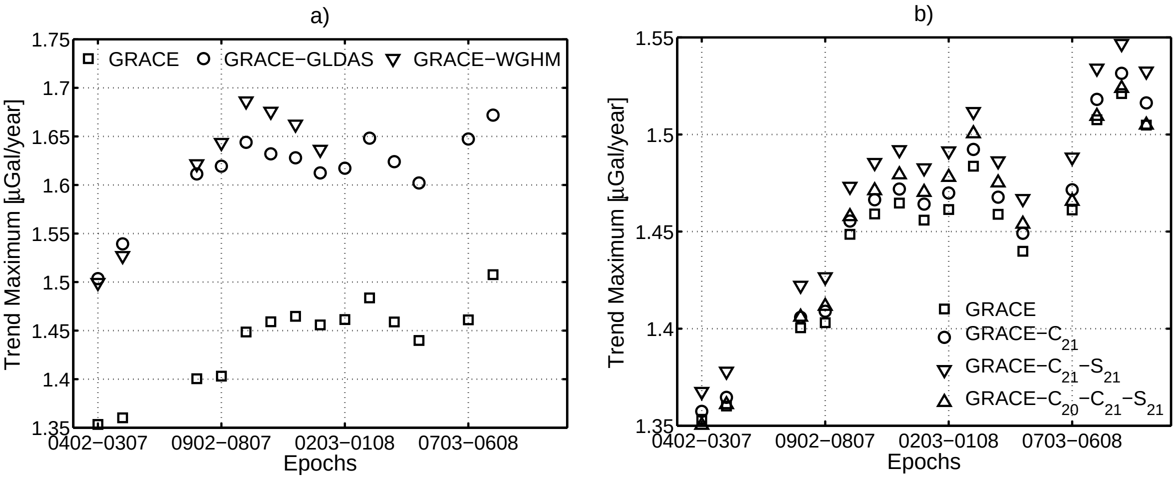

Figure 5.27: (a) Gravity rate estimated from 5 years of GRACE data. The first data point corresponds to time period April 2002 – March 2007, the last data point corresponds to August 2003 – July 2008. (b): Gravity rate estimated from 5 years of GRACE data with low degree coefficients removed.

Because of the longer time series and the good agreement between GRACE and GLDAS in Table 5.2, the GLDAS model is preferred to remove continental water storage variations. Lake level data are included in the GLDAS model. The gravity rate estimated for the longest time series available at the time of this work is shown in Figure 5.28 for CSR and GFZ fields. GFZ does not provide solutions for the months September 2002, December 2002, January 2003, June 2003, January 2004. The agreement between Figure 5.28a and b is very good in the area of the maximum gravity rate southeast of Hudson Bay, corresponding to the location of the Labrador ice dome. Note that also Lee et al. (2008), Figure 7, and Peltier and Drummond (2008), Figure 2, show the maximum gravity rate in this area. However, the second peak is diminished in the GFZ-derived gravity rate, compared to the gravity rate derived from CSR. This is contrary to what is observed in Fennoscandia where GFZ solutions resulted in gravity rate with higher maximum and closer to the center of uplift (Steffen et al., 2008a).

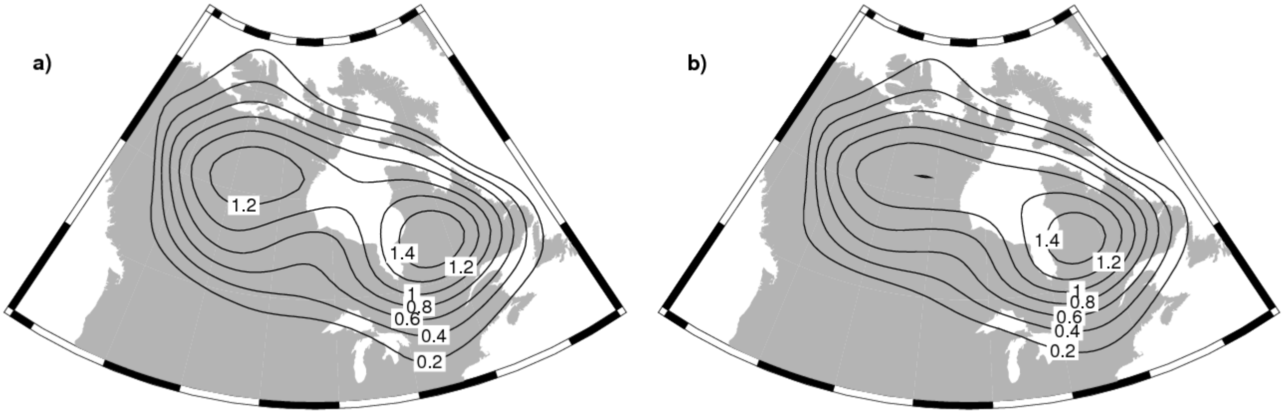

Figure 5.28: GRACE-derived gravity rate [µGal/year] estimated from (a) CSR fields and (b) GFZ fields. Time period is Aug 2002 – July 2008 and the GLDAS model is removed.

In order to be able to give uncertainty estimates in terms of differences in hydrology model, the time period is limited by the availability of a second hydrology model. Since LaD is only available up to July 2007 and CPC clearly performs the worst in the comparison with GRACE in Table 5.2, WGHM is selected for this purpose, with output available from August 2002 up to November 2007. It was found that the difference between the WGHM and GLDAS model is larger than the maximum secular gravity rate found in GLDAS alone. It can thus be argued that it is better to not remove hydrological signal in GRACE, because doing so only introduces more errors. However, the good agreement between GLDAS and GRACE in Figure 5.7 and Figure 5.5 suggests that GLDAS successfully simulates a good part of the interannual hydrology signal. Thus, the choice is made here to use GLDAS to remove hydrologic signal in GRACE and to use the differences between models as an imperfect way to account for uncertainty.

5.4.1.2 Principal Component Analysis

Principal component analysis (PCA) is applied to the GRACE data after filtering as described in section 5.3.3. The grid resolution is $1^{o} \times 1^{o}$; smaller resolution has a negligible influence on the spatial patterns and time series. In the time series in Figure 5.30a it can be seen that the first component, which accounts for 60 % of the variance, contains a trend with a small annual signal. The second component accounts for 20% of the variance and mostly consists of annual signal with a small trend superimposed. The presence of the GIA signal in different principal components makes it hard to isolate the GIA signal from other signals using PCA alone.

When the first two principal components are added and a trend is estimated, the pattern in Figure 5.30b is obtained. This pattern is very similar to that obtained with least-squares, but the contour lines are bulging south-westward, which might be due to residual hydrology signal. Also, the maximum gravity rate of 1.43 µGal/year is lower than in the least-squares pattern. The existence two domes is confirmed, with the dome south-east of Hudson Bay the larger one. The location of that maximum agrees better with the location of the Labrador ice dome (Dyke and Prest, 1987) than the trends in Figure 5.28.

PCA has the possible advantage that more noise is filtered out by removing the third and higher principal components. However, these higher components can contain part of the GIA signal (although the trend in them is small). Also the PCA spatial patterns depend on the size of the area that is used in the PCA. One solution to remove such dependence and get a more robust pattern is to apply rotation of principal components as in Rangelova (2007), but this is not pursued here.

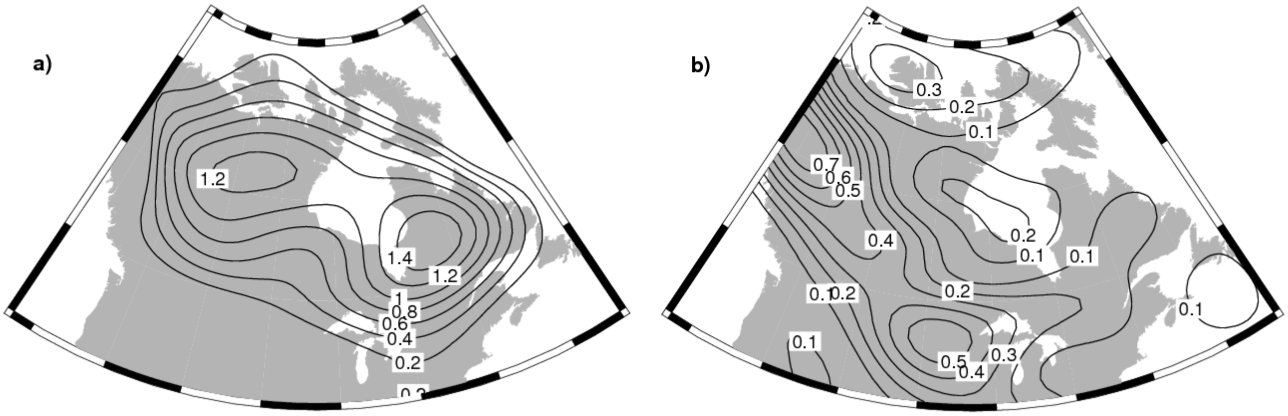

Figure 5.29: (a) Gravity rate [µGal/year] from Aug 2002 – Nov 2007 with GLDAS removed. The maximum gravity rate is 1.58 µGal/year. (b) Uncertainty in the gravity rate, consisting of the difference between GLDAS (+ lakes) and WGHM, and measurement errors.

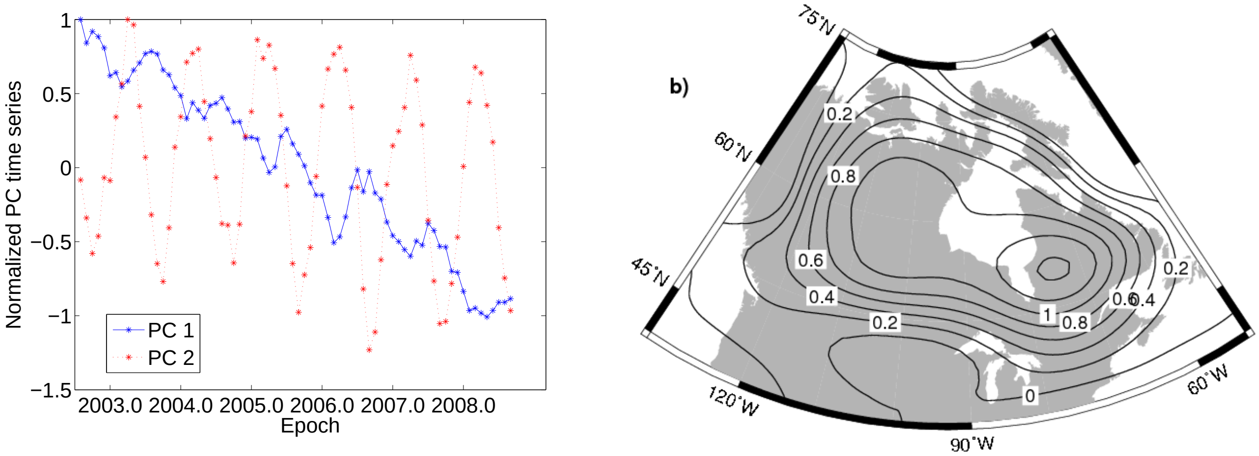

Figure 5.30: (a) Time series of the first and second principal components. (b) The spatial pattern of the trend is estimated from the combination of the first and second principal components.

5.5 Geoid rate from GRACE

Until now, the observations of GRACE have been studied in terms of gravity rate. It is useful to look at the GRACE observations in terms of geoid rate because the sea level code that was used for the FEM computations provides present-day geoid rate as output. Also, the geoid is planned to become the vertical reference surface for heights in Canada. The accuracy of this surface has reached a level where time-dependent effects become significant and GRACE data can be used to provide an epoch update to the geoid-based vertical datum.

Results for a GRACE-derived geoid rate will be presented here, using the methods, data sets and non-GIA models described in the previous sections. The results reported here are those of Van der Wal et al. (2008b). As explained there, the continental water storage changes and present-day ice melt are removed from the GRACE data for the purpose of providing a vertical datum update.

5.5.1 Methodology

The procedure described herein is that followed by Van der Wal et al. (2008b). The data span and parameters are:

- CSR release 4, Aug 2002 – July 2007;
- C_{20} is replaced with SLR derived values. This replacement was found to have little effect on the spatial pattern, but increased the secular geoid rate by 0.33 mm/year.
- Greenland ice melt: 183 Gt/year, Alaska ice melt: 84 Gt/year (see section 5.1.1).

Errors sources are combined in a vector sum as follows:

$$\sigma_{\dot{N}} = \sqrt{\left(\dot{N}_{LaD,i} - \dot{N}_{WGHM,i}\right)^2 + \left(\sigma_{\dot{N}_{GRACE},i}\right)^2 + \left(\sigma_{\dot{N}_{glaciers},i}\right)^2} \qquad (5.8)$$

where $\dot{N}_{LaD,i}$ is the secular geoid rate for grid point *i* from the LaD hydrology model (Milly and Shmakin, 2002); and $\dot{N}_{WGHM,i}$ is the geoid rate from the WGHM model. Measurement errors computed by standard deviations and residuals after trend estimation are close, with slightly higher numbers for the residuals in the GIA area.

Tuning the destriping filter is not as important for the geoid rate as it is for the gravity rate, because of the diminished short-wavelength power in the geoid rate compared to the gravity rate. However, applying the filter at low degrees would still greatly affect GIA, therefore it is still a good idea to look at the SNR to find the cut-off parameters. Note that the analysis of Van der Wal et al. (2008b) only looked at SNR for the cut-off parameters, and this is the procedure followed here. Signal-to-noise contours are presented in Figure 5.31 for different cut-off parameters. The maximum SNR is obtained for cut-off degree 23 and order 5 (using LaD instead of GLDAS to remove the effect of hydrology yields degree 23 and order 6; use of an ICE-5G GIA model does not change the SNR much).

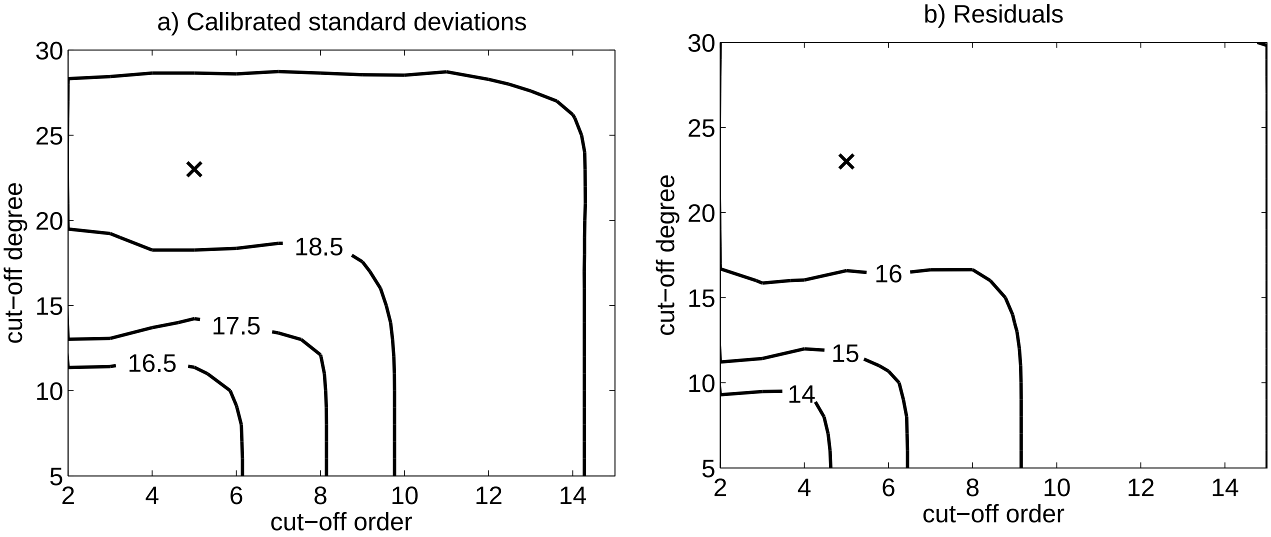

Figure 5.31: Contours of signal-to-noise ratio for the minimum spherical harmonic degree and order that is used in the destriping filter. (a): calibrated standard deviations used to compute random errors, (b): residuals used to compute random errors.

In section (5.3.1) it is shown that the Gaussian filter influences the sensitivity of the gravity rate with respect to viscosity at a certain depth. For the dynamic geoid, such sensitivity is not relevant, and a choice for smoothing the geoid rate will have to be made based on different aspects. Some smoothing seems sensible based on visual inspection of the geoid rate which contains north-south stripes if no smoothing is applied.

Here, the effect of the 400 km halfwidth Gaussian filter on cumulative degree variances is shown in Figure 5.32. The GIA model is above the total uncertainty (note the semi-log scale of the graphs). The most obvious effect of smoothing is the reduction of measurements errors (residuals) above degree 40.

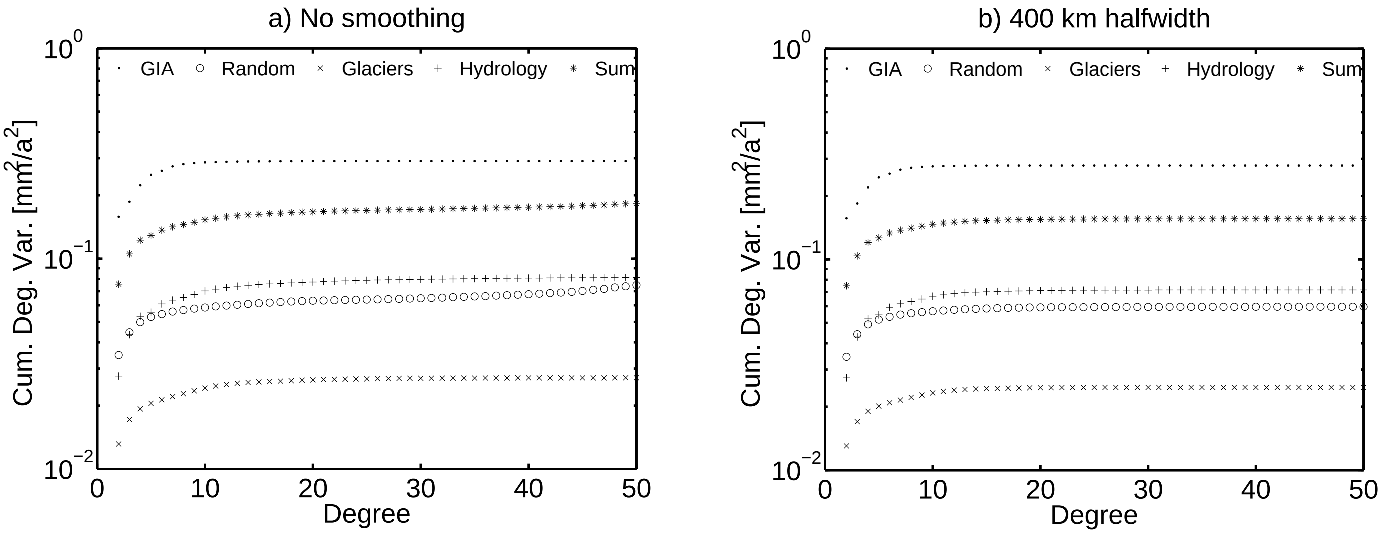

Figure 5.32: Cumulative error degree variances (see equation (4.10)) for the GIA model, glacier melting uncertainty, hydrology model uncertainty, random errors and the sum of all uncertainty. (a): no Gaussian smoothing, (b): 400 km Gaussian filter halfwidth.

5.5.2 Results: geoid rate and its uncertainty

The geoid rate with the filtering parameters discussed above is presented in Figure 5.33a, with uncertainties in Figure 5.33b. The uncertainty reflects unknown glacier melting in Alaska, and differences in hydrology models southwest of Hudson Bay and in the Great Lakes area. These large differences raise the question whether it is not better to not remove a hydrology model, since using a model might introduce more uncertainty than the secular continental water storage present in GRACE data. This problem is mitigated in Rangelova (2007) by combining the spatially homogeneous dataset of GRACE with the long-time record of terrestrial gravity.

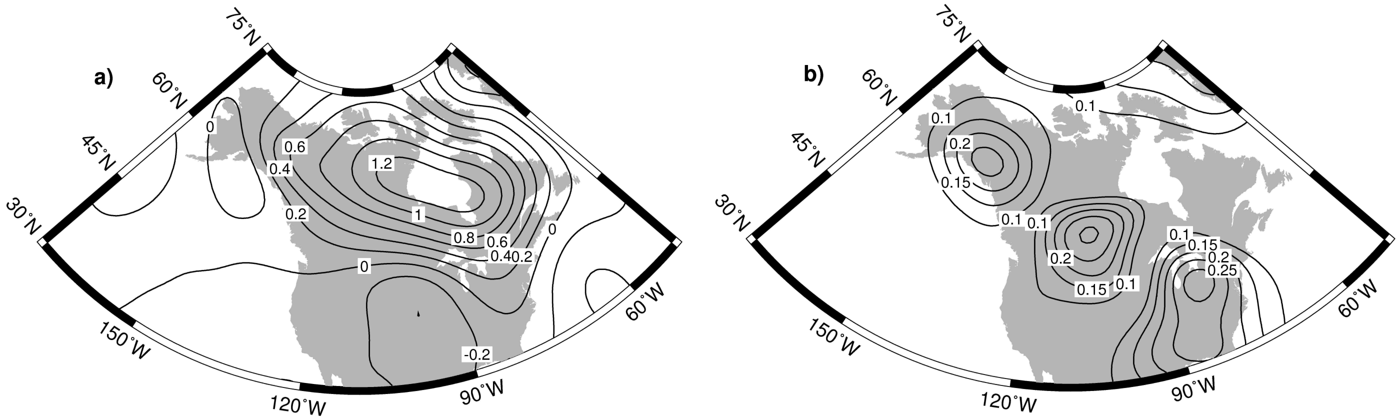

Figure 5.33 (a): Geoid rate computed from GRACE with WGHM and Alaska and Greenland glaciers subtracted, after the destriping filter (applied to coefficients with degree greater than 22 and order greater than 4) and Gaussian smoothing with a 400 km halfwidth. The maximum is 1.33 mm/year. (b): uncertainty of the geoid rate computed by equation (5.8) with random errors computed with method 3. The maximum is 0.33 mm/year.

5.5.3 Results: geoid rate for composite rheology

In this section the maximum geoid rate from GRACE data is presented which will be used in Chapter Six: as constraint for GIA models with composite rheology. For the GIA model with composite rheology, coefficients are used up to degree 90. The Gaussian smoothing that is performed on the spherical harmonic coefficients can not be ‘reversed’, but for the purpose of constraining composite rheology it is sufficient to get a rough estimate of the reduction in maximum geoid rate that results from application of the Gaussian filter. Reduction in maximum geoid rate is presented in Table 5.4 for a number of GIA models. Two models (in bold) give a maximum geoid rate close to that in Figure 5.33. The average reduction after applying the Gaussian filter for the two models is 5.5%, thus the maximum geoid rate of Figure 5.33 is multiplied by 1.055 to get an ‘unfiltered’ maximum geoid rate of 1.40 mm/year. This number is used in section 6.5 as a comparison for the models with composite rheology. Since the objective is only to see which modifications in ice history and which composite rheology parameters give an acceptable geoid rate, misfit computation with the geoid rate pattern is not useful.

Table 5.4: Maximum geoid rate and reduction in maximum geoid rate due to the application of a 400 km halfwidth Gaussian filter and destriping, for GIA models with varying upper and lower mantle viscosity and ICE-3G.

	upper mantle viscosity [Pas]				
lower mantle viscosity [Pas]		1 x 10^{21}	2 x 10^{21}	4 x 10^{21}	8 x 10^{21}
6 x 10^{21}	max. geoid rate [mm/year]	**1.41**	1.79	2.00	2.12
	reduction [%]	**4.2**	6.0	6.4	7
3 x 10^{21}	max. geoid rate [mm/year]	0.93	1.18	**1.36**	1.54
	reduction [%]	3.8	5.7	**6.7**	9.0

5.6 Summary

This chapter dealt with the post-processing of GRACE data and the uncertainty when the post-processed data are used for studying GIA in North-America. The main results are:

1. Three deterministic filters are investigated: the Gaussian filter (Wahr et al. 1998), the non-isotropic filter (Han et al. 2005) and the destriping filter (Swenson and Wahr, 2006). Of those, the combination of the destriping filter with Gaussian filtering is most practical for GIA studies because removal of stripe errors can be done separately from smoothing the data, which adversely affects the GIA signal.
2. The number of coefficients that are filtered by the destriping filter are changed to improve a signal-to-noise ratio based on simulations and to reduce the RMS reduction of certain GIA models. Filtering coefficients with degree above 20 and order above 7 resulted in a high SNR and small (~0.03 μGal/year) RMS reduction of the GIA models.

3. Water level changes in Lake Superior and Lake Winnipeg, and simulated glacier melting in Alaska and Greenland all result in secular gravity rate values in the GIA area above or at the measurement error level. It is suggested to include water level changes measured by tide gauges in the global hydrology models GLDAS, CPC and LaD since these models do not account for surface water variations. It was decided not to remove present day ice melt based on visual inspection of the resulting gravity rate map.
4. Three methods to estimating GRACE measurement error in terms of secular gravity rate were investigated: (i) propagating calibrated standard deviations, (ii) propagating a fully populated covariance matrix, and (iii) residuals after estimation of a trend, annual and semi-annual period in the monthly Stokes coefficients. All methods resulted in measurement errors of similar magnitude and a small (~0.05 μGal/year) magnitude.
5. Smoothing of the GRACE data by Gaussian filtering with an increasingly large halfwidth reduces the sensitivity of the GRACE derived gravity rate to the upper mantle viscosity.
6. The uncertainty in continental water storage changes is the largest source of uncertainty for the secular gravity rate derived from GRACE for GIA studies. Increase in water storage was shown to be large between the summer of 2003 and the summer of 2006 in an area south-west of Hudson Bay.
7. The maximum gravity rate and the gravity rate map estimated from GRACE depend on the length of the GRACE time series. Thus, one should be aware that previous and current gravity rates estimated from GRACE are influenced by this effect.

The results of this chapter are used at different places in this thesis:

- The maximum geoid rate derived in section 5.5.3 is used in section 6.5 in comparison with prediction of GIA models with composite rheology.
- The gravity rates in Figure 5.28 and Figure 5.29 are used to draw conclusions about the ice sheet history in Chapter 7.

Chapter Six: Composite Rheology in GIA modeling

This chapter studies how GIA models behave if both linear and non-linear rheology are active in the Earth's mantle, cf. section (1.1.1). This rheology is dubbed composite rheology and was first studied in the context of GIA by Gasperini et al. (1992). The effects of such a composite rheology on relative sea levels, uplift rate and gravity rate will be investigated in this chapter.

Since Gasperini et al. (1992), composite rheology has been studied by Gasperini et al. (1992, 2004), Giunchi and Spada (2000), Dal Forno et al. (2005) and Dal Forno and Gasperini (2007). These studies take the approach of using a simplified flat 3D model which requires only a relatively short computation time, to search many parameters. Here the more realistic spherical 3D model of Wu (2004) is used, at the expense of computation time. Both approaches are complementary.

A short review of literature on composite rheology in GIA modelling is followed by an analysis of stress distribution in the axisymmetric model. Results will be presented for composite rheology in the 2D and 3D models of Chapter 3. Relative sea level data will be used to find the best fitting composite rheology and sea level curves are presented and analyzed for some best fitting models. After that uplift rate and geoid rates of the model will be compared with maximum observed uplift rate and maximum GRACE observed geoid rate of section 5.5.3. Uplift rate and geoid rate are found to be too low for models with a considerable non-linear component. Therefore, section 6.6 investigates the effect of two simple modifications to the ICE-4G history: delay in ice history and scaling of ice height. Most of the material in this chapter is taken from (Van der Wal et al., submitted) but simulation results are added for a viscosity of 9 x 10^{21} Pas. Dr. Hansheng Wang coded the sea level equation which was used for this chapter.

6.1 Previous studies with non-linear or composite rheology

6.1.1 Literature review on non-linear rheology

The most recent study of non-linear rheology in (parts of) the mantle is by Wu and Wang (2007). They reviewed earlier findings, a short summary of which will be given below. Schmeling (1987) finds that the creep law seen by GIA appears to be a linear one even if mantle rheology is actually non-linear. However, Wu (1995) demonstrated in a simple study that this is true only near the center of rebound; the RSL curves near the ice margin are sensitive to whether mantle rheology is linear or non-linear. This was later confirmed for a more realistic ice history and ocean loading (Wu, 2001). Thus, non-linear rheology, which is expected to occur at mantle conditions based on laboratory experiments, influence GIA model predictions and this should be taken into account in a realistic description of the mantle rheology.

The current ice models are constructed with linear rheologies (e.g., Peltier, 2004). It was found that ice thickness should increase significantly if a good fit with relative sea level data, uplift rate and gravity rate is to be obtained with non-linear rheology (Wu, 1998; 1999). Another option to obtain good overall fit is to delay the entire deglaciation by about 2 ka (Wu and Wang, 2008) as non-linear rheology generally leads to faster relaxation near the end of deglaciation and lower present day uplift rates. Best fit to RSL data is obtained if power-law rheology is restricted to the lower mantle (Wu, 2002a; Wu and Wang, 2008).

6.1.2 Composite rheology

Composite rheology can be seen as a way to reconcile GIA observations with findings from laboratory experiments and microphysics that indicate that both diffusion and dislocation creep can operate at realistic mantle conditions. The first study of composite rheology in GIA by Gasperini et al. (1992) demonstrated that the Earth’s response with Newtonian rheology could be mimicked by a composite rheology. It was concluded that the effective viscosity directly beneath the ice load at the end of deglaciation is critical for the postglacial uplift. More recent results (Giunchi and Spada 2000; Gasperini et al., 2004; Dal Forno et al., 2005; Dal Forno and Gasperini, 2007) have introduced refinements in the reproduction of a 3D ice model on a flat grid, and a statistically more rigorous analysis of the improvement in misfit. Their studies found that the best fit could be obtained with a composite rheology, see Table 6.1.

Table 6.1: Summary of previous works on composite rheology in GIA modeling. G2004: Gasperini et al. (2004), DF2005: Dal Forno et al. (2005), DF2007: Dal Forno and Gasperini (2007). All of these study the Laurentian ice sheet. A and η are the pre-stress exponent and Newtonian viscosity of equation (3.26), σ_B is the (scalar) background stress in the implementation of equation (6.1).

	domain	**ice model**	**best fitting model**
G2004	flat axisymmetric 40x82 elements	parabolic (same volume as ICE-3G)	$\sigma_B=1.6$ $A = 2.7 \times 10^{-35}$ $\eta = 8.3 \times 10^{21}$
DF2005	3D flat, 20x10x20 elements	ICE-3G (stereographically projected)	$\sigma_B=1.6$ $A = 3.4 \times 10^{-35}$ $\eta = 4.3 \times 10^{21}$
DF2007	3D flat axisymmetric 40x82 elements	ICE-1G (zonal harmonic expansion)	$\sigma_B=0.0$ $A = 2.2 \times 10^{-34}$ $\eta = 1.6 \times 10^{21}$
		ICE-3G (zonal harmonic expansion)	$\sigma_B=0.2$ $A = 8.2 \times 10^{-35}$ $\eta = 2.7 \times 10^{21}$

These studies are all based on a flat Earth geometry, while the influence of sphericity can be notable for a large ice sheet like the Laurentide one (Wu et al., 2005). Also, the effect of self-gravitation in the Earth and in the sea-level equation is not included in these studies. Dal Forno and Gasperini (2007) found only a small difference between models with and without self-gravitation and minimize this difference by using only the last 6 ka of the deglaciation. However, at the edge of the ice sheet, the gravitation of the ice attracts large amounts of water. It is known that linear and non-linear rheology behave differently there (Wu, 1995) and that the viscosity directly beneath the ice is important for the relaxation process. Thus, the introduction of self-gravitation through the sea-level equation can introduce differences in the response of the linear and non-linear rheologies. In this thesis, the effects of Earth sphericity and self-gravitation will be included in our study of composite rheology. These effects were already present in the model of Wang and Wu (2006).

With the exception of figure 5 in Dal Forno et al. (2005), the behaviour of composite rheology for individual RSL sites is not shown in previous studies. However, the RSL behaviour at a specific location can be diagnostic of a linear and non-linear rheology (e.g. Wu, 1995). Now it is unknown at what location and what epoch purely linear/non-linear rheologies differ from composite rheology and how the value of the creep parameter *A* affects this. Misfit gives a global number for model comparison, but it will be shown in section 6.4 that misfit can depend strongly on individual sites. More detailed comparisons of the RSL behaviour of different rheologies can help to relate studies with non-linear rheology (Wu, 2002a, Wu and Wang, 2008) to studies of composite rheology.

Uplift rates computed with non-linear rheology are known to be too low (Wu, 1999). This could mean that non-linear rheology does not reflect the true deformation mechanism, or that ice models based on linear rheology need to be modified. To investigate the second point, simple modifications have been studied for non-linear rheology in the past. An increase in ice thickness improves fit with RSL data within the Laurentide ice sheet margin (Wu, 1999). Delaying deglaciation of ICE-4G by 2 ka increased uplift rates and gravity rates and improved RSL fit in the center of the Laurentide ice sheet (Wu and Wang, 2008). However, previous studies of composite rheology only compare observations and predictions of RSL, but not land uplift rate or gravity rate.

For most of the results in this chapter, background stress is omitted for the following reasons. Firstly, the locations of convection cells are not well known. Secondly, if the locations are known, the magnitude of the stress can only be derived indirectly through the use of material parameters that are uncertain. Thirdly, a microphysical argument is given by Karato (1998): strain rate resulting from GIA is orders of magnitude smaller than tectonics. Therefore, the average density of dislocations does not change much due to tectonics, over the period that GIA acts. As a result, little interaction can be expected between ambient tectonics and GIA. Finally, introduction of background stress introduces an extra parameter (or rather many extra parameters) which increase computational burden and obscure the comparison between rheologies. Note that the Gasperini et al. (1992, 2004) and Dal Forno et al. (2005), Dal Forno and Gasperini (2007) include background stress in the following way:

$$\dot{\varepsilon}_{ij} = \frac{1}{2\eta}\left[1+\left(\frac{\sigma_E+\sigma_B}{\sigma_T}\right)^{n-1}\right]\sigma_{ij}\,, \tag{6.1}$$

Where σ_E is the equivalent stress, σ_B is the background stress and σ_T is the transition stress. In this formulation background stress can only increase the effective stress. Indeed Gasperini et al. (1992) state that an increase in background stress reduces the effective viscosity. However, the tensorial nature of stresses requires that stresses in all directions are added before the effective or Mises stress is computed. Therefore, depending on the direction of the ambient tectonic stress the effective viscosity can be reduced or increased (Schmeling, 1987, and section 3.3).

6.2 Model summary

The model used here is the coupled Laplace finite element method (Wu 2004 and Wang and Wu, 2006) described in Chapter 3, which solves for deformation on a spherically stratified self-gravitating incompressible Earth with self-gravitating oceans. The axisymmetric model benchmarked in Wu and Van der Wal (2003) is used as well, because of its fast computation time and simplicity for visualization.

For the linear case, the Newtonian viscosity of 1, 3 or 9 x 10^{21} Pas, respectively. A is varied between 3.3 x 10^{-33} $Pa^{-3}s^{-1}$, 3.3 x 10^{-34} $Pa^{-3}s^{-1}$, 3.3 x 10^{-35} $Pa^{-3}s^{-1}$ and 3.3 x 10^{-36} $Pa^{-3}s^{-1}$ as already stated in section 3.2.3. The combination of the Newtonian viscosities with the 4 values of A gives a total of twelve composite theologies investigated in this thesis.

6.2.1 Ice model

For ice models, we choose to use ICE-4G (Peltier, 1994) and ICE-5G model (Peltier, 2004). The global ice models developed by Peltier and colleagues are tied to a linear rheology for the Earth model that is used in the iterative inference of ice heights. This led Dal Forno and Gasperini (2007) to revert to the older ice models (ICE-1G and ICE-3G). However, the choice here is for the global ice models that are widely used. The glaciation phase of ICE-5G is assumed to increase linearly from the start of glaciation to the last glacial maximum (LGM) which, in ICE-5G, is at 26 ka before present (BP). For the axisymmetric model, the LGM is at 20 ka BP, more in accord with the ICE-4G model (Peltier, 1994).

6.3 Stress distribution

Equation (3.23) shows that with non-linear rheology the effective viscosity becomes a function of the Mises (or effective) stress, which itself depends on location and time of the deglaciation process. In order to see whether linear or non-linear rheology dominates, it is necessary to know the stress at different locations and epochs. Therefore, in Figure 6.1 the Mises stress distribution is plotted for the axisymmetric model with a Newtonian viscosity of 3×10^{21} Pas and $A = 3.3 \times 10^{-34}$ $\mathrm{Pa}^{-3}\mathrm{s}^{-1}$. This model is found to be the best fitting model for $\eta = 3 \times 10^{21}$ Pas, in Figure 6.6a. Other models might have a slightly lower misfit, but this model has a large non-linear component which is useful to illustrate where non-linear deformation can dominate.

Another composite rheology was investigated in which the rheology used was purely linear (non-linear) if the Mises stress was below (above) the transition stress. This rheology is labelled ‘case 2’. Such rheology was found to give sea level curves close to the composite rheology formulation of Gasperini et al. (1992) (not shown). That means that we can simplify the plot and visualize the rheology as simple on-off shading. The dark grey coloured areas in Figure 6.1 show the regions that are deformed by power-law creep according to case 2. Note that only the mantle is plotted; the lithosphere is taken to be effectively elastic, but still supports a large part of the 37 MPa ice load. Stresses there are about 40 times higher. Thus, lithosphere which is taken to be visco-elastic could influence predictions, but this is not investigated here.

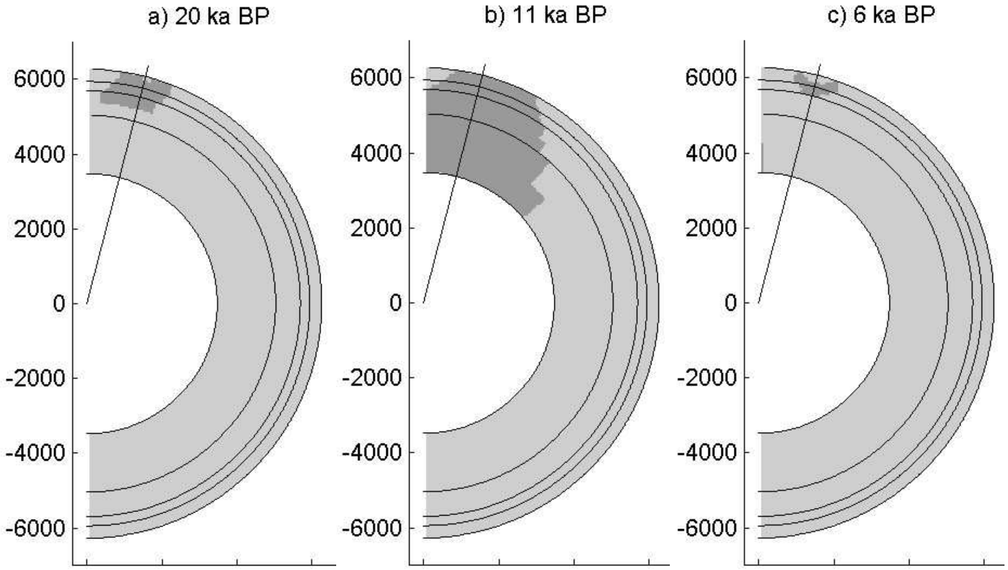

Figure 6.1: Area below the lithosphere layers of the axisymmetric model where linear rheology (light grey) or non-linear rheology (dark grey) dominates for composite rheology with a Newtonian viscosity of 3 x 10^{21} Pas and A = 3.3 x 10^{-34} $Pa^{-3}s^{-1}$. The epochs shown are 20 ka BP or LGM, 11 ka BP or end of melting, and 6 ka BP. The solid radial line at a 15° angle to the vertical denotes the location of the edge of the ice sheet.

The region in which non-linear creep occurs is small at LGM, just below the edge of the ice sheet. This region increases until the end of melting and then quickly decreases within a few kyears of the disappearance of the ice. Non-linear creep according to case 2 does not occur anymore after 5 ka BP. The large area of non-linear creep at the end of deglaciation agrees with Figure 4 of Gasperini et al. (1992), which shows the smallest horizontally averaged effective viscosity at the end of deglaciation. These results suggest that modeling lateral variations at the ice sheet margin might be important in future work, as these variations can have strong impact on non-linear rheology through the low effective viscosity there. Note that the higher stress that exists in the uppermost layers of the mantle during most of the deglaciation implies an increase in viscosity with depth. Therefore, non-linear rheology can recreate a depth-dependence that is found by most GIA inversion studies (e.g., Peltier 2004; Kaufmann and Lambeck, 2002).

The transition stress (equation (3.29)) depends on the selected linear viscosity and *A*. In Figure 6.2 the transition Mises stress is plotted for four different viscosities with $n = 3$, versus $\log_{10}(A)$. If the Mises stress is above these curves, non-linear rheology will dominate (see also Gasperini et al., 2004). Considering that the peak Mises stress in the mantle is generally of the order of a few MPa, Figure 6.2 can be used to see find out for which combination of *A* and η non-linear behaviour can be expected and which composite rheology models will behave effectively linear. Increasing the linear viscosity reduces the transition stress and effectively makes the behaviour of composite rheology closer to that of nonlinear rheology. Conversely, decreasing *A* leads to higher transition stress, which makes composite behave as linear rheology.

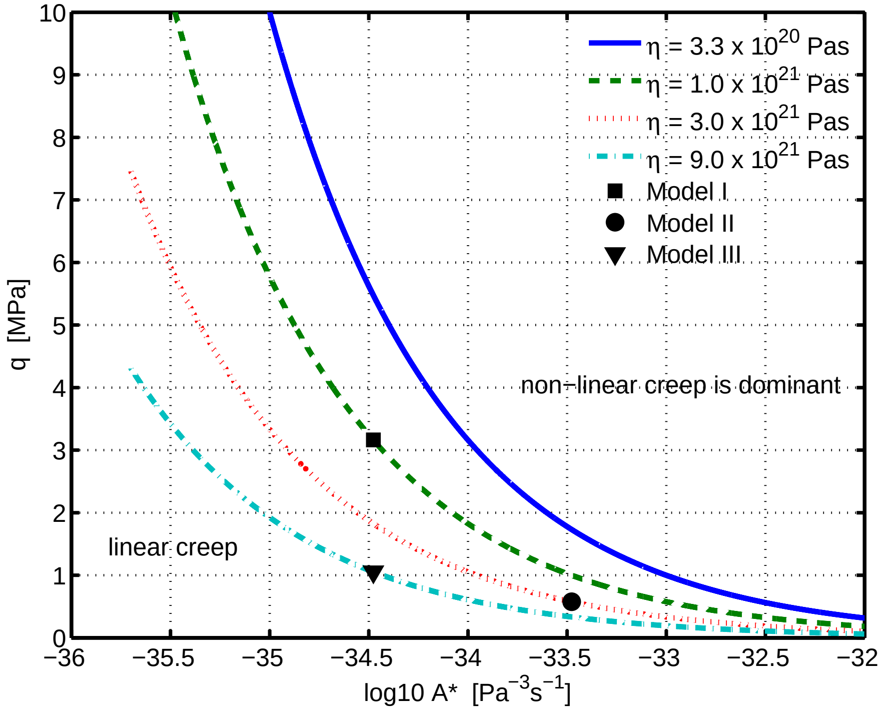

Figure 6.2: Transition Mises Stress q_t versus $\log_{10}$(A) for four typical values of η in the mantle and $n = 3$. For a given Newtonian viscosity, if the Mises stress at a certain location in the Earth is higher than given by the curve, non-linear creep is dominant at that location.

To show the temporal evolution in more detail than Figure 6.1, Figure 6.3 plots the Mises stress at 4 locations ($\theta = 0.25^{o}$, 10.25^{o}, 15.25^{o} and 30.25^{o} from the centre of the load) just below the lithosphere. Note that the Mises stress is computed from deviatoric stresses.

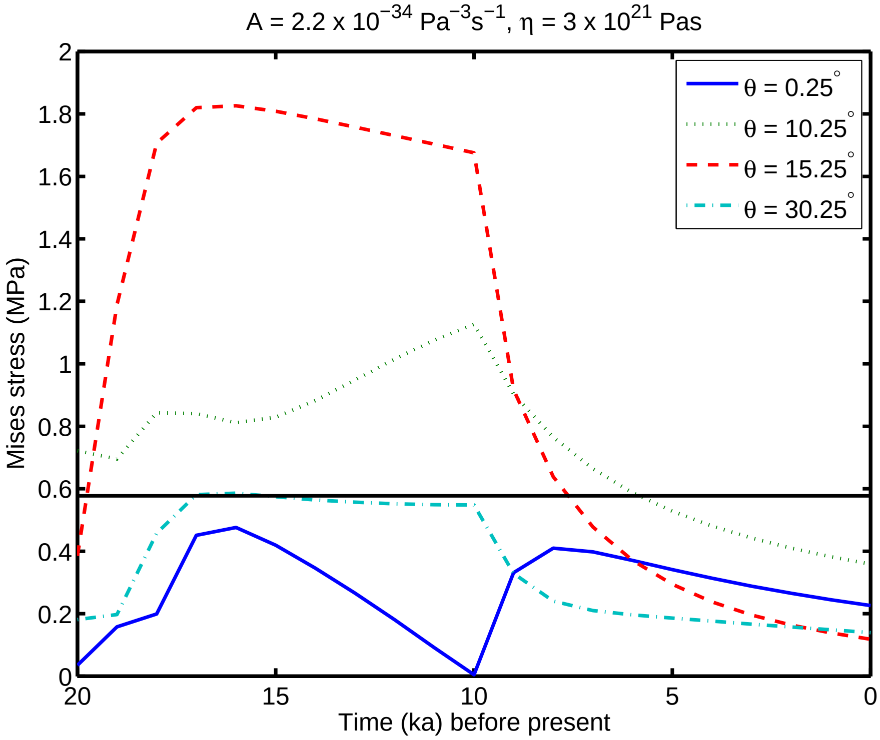

Figure 6.3: Time evolution of Mises stress q at four locations just below the lithosphere (at r = 6220 km) in the axisymmetric model of Fig. 1. The horizontal thick line indicates the transition stress level (see Fig. 3), above which the dominant creep is non-linear.

For A= 3.3 x 10^{-34} Pa^{-3}s^{-1} and η = 3 x 10^{21} Pas the transition stress is 0.58 MPa and is indicated in Figure 6.3 as the solid horizontal line. According to case 2, non-linear creep dominates when the Mises stress (coloured lines) rises above the transition stress (solid black line). Figure 6.3 shows that at the center of the load and far away from the ice ($\theta = 30.25^{o}$), the Mises stress is not high enough to allow non-linear creep, thus linear creep dominates. The highest stresses occur around the ice margin ($\theta = 15.25^{o}$), where non-linear rheology becomes dominant after 19 ka BP and until 8 ka BP. Closer to the center of the ice sheet ($\theta = 10.25^{o}$) power-law creep is the dominant flow mechanism only from 18 ka to 15 ka BP.

The spatial evolution in Figure 6.1, the temporal evolution in Figure 6.3, and the level of transition stress in Figure 6.2 help to understand the behaviour of the more complicated 3-D model in the following sections.

6.4 Comparison with RSL observations

The previous sections supply the 'tools' to understand how the state of stress, through the transition stress, decides which of the two rheologies contributes more to the total relaxation. In this and the following sections, the predictions of the GIA model with composite rheology and parameters listed in section 6.2 are compared to data. To judge the performance of a GIA model, RSL data are arguably the most important data set. Therefore this section is concerned with RSL data, in the form of global misfit in section 6.4.1 and curves for individual sites in section 6.4.2.

6.4.1 Global Misfit

The 30 RSL observations from Tushingham and Peltier (1991) that are used here are listed and plotted in Appendix E. They are C^{14} age calibrated according to Fairbanks et al. (2005). Misfit with respect to globally spread RSL observations is widely used to compare model performance, but can be sensitive to large misfit values at individual sites. The sensitivity of global misfit to RSL data is investigated in Figure 6.4, where the misfit is plotted for individual sites. It can be seen that stations 16 (McMurdo) 22 (Onsala) have large peaks. Note that these are not outliers because of the bad quality of data; the large values are caused by a combination of bad fit and small errors in the observations (only the height errors in the RSL observations are used, not the time errors). This is shown in Figure 6.5, where the sea level curves for these two stations are plotted. Station McMurdo has inconsistent observations that are likely impossible to fit with any model, while in Onsala the data lie on a smooth curve, but the models do not provide a good fit. Therefore, McMurdo will be left out of comparison in the following but Onsala is included.

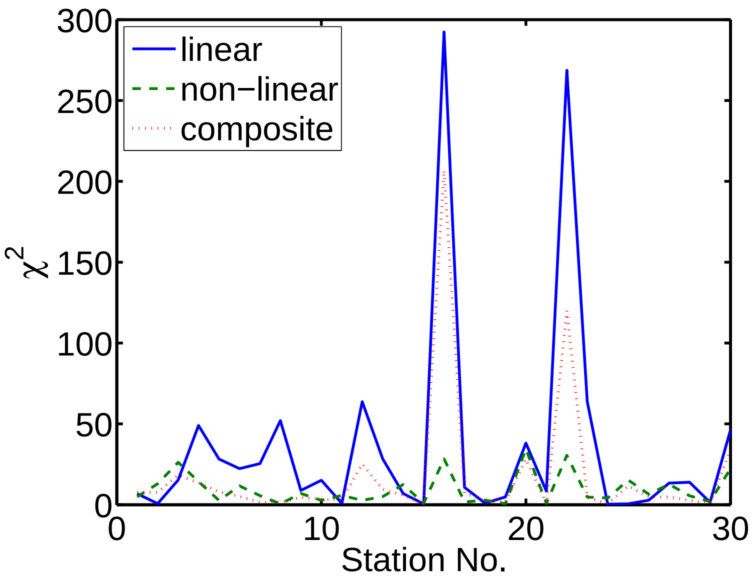

Figure 6.4: Misfit per site for all 30 sites of Appendix E for a linear, composite and non-linear rheology with one or both of the following parameters: $A = 3.3 \times 10^{-35}$ Pa^{-3}s^{-1}, $\eta = 3 \times 10^{21}$ Pas.

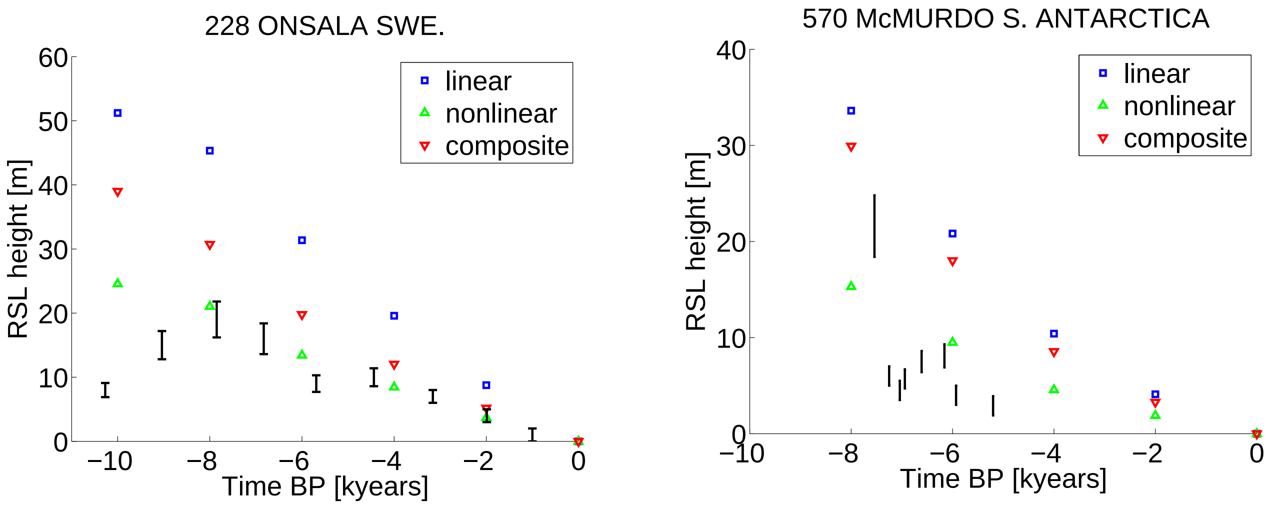

Figure 6.5: Relative sea level predictions for the same models as Figure 5.1 and observations (black vertical lines) for stations McMurdo and Onsala.

The question is what is the effect on the misfit value of leaving out some sites? Figure 6.6 plots the misfit for different sites left out. It can be seen that one or two stations can make a large difference in the relative performance of linear and non-linear rheology. From Figure 6.6a it can be concluded that the best fitting composite rheology model has A = 3.3 x 10^{-34} $Pa^{-3}s^{-1}$, while from Figure 6.6c the best-fitting model has A = 3.3 x 10^{-35} $Pa^{-3}s^{-1}$. From Figure 6.6c it can be concluded that composite rheology and non-linear rheology perform equally well, while from Figure 6.6a it seems as if composite rheology performs much worse. In Figure 6.5b it can be seen that data for station McMurdo is inconsistent with an exponential sea level curve therefore it can be concluded that the data is bad or the ice model is in error. However, for station Onsala this can not be concluded. Therefore it can not be argued that the Onsala site should simply be removed. One way to limit the influence of excessive misfit values is to use a more robust statistic instead of the chi-squared misfit. The absolute value of the weighted differences (or L1-norm) is a more robust statistic (e.g. Press et al. 1992, section 15.7). It is defined as

$$\chi^2 = \frac{1}{n}\sum_{i=1}^{n}\left|\frac{o_i - p_i}{\sigma_{oi}}\right|, \tag{6.2}$$

where the vertical lines denote the absolute value.

The L1-misfit is demonstrated in Figure 6.7 for the same composite rheology model as in Figure 6.4. Leaving out one site changes the L1-misfit value of composite rheology so that is actually becomes lower than that for non-linear rheology. However, in both Figure 6.7a and Figure 6.7b, the best fitting composite rheology model is the same, which is reassuring. Because the conclusions on best fitting rheology based on L1-misfit seem to be more robust, L1-misfit will be used in this chapter in addition to L2-misfit, although conclusions about best fitting models will be based on L2-misfit, in line with previous GIA studies.

The misfit for linear, non-linear and composite model is plotted in Figure 6.8a for four different values of A and a Newtonian viscosity of 1 x 10^{21} Pas. The lowest misfit is found for non-linear rheology with A = 3.3 x 10^{-35} $Pa^{-3}s^{-1}$ (the same value as found in Wu, 1999). The misfit for composite rheologies is close to that of non-linear rheology for large value of A and transitions to that of linear rheology for a small value of A, with a minimum (11.8) for A = 3.3 x 10^{-35} $Pa^{-3}s^{-1}$. The model with this combination of A and η will be labelled ‘model I’ for future use. In Figure 6.8b the L1-misfit shows the minimum misfit is still reached by non-linear rheology with $A = 3.3 \times 10^{-35}$ Pa^{-3}s^{-1}. However, there is no clear minimum for composite rheology models anymore.

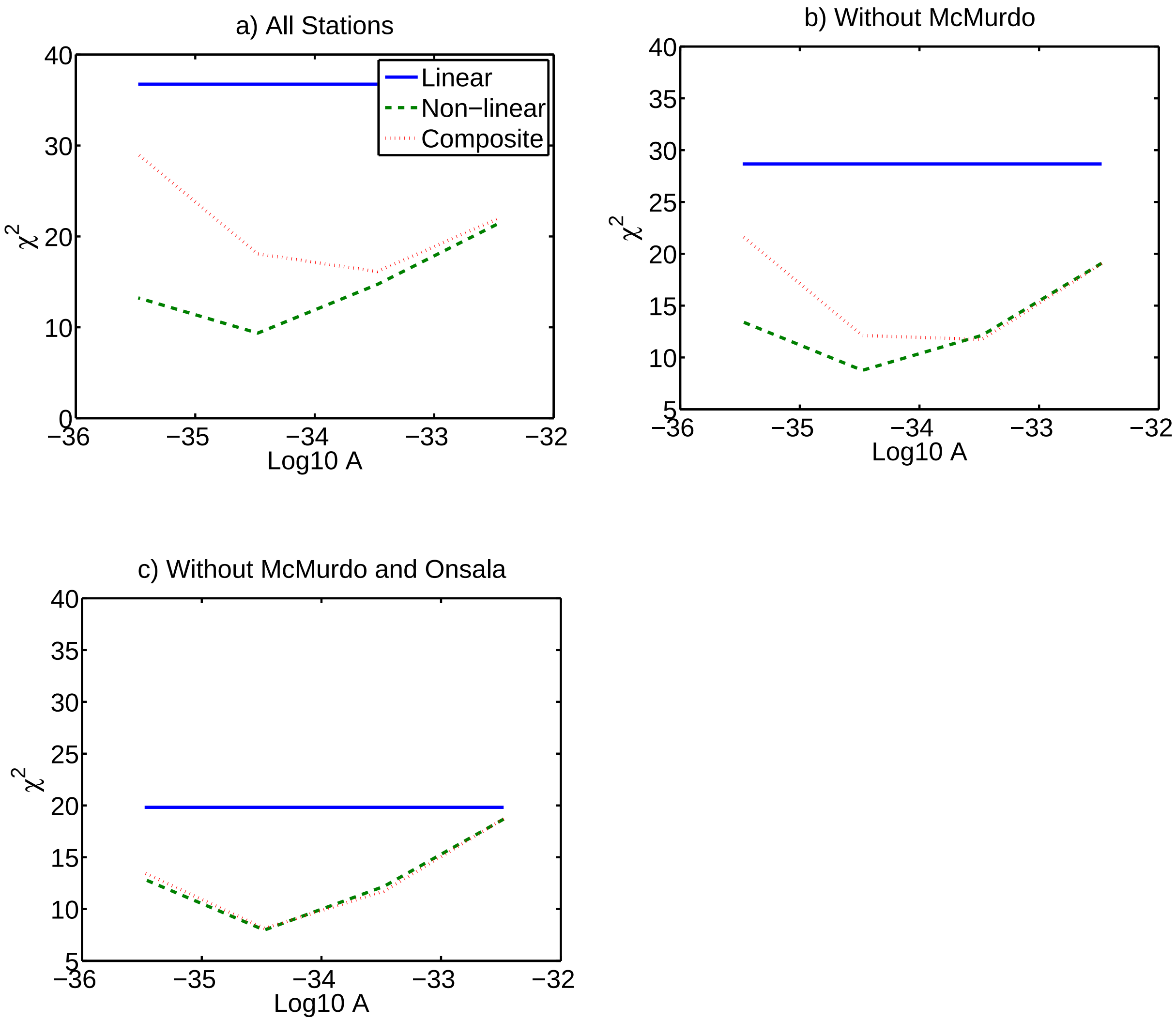

Figure 6.6: RSL misfit for a composite rheology with Newtonian viscosity of 3×10^{21} Pas and three different values for A, for three cases: (a) all station; (b) McMurdo is left out, and c) McMurdo and Onsala are left out.

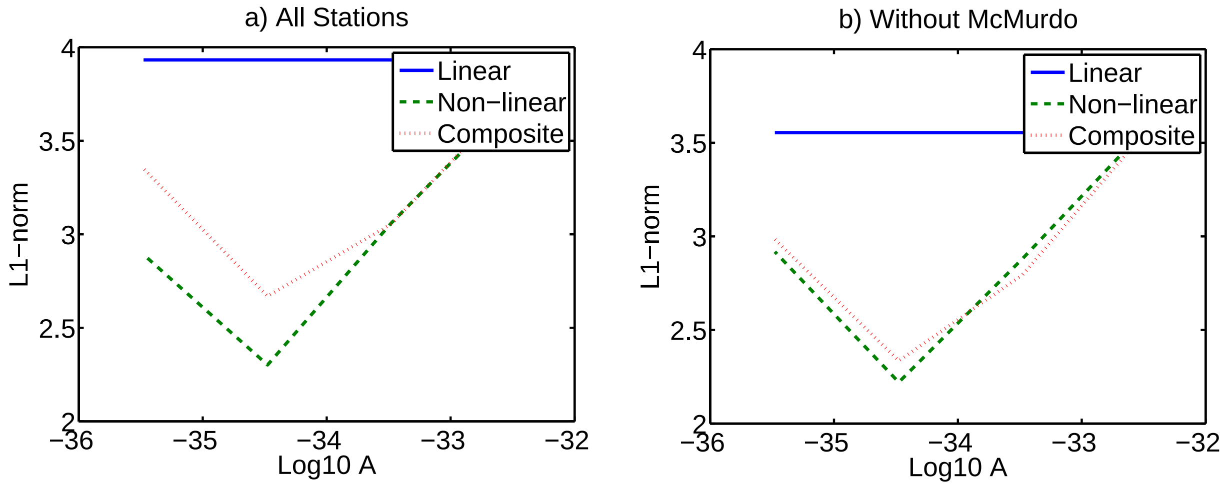

Figure 6.7: L1-norm misfit for model with η = 3 x 10^{21} Pas and varying *A* for two cases: (a) all stations; (b) Without McMurdo.

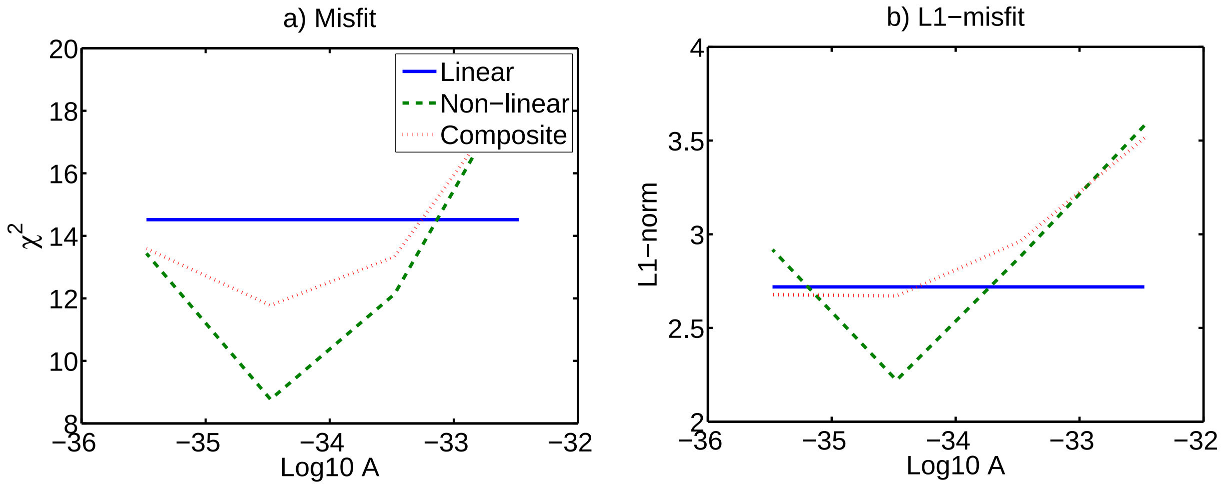

Figure 6.8: L2-misfit and L1-misfit for models with Newtonian viscosity of 1 x 10^{21}Pas.

The presence of dislocation creep in addition to diffusion creep probably means that the best fit Newtonian viscosity is larger than the value of 1 x 10^{21} Pas that provides a good fit for purely linear rheology (Mitrovica, 1996) because the dislocation creep provides an additional relaxation mechanism. For example, Dal Forno and Gasperini (2007) find a Newtonian viscosity of 2.7 x 10^{21} Pas for the best-fitting composite rheology. The misfit curve for composite rheology in Figure 6.6b (η = 3 x 10^{21} Pas) follows the misfit curve of non-linear rheology up to smaller values of A than in Figure 6.8. This can be explained by the transition stress in Figure 6.2, which for a Newtonian viscosity of 3 x 10^{21} Pas (dotted curve) is below that for a Newtonian viscosity of 1 x 10^{21} Pas. Assuming that an element is under the same stress, it will have a larger non-linear deformation component in case the Newtonian viscosity is raised to 3 x 10^{21}Pas.

The best fitting composite rheology for η = 3 x 10^{21} Pas is found to be A = 3.3 x 10^{-34} $Pa^{-3}s^{-1}$ for L2-misfit (with Onsala but without McMurdo, see Figure 6.6b), while the model with L1-misfit has A = 3.3 x 10^{-35} $Pa^{-3}s^{-1}$ and misfit close to that of non-linear rheology. It was shown before that the misfit curve keeps its shape if L1-misfit is computed, while the shape is sensitive to removal of 'outliers' under L2-misfit. However, the best fitting model of Figure 6.6b is accepted for now as the best fitting model and is labelled 'model II'. The value of A of model II is an order of magnitude larger than that found by Dal Forno and Gasperini (2007) who obtained the best fit for a model with transition stress of 1.5 MPa, which from Figure 6.7b. This translates to an A of 1.8 x 10^{-35} $Pa^{-3}s^{-1}$. However, the 0.2 MPa background stress in their best fit model acts to slightly decrease the effective viscosity.

Increasing the viscosity once more by a factor of three yields the misfit curves in Figure 6.9. The best fitting rheology is still the non-linear rheology in all cases. However, the best fitting model in Figure 6.9 has a smaller A than model II: 3.3 x 10^{-35} $Pa^{-3}s^{-1}$. The best fitting model for the L2 and L1-misfit has the same value of A as in Figure 6.8, with the misfit value for the L1-misfit almost the same as in Figure 6.7b. This model is labelled 'model III'.

In this section it is concluded that station McMurdo is left out of RSL misfit computations. Based on L2-misfit (χ^2) analysis, best fitting models for three values of the Newtonian viscosity are selected. Model I and III both have a value of A equal to 3.3 x 10^{-35} $Pa^{-3}s^{-1}$, while model II has a value of A equal to 3.3 x 10^{-34} $Pa^{-3}s^{-1}$. L1-misfit was shown to be less sensitive to individual stations so it will be used alongside L2-misfit.

6.4.2 RSL curves

Global misfit provides one number for model comparison, which is easy for visualizing results, but detailed features are not reflected by this number. Therefore, here a few sites are selected (see Figure 6.10) for which the sea level curves for linear, non-linear and composite rheology are compared. The sites are thought to be representative for the center of the ice sheet, the ice sheet margin of the Laurentian and Fennoscandian ice sheets, and the far-field; see Table 6.2.

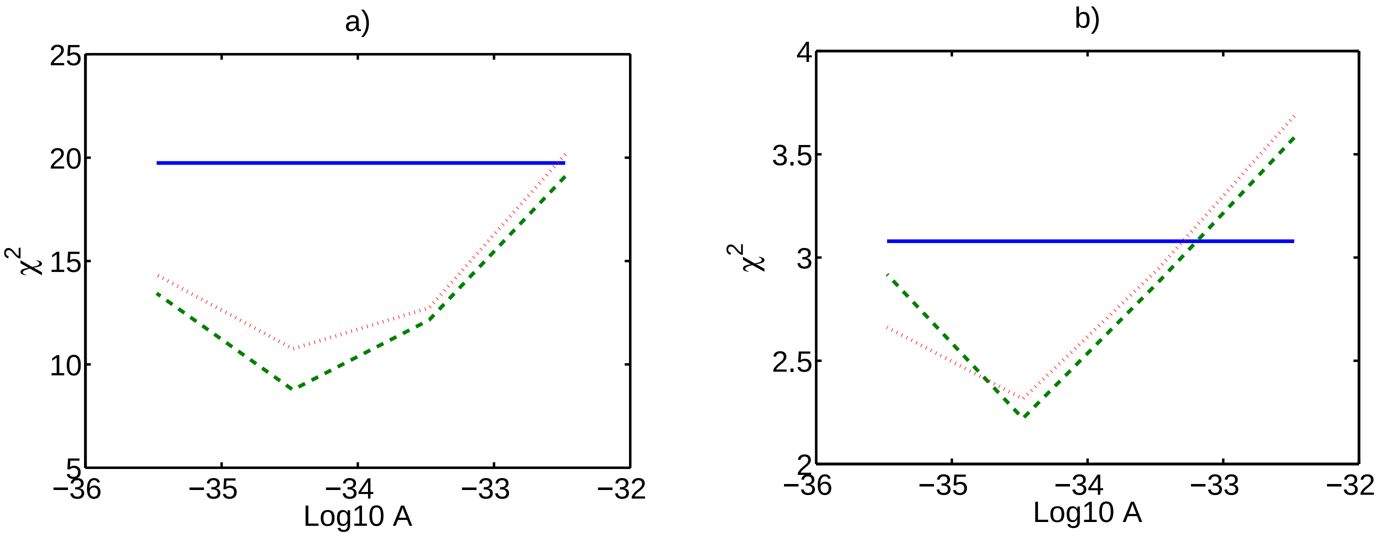

Figure 6.9: (a) L2-misfit and (b) L1-misfit for models with Newtonian viscosity of 9 x 10^{21}Pas.

Relative sea level curves for model I (A = 3.3 x 10^{-35} Pa^{-3}s^{-1} and η = 1 x 10^{21} Pas) are shown in Figure 6.11. For this model the transition stress is as high as 3.17 MPa (see Figure 6.2), which means that the Mises stress in the mantle rises above the transition stress only for sites close to the ice margin, see Figure 6.3. At these sites the stress is higher and effective viscosity is lower, which leads to faster relaxation. The sea level curves confirm this: the composite rheology curve is close to the curves for the linear rheology for most sites at early times with the exception of Brigantine and Kong Karls Land, which deviate from linear rheology and become close to nonlinear rheology probably because they are closer to the ice margin where larger stresses occur.

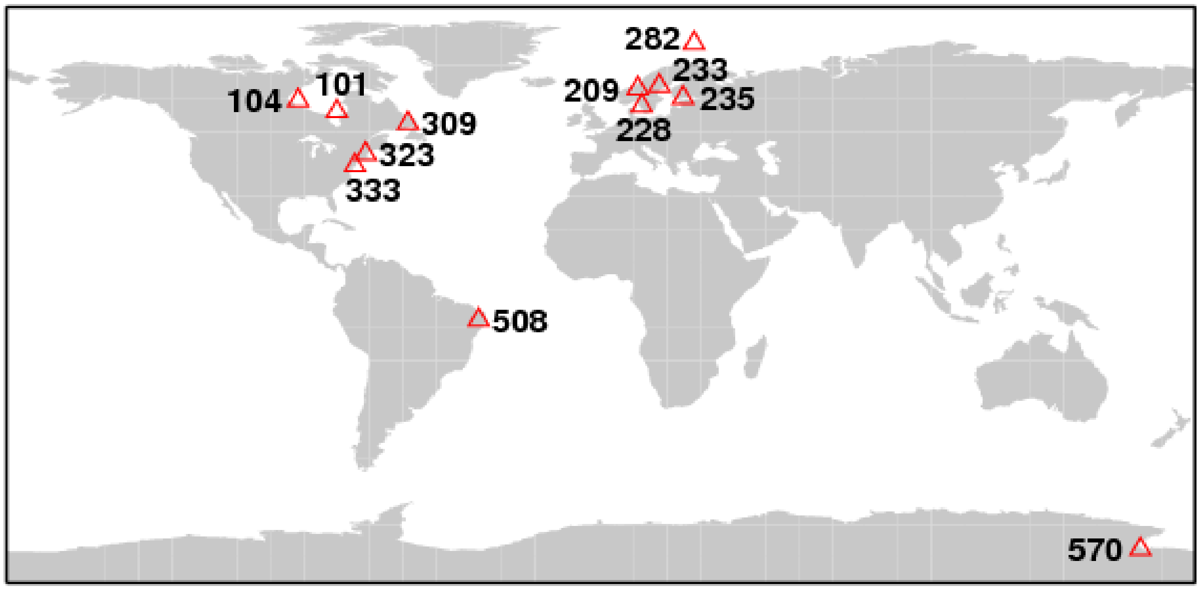

Figure 6.10: Location of the 12 RSL sites used for Figure 6.11 to Figure 6.13.

Table 6.2: Classification of RSL sites in Figure 6.10.

	center	**margin**	**far-field / other**
Laurentide	Richmond (101), Churchill (104), NW Newfoundland (309)	Boston (323), Brigantine (333)	Recife (508), McMurdo (570)
Fennoscandia[1]	Bjugn (209), Ångermanland (233), Helsinki (235), Kong Karlsland (282)	Onsala (228)	

[1] Because the RSL curves of Ångermanland (233), Helsinki (235), Kong Karlsland (282) show uplift they are classified as close to the center of the ice sheet.

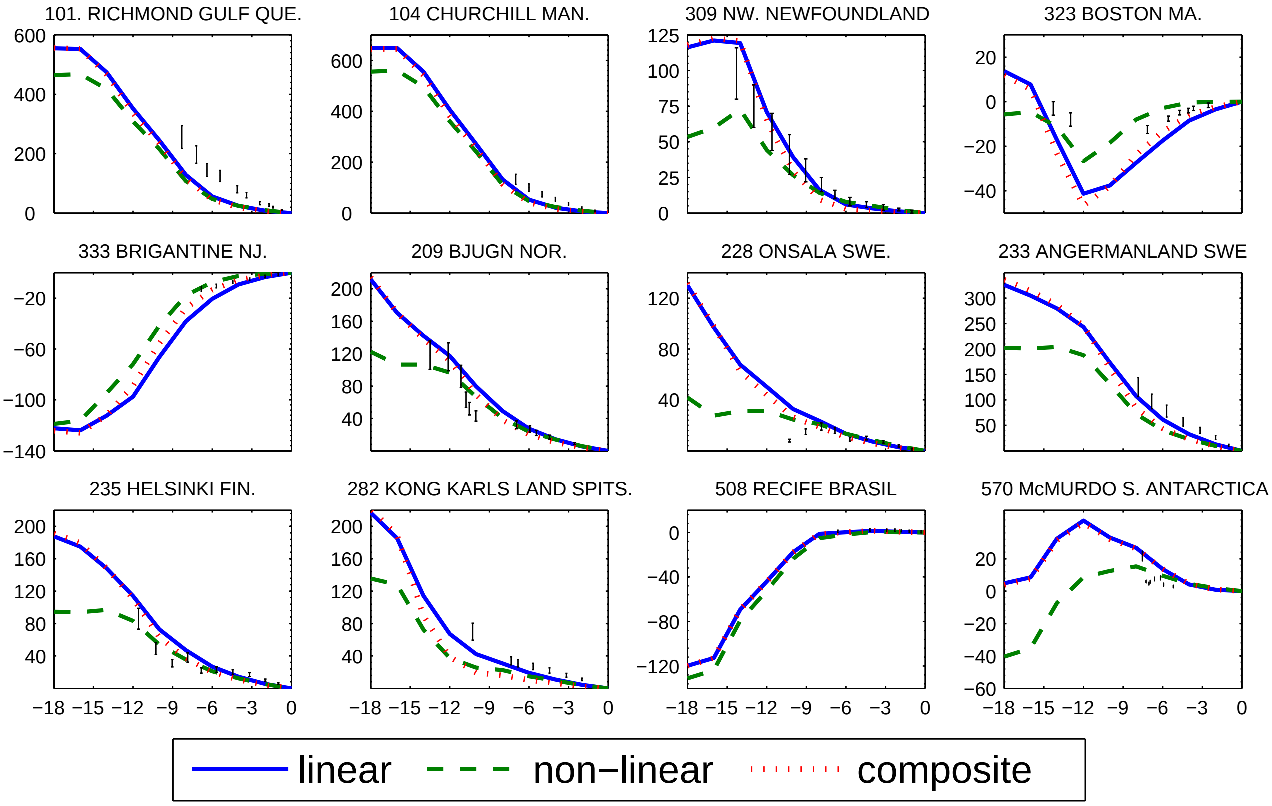

Figure 6.11: RSL predictions from models with three different rheologies: linear, non-linear and composite rheology, for the twelve RSL sites of Figure 6.10. The stress exponent n = 3, A = 3.3 x 10^{-35} $\mathrm{Pa}^{-3}\mathrm{s}^{-1}$ and η = 1 x 10^{21} Pas.

Figure 6.12 shows sea level curves for model II (A = 3.3 x 10^{-34} $\mathrm{Pa}^{-3}\mathrm{s}^{-1}$, η = 3 x 10^{21} Pas) and linear and non-linear rheology models. This model has a transition stress of only 0.58 MPa, so that the RSL curves for composite rheology are closer to the curves for non-linear rheology. There are a few exceptions, one of which is Antarctica, where it seems that stress is too low to trigger large non-linear deformation at the LGM. Looking at stress evolution in Figure 6.3, the interpretation can be that stress increases underneath Antarctica until 12 ka BP when the non-linear part of the creep rate becomes significant enough to drive fast relaxation and deviate from the linear RSL curve. Other sites where the early part of the curve for composite rheology deviates from that of non-linear rheology are at the margin of the Laurentide ice sheet (Newfoundland, Boston) or the center and margin of the Fennoscandian ice sheet (Bjugn, Onsala, Ångermanland, Helsinki). The composite rheology has attained a larger vertical deformation at LGM and drops faster than non-linear rheology. Apparently linear deformation contributes somewhat to relaxation at these sites just after the LGM. Note in Figure 6.1 that below the center of the ice sheet the stress is less than at the margin, thus linear creep rates can contribute more in the center of the ice sheet, as is indeed the case for the Laurentide ice sheet.

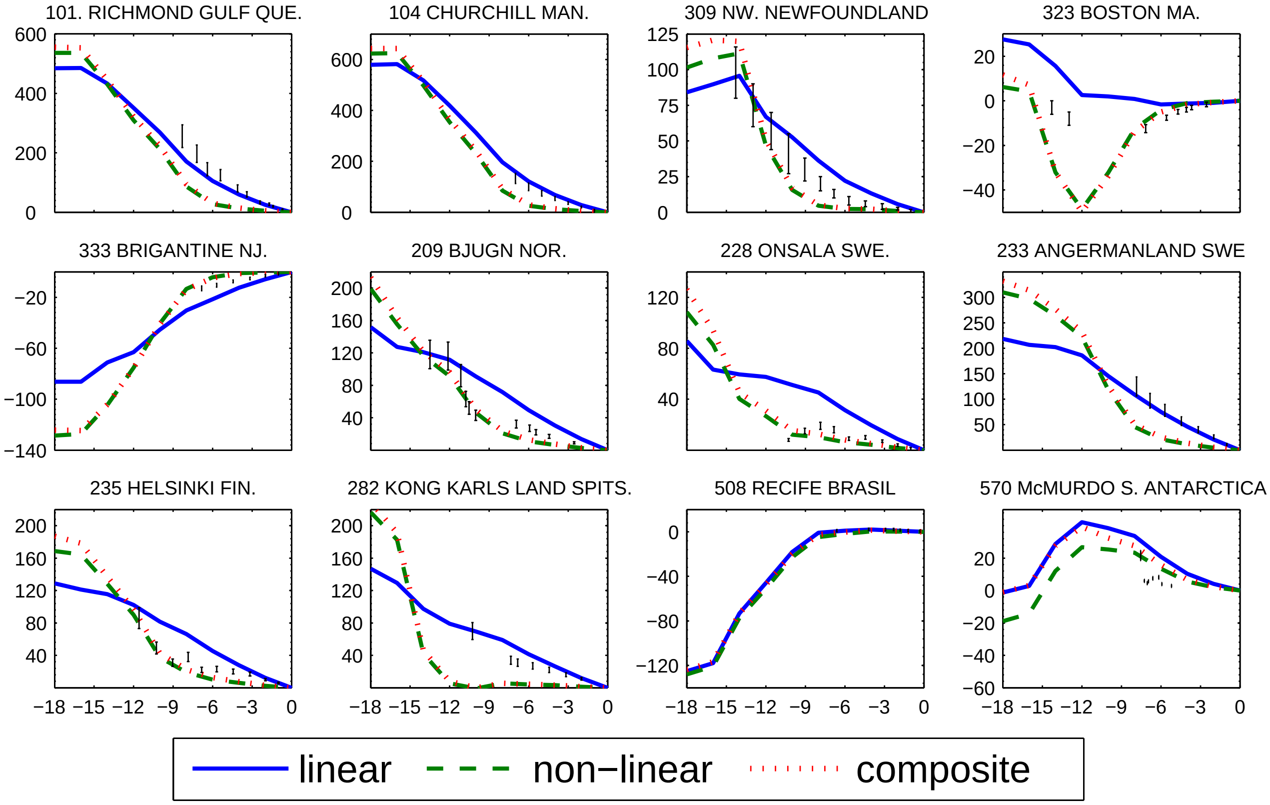

Figure 6.12: As Figure 6.11, but with $n = 3$, $A = 3.3 \times 10^{-34}$ Pa^{-3}s^{-1} and $\eta = 3 \times 10^{21}$ Pas.

Finally, Figure 6.13 shows model III ($A = 3.3 \times 10^{-35}$ Pa^{-3}s^{-1}, $\eta = 9 \times 10^{21}$ Pas). The linear relaxation in this Figure is clearly much smaller than in Figure 6.11, e.g. compare the ~600 m vertical displacement at Churchill in Figure 6.11, with the ~400 m in Figure 6.13. The transition stress of 1 MPa ensures mostly non-linear deformation. However, the same exceptions hold true as in Figure 6.12: significant contribution from linear rheology in the margin (Laurentide ice sheet) and center / margin (Fennoscandian) ice sheet, and mostly linear deformation in Antarctica.

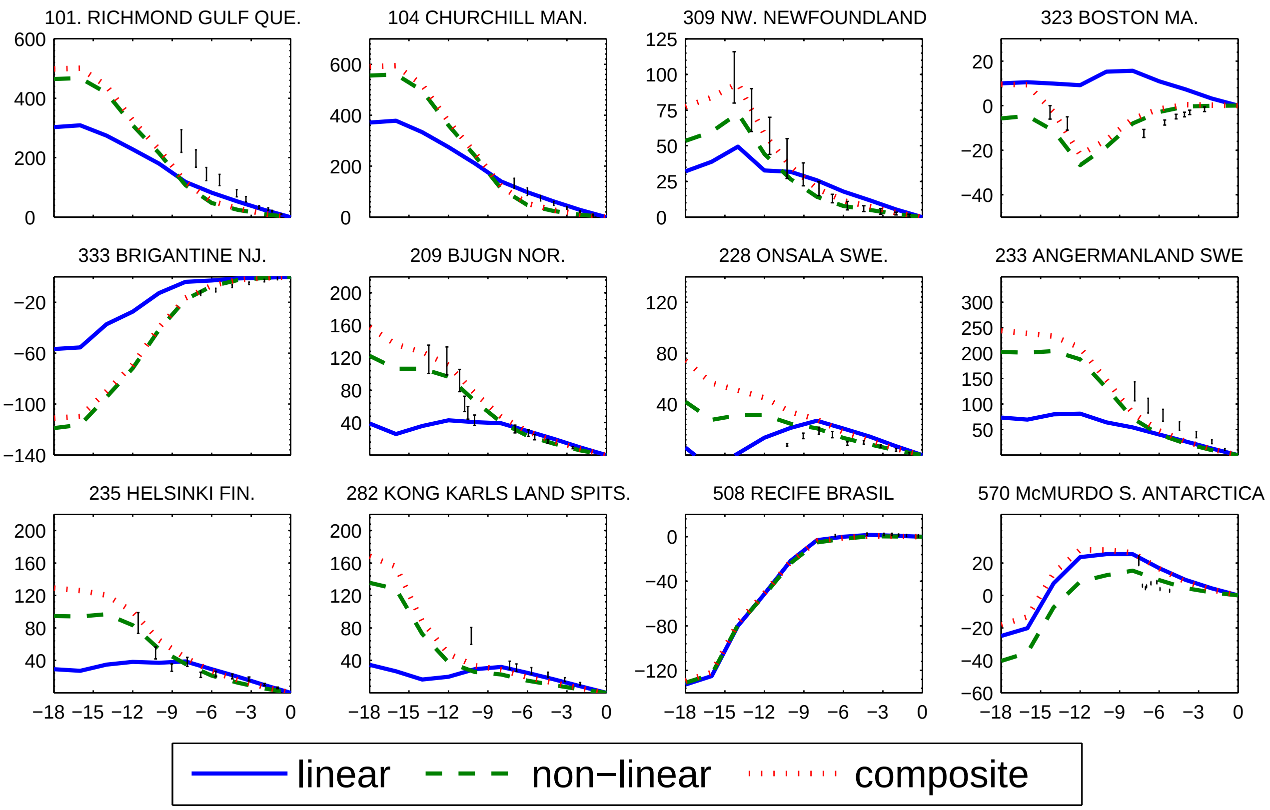

Figure 6.13: As Figure 6.11, but with n = 3, A = 3.3 x 10^{-35} $\mathrm{Pa}^{-3}\mathrm{s}^{-1}$ and η = 9 x 10^{21} Pas

6.4.3 Discussion

For model I, the transition stress level of 3.2 MPa causes the sea level curves to behave mostly linear, except for sites near the ice margin. If A is increased to 3.3 x 10^{-34} $\mathrm{Pa}^{-3}\mathrm{s}^{-1}$, not shown here, the transition Mises stress is 1 MPa and sea level curves are close to non-linear rheology. For model II, the transition stress is as low as 0.6 MPa and sea level curves follow non-linear sea level curves. For a lower value of A (3.3 x 10^{-35} $\mathrm{Pa}^{-3}\mathrm{s}^{-1}$, transition stress level of 1.8 MPa) linear rheology has a stronger contribution. For model II, the transition stress is 1.05 MPa, and much the same behaviour is found as for model II. In section 3.2.4.1 the possibility was mentioned that dynamic recrystallization balances diffusion and dislocation creep. It is interesting to note that it is found here that the best fit to RSL data is obtained for values of A and η for which dislocation and diffusion creep are of the same order of magnitude.

It should be noted that Figure 6.7b (L1-misfit) actually suggests that the best fitting model with viscosity of 3 x 10^{21} Pas, has A = 3.3 x 10^{-35} $Pa^{-3}s^{-1}$ as opposed to A = 3.3 x 10^{-34} $Pa^{-3}s^{-1}$ in model II. Figure 6.9 even shows a slightly lower misfit value for model III than the best fitting model in Figure 6.6b. Based on the ambiguity that results from the selection of RSL sites, and the misfit values that are close (for model II and model III), a best fitting model can not be based on RSL data alone for the models investigated here. In future work a more detailed variation in viscosity and A should be achieved. However, it is also possible to use extra information in the form of uplift rates and gravity rates to constrain models, as is done in section 6.5.

Does the conclusion hold that non-linear rheology provides the best fit? This seems to be justified based on Figures Figure 6.6 to Figure 6.9. However, removing the site with the largest misfit value from the computation results in a different picture, see Figure 6.14. The L2-misfit for the best-fitting composite rheology is only slightly higher than the best-fitting non-linear rheology. For the L1-misfit, the composite rheology is even smaller than the non-linear rheology. Thus, we can conclude that straightforward analysis of misfit (with no outliers removed) does not support the conclusion reached before that composite rheology has a significant lower misfit than purely non-linear models (Gasperini et al. 2004, Dal Forno and Gasperini, 2007). However, the converse can also not be claimed yet, due to the sensitivity in the misfit to specific sites, demonstrated here by the comparison of Figure 6.14b with Figure 6.7b, and due to the limited parameter spacing in η. Previous studies (e.g. Wu and Wang, 2008) with purely non-linear rheology can still be valid for two reasons: i) the best fitting composite rheology looks like a non-linear rheology (e.g. model II); and ii) the best fitting model is one with purely non-linear rheology.

Note that Wu and Wang’s (2008) preferred Earth model with a non-linear lower mantle and linear upper mantle still provides lower misfits than any of the composite rheology models used here (although their model contains an extra degree of freedom in the form of an extra layer in the mantle).

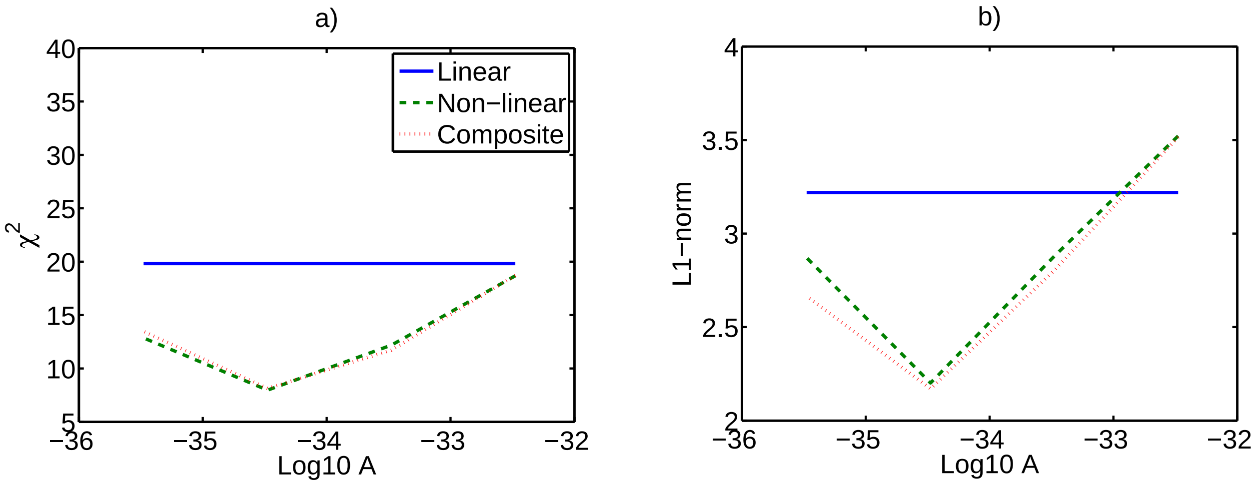

Figure 6.14: (a) L2-misfit and (b) L1-misfit for models with Newtonian viscosity of 3 x 10^{21} Pas. Onsala is left out of the misfit computation.

Composite rheology has an extra parameter (*A* and η) compared to purely non-linear rheology (only *A*). Therefore, should it not always have the smallest misfit, when the entire parameter space is sampled? This is not necessarily the case, as both η and *A* are coupled through the state of stress. For example, consider the composite rheology models with A = 3.3 x 10^{-35} $Pa^{-3}s^{-1}$ and η = 1 x 10^{21} Pas which has sea level curves that are closer to linear rheology (see Figure 6.11). Increasing the viscosity to 3 x 10^{21} Pas makes the sea level curves closer to that of non-linear rheology, but the misfit is still larger than that of non-linear rheology (Figure 6.7). It seems that the misfit can only be decreased for the same value of *A*, by increasing the viscosity, which makes the model effectively non-linear. Therefore, the extra parameter (viscosity) that composite rheology has compared to purely non-linear rheology, does not necessary help to decrease misfit for this value of *A*.

6.5 Uplift rate and geoid rate constraints

The previous section showed that the model that best fits RSL data has purely non-linear rheology in the mantle. A known problem with a purely non-linear rheology is the low uplift rates that are the result of the faster relaxation (e.g. Wu, 1999). Note that the present day uplift rate is approximately the time derivative of the curves at t = 0 in Figure

6.11 to Figure 6.13 which indeed looks to be smaller for non-linear models. Although sea level records are most important for GIA inferences because they extend back in time, an uplift rate that is too low does indicate a problem in either Earth rheology or ice history. Since composite rheology includes a linear component in the rheology which tends to stabilize the non-linear relaxation (Gasperini et al., 2004), it can possibly combine a good fit with sea level data with reasonable uplift rates.

The spatial pattern of uplift rate or, to a lesser extent the geoid rate, for the most part reflect the past ice sheet cover. Therefore, to judge whether composite rheology can attain reasonable uplift and geoid rate the maximum uplift and geoid rate will be used. The maximum uplift rate found by Sella et al. (2007) at one GPS station is 13.8 mm/year. Based on a number of sources, Wu and Wang (2008) take the maximum uplift rate to be 11 +/- 2 mm/year. The maximum geoid rate was determined in section 5.5.3 to be 1.4 mm/year. Rangelova (2007, p. 154) obtained a maximum of 1.5 mm/year with a combination of GPS, terrestrial gravity and GPS data.

Maximum uplift and geoid rates plotted in Figure 6.15 for composite rheology with $\eta = 1 \times 10^{21}$ Pas and $\eta = 3 \times 10^{21}$ Pas are above that for non-linear rheology, demonstrating that indeed composite rheology can enhance uplift rates. At first sight, it might not be clear how it is possible that an extra deformation mechanism (Newtonian creep) slows down relaxation compared to a single deformation mechanism (power-law creep). The answer lies in the relative importance of the mechanisms, as discussed in relation to the sea level curves. Models with $A = 3.3 \times 10^{-36}$ $Pa^{-3}s^{-1}$ and consequently high transition stress behave in a linear way so that the Newtonian viscosity determines the uplift rate to a large extent. Increasing (decreasing) the Newtonian viscosity of such models leads to slower (faster) relaxation at the present which results in a larger (smaller) uplift rate. For model II the Newtonian viscosity has little influence on the present day uplift rate, because most of the relaxation is handled by power-law creep. For this model, Figure 6.1 does show a small region of linear deformation directly below the lithosphere, underneath the center of the ice sheet, but that might be due to the boundary conditions of the axisymmetric model. Moreover, the lower part of the upper mantle and lower mantle in that figure are still dominated by non-linear deformation.

The maximum geoid rate in Figure 6.15b shows the same behaviour: for models with smaller value of *A*, increasing the viscosity increases the maximum geoid rate. Interestingly, the increase is not the same in uplift rate as in geoid rate. The maximum uplift rate curves for $\eta = 3 \times 10^{21}$ Pas and $\eta = 9 \times 10^{21}$ Pas are almost on top of each other, while the maximum geoid rate curve for $\eta = 9 \times 10^{21}$ Pas is clearly above that of $\eta = 3 \times 10^{21}$ Pas. This points to a different sensitivity of uplift rate and geoid rate in terms of the relaxation process in the mantle. This idea should be further explored in future work. Note that a value of $A \sim 10^{-36}$ $Pa^{-3}s^{-1}$ gives uplift and geoid rate close to what is expected, but RSL fit is somewhat degraded (see Figure 6.6b and Figure 6.7b).

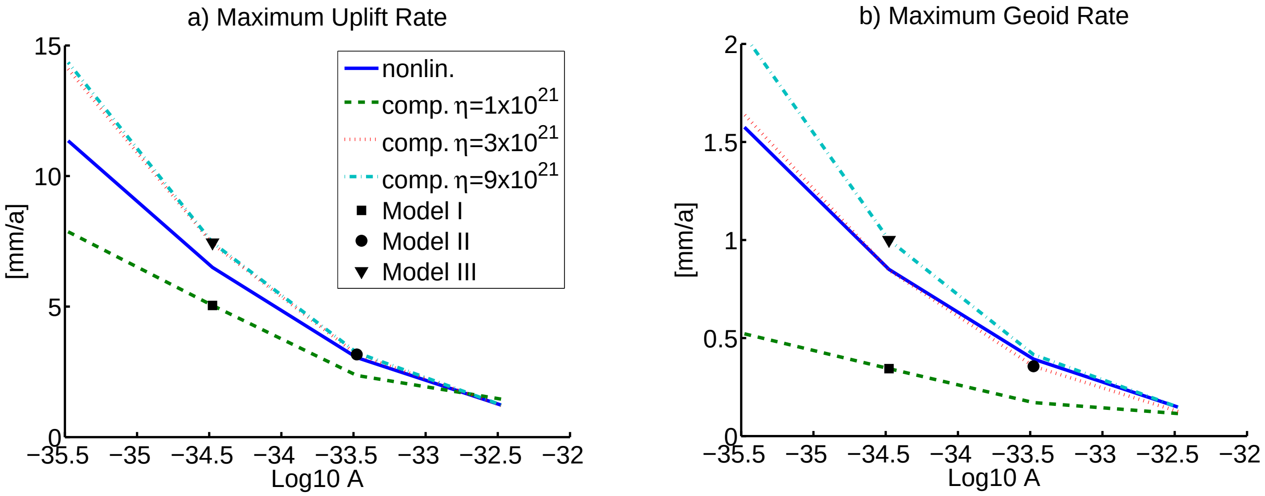

Figure 6.15: (a) Maximum uplift rate in North America and (b) maximum geoid rate in North America, for non-linear and composite rheologies for ICE-5G and different values of A. Dashed line: $\eta = 1 \times 10^{21}$ Pas, Dotted line: $\eta = 3 \times 10^{21}$ Pas, dashed-dotted: $\eta = 9 \times 10^{21}$ Pas.

Model I, II and III have small uplift rates of 5.0, 3.2 and 7.5 mm/year, respectively, which is considerably lower than the observational constraints of 11 mm/year. The geoid rates for the same models are 0.34, 0.36 and 1.0 mm/year, respectively, again smaller than the observed 1.4-1.5 mm/year. On the positive side, composite rheology model III manages to increase both uplift rate and geoid rate compared to the best fitting non-linear rheology, while model II increases only the maximum uplift rate. Both models have an RSL misfit which is slightly larger than the best-fitting non-linear rheology, but still much smaller than purely linear rheology (Figure 6.12 and Figure 6.13). It can be concluded that composite rheology can increase uplift rates and geoid rate, at the expense of a small increase in RSL misfit. Furthermore, recall that the model II was obtained from L2-misfit with sea level data, while L-1 misfit allowed a best-fit model with $A = 3.3 \times 10^{-36}$ Pa^{-3}s^{-1} and $\eta = 3 \times 10^{21}$ Pas, which fit even better than non-linear rheology if one outlier station was removed (see Figure 6.14b). Therefore, it is not ruled out that model II can provide better fit to sea level data and increase uplift rate. Finally, sub-dividing the parameter space of Newtonian viscosity could result in an optimal fit model with increased sea level fit and increased uplift rates and geoid rates.

With the current results, sea level data selected model II and model III as equally plausible, uplift rates favours a value of A of close to $A = 3.3 \times 10^{-35}$ Pa^{-3}s^{-1} or smaller, geoid rate favours a viscosity of $\eta = 9 \times 10^{21}$ Pas. This is a higher viscosity than that found in Dal Forno et al. (2005) and Dal Forno and Gasperini (2007), but close to that of Gasperini et al. (2004), see Table 6.1. Misfit is quite sensitive to value of Newtonian viscosity, see e.g. Figure 5 of Dal Forno et al. (2005), but differences can be expected because the more realistic model of Wang and Wu (2006) is used here as well as the ICE-5G model, which has larger ice thicknesses at LGM and consequently larger maximum uplift and geoid rates than ICE-4G. The fact that both ice histories were obtained with a linear rheology still leaves room for modification of the ice history that will increase uplift rates and geoid rates.

6.6 Modifications to the ice history

The effects of two types of modifications in the Laurentide ice history will be investigated:

i) Delay in the glaciation, which increase uplift rates as can be deduced from the sea level curves in Figure 6.11 to Figure 6.13.

ii) Increase in ice height, suggested by Wu and Wang (2008).

Because of the long computation time of the 3-D FEM model, only a handful of cases is investigated. They merely serve as direction for the development of ice models based on composite rheology; it is not claimed that the delay and scaling of the ice history are allowed by geological constraints or can fit GIA constraints other than the ones considered here. The predicted uplift rates from ICE-5G generally fit worse than ICE-4G (Braun et al., 2008, Fig. 4 and section (7.5.2)) as they are too high and the maximum is west of Hudson Bay instead of south-east. Therefore, the ICE-4G model is used in this section instead of the ICE-5G model to investigate RSL misfit, RSL curves, uplift rates and geoid rate. Newtonian viscosity is taken to be 1 x 10^{21} Pas and 3 x 10^{21} Pas, A is varied between 3.3 x 10^{-34} $Pa^{-3}s^{-1}$ and 3.3 x 10^{-36} $Pa^{-3}s^{-1}$.

6.6.1 Delay in glaciation

Figure 6.16 shows the maximum uplift rate and geoid rate with the parameters mentioned at the end of the previous section for the ICE-4G history and with delay applied to the glaciation. Indeed, the delay in glaciation increases the uplift rate and geoid rate for all models, but less so for models with a larger value of A that tend to have a flatter sea level curve at present. It is interesting to note that an increase in viscosity from η = 1 x 10^{21} Pas to η = 3 x 10^{21} Pas has a greater effect on the geoid rate than on the uplift rate. The question is now whether a delay in glaciation worsens the RSL fit or not.

Because only the glaciation in Laurentide is modified, the RSL fit will be computed for stations in North America only. These sites are depicted in Figure 6.17 and the misfit curves are shown in Figure 6.18. There is one site with large misfit values (326, Clinton), therefore results are also shown for L1-misfit since L1-misfit was shown to provide more robust conclusions about best fitting rheology in the presence of large misfit values for individual sites. It becomes clear from the figure that a 1 ka delay in glaciation actually improves RSL L1-misfit for A > 3.3 x 10^{-34} $Pa^{-3}s^{-1}$, but delay by 2 ka worsens the fit for all models.

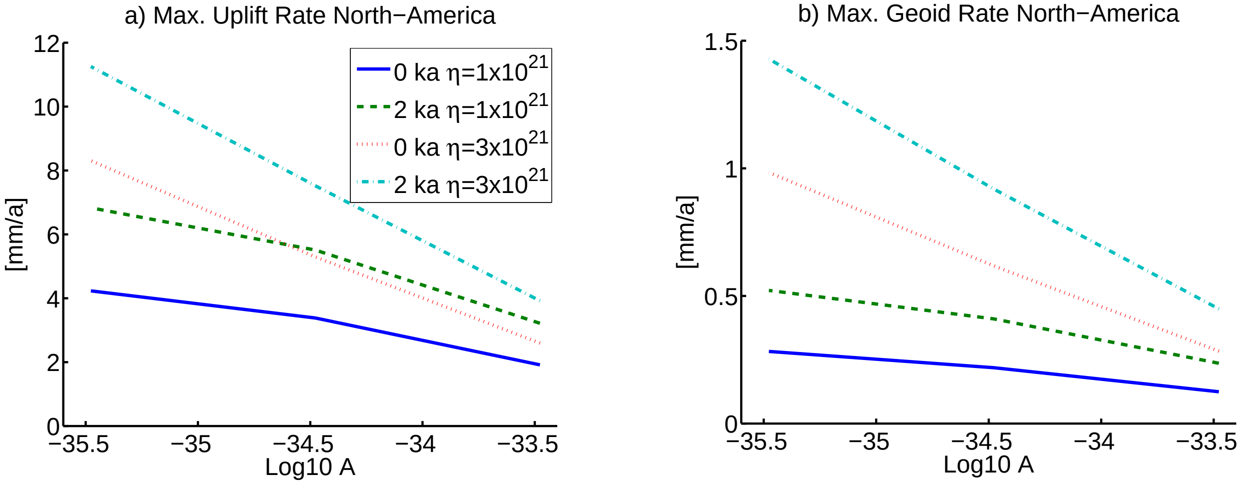

Figure 6.16: Maximum uplift rate (a) and geoid rate (b) in North America for six composite rheologies with (delayed versions of) ICE-4G.

Misfit for models with $\eta = 3 \times 10^{21}$ Pas is shown in Figure 6.19 for both L2 and L1-misfit. The type of misfit does not affect the shape of the curves much (not shown). However, removing sites with large misfit values favours the misfit for 2 ka delay (not shown). A 1 ka delay leads to a lower misfit for $A = 3.3 \times 10^{-34}$ Pa^{-3}s^{-1} and similar misfit for $A = 3.3 \times 10^{-35}$ Pa^{-3}s^{-1}. 2 ka delay greatly increases misfit (L1 and L2) for $A < 3.3 \times 10^{-34}$ Pa^{-3}s^{-1}, but can lead to lower L1-misfit for $A = 3.3 \times 10^{-34}$ Pa^{-3}s^{-1}. The best fitting model is for $A = 3.3 \times 10^{-35}$ Pa^{-3}s^{-1}; the same as the best-fitting model as in Figure 6.7.

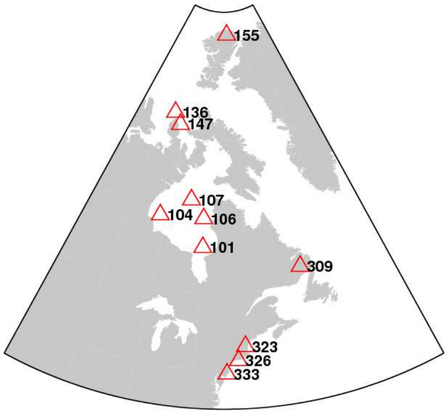

Figure 6.17: Location of the North American RSL sites used for misfit computations with modified ICE-4G history.

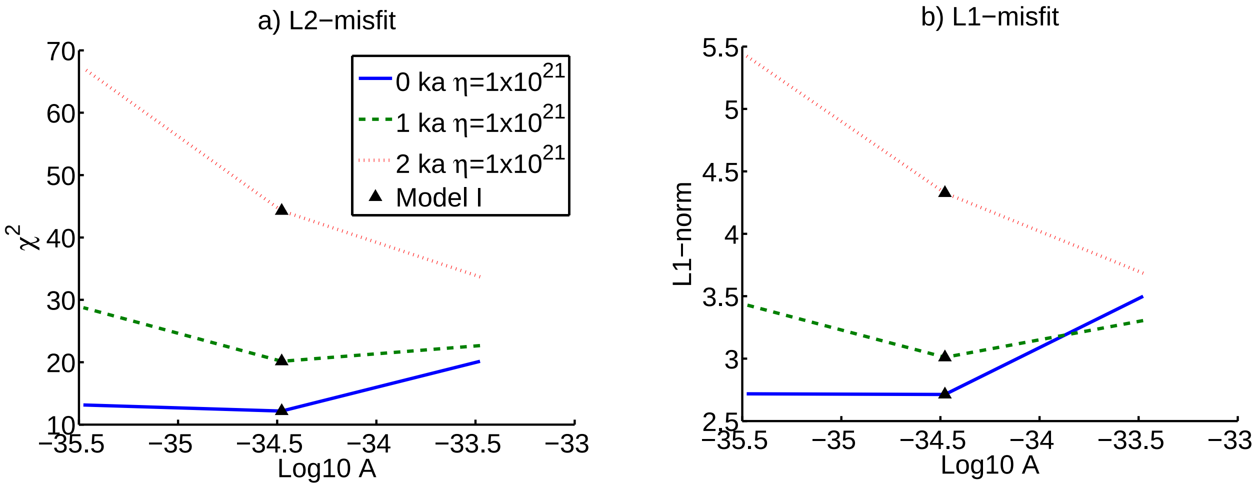

Figure 6.18: RSL Misfit of GIA models with η = 1 x 10^{21} Pas, w.r.t the 12 sites of Figure 6.17 for (a) L2-misfit (b) L1-misfit.

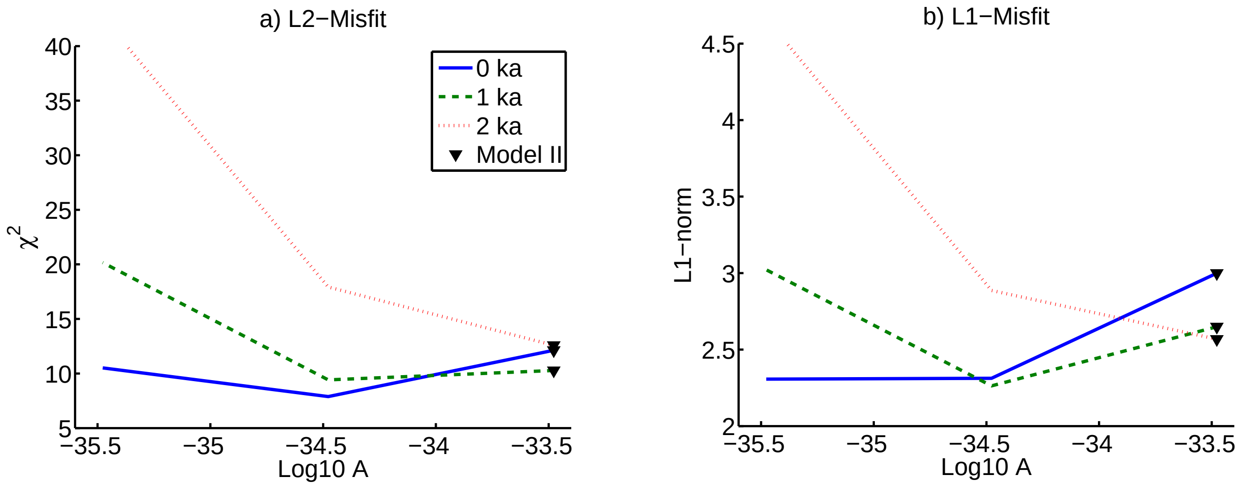

Figure 6.19: RSL Misfit of GIA models with η = 3 x 10^{21} Pas, with respect to the 12 sites of Figure 6.17 for: (a) L2-misfit; (b) L1-misfit.

In order to analyze at the detailed spatial response, sea level curves are plotted for the best fitting models of Figure 6.19. It is clear that a delay in glaciation provides a better fit to many of the sites: Richmond, Churchill, Southampton Island, East Axel Heiberg Island and Brigantine. The worse fit at Clinton, in combination with the small RSL errors there, causes the large misfit in Figure 6.19 for the case of 2 ka delay.

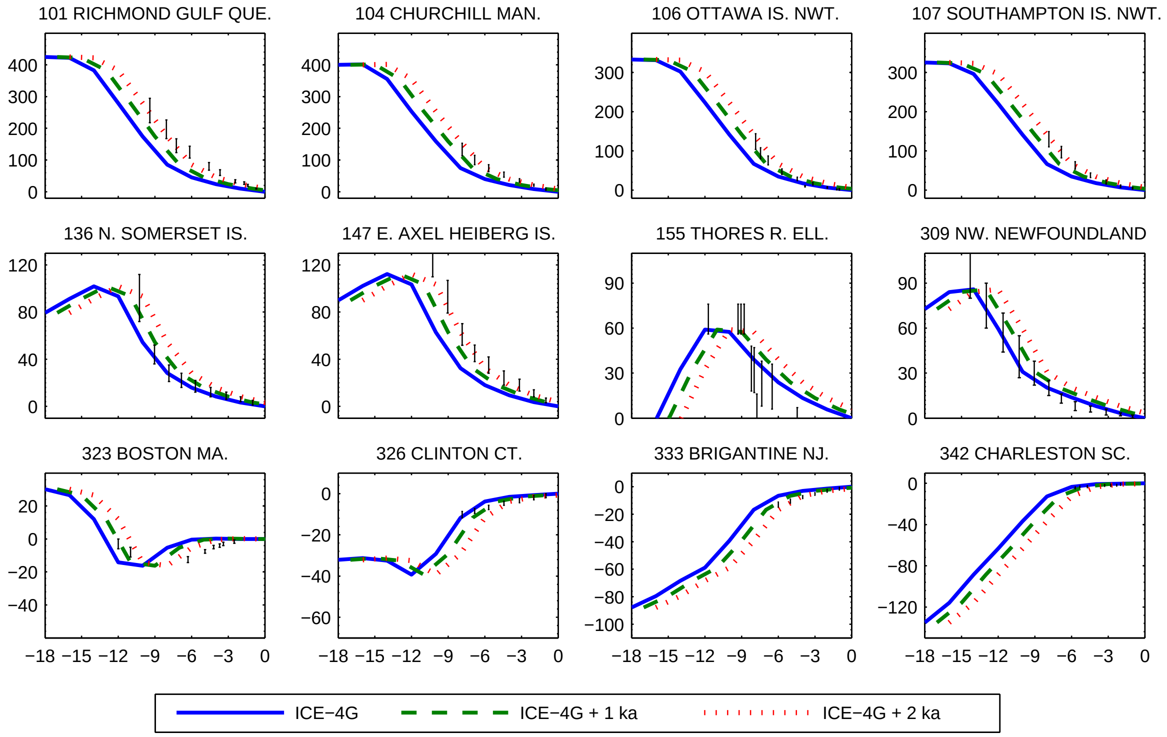

Figure 6.20: RSL predictions for the 12 North American sites in Fig. 9, using the ICE-4G model with delayed ice heights, $A = 3.3 \times 10^{-35}$ Pa^{-3}s^{-1} and $\eta = 3 \times 10^{21}$ Pas.

6.6.2 Increased ice heights

Ice heights in Laurentide at all time steps are multiplied by 1.5 and 2.0 to investigate the effect of an increase in ice thicknesses (Wu, 1999, Wu and Wang, 2008). The maximum uplift rate with these scaled versions of ICE-4G is plotted in Figure 6.21 and the maximum geoid rate in Figure 6.22. Model I and II are denoted by upward and downward triangles in Figure 6.21a and Figure 6.21b respectively. The uplift rate of model I increases by 3.3 mm/year upon doubling of the ice heights. Model II behaves more like non-linear rheology and the effective viscosity is lowered upon increasing the stress level. Therefore, total solid Earth displacement at LGM is larger as a result of the higher ice, but relaxation proceeds faster due to the lower viscosity. Thus the maximum geoid rate also shows little increase for models that behave mostly in a purely non-linear way. Figure 6.22a in combination with Figure 6.16 rules out a viscosity of 1 x 10^{21} Pas for a composite rheology because even with larger ice thicknesses or delay in glaciation the maximum geoid rate is only around 0.5 mm/year, compared to 1.4 mm/year observational constraint. Note that the maximum uplift rate in Figure 6.21a is close to 8 mm/year which is relatively closer to the observed 11 mm/year.

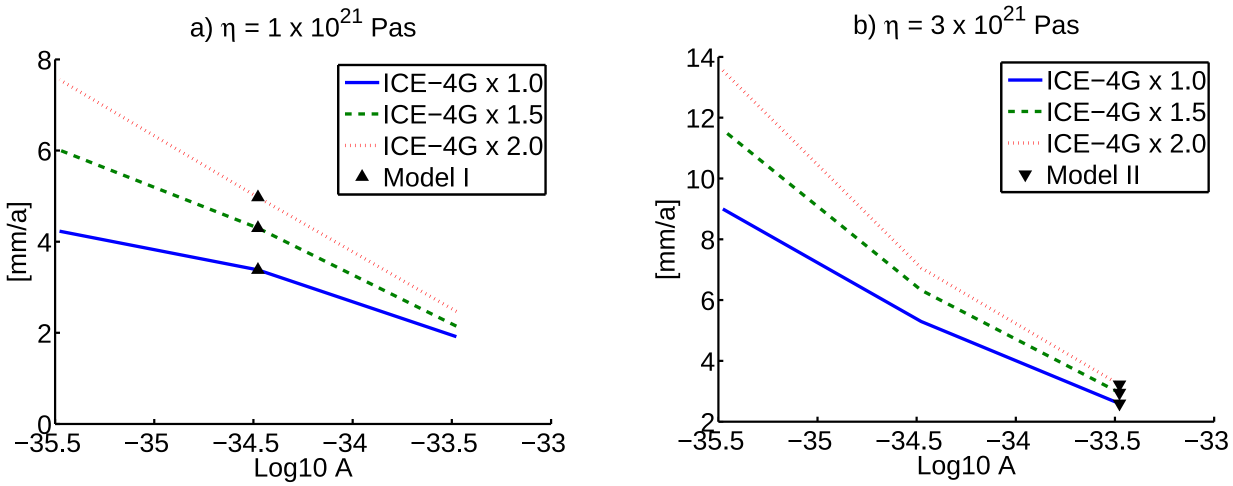

Figure 6.21: Maximum uplift rate for four composite rheologies with (scaled versions) of ICE-4G for (a) $\eta = 1 \times 10^{21}$ Pas and (b) $\eta = 3 \times 10^{21}$ Pas.

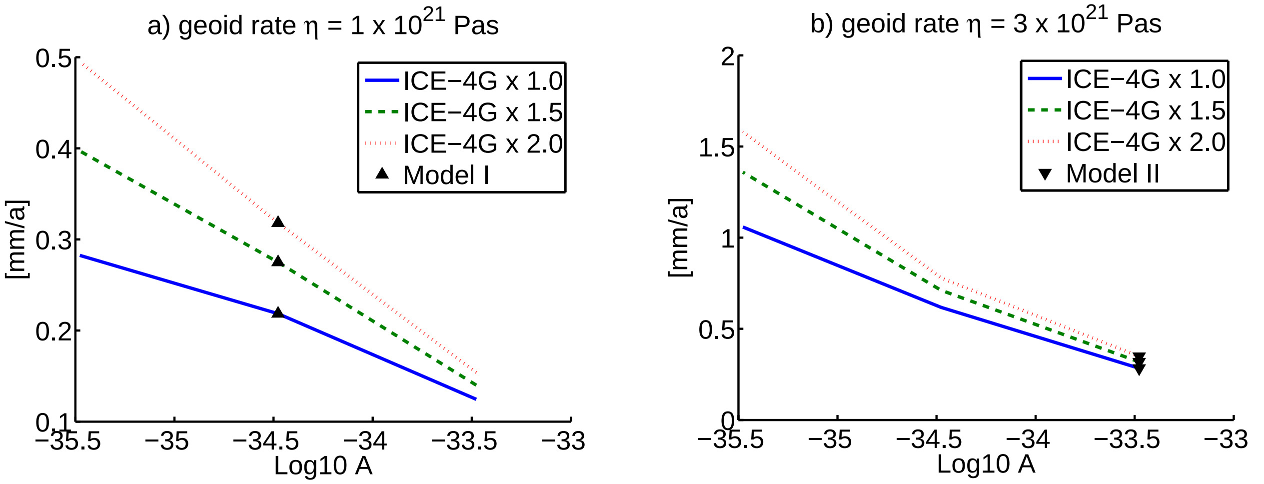

Figure 6.22: Maximum geoid rate for four composite rheologies with (scaled versions) of ICE-4G for (a) $\eta = 1 \times 10^{21}$ Pas and (b) $\eta = 3 \times 10^{21}$ Pas.

Clearly worse misfit is obtained in Figure 6.23b for inceases in ice thicknesses, both for L2 and L1-misfit. However, outliers in RSL data strongly influence the misfit increases as will be shown in the detailed sea level history. The same conclusions hold for $\eta = 3 \times 10^{21}$ Pas, for which misfits are a little lower. For a model with $A = 3.3 \times 10^{-35}$ $Pa^{-3}s^{-1}$ and $\eta = 3 \times 10^{21}$ Pas, the maximum geoid rate increases from 0.62 to 0.71 to 0.78 mm/year for multiplying the ice thicknesses by 1.0, 1.5 and 2.0 respectively (see Figure 6.22b).

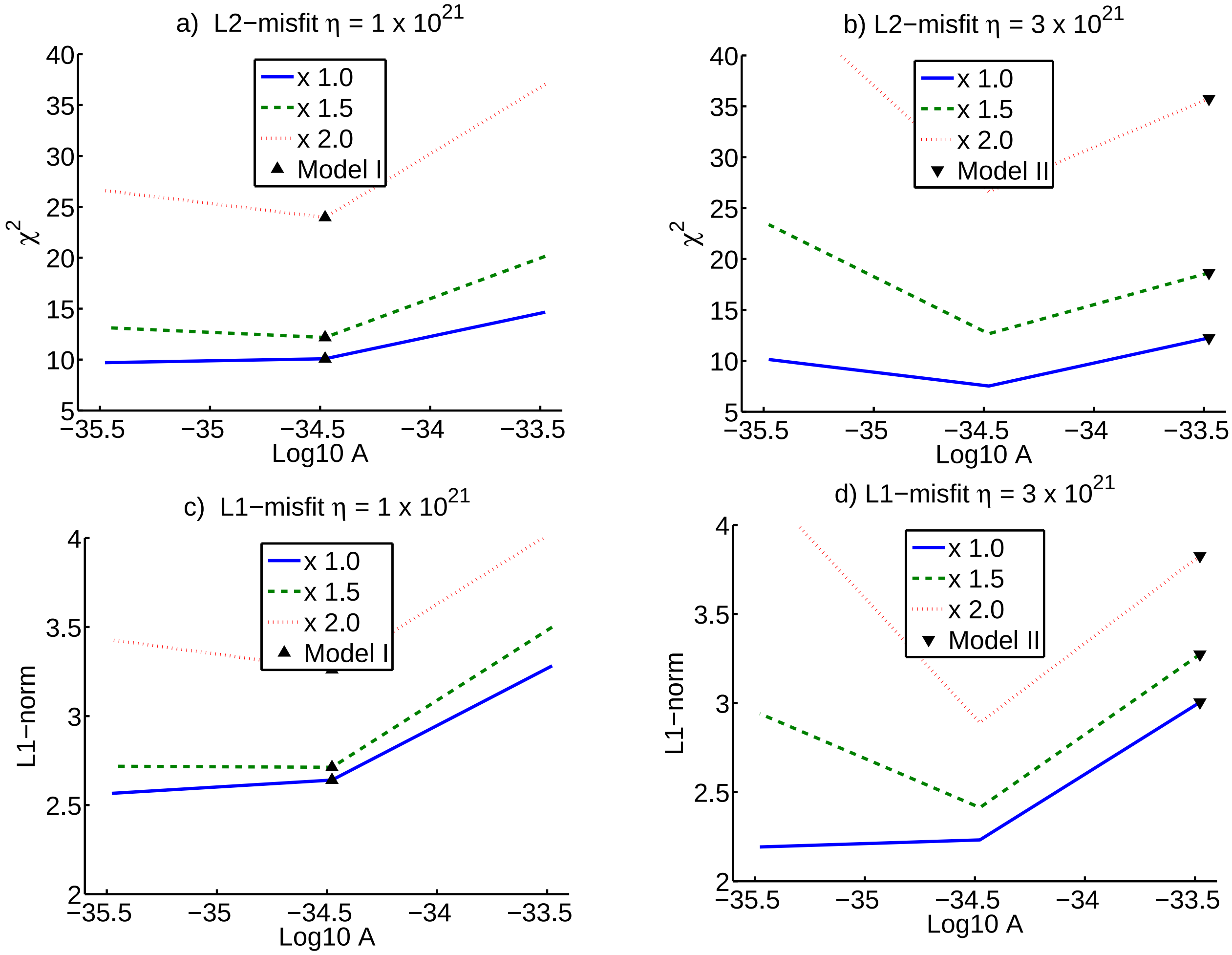

Figure 6.23: RSL misfit for the 12 sites of Figure 6.17. (a) $\eta = 1 \times 10^{21}$ Pas and (b) $\eta = 3 \times 10^{21}$ Pas, c) L1-misfit, $\eta = 1 \times 10^{21}$ Pas, d) L1-misfit, $\eta = 3 \times 10^{21}$ Pas.

It is interesting that the best fitting models with unscaled ice thicknesses in Figure 6.23a and Figure 6.23b are found for a value of A smaller than that in model I and II which were best fitting models determined with ICE-5G. This could be the result of the larger ice mass in ICE-5G which agrees with a rheology that is more non-linear. Figure 6.24 shows the individual sea level curves for the best fitting model in Figure 6.23b. The worse fit of the scaled ice models is not supported by all of the curves. For example, fit for e.g. Ottawa Island and East Axel Heiberg Island is rather good, which agrees with the finding of Wu (1999). On the other hand, the fit is poor in Newfoundland, and the data at the peripheral bulge are indifferent except for Boston which does not permit a large increase in ICE-4G height. Comparing Figure 6.20 with Figure 6.24 one can conclude that the shape of the sea level curves better matches the observations when the ice history is delayed as opposed to increased. This is most notable in the first row of both figures, which are the sites in the center of the ice sheet.

The model with lowest RSL misfit among those investigated with a modified ICE-4G ice history has A = 3.3 x 10^{-35} $Pa^{-3}s^{-1}$ and η = 3 x 10^{21} Pas, with 0 (or 1 ka) delay in glaciation, depending on whether L1 or L2-misfit is used. However, this model still has a low uplift rate of 5.3 mm/year (or between 5.3 and 7.5 mm/year for 1 ka delay). Note that this model increases the uplift rate (but not the geoid rate) compared to a purely non-linear rheology model, as shown in Figure 6.15 for ICE-5G.

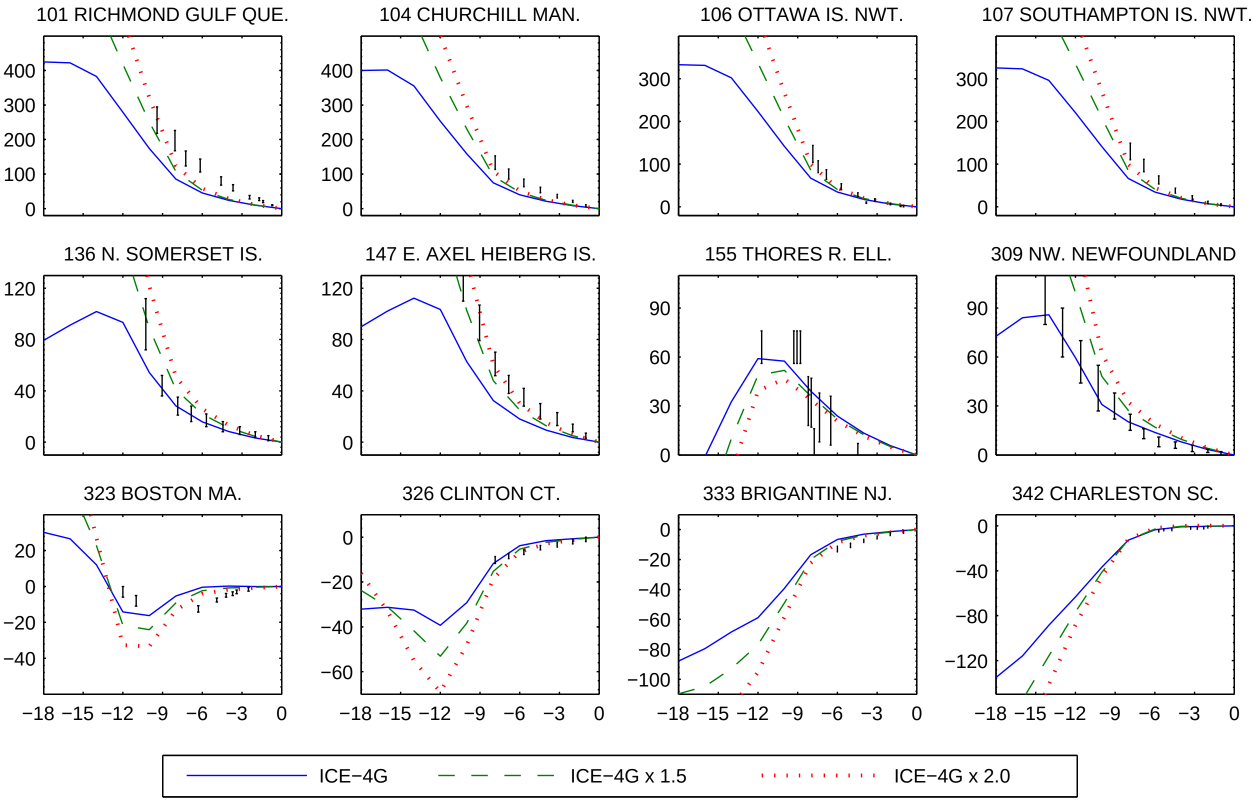

Figure 6.24: RSL predictions for the 12 North American sites in Fig. 9, using the ICE-4G model with increased ice heights, A = 3.3 x 10^{-35} $Pa^{-3}s^{-1}$ and η = 3 x 10^{21} Pas.

6.7 Summary of RLS and uplift rate constraints

The best RSL fit with a GIA model based on ICE-5G with composite rheology is obtained for a model with A = 3.3 x 10^{-35} $Pa^{-3}s^{-1}$ and η = 9 x 10^{21} Pas, see Table 6.3. Although this model has a larger misfit value than the best-fitting purely non-linear rheology (L1-misfit value: 2.2), the model does increase uplift rate and geoid rate with respect to the purely non-linear rheology model. With a value of A smaller than 3.3 x 10^{-35} $Pa^{-3}s^{-1}$ it seems possible to have an acceptable uplift and geoid rate at the expense of a slightly worse RSL fit. There is also a possibility that the RSL misfit for composite rheology decreases below that of a purely non-linear rheology model if more viscosities are investigated, particularly between 3 x 10^{21} Pas and 9 x 10^{21} Pas or higher than 9 x 10^{21} Pas. However, since higher values of the Newtonian viscosity are not investigated in this thesis due to time constraints, it is possible that a better fitting model can be obtained with higher values of the Newtonian viscosity.

Table 6.3: L2-misfit/L1-misfit with respect to sites in Appendix E for all models with ICE-5G. The second row in each cell gives the uplift rate/geoid rate.

	mantle viscosity		
***A* [Pa^{-3}s^{-1}]**	**1 x 10^{21} Pas**	**3 x 10^{21} Pas**	**9 x 10^{21} Pas**
3.3 x 10^{-33}	19.0/3.5 1.46/0.11	18.8/3.6 1.22/0.13	18.9/3.6 1.24/0.15
3.3 x 10^{-34}	11.7/3.0 2.36/0.17	13.3/2.8 3.17/0.36	11.9/2.8 3.24/0.42
3.3 x 10^{-35}	12.1/2.7 5.04/0.34	11.8/**2.3** **7.40/0.85**	**10.8/2.3** **7.45/1.00**
3.3 x 10^{-36}	21.7/2.7 7.87/0.52	13.6/3.0 14.10/1.64	14.3/2.7 14.35/2.05

From Table 6.4 it follows that the best fitting model with ICE-4G is found for A = 3.3 x 10^{-35} Pa^{-3}s^{-1} and η = 3 x 10^{21} Pas. Higher viscosities are not investigated due to time constraints. L1-misfit gives an even lower misfit when 1 ka delay is applied to the ice history, which also increases uplift rate from 5.7 to somewhere in between 5.7 and 7.5 mm/year. Moreover, Figure 6.20 tells that a better fit is obtained for sites in the center of the ice sheet when 2 ka delay is applied. Such delay would increase the uplift to 7.5 mm/year.

Increasing the ice thickness does not lead to better fit with RSL data (see Table 6.5) and leads to marginal increase in uplift and geoid rate (see discussion of Figure 6.21). Although Figure 6.24 shows that smaller misfit values are obtained for sites in the center of the ice sheet margin, the shape of the curves does not match the shape of the observations very well, with the exception of East Axel Heiberg Island. Misfit values for both an increase of ice thickness and delay in glaciation increases are not shown here, but the misfit values increase for all models.

Table 6.4: L2-misfit/L1-misfit with respect to sites in Figure 6.17 for all models with ICE-4G with 0, 1, and 2 ka delay.

	0 ka		**1 ka**		**2 ka**	
A [Pa^{-3}s^{-1}]	**1 x 10^{21}**	**3 x 10^{21}**	**1 x 10^{21}**	**3 x 10^{21}**	**1 x 10^{21}**	**3 x 10^{21}**
3.3 x 10^{-34}	14.7/3.3	12.2/3.0	12.1/2.9	9.6/2.5	14.5/2.8	11.0/2.4
3.3 x 10^{-35}	10.1/2.6	**7.5/2.2**	9.9/2.5	8.4/**2.1**	18.5/2.9	16.2/2.7
3.3 x 10^{-36}	9.7/2.6	9.7/2.6	11.9/2.6	11.9/2.6	25.1/3.2	25.1/3.2

Table 6.5: Same as Table 6.4 for 1, 1.5, and 2.0 ice thickness scaling.

	x 1.0		**x 1.5**		**x 2.0**	
A [Pa^{-3}s^{-1}]	**1 x 10^{21}**	**3 x 10^{21}**	**1 x 10^{21}**	**3 x 10^{21}**	**1 x 10^{21}**	**3 x 10^{21}**
3.3 x 10^{-34}	14.7/3.3	12.2/3.0	20.1/3.5	18.6/3.3	37.0/4.0	35.7/3.8
3.3 x 10^{-35}	10.1/2.6	**7.5/2.2**	12.2/2.7	12.7/2.4	24.0/3.3	26.6/2.9
3.3 x 10^{-36}	9.7/2.6	9.7/2.6	13.1/2.7	23.4/2.9	26.6/3.4	19.9/2.8

Chapter Seven: GRACE constraints on the ice loading history

The spatial distribution of uplift and gravity rates within the ice margin mainly reflects the distribution and height of the ice sheet (e.g., Wu, 2002a). Therefore, GRACE data can be expected to offer constraints on the past ice distribution especially in areas where GPS and terrestrial gravity measurements are absent.

Tamisiea et al. (2007) stated that “Our results strongly support the multi-domal Laurentide ice geometry advocated by Dyke and Prest and allow us to reject the mono-domal model.” Indeed the two domes that were found in that paper seem to be a robust feature in the GRACE data (see Figure 5.28, and Figure 5.29 in this thesis). The ICE-3G and ICE-4G histories are characterized in that paper as mainly mono-domal Laurentide ice sheets, and the ICE-5G as multi-domal. The results of Tamisiea clearly favour a multi-domal structure put forward by Dyke and Prest (1987). Therefore, the results of Tamisiea et al. (2007) appear to favour ICE-5G (being a multi-domal model) over ICE-3G or ICE-4G (being mainly mono-domal). However, Figure 2.2 confirms that the maximum gravity rate based on ICE-3G can show a weak two-domal structure and can thus potentially fit well to the GRACE data.

The trend estimated from 4 years of data was shown to cause large changes in the location of the maximum depending on whether an ‘early’ or ‘late’ four year period was selected, probably caused by a strong increase in water storage from the summer of 2003 until the summer of 2006 (Van der Wal et al., 2008a). Moreover, it is shown in section 5.4 that April and May 2002 have a big impact on the estimated trend. In fact, it is even claimed that GRACE monthly gravity fields from before February 2003 are of less quality and perform worse in comparisons with independent data (Frank Flechtner, personal communication, 2009). Thus, the visual agreement between the GRACE-derived geoid rate (Figure 1 of Tamisiea et al., 2007) and the gravity rate from a GIA model based on the ICE-5G loading history can therefore very well be a result of the short time series, the use of the older release 1 data and the use of data of lesser quality for April and May 2002.

Paulson et al. (2007b) also found a better agreement was found with ICE-5G than with ICE-3G. However, their conclusion relies on their claims that the hydrology correction is only 10%, which understates the hydrology contribution expected from the investigation of hydrology models (Van der Wal et al., 2008a). Even the maximum gravity rate in the trend estimated from 5 years of data (which is more than used in Paulson et al. 2007b) is shown in section 5.4 to be subject to large changes in the maximum gravity rate. Based on these arguments, the use of GRACE data as a constraint on ice loading history in North America needs further study, if only because the constraint on ice loading history in North America was not the objective from the previous papers, but rather a secondary result.

In this chapter, the GRACE data discussed in chapter 4 will be used to answer the question if GRACE data with the current time span can offer a constraint on the ice history and which ice loading history is preferred. First, GRACE data are validated with GPS data and terrestrial gravity data. Following, the sensitivity of gravity rates to changes in ice thicknesses is discussed. Then GRACE data are compared to uplift rate and gravity rate in North America. Simulations are performed to show whether the difference in the ice loading histories of ICE-3G, ICE-4G and ICE-5G are resolvable. Misfit between modeled gravity rate and GRACE-derived gravity rate for varying mantle viscosity and varying Gaussian smoothing radii is shown.

7.1 Comparison between GRACE and GPS data

Wahr et al. (2000) found a relation that approximates well the relation between spherical harmonic coefficients of uplift and spherical harmonic coefficients of the geoid rate (Stokes coefficients C_{lm} and S_{lm}) for GIA:

$$\left\{ \begin{matrix} U_{lm} \\ V_{lm} \end{matrix} \right\} = \frac{2l+1}{2} \left\{ \begin{matrix} C_{lm} \\ S_{lm} \end{matrix} \right\} \tag{7.1}$$

where U_{lm} and V_{lm} are the coefficients in the spherical harmonic expansion of the uplift rate. In Figure 7.1 it is verified how good this approximation is for model i3_8-60. The uplift rates computed directly from the model are little smaller than the uplift rates computed with equation (7.1)

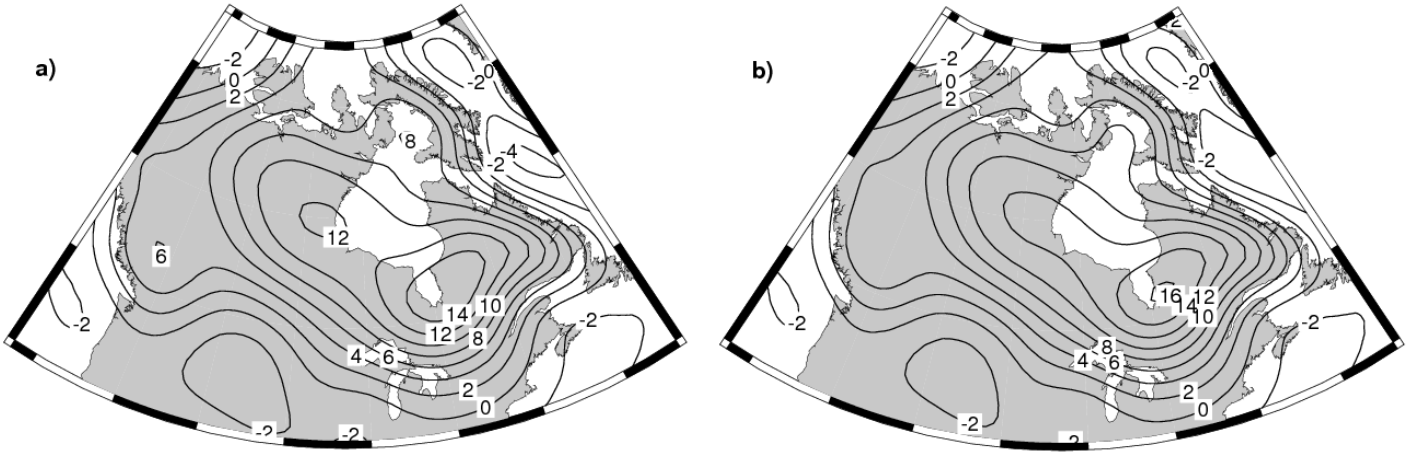

Figure 7.1: (a) Uplift rate for model i3_8_60. (b) Uplift rate computed from geoid rate coefficient according to equation (7.1).

As in Rangelova (2007), this relation is now applied to compute uplift rates from the GRACE results in section 5.4. Differences between the observed uplift rates and the uplift rates converted from GRACE (the results of section 5.4.1.1_ are shown in Figure 7.3.

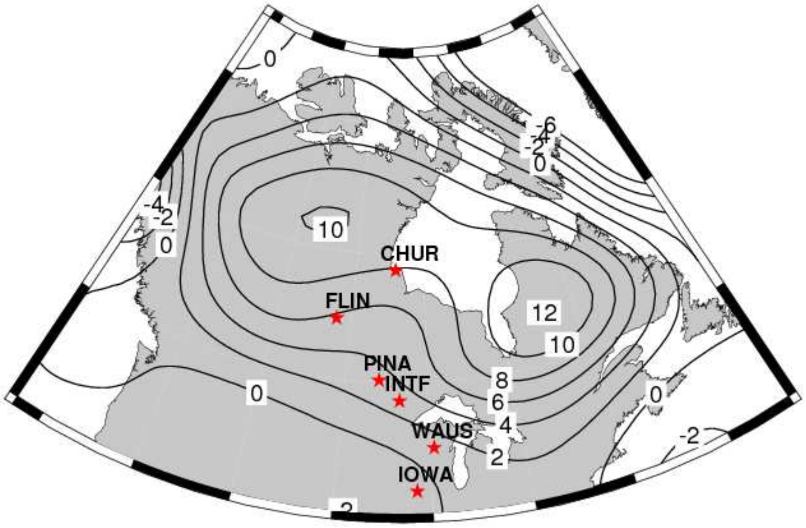

Figure 7.2: GRACE-derived gravity rates (Figure 5.28) converted to uplift rate according to equation (7.1). The Lambert et al. (2006) absolute gravity sites are indicated with stars.

To obtain the GRACE-derived uplift rates at the GPS locations in Figure 7.3, the *grdtrack* routine in GMT (Wessel and Smith, 1991) is used, which uses bicubic interpolation. Note that the Stokes coefficients from GRACE are filtered while the GPS data are not. There is very good agreement between both data sets around Hudson Bay, where the two peak gravity rates are located, although GPS observations are few and far apart there. The site with the largest difference, in the Canadian Prairies, could be an outlier or a strong local effect. However, there is a consistent difference west and north-west of the Great Lakes which is too large to be explained by the effect of filtering. Here an increase in water storage in this area (such as seen in Figure 5.4) is a possible explanation for the larger uplift rates in GRACE.

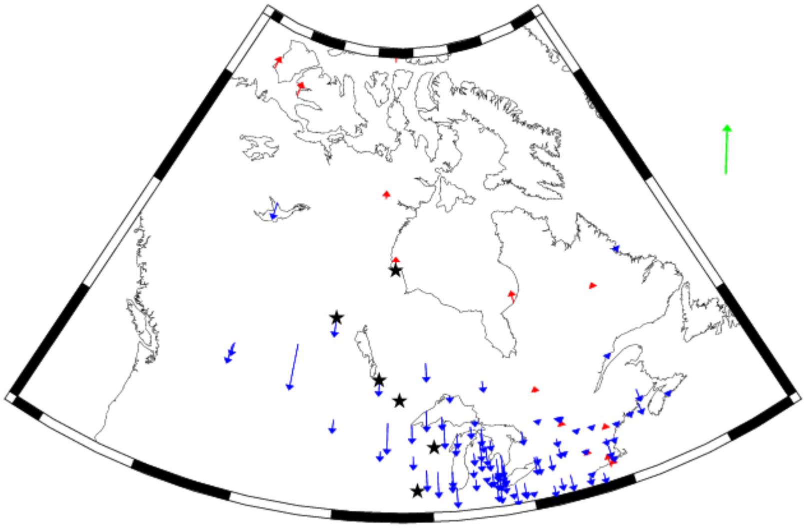

Figure 7.3: Observations at the continuous GPS stations of Sella et al. (2007) minus uplift rate from GRACE interpolated at the same stations. The length of the green arrow corresponds to a difference 10 mm/year. Stars denote the Lambert et al. (2006) sites.

7.2 Comparison between GRACE- and absolute gravity data

Terrestrial gravity data in North America is of high enough quality and long enough time span to be useful for GIA studies (Lambert et al., 2001). Therefore, to allow a second assessment of the GRACE results they are compared here with results from terrestrial gravity data from Lambert et al. (2001, 2006). The locations of the measurements are plotted in Figure 7.2. In the next section a comparison will be made with the map of gravity rates derived from the Canadian Gravity Standardization Network (CGSN) (Pagiatakis and Salib, 2003). Terrestrial gravity data are mostly sensitive to local effects (see section 4.4). This can be both an advantage because the large scale hydrology behaviour does not need to be known, or a disadvantage because the local water and snow distribution needs to be known, among others.

Lambert et al. (2001) present measurements with JILA and FG5 absolute gravity measurements across the southern margin of the Laurentide ice sheet. It was shown that ICE-3G in combination with viscosities of 1 x 10^{21} Pas and 2 x 10^{21} Pas in the upper and lower mantle, respectively, under predict the gravity measurements at some sites. This finding was one of the reasons that motivated Peltier (2004) to add extra mass in the ICE-5G model, in the form of a large Keewatin ice dome in the Yellowknife region. However, later a large inter-annual term in the data was found and corrected for (Lambert et al., 2006). The more recent data set is used here.

To compare the gravity rates measured at the deforming surface with those obtained with GRACE, both GRACE-derived and terrestrial gravity rates will be converted to uplift rate. For terrestrial gravity rates caused by GIA it is observed that the gravity to height ratio is close to that of the effect of free-air correction in combination with a Bouguer reduction with density equal to that of the upper mantle (see review in Rangelova, 2007). Here a ratio of -0.18 µGal/mm of Rangelova (2007), Figure 2.9, is used, which is derived from gravity rates from the Pagiatakis and Salib (2003) and Canadian Base Network (CBN) GPS observations (Henton et al., 2006) that are within 100 km of the CGSN sites. It is preferred to use one number for the whole GIA area, as opposed to using an individual gravity-to height ratio for each point. Such a procedure, used e.g. in Steffen et al. (2009), might be prone to local effects in either the GPS or gravity measurements and is sensitive to uplift rates or gravity rates with a small magnitude.

Errors in the uplift rate are obtained by propagating the errors in the gravity rates from Lambert et al. (2006) and the error in the gravity-to-height ratio of Rangelova (2007), as follows:

$$\sigma_{\dot{h}}^2 = \left(\frac{\partial \dot{h}}{\partial \dot{g}}\right)^2 \sigma_{\dot{g}}^2 + \left(\frac{\partial \dot{h}}{\partial r}\right)^2 \sigma_r^2$$

Where r and subscript r refer to the gravity to height ratio, and σ is the standard deviation.

The GRACE-derived gravity in Figure 5.28a is converted to uplift rate with equation (7.1). To account for loss of signal through filtering of the GRACE data, the same filtering that is applied to GRACE data is also applied to datasets or model outputs if these are compared to GRACE data. However, it is hard to apply the GRACE filters to scattered point data in a straight forward way, therefore an attempt is made to recover the signal that is lost by the filtering of the GRACE data (similar to section 5.5.3) and correct the GRACE data for this loss. The spherical harmonic expansion of GIA model i3_8_60 is truncated to degree 60 and subsequently Gaussian filtered with a 400 km halfwidth. This truncation and smoothing results in a change of signal at each of the locations in Table 7.1. The relative change can be used to correct the GRACE data by applying the inverse change. For example, if the Gaussian filtering leads to a reduction in signal of 5%, then the GRACE-derived gravity rate for that location is multiplied with 1.05 to get the ‘unfiltered’ gravity rate. This correction is rather crude, but sufficient for this comparison in which we only want to identify differences much larger than the error bars.

Uplift rates derived or taken from Lambert et al. (2006) data, Sella et al. (2007) and Pagiatakis and Salib (2003) are shown in Table 7.1. Note that the Lambert et al. (2006) data agree with the GPS data in Churchill and Flin Flon, which indicates that the removal of the interannual signal in the absolute gravity data made the data more consistent with GPS measurements. The GRACE-derived uplift rates agree with the uplift rates derived from the absolute gravity measurements within the errors bars, with the exception of the measurements in Flin Flon. GRACE also has larger uplift rates at Pinawa and International Falls. This could again be explained by a larger remaining hydrology signal in GRACE. However, local effects in the terrestrial gravity data could also play a role, and violations of the assumption of a constant gravity to height ratio.

Table 7.1: Uplift rates from three sources: (i) Absolute gravity rate (Lambert et al., 2006, L2006) converted to uplift rate with the gravity to height ratio of Rangelova (2007), p. 41; (ii) Gravity rate (Pagiatakis and Salib, 2003) converted to uplift rate with the same ratio; (iii) uplift rate from Sella et al. (2007), see Figure 7.3; (iv) uplift rate from GRACE (Figure 5.28a), converted with equation (7.1).

	L2006	PS2003	S2007	GRACE
Churchill	10.49 +/- 1.48	9.27	10.7 +/- 0.6	9.05
Flin Flon	2.80 +/- 1.51	5.26	1.7 +/- 0.7	7.43
Pinawa	2.77 +/- 1.03	-2.13	-0.2 +/- 0.8*	3.85
International Falls	2.55 +/- 0.79	-2.41	--	2.79
Wausau	1.94 +/- 1.38	--	--	0.27
Iowa City	0.44 +/- 1.43	--	--	-0.31

* uplift rate for the nearby site Lac DuBonnet is used.

7.3 Comparison between GRACE and CGSN data

Pagatakis and Salib (2003) performed a readjustment of the Canadian Gravity Standardization Network (CGSN) using as constraints the gravity measurements and their rates of change derived from absolute gravity measurements. The dataset spans a period of 40 years, longer than the absolute gravity measurements from Lambert et al. (2006) and the GPS uplift data.

The difference between the gravity rates from Pagiatakis and Salib (2003) and GRACE data is shown in Figure 7.4. GRACE has smaller uplift rates over the south-west portion of Hudson Bay, but more signal west and north-west of the Great Lakes. This is the same region where also GPS data show smaller uplifts, compare Figure 7.3. Note that in this area also the uplift rate disagrees with the GRACE-derived gravity rates (see

Figure 7.3). As is concluded in the discussion of that figure, the disagreement could be due to effect of remaining continental water storage changes (which are not described by GLDAS) in this area, which is picked up by the GRACE satellites but not by the terrestrial measurements because of their longer measurement span or because they are corrected for hydrologic effects.

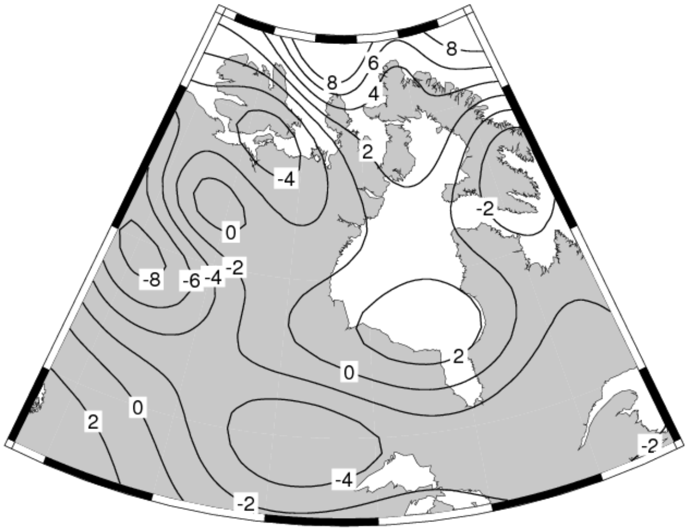

Figure 7.4: Uplift rate derived from Pagiatakis and Salib (2003) minus uplift rate derived from GRACE data, in mm/year.

Summarizing the conclusions from this and the previous sections: GRACE-derived uplift rates around Hudson Bay are slightly smaller than uplift rates from Pagiatakis and Salib (2003) and Sella et al. (2007). On the other hand, more signal is seen in GRACE compared to the three terrestrial data in an area west and north-west of the Great Lakes region. Remaining hydrology signal contained in the GRACE data could account for this mismatch.

7.4 GRACE and ice model: simulations

Before conclusions are drawn about the past ice distribution it is necessary to see how past ice distribution relates to present day gravity rate. Increase in ice thickness is linearly related to an increase in present-day gravity rate because of the linear rheology. A small sensitivity study is described in section 7.4.1 which investigates the relation between change in ice thickness and change in gravity rate for different viscosities.

7.4.1 Sensitivity of gravity with respect to ice heights

In the original ICE-4G model, ice thicknesses are specified for blocks with a certain length and width. Here, the block which has the largest ice thickness at LGM is used for the sensitivity study. Ice heights at this block for all time steps are multiplied by a factor of 1.1 to 2.0 in steps of 0.1. Other modifications could be selected, such as changing the time of LGM or changing the rate of decay, but that is not pursued here. The viscosity profile used is the one that provides best fit to the GRACE data in combination with ICE-4G (see section 7.6), with upper mantle viscosity of 4 x 10^{20} Pas and lower mantle viscosity of 128 x 10^{20} Pas. Variations of the upper and lower mantle viscosity with respect to this model are also investigated.

Figure 7.5 and Figure 7.6 show the change in gravity versus the scale factor applied to a block that has the highest ice thickness in the original ICE-4G ice model. The relation between increase in ice thickness, and the increase in gravity is indeed linear. That means that an increase in gravity translates in a local increase in past ice thickness independent of the local ice thickness itself. Thus, the differences between the GRACE-derived gravity rate and the gravity rate from some model can be used to improve the ice model, provided the scale factor is known. It becomes clear that a low upper mantle viscosity can almost nullify the effect of increased ice thickness. However, such a low upper mantle viscosity would probably also lead to uplift and gravity rates that are too low. A change in lower mantle viscosity has much less effect on the slope, because of the small horizontal size of the blocks. Since the exact viscosity profiles is of course unknown, that scale factor can be used that leads to reasonable total melt water predictions. However, such improvement of the ice model is left to future work.

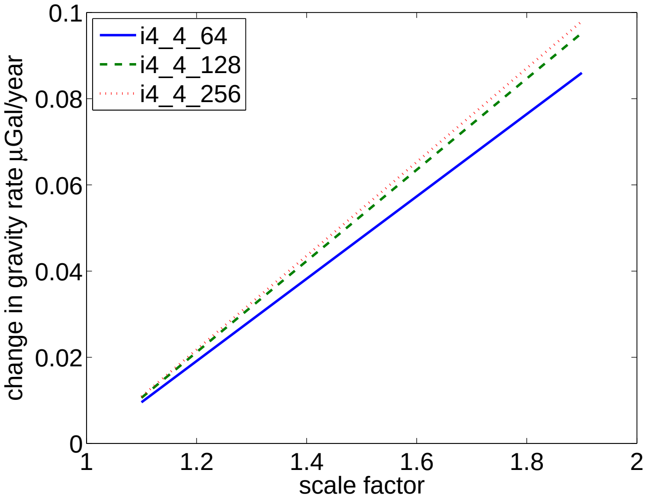

Figure 7.5: Relation between scale factor for ice thickness and increase in gravity rate, for a block at location of maximum ice thickness south-east of Hudson Bay (see Figure 7.9) with Δθ = 1.55° and Δλ = 1.25°.

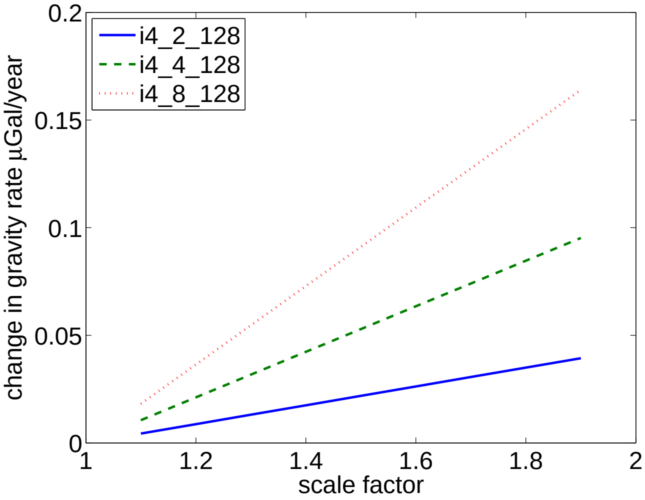

Figure 7.6: Same as Figure 7.5 for GIA models with varying upper mantle viscosity.

7.4.2 Simulations with known spatial patterns

Presence of continental water storage changes that are not corrected for can mask the influence of the ice loading history. To investigate to what extent this can happen a simulation is performed with observations consisting of the sum of a GIA model, the secular trend in a hydrology model and errors. It is assumed that the spatial pattern of GIA and the spatial pattern of hydrology are known, but these patterns can be multiplied with unknown factors α and β, respectively. This is a strong assumption which is only useful to get a first idea of the mixing of the hydrology and GIA signal. The question is, in the presence of this unknown factor, do we get the smallest misfit for the GIA model that is used in the simulated observations, irrespective of the errors and the hydrology pattern?

We determine the factors α and β by a least-squares procedure in which these parameters are to be estimated. The observation equation is

$$\mathbf{l} = \mathbf{A}\mathbf{x} + \boldsymbol{\sigma}, \qquad (7.2)$$

where $\mathbf{l}$ is a vector that contains the simulated gravity rate observations; $\mathbf{x}$ contains the scale factors α and β: $\mathbf{x} = \begin{bmatrix} \alpha \\ \beta \end{bmatrix}$; $\mathbf{A}$ contains the (assumed known) GIA pattern $\mathbf{a}$ and hydrology pattern $\mathbf{b}$: $\mathbf{A} = [\mathbf{a} \quad \mathbf{b}]$, and $\boldsymbol{\sigma}$ is a vector that contains the errors as in section 4.3.3. The objective is to find the values of α and β that minimize the difference between observations and scaled GIA and hydrology models in a least-squares sense. In this way it is possible to account for some uncertainty in our knowledge of GIA and hydrology. Because of correlation between the GIA pattern and the hydrology pattern, some features in the observation can be fitted either by scaling the GIA pattern or by scaling the hydrology pattern.

In this simulation, the observations are formed by a combination of the i3_8-60 model and any of the hydrology models: GLDAS, WGHM, CPC. The vector **a** consists of a GIA model (i3_8-60 or i5_2-60) divided by its maximum value, and **b** consists of the trend in one of the hydrology models divided by its maximum value. For the errors, trend residuals are used, as described in section 4.3.3. The grid for the simulation is formed by the 554 pixels of Figure 5.18 and the time period, limited by the availability of hydrology models and lake water levels, is August 2002 – November 2007. The Gaussian filter halfwidth is 400 km.

As an example of the minimization procedure, when using model i5_3_20 for **a** and WGHM as **b**, the maximum gravity rate values are 0.72 and 0.76 respectively. In this case, the values of α and β for which the least-squares residuals of equation (7.2) are minimized are 1.71 and 0.62 respectively. Thus, the minization procedure leads to magnitudes that are quite different than the models from which the patterns **a** and **b** are derived. In the following, only the fit between the synthetic data and the 'model' with the optimal parameters α and β are discussed. The values in Figure 7.7 show the minimized misfit between the observations and the 'model', defined as:

$$\chi^2 = \frac{1}{n}\sum_{i=1}^{n} \frac{l_i - \left(\mathbf{A}x\right)_i}{\sigma_i} \quad , \tag{7.3}$$

where n is the number of pixels for the simulated data. With GIA model i3_8-60 and hydrology model GLDAS used as observations, the misfits for **a** and **b** for different hydrology models, are shown in Figure 7.7. Of course, the smallest misfit occurs when i3_8-60 and GLDAS are also used as vectors **a** and **b** respectively. The good news is that for all hydrology models, the smallest misfit is obtained with the correct GIA model. However, the misfits for model i5_3_20 with WGHM are almost as small as WGHM with i3_8-60.

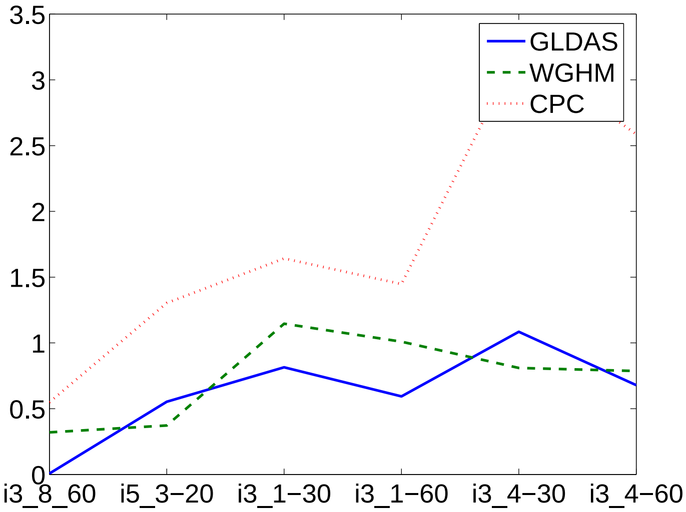

Figure 7.7: Misfit (defined in equation (7.3)) for cases when different GIA models are used for vector **a**, for different hydrology models.

Thus, in the optimistic case that both GIA and hydrology patterns are known, the imperfect knowledge of hydrology or the viscosity profile can have as large an effect on misfit, as the difference between GIA models with two different ice models. This simulation with the optimistic scenario that both GIA and hydrology patterns are known should caution that uncertainty in hydrology and viscosity possibly prevents the difference in ice models to be resolved through a misfit comparison.

7.4.3 Simulations with known spatial patterns and changing Gaussian filter halfwidth

The previous section led to the conclusion that uncertainty in hydrology is almost as important for misfit, as uncertainty in the ice models. However, the simulation in the previous section was done for a constant Gaussian filter halfwidth. Possibly, by adjusting the filtering, use can be made of the different spectral signatures of the GIA model and the hydrology model (Figure 5.16): GIA degree amplitude peaks at lower wavelengths than continental water storage. Therefore, more smoothing can potentially bring out the GIA signal relative to the hydrology signal.

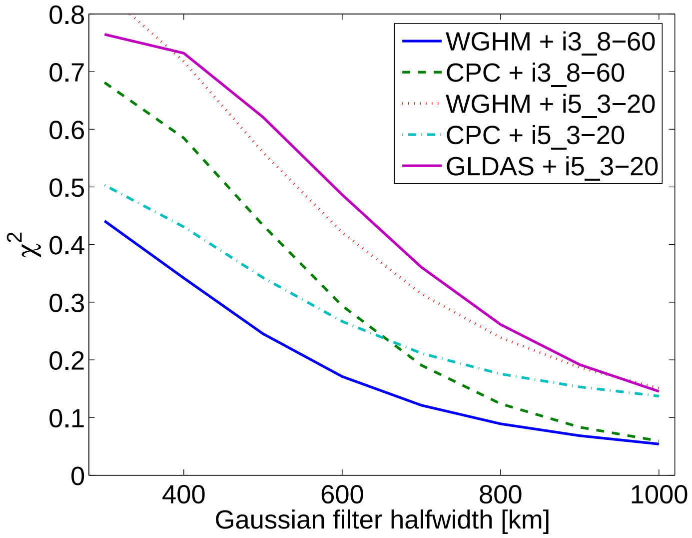

Figure 7.8: Misfit for the simulation described in the text, for varying Gaussian filter halfwidths.

This is investigated in Figure 7.8 for the same simulations as the previous section. As is expected, for large halfwidths the curves for the same GIA models converge so that the GIA models determine the difference in misfit. However, the difference in misfit value is small; it is unlikely that such a small difference can be discerned in practice.

7.5 GRACE and ice model: results

The simulations from the previous section show that misfit can not be expected to clearly discriminate between GIA models in the presence of uncertainty in the hydrology model. However, the real GRACE data should be investigated to see if very different ice models can explain the GRACE data as the simulations suggest. Here, the first subsection investigates the variation of the location of the maximum gravity rate, since the location is less sensitive to smoothing than the magnitude of the maximum gravity rate. In the second and third section, misfit is computed between models and the GRACE and GPS data, respectively.

7.5.1 Location of maximum with no scaling in hydrology model

It is shown in section (5.4.1.1) that the magnitude of the maximum in the gravity rate estimated from GRACE data varies with the length of the GRACE time series. Here, the location of the peak magnitude as a function of the time series will be investigated as follows. The GRACE data are synthesized on a 1 x 1 degree grid. The pixel in this grid which has the largest gravity rate is plotted in Figure 7.9a and Figure 7.9b for gravity rate trends estimated from 4 and 5 years of GRACE data, respectively (April and May of 2002 are not used). Different hydrology models are removed, of which GLDAS and CPC include water level variations in large lakes (see section 5.1.3). The location of the maximum ice thickness and the second maximum in ice thickness as determined by visual inspection of the maps of Dyke and Prest (1987) and the locations of the two maxima in ice thickness for the ICE-3G, ICE-4G and ICE-5G models are also indicated.

The scatter of the location for different four year time periods is small, indicating that the location of the maximum is fairly robust with respect to different 4 or 5-year time series being used. Moreover, it can be seen that removing GLDAS or WGHM leads to the location of the maximum that agrees with a maximum ice thickness at the Labrador ice dome (except one four year period for WGHM). Only removing the CPC model leads to a maximum gravity rate coinciding with the Keewatin ice dome. The same observations can be made for the 5-year trend in Figure 7.9b. Since GLDAS and WGHM seem to be the more advanced models (although LaD does perform better than WGHM over the Nelson River basin, see Table 5.2), the location of the largest ice thickness coinciding with the Labrador ice dome is more likely based on GRACE data. This also agrees with the findings of Dyke and Prest (1987). Note also that the location of the maximum derived from GRACE agrees better with the location found in the ICE-4G model and the ICE-3G model which in turn agree better than the ICE-5G model. The location of the secondary dome in GRACE agrees better with ICE-5G (not shown here) as ICE-3G and ICE-4G predict a weak secondary dome in the center of Hudson Bay.

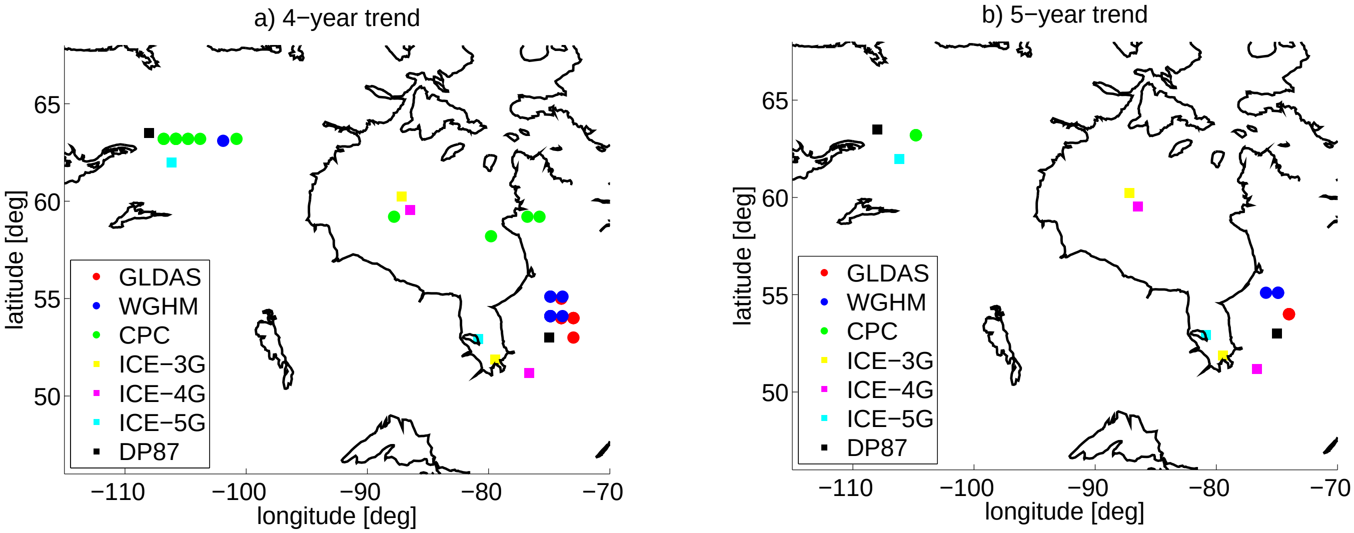

Figure 7.9: Location of the maximum estimated after removing different hydrology models. (a) trend estimated for a 4-year window (b) trend estimated for a 5-year window. The location of maximum ice thicknesses at LGM in the ICE-3G, ICE-4G and ICE-5G models and the location of the domes in Dyke and Prest (1987) (determined by visual inspection) are also indicated.

7.5.2 Model misfit with respect to GRACE data

The simulations in sections 7.4.2 and 7.4.3 showed that it is unlikely that misfit from GRACE data can distinguish between different ice models in the GIA modeling, in the presence of uncertainty in continental water storage, and if uncertainty in the GIA model and hydrology models is accounted for by scaling. However, based on the excellent agreement between GRACE and the study of Dyke and Prest (1987) in the previous section, it can be concluded that the uncertainty in hydrology models is not as large as assumed in the simulations of section 7.4. Therefore, we proceed now by assuming that the influence of hydrology can be reasonably well described by one of the global models used in this thesis and we compute misfit between GRACE data and GIA models with the different global ice histories used in this thesis: ICE-3G, ICE-4G and ICE-5G. Uncertainty in GIA models is now introduced by varying the mantle viscosity. The amount of smoothing is varied by changing the Gaussian filter halfwidth, following the results in section 7.4.3 which show that for increased halfwidth, the effect of the hydrology model on misfit decreases with respect to that of the GIA model.

Since GIA data can likely only constrain two layers in a global GIA model (Paulson et al. 2007a), only the viscosities of the upper and lower mantle are varied. Furthermore, the relaxation is sensitive to the logarithm of the viscosity (e.g. Paulson at al. 2007a), so the viscosity is incremented by a factor of two, starting at a value of 1 x 10^{20} Pas up to 256 x 10^{20} Pas. The influence of lateral variations or non-linear rheology is not investigated here, but deserves attention in future work on this topic.

To study whether the misfit numbers are the result of the particular spatial patterns in the hydrology models, the minimum misfit (i.e. the lowest misfit value among all the models with upper and lower mantle viscosity in the range mentioned in the previous paragraph) is plotted for different Gaussian filter halfwidths in Figure 7.10. The minimum misfit is not always found for the same viscosity profile, but the focus is on the ice loading history. The monotonic decrease of section (5.3.1) does not appear in this figure, which could indicate that there is considerable signal in the GRACE data which is not included in the simulations of section 7.4.3. As in section (5.3.1), the misfit decreases when the Gaussian filter halfwidth is increased from 500 km to 1000 km. Clearly, the

ICE-3G and ICE-4G loading history have the lowest misfit for all halfwidths. Especially the larger misfit of ICE-5G for large halfwidths (>700 km) suggests that the basic shape of ICE-5G (with maximum ice thickness west of Hudson Bay) does not match the GRACE-derived pattern. Using GFZ instead of CSR data (not shown) gives similar results, but for CPC removed (Figure 7.10b) there is a sharp increase in misfit, the reason for which might be related to the deficiencies of the CPC model.

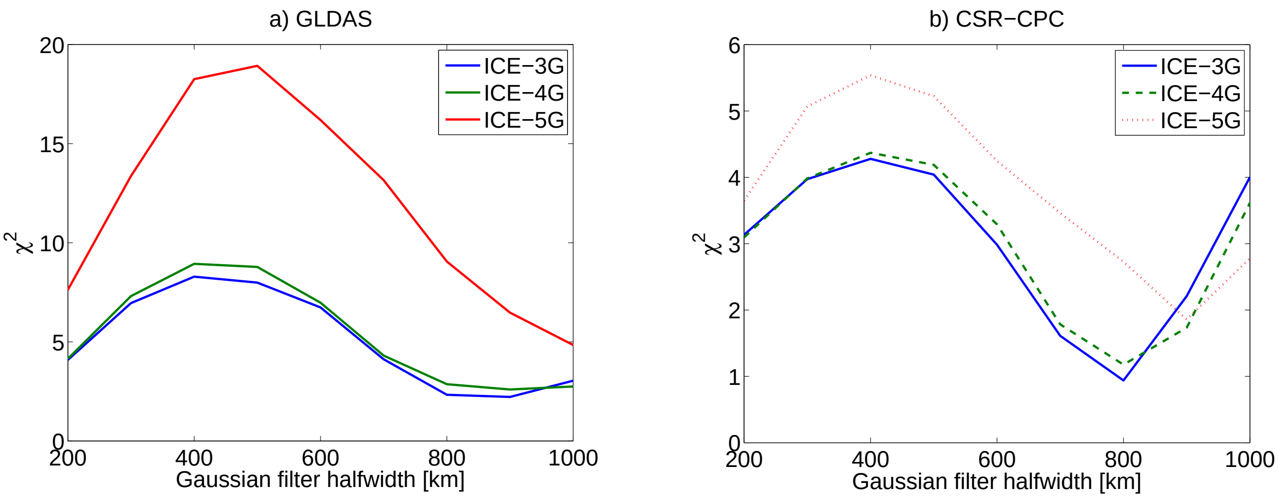

Figure 7.10: Minimum misfit out of the range of models with upper and lower mantle viscosity varied in the range of 1-256 x 10^{20} Pas for varying Gaussian filter halfwidths, for GIA models with three different ice loading histories. (a) GLDAS is removed; (b) CPC is removed.

7.5.3 Model misfit with respect to GPS uplift rate data

Compared to GRACE data, GPS uplift rate data have the advantage of being less sensitive to large scale continental water storage changes and having longer time series. Misfit between GIA models and uplift rate data from Sella et al. (2007) is shown in Figure 7.11 and Figure 7.12 for ice models ICE-3G, ICE-4G and ICE-5G. The best fitting viscosities are the same for ICE-3G and ICE-4G: upper mantle viscosity of 8 x 10^{20} Pas, and lower mantle viscosity of 32 x 10^{20} Pas, while for ICE-5G the upper mantle viscosity is a factor of two lower. The best fitting viscosity values obtained with ICE-5G are reasonably close to a two-layer approximation of VM2 model of Peltier (2004), with upper mantle viscosity of 9 x 10^{20} Pas, and lower mantle viscosity of 32 x 10^{20} Pas (see Paulson et al. 2007b) but note that the GPS data of Sella et al. (2007) are not used for constraining ICE-5G. Table 7.2 shows the misfit values for the best fitting models. Similarly to what was found for the GRACE misfits, misfit values for ICE-3G and ICE-4G are considerably lower than for the best-fitting model of ICE-5G.

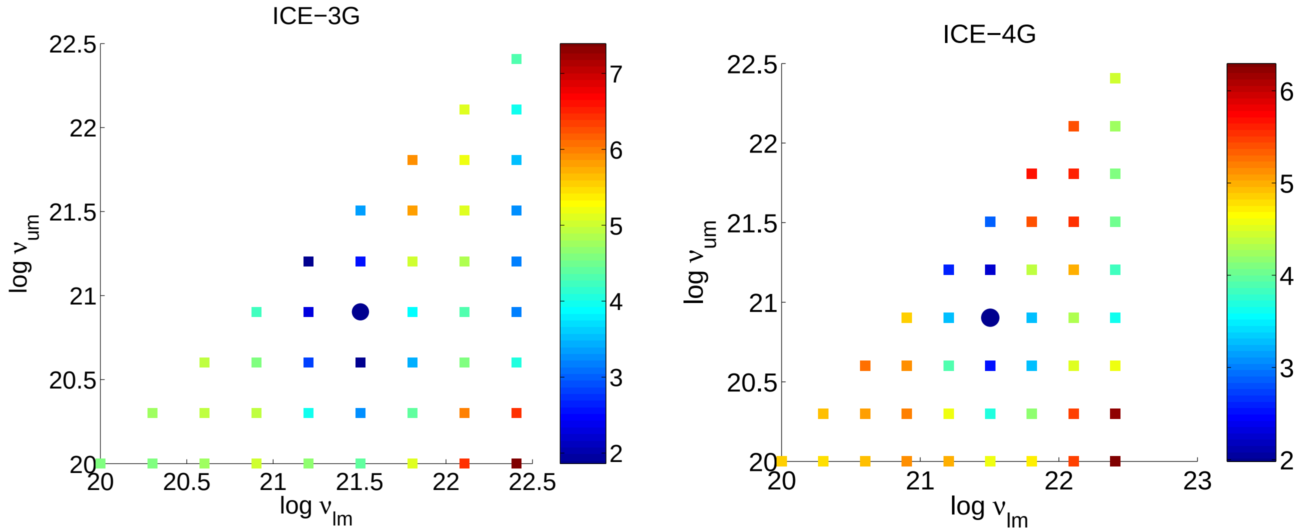

Figure 7.11: Minimum misfit with respect to uplift rate data of Sella et al. (2007) out of the range of models with upper and lower mantle viscosity between 1-256 x 10^{20}, for GIA models with (a) the ICE-3G model (b) the ICE-4G model. The minimum misfit is denoted with a circle.

What about the terrestrial gravity data sets? Terrestrial gravity from the CGSN and uplift rates from the CBN compare well with the ICE-3G model (Pagiatakis and Salib, 2003, Henton et al., 2006,). The uplift rates resulting from the combination of these datasets in Rangelova (2007), fig. 4.16, gives a pattern that resembles more the ICE-3G/ICE-4G history than the ICE-5G loading history. In Rangelova (2007) Figure 5.16, there is still a reasonable match between GRACE-derived gravity rate (from a shorter GRACE time period than used here) and ICE5G-VM2. However, the solution which combines GRACE data with terrestrial data does not show the large signal west of

Hudson Bay that is present in the ICE-5G/VM2 model, and shorter time series of GRACE data are used there.

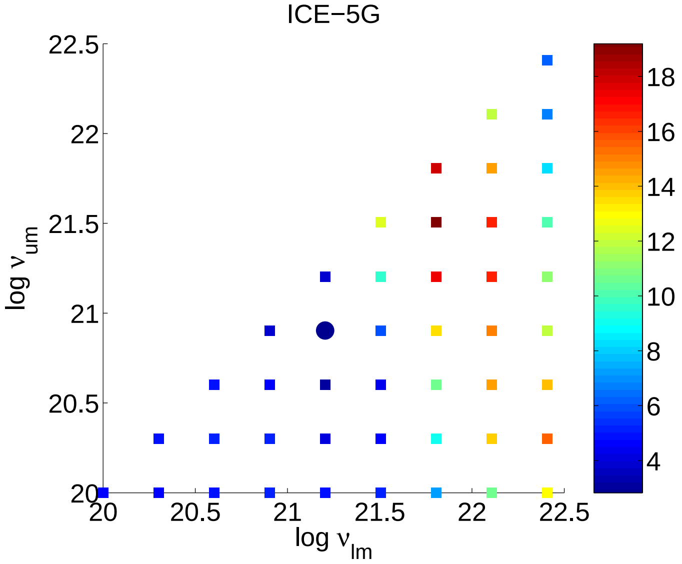

Figure 7.12: Same as Figure 7.11 but for the ICE-5G model.

Table 7.2: Viscosities and misfit of best fitting models for the three global ice loading histories.

	ICE-3G	ICE-4G	ICE-5G
η_{UM} [x 10^{20} Pas]	8	8	4
η_{LM} [x 10^{20} Pas]	32	32	32
χ^2	1.86	1.98	2.83

7.6 Best fitting viscosity

A robust viscosity profile can not be inferred from present-day uplift or gravity rate data alone; RSL data are a necessary data set because they extend in time. However, it is interesting to compare the viscosity profile that best fits GRACE data with other estimates in the literature. If agreement exists, that would strengthen the conclusions about the fit of different ice histories shown the previous section.

The minimum misfit for ICE-4G with smoothing varied from 200 to 500 km Gaussian filter is found for upper mantle viscosity of 4 x 10^{20} Pas and lower mantle viscosity of 1.28 x 10^{22} Pas. The same model provides a best fit when the ICE-3G model is used, for a range of halfwidths from 200 to 600 km. This is close to the values found with ice models ICE-1, ICE-3G and ICE-4G in other studies, see the overview in Table 7.3. An exception is the VM1 model of Tushingham and Peltier (1991) which has a much smaller viscosity contrast. Results are also somewhat different from Paulson et al. (2007b) where ICE-5G is used, but it is noted there that a more ductile upper mantle and stronger lower mantle also has a small misfit with respect to the data sets employed in that paper. More reasons for the discrepancy are the use of ice models that are biased by the viscosity profile used in the inversion of RSL data (Kaufmann and Lambeck, 2002) and possible trade-off effects between different layers (Paulson et al., 2007a).

As noted before, the best fitting model is not well constrained by uplift rate alone. However, such a model can be useful as interpolator surface of the uplift rates. Such an interpolation offers advantages compared to straight forward interpolation of the uplift rates: (i) it is less sensitive to local effects; (ii) it introduces extra information (ice loading history, elastic behaviour of the Earth, relaxation of the Earth) which can help to interpolate uplift rate across regions that are not well sampled by GPS observations. Thus, the uplift rate from a GIA model which best fits GPS data can be interpolated at desired locations in the GIA area, so that estimates for glacial isostatic uplift rates can be included in geomorphological models or local studies (Van der Wal et al., submitted).

Table 7.3: Best fitting viscosity profiles from selected studies on GIA in North America: P2007 = Paulson et al. (2007b), W2006 = Wolf et al. (2006). KL2002 = Kaufmann and Lambeck (2002). MF2002 = Mitrovica and Forte (2002).

	η_{UM} [10^{20} Pas]	η_{LM} [10^{21} Pas]	**ice model**	**data used**
P2007	5.3	23	ICE-5G	selected RSL, GRACE
W2006	3.2	160	ICE-3G	RSL, uplift, gravity and tide gauges rates at Churchill
KL2002	7	200	ICE-1[2)]	RSL, True Polar Wander, $\dot{C}_{20}$, gravity and uplift rates in Fennoscandia
MF2002[1)]	3.9-0.43	65-110	ICE-3G	RSL, mantle convection
TP1991	10	20	ICE-3G	RSL
GRACE this thesis	4	64	ICE-3G	gravity rates (GRACE)
GRACE this thesis	4	128	ICE-4G	gravity rates (GRACE)
GPS this thesis	8	32	ICE-3G/ICE-4G	uplift rates

1) as cited in Wolf et al. (2006).

2) for ice sheets other than the Laurentide ice sheet other ice models are used.

7.7 Discussion on the Laurentide ice history

The newer ICE-5G ice loading history represents an improvement compared to the older ICE-4G and ICE-3G model in many ways (Peltier, 2004). For example, while ICE-4G ice thicknesses in the interior of North America were constrained solely by relative sea level histories and the ice margin chronology of Dyke and Prest (1987), ICE-5G includes newer ice margin chronologies and a 3D thermo-mechanical ice sheet model of Tarasov and Peltier (2003). Furthermore, ICE-5G contains improvements to other ice sheets which are not discussed here, because the focus here is on North America.

Based on newer RSL observations at Sunda Shelf and J. Bonaparte Gulf, it was found that ICE-4G contains too little ice. The missing ice was placed on the Keewatin ice dome in North America based on two geodetic data types are invoked by Peltier (2004): Very Long Baseline Interferometry (VLBI) data from Argus et al. (1999), and absolute gravity data from Lambert et al. (2001). Uplift and gravity rates presented in those papers were underpredicted by the ICE-4G model. Using multiple runs of the Tarasov and Peltier (2003) thermomechanical ice sheet model, ice thicknesses were fitted to the new ice margin chronology and the gravity rate and VLBI data, which presumably resulted in the ice thicknesses shown in Figure 7.13.

A critical look at the VLBI and gravity data sets is warranted. VLBI data at Yellowknife, is 8 mm/year +/- 5.5 mm/year (of Argus et al., 1999, p. 29,086). An estimate with such large errors bar can be matched with GIA models with a great variety in ice thickness. Tarasov and Peltier (2004) cite the VLBI estimate as 8 mm/year +/- 1.5 mm/year, possibly as a result of an extension of the VLBI time series that was not published elsewhere. As mentioned before, the secular gravity rates of Lambert et al. (2001) were corrected for an interannual signal in Lambert et al. (2006) such that the ICE-5G/VM2 model overpredicts the gravity rates in Figure 9 of Lambert et al. (2006). A better fit with the gravity rates is obtained by an adjusted version of the ICE-3G model.

One of the results of the inclusion of the ice dynamical model is the occurrence of fast ice flow in Hudson Bay, which results in a region of local minimum ice thicknesses over Hudson Bay. ICE-3G and ICE-4G have a local maximum right in the center of Hudson Bay (see Figure 7.9). GRACE seems to confirm the local minimum, because the maximum gravity rates are located on the Labrador and Keewatin ice dome. GRACE data in fact confirms the multi-domal nature of ICE-5G with a Keewatin and Labrador ice dome, as already concluded by Tamisiea et al. (2007). However, ICE-5G contains such thick ice extending from the Keewatin ice dome southeast-ward, see Figure 7.13a, that for any viscosity profile the maximum uplift and gravity rate will be located west of Hudson Bay; see Figure 7.13b. Such a maximum is not seen in the GRACE data (Figure

5.28). The bulge extending over Lake Winnipeg can not be seen in the GRACE-derived gravity rate when gravity rate from any of the hydrology models is subtracted. This difference in patterns manifests in the higher misfits for ICE-5G as in Figure 7.11.

Note that Figure 21 in Peltier (2004) shows maximum uplift rate below 14 mm/year for ICE-5G/VM2 (which is likely ICE-5G version 1). The same plot is shown in Tarasov and Peltier (2004) for one of their best fitting models. However, the ICE-5Gv1.2/VM2 results published on the Special Bureau for Loading website which are used throughout this thesis have a much larger maximum uplift rate of 17.4 mm/year, see Figure 7.13b.

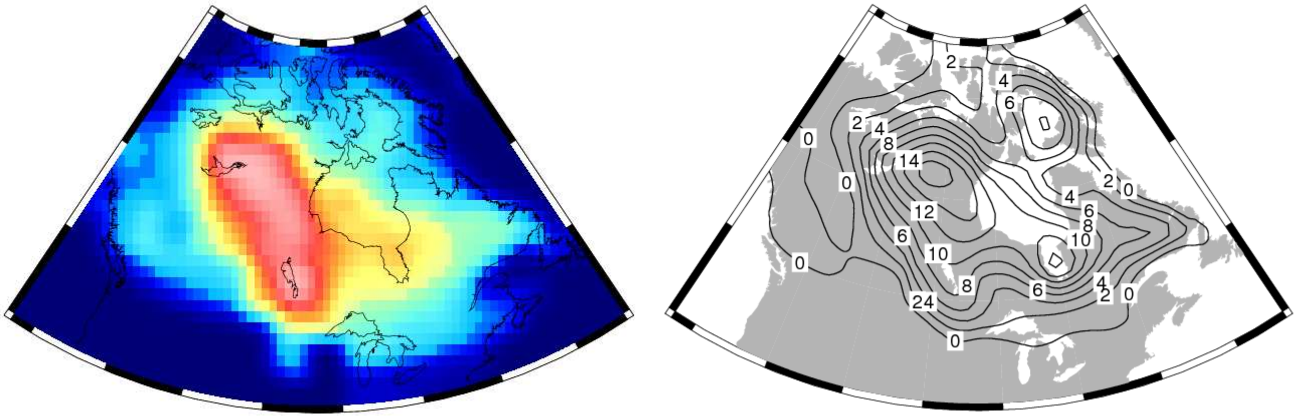

Figure 7.13 (a): Ice height prescribed by the ICE-5Gv1.2 model at LGM, 26 ka BP, (b): uplift rates of the ICE-5Gv1.2/VM2 model.

Is there evidence in the literature for or against the large ice thicknesses at the Keewatin dome as specified in ICE-5G? Firstly, Dyke and Prest (1987) state on page 255: “Crustal depression remained much larger adjacent to western Labrador Ice than adjacent to Keewatin Ice at 8 ka because much of the recovery from the Keewatin load had been achieved before 8 ka. Recovery from the Labrador load was comparatively delayed.” The fact recovery from the Labrador ice load was delayed does not support the larger ice thicknesses in Figure 7.13a.

A comparison of two thermomechanical models with a flow law that fits the observations in Greenland and Antarctica resulted in a maximum ice sheet thickness of

3805 for a model by Tarasov and Peltier and 4221 m for a model by Marshall and Clarke, (Marshall et al., 2000). In the Marshall and Clarke model a single dome is centered on the south of Hudson Bay. Thick ice (4239 m) is found also by Tarasov and Peltier (1999) if they tune their model to fit Greenland ice. However, in that case, complete deglaciation is not achieved in the simulation and the margin of the ice does not extend far enough south.

Tarasov and Peltier (2004) impose the gravity rate of Lambert (2001) as constraint, but are not able to achieve a perfect match, because that would require higher ice thickness. That is not likely, as the authors state, given the tendency for fast ice flow and the requirement of thin ice on Hudson Bay to satisfy sea level requirements. They state that the VLBI observation in Yellowknife requires ice to have been between 3.3 and 4.3 km thick. Interestingly, one of the best fitting models of Tarasov and Peltier (2004) (nn2059) was incorporated in the ICE-5G model of Peltier (2004), but ice thicknesses in the ICE-5Gv1.2 model are markedly increased to over 5500 m.

From this short review it can not be concluded that the thick ice (>5500 m) in ICE-5G is not supported by studies discussed here which focus explicitly on the ice history in North America. Also, thick ice is apparently not a ‘natural’ feature in thermo-mechanical ice models. Thus, the too large ice thicknesses in ICE-5Gv1.2 which cause a worse fit with GRACE data do not appear necessary. Then in future work on improving ice models, it seems sensible to decrease ice thicknesses in the ICE-5G model. GRACE data can help in constraining the ice heights.

7.8 Summary

In this chapter, a simulation was performed to see whether GRACE data can discern between difference ice models in GIA modeling based on misfit. It was shown that, when scaling is allowed for the GIA model and the hydrology models, the uncertainty in hydrology models (represented by the difference between different hydrology models) has as large an effect on gravity rate misfit values as do different ice histories. Therefore, insofar as the simulation is realistic, it is likely that differences in ice models can not be discerned in the GRACE data based on misfit.

However, the location of the two maxima in the spatial pattern of the GRACE-derived gravity rate lie closely to the centres of the ice domes at LGM in maps constructed based on geomorphological data by Dyke and Prest (1987). This is the case for different hydrological corrections and for different time periods of the GRACE data. The agreement between GRACE data and a geomorphological study confirms that GRACE data can provide meaningful constraints on the past ice distribution.

ICE-3G and ICE-4G model gives smaller misfits to the GRACE data than the ICE-5G model, for all Gaussian filter halfwidths and for a wide range of upper and lower mantle viscosities. The same is found when models are compared with GPS uplift rate data. This is due to the large ice thickness (> 5 km) west and south-west of Hudson Bay in the ICE-5G model. Such large ice thicknesses are also not supported by studies that consider ice dynamics.

Thus, an improved ice loading history should have a smaller ice thickness at the Keewatin dome than the ICE-5G model. Since GRACE data are shown to contain valuable information about the past ice sheet distribution, it seems sensible to use GRACE data to test or constrain future versions of Pleistocene ice models in North-America.

Chapter Eight: Concluding Remarks

This chapter summarizes the conclusions relating to the research questions posed in section 1.2 and gives recommendations for future research directions. The main findings of this thesis are the following:

i) The uncertainty in GRACE data when it is used for GIA studies is larger than previously thought;

ii) GRACE data shows two peaks in the spatial pattern of the gravity rate, with the largest peak corresponding to the maximum ice height in the Quebec-Labrador region;

iii) Composite rheology, while providing a fit to relative sea-level data almost as good as non-linear rheology, can increase uplift rate compared to non-linear rheology.

More detailed conclusions are presented in section 8.1, and recommendations for future research are given in section 8.2.

8.1 Conclusions

GRACE data exhibits significant north-south oriented errors, which can be removed by post-processing the data. The question is how much post-processing should be applied to extract the GIA signal from the GRACE monthly gravity fields. Even though visual improvement in the secular gravity rate pattern derived from GRACE is achieved by filtering, GIA has power at long wavelengths that should not be removed by a filter. In this thesis it is shown that, by varying the spherical harmonics coefficients that are filtered by the Swenson and Wahr (2006) filter, a trade-off is achieved between removal of GIA signal and removal of errors. Other filters used in this thesis are shown to smooth or remove signal which reduces the sensitivity of the data with respect to upper mantle viscosity. If one wishes to use more recently developed filters which are not used in this thesis, these filters should be applied on simulated data first to assess how much signal is removed by their application.

A map of the gravity rate pattern derived from GRACE appears to reflect the location of past ice masses. However, it has been shown in this thesis that the uncertainty in GRACE data, when used for study of GIA, is larger than previously thought. For example, hydrology appears as inter-annual signal in principal component analysis and likely causes differences between the GRACE-derived uplift rate and the uplift rate derived from terrestrial data.

Measurement errors in the secular gravity rate derived from GRACE can equally well be described by propagated calibrated standard deviations or point variances constructed from the propagated full variance-covariance matrix, or by the residuals after estimation of a trend, annual and semi-annual period in the time series of spherical harmonic coefficients of the monthly gravity fields from GRACE. All of these methods results in a small remaining error of.0.05 μGal/year after applying the tuned filter.

Using simulated GRACE data it is shown that, in the presence of uncertainty in hydrology, ICE-5Gv1.2 is able to fit the simulated data that is constructed using ICE-3G almost as well as ICE-3G models. Therefore, if uncertainty in hydrology models is represented by the differences between models, and if scaling of the hydrology models and GIA models is allowed, it can not be expected that misfit to GRACE data can discern difference between GIA models with different ice models.

Despite the conservative results from simulations, it has been observed previously that the GRACE-derived gravity rate pattern contains two domes in North America, in agreement with earlier geomorphological studies. However, results in this thesis show how earlier estimates of the gravity rate from GRACE were sensitive to the short (<5 years) time span and the inclusion of lesser quality data in 2002. Still, the two peaks appear to be a robust feature. It is shown in this thesis that the location of the maximum gravity rate is close to the center of Keewatin and Labrador ice domes inferred in Dyke and Prest (1987) from clues in the North American landscape. The existing ice models ICE-3G/ICE-4G/ICE-5Gv1.2 did not match the geomorphological data of Dyke and Prest (1987) as well. This clearly shows the potential of GRACE for improving ice models.

The observation that the GRACE-derived gravity rate has two domes should lead to a better fit with the multi-domal ICE-5Gv1.2 ice model than with the more mono-domal ICE-3G and ICE-4G. Also the location of maximum gravity rates better matches the location of maximum ice thicknesses in ICE-5Gv1.2 than the other models. However, it is observed that ICE-3G and ICE-4G have smaller misfit values for all realistic values of Gaussian smoothing. This indicates that ice thicknesses in ICE-5Gv1.2 west of Hudson Bay (Keewatin ice dome) and southwards from there, are too large. A literature search found that published ice dynamic models also do not require such large ice heights.

A completely new ice model based on non-linear rheology is going to be a multi-disciplinary effort. Some steps towards such a model are made in this thesis. First, it is necessary to get a handle on the non-linear rheology parameters that fit well available GIA data. It was selected to use composite rheology, which adds the creep rate from linear rheology and non-linear flow laws. Such a rheology is a more realistic description of laboratory experiments which show both diffusion and dislocation creep operating at mantle conditions. Since the gravity rate spatial pattern is mostly determined by the ice heights, it is sufficient to use the maximum gravity rate (or geoid rate as is done in this thesis) to provide constraints on composite rheology in addition to RSL data.

With respect to a selection of 30 RSL sites, composite rheology provides a slightly worse misfit than non-linear rheology, and a much better fit than linear rheology. However, it is shown that the fit is sensitive to single stations with large misfit values. A slightly better fit for composite rheology can also be obtained if some stations are left out, which is a reason to not focus exclusively on misfit in comparisons with RSL data.

It is found that individual RSL curves can sometimes be close to purely non-linear rheology for larger values of the pre-stress exponent A, for large values of the Newtonian viscosity, or both. The question is whether deviatoric stress is large enough to excite a strong non-linear component in the deformation. Large deviatoric stresses are found around the end of melting, and for some sites. This is a second reason to look at individual RSL curves when comparing the performance of linear, non-linear and composite rheology, in addition to global misfit.

The model that best fits RSL data in combination with ICE-5G has A = 3.3 x 10^{-35} $Pa^{-3}s^{-1}$ and η = 9 x 10^{21} Pas, but it is possible that better fit can be obtained with a higher Newtonian viscosity, or with a viscosity between 3 x 10^{21} Pas and 9 x 10^{21} Pas, which is not investigated here. RSL curves for the best fitting model are close to those of purely non-linear rheology. A contribution of linear rheology in sea level curves for this model is found at the beginning of deglaciation, for sites at the margin of the Laurentide ice history and at the center and margin of the Fennoscandian ice sheet. Surprisingly, for this model, uplift and geoid rate are closer to values observed by GPS and GRACE, respectively, than those predicted by a model with purely non-linear rheology. This represents an important argument in support of composite rheology, as GIA models with a non-linear rheology always suffered from very low present-day uplift rates. This has implications for future improvements in ice loading history, as it means that less dramatic changes to the ice loading history are required to be able to fit GIA observations with a composite rheology compared to a purely non-linear rheology.

To see if fit with RSL data and geoid rate can be improved, two simple modifications of the ICE-4G ice loading history were made: increasing ice thickness and delaying the entire glaciation. Increasing thickness of the Laurentide ice sheet for the model that best fits RSL data hardly increases uplift rate, and worsens the RSL fit. A 1 ka delay in glaciation improves both RSL fit and the visual match with observations for RSL curves at some stations, and increases uplift rate. Therefore, future ice models based on composite rheology should start by melting more ice later in time, within limits allowed by other constraints on the past ice sheets.

8.2 Outlook

Since the gravity rate estimated from GRACE monthly gravity fields has been shown to provide constraints on the ice model, it is recommended that GRACE data is used to improve or at least test a future ice model in North America. However, improvements are needed in our knowledge of continental water storage changes and inter-annual signals that appear in GRACE data over North America.

Current global hydrology models do not perform well in areas of permanent snow, thus improvements can come from using datasets to describe snow and ice cover changes. Also, extreme events such as droughts or snow storms will be less significant in the GRACE-derived gravity rate estimated from longer time spans.

The interannual variations in the spatial pattern and magnitude of the gravity rate derived from GRACE time series with different lengths need to be understood. Also here, increased length of GRACE data span can help to separate signals and to resolve some ocean tidal components with long aliasing periods. A technique such as principal component analysis or its extensions might be better able to separate the different signals in GRACE data and in that way remove inter-annual non-GIA signals, if the time series are longer.

For development of an ice model with non-linear rheology, it is important to focus on specific areas with good quality GIA data and seismic and field data. Sensitivity studies should be done to show if rheological parameters can be extracted from GIA studies in the presence of uncertainty in other parameters. Furthermore, the finite element model used here should be improved by adding realistic background stress arising from plate motion and mantle convection. Stress concentration occurs close to the edge of the ice sheet. Therefore, it should also be checked whether the finite element mesh is fine enough at such locations.

APPENDIX A: TIME FOMAIN SOLUTION FOR FREE-AIR GRAVITY, GEOID AND SEA LEVEL

The first section of this appendix derives the solution for free-air gravity or sea level as a function of an impulse surface load. In the second section the expressions are given for a load consisting of Heaviside increments.

A.1. Time-domain expressions

For a general surface load $L(\theta,\lambda,t)$ with units of mass per area, the response *RE* is a convolution of the load with the Greens function *GF* that is valid for that particular response:

$$RE(\theta,\lambda,t)=\int_{-\infty}^{t}\iint_{\Omega} a_e^2 L(\theta',\lambda',t')\, GF(\psi,t-t')\,d\Omega' dt', \tag{A.1}$$

where θ is colatitude; λ is longitude; Ω is the volume of the spherical Earth and ψ is the spherical angle from the load to the point where the response is to be computed. Expanding the load in spherical harmonics:

$$L(\theta,\lambda,t)=\sum_{l=0}^{\infty}\sum_{m=0}^{l} L_{lm}(t) Y_{lm}(\theta,\lambda), \tag{A.2}$$

and expanding the Greens function in Legendre polynomials:

$$GF(\psi,t-t')=\sum_{l=0}^{\infty} GF_l(t-t') P_l(\cos\psi),$$

where P_l is the Legendre polynomial of harmonic degree *l*, and using the orthogonality property:

$$\iint_{\Omega} Y_{l'm'}^{*} Y_{lm}\, d\Omega = 4\pi\delta_{ll'}\delta_{mm'},$$

equation (A.1) becomes (Mitrovica et al., 1994, equation 33)

$$RE(\theta,\lambda,t)=\sum_{l=0}^{\infty}\sum_{m=-l}^{l}\left(\frac{4\pi}{2l+1}\int_{-\infty}^{t} GF_l(t-t') L_{lm}(t')\,dt'\right)\times Y_{lm}. \tag{A.3}$$

Since we want to compute the gravity rates, we need to find the Legendre coefficient of the Greens function for the free-air gravity anomaly. The Legendre coefficient of the

Laplace transformed free-air gravity anomaly is given by (Mitrovica and Peltier, 1989, equation 5)

$$\Delta g_l\left(s\right)=\frac{g}{M_e}\left(l+2-\left(l-1\right)k_l\left(s\right)\right). \tag{A.4}$$

To check the units, note that the k-Love number needs to be multiplied with $a_e g_0/M_e$ to give it the dimension of potential. To go from potential to gravity multiply with $1/a_e$. Then the left hand side has the units of gravitational acceleration for a unit load of 1 kg. Note that in the derivation of this equation in Mitrovica and Peltier (1989), a free-air correction is applied to the distance from the perturbed surface to the geoid (which is a reference sphere in the simulations). When gravity anomaly is computed from observations, the observations are downward continued to the ‘real’ geoid, as opposed to the ‘simulated’ geoid which is a sphere in a GIA model. However, it does not matter for the gravity rates or uplift rates whether the geoid is a spherical reference surface as for geophysical simulations, or the real geoid, which is a more complex surface.

Transform equation (A.4) to the time domain:

$$\Delta g_l\left(t\right)=\frac{g}{M_E}\left(l+2\right)\delta\left(t\right)-\frac{g}{M_E}\left(l-1\right)k_l\left(t\right), \tag{A.5}$$

with the time-domain form of the k-Love number given by

$$k_l\left(t\right)=k_{l,e}+\sum_{p=1}^{M}r_{l,p}^{'}\exp\left(s_{l,p}t\right), \tag{A.6}$$

where $k_{l,e}$ is the third component of $\mathbf{K}_l^e\left(a_e\right)$ from equation (2.7) made dimensionless, and $r_{l,p}^{'}$ is the third component of $\mathbf{K}_{l,p}\left(a_e\right)$ from equation (2.7) made dimensionless. Both are output from the computer codes. Substituting in equation (A.5) yields:

$$\Delta g_l\left(t\right)=\frac{g}{M_E}\left(l+2-k_l^e\left(l-1\right)\right)\delta\left(t\right)-\frac{g}{M_E}\left(l-1\right)\sum_{p=1}^{M}r_{l,p}^{'}\exp\left(s_{l,p}t\right). \tag{A.7}$$

Replacing $GF_l\left(t-t'\right)$ with the coefficients for the gravity anomaly, equation (A.1) yields:

$$\Delta g\left(\theta,\lambda,t\right)=\frac{4\pi a_e^2}{2l+1}\frac{g}{M_e}\sum_{l=0}^{\infty}\sum_{m=-l}^{l}\Big\{L_{lm}\left(t\right)\left[l+2-k_l^e\left(l-1\right)\right]$$

$$-\left(l-1\right)\sum_{p=1}^{P}r_{l,j}^{'}\int_{-\infty}^{t}L_{lm}\left(t'\right)\exp\left[s_{l,p}\left(t-t'\right)\right]dt'\Big\}\times Y_{lm}\qquad .$$

(A.8)

A similar expression as equation (A.7) for the geoid height change is:

$$\Delta N_l\left(t\right)=\frac{a_e}{M_E}\left(1+k_l^e\left(l-1\right)\right)\delta\left(t\right)+\frac{a_e}{M_E}\sum_{p=1}^{M}r_{l,p}^{'}\exp\left(s_{l,p}t\right). \qquad \text{(A.9)}$$

A.2. Heaviside loading

Because the ice load on the Earth's surface increases or decreases only slowly in time, modeling the load as a series of Heaviside increments is appropriate. Assuming that the surface load is a series of Heaviside increments is equivalent to taking the spherical harmonic coefficients of the load to be Heaviside increments:

$$L_{lm}\left(t\right)=\sum_{j=1}^{N}\delta L_{lm}^{j}H\left(t-t_j\right), \qquad \text{(A.10)}$$

where *j* denotes the time steps from 0 (start of loading) to *N*, and the Heaviside function is defined as

$$H\left(t-t_n\right)=\begin{cases}1 & \text{if } t>t_n\\ 0 & \text{if } t<t_n\end{cases}. \qquad \text{(A.11)}$$

Substituting (A.10) into the time integral from equation (A.8) yields

$$\int_{-\infty}^{t}\left(t'\right)\exp\left[s_{l,p}\left(t-t'\right)\right]dt'=\sum_{j=1}^{N}\delta L_{lm}^{j}\left[-\frac{1}{s_{l,p}}+\frac{1}{s_{l,p}}\exp\left(s_{l,p}\left(t-t_n\right)\right)\right], \qquad \text{(A.12)}$$

Thus, the spherical harmonic coefficients of the gravity anomaly in equation (A.8) become

$$\Delta g_{lm}\left(t\right)=\frac{4\pi a_e^2}{2l+1}\frac{g}{M_e}\left(L_{lm}\left(t\right)E_l^{\Delta g}-\sum_{j=1}^{N-1}\delta L_{lm}^{j}\beta_l^{\Delta g}\left(\Delta t\right)\right), \qquad \text{(A.13)}$$

where

$$E_l^{\Delta g}=\left[l+2-k_l^e\left(l-1\right)\right]; \qquad \text{(A.14)}$$

$$\beta_l^{\Delta g}\left(\Delta t\right)=\left(l-1\right)\sum_{p=1}^{M}\frac{r_{l,p}^{'}}{s_{l,p}}\left[-1+\exp\left(s_{l,p}\Delta t\right)\right],$$

(A.15)

and $\Delta t = t_n - t_j$ .The Earth model parameters enter the equation solely through the parameters $E_l^{\Delta g}$ and $\beta_l^{\Delta g}\left(\Delta t\right)$ which contain the elastic and viscous Love numbers that are outputted from the normal mode code.

The relative sea level change (spatially varying part) is defined as

$$\Delta\mathbb{S}\mathscr{L}_{lm}\left(\theta,\lambda,t\right)=\Delta\mathcal{G}_{lm}\left(\theta,\lambda,t\right)-\Delta R\left(\theta,\lambda,t\right), \tag{A.16}$$

where $\Delta\mathcal{G}_{lm}$ is the spatially varying part of the geoid change, and ΔR is the change in solid earth displacement. Similar to equation (A.13) it can be derived that:

$$\Delta\mathbb{S}\mathscr{L}_{lm}\left(\theta,\lambda,t\right)=\frac{4\pi a_e^2}{2l+1}\frac{a_e}{M_e}\cdot\left[L_{lm}\left(t\right)E_l^{\Delta\mathbb{S}\mathscr{L}}-\sum_{j=0}^{N-1}\delta L_{lm}^{j}\beta_l^{\Delta\mathbb{S}\mathscr{L}}\left(\Delta t\right)\right], \tag{A.17}$$

where $E_l^{\Delta\mathbb{S}\mathscr{L}}=\left[1+k_l^e-h_l^e\right]$, and $\beta_l^{\Delta\mathbb{S}\mathscr{L}}\left(\Delta t\right)=\sum_{p=1}^{P}\frac{r_{l,p}^{'}-r_{l,p}}{s_{l,p}}\left[-1+\exp\left(s_{l,p}\Delta t\right)\right]$; $r_{l,p}$ is the h-Love number residue (first element of $\mathbf{K}_{l,p}\left(a_e\right)$ from equation (2.7)) and $h_{l,e}$ is the elastic h-Love number (first element of $\mathbf{K}_l^e\left(a_e\right)$ from equation (2.7).

APPENDIX B: COMPARISON OF SEA LEVEL CODE PREDICTIONS

A comparison of predicted uplift rates is undertaken with results of Dr. Giorgio Spada and Dr. Paolo Stocchi (Spada and Stocchi, 2005), published at the website of the Special Bureau for Loading (http://www.sbl.statkart.no/projects/pgs/authors/spada_stocchi/). Factors that are treated differently in the implementation of Spada and Stocchi (2005) compared to the implementation discussed in this chapter are the following:

- The sea level equation is solved using a finite-element scheme, which requires the ice loads to be discretized accordingly.
- The sea level equation is self-consistent but does not include time-dependent ocean margins.

The uplift rate is plotted in Figure B.1, along with the uplift rate computed with the model described in Chapter 2, for the same elastic and viscous Earth model parameters. It can be seen that the uplift rate pattern is similar in both plots. However, the magnitude of the uplift rate is higher for the Spada and Stocchi model. Note that a local maximum over Hudson Bay in Figure B.1a is not what is expected in an uplift rate pattern with ICE-3G.

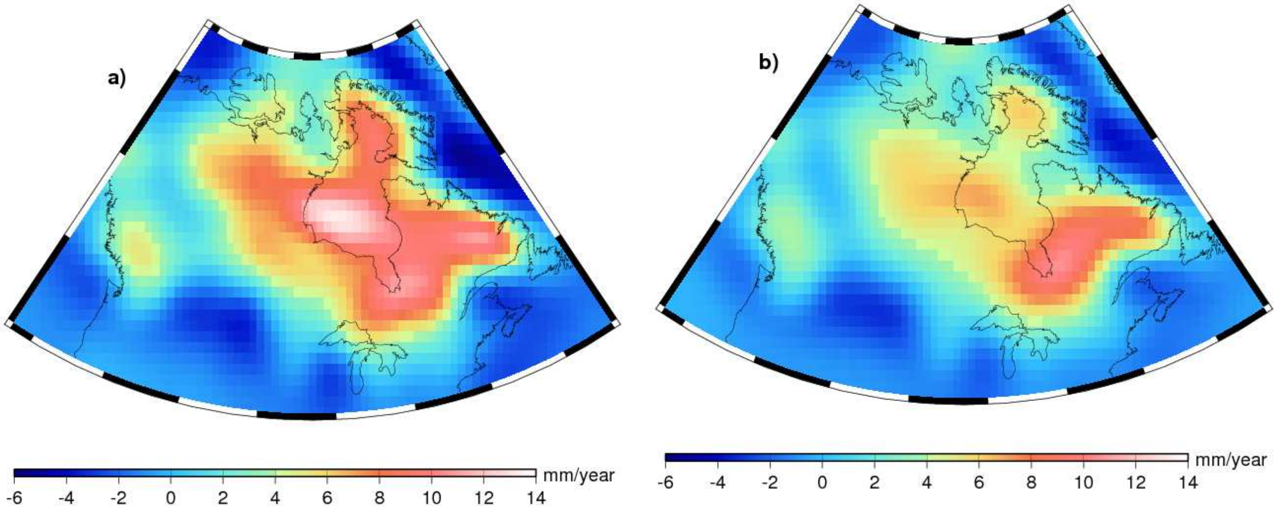

Figure B.1: (a) Uplift rate from Spada and Stocchi (2005) and (b) uplift rate reproduced with the spectral model of Chapter Two:.

A comparison with Figure 3 of Paulson et al. (2007b) in terms of gravity disturbance rate is shown in Figure B.2, after applying Gaussian filtering with a 400 km halfwidth. The magnitude of Paulson et al. (2007b) is larger, which can be caused by the inclusion of rotational feedback, differences in layer depths and elastic constants, and implementation of the ice growth phase.

The comparisons in this appendix show that the GIA model in this chapter gives results in terms of rate of change which are both higher and lower than other models used in the literature. It is possible that the spread in results comes from different modeling and implementation.

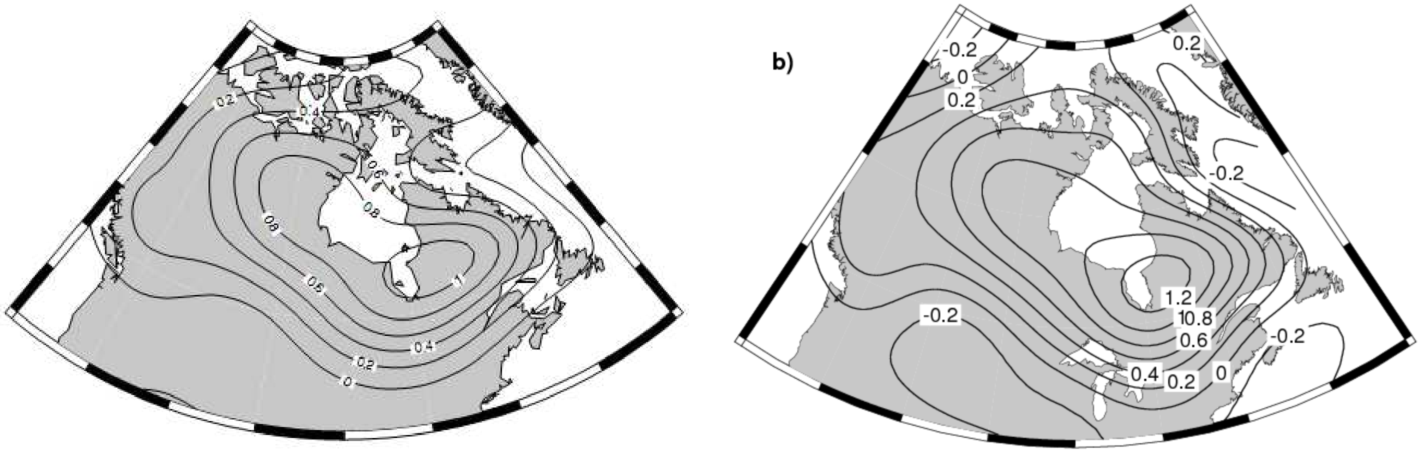

Figure B.2: (a) Gravity disturbance rate copied from Figure 3 of Paulson et al. (2007b). (b) Gravity disturbance rate computed with ICE-3G, upper mantle viscosity of 1 x 10^{21} Pas and lower mantle viscosity of 2 x 10^{21} Pas (the VM1 model; see Peltier, 2004), after 400 km filtering.

APPENDIX C: TENSOR FORM OF THE STRESS-STRAIN RELATION

In this appendix a tensor form of the stress-strain rate relationship is derived starting at the experimental results, equation (3.20). The second stress invariant I_2 and the second strain rate invariant $\dot{E}_2$ can be rewritten as (Ranalli, 1995, p. 76)

$$\begin{aligned} I_2 &= \frac{1}{2} S_{ij} S_{ij} \\ \dot{E}_2 &= \frac{1}{2} \dot{e}_{ij} \dot{e}_{ij} \end{aligned} \tag{C.1}$$

where $\dot{e}_{ij}$ is the deviatoric strain rate, defined as

$$\dot{e}_{ij} = \dot{\varepsilon}_{ij} - \frac{1}{3}\dot{\varepsilon}_{kk}\,, \tag{C.2}$$

and S_{ij} is the deviatoric stress, defined as

$$S_{ij} = \sigma_{ij} - \frac{1}{3}\sigma_{kk}\,. \tag{C.3}$$

The square root of the quantities I_2 and $\dot{E}_2$ is denoted as the effective shear stress and the effective shear strain, respectively. However, here the uni-axial equivalent Mises stress will be used because it is the stress invariant implemented in ABAQUS:

$$\tilde{q} = \sqrt{\frac{3}{2} S_{ij} S_{ij}} = \sqrt{\frac{3}{2}\left(S_{11}S_{22} + S_{11}S_{33} + S_{22}S_{11} + S_{22}S_{33} + S_{33}S_{11} + S_{33}S_{22}\right)} \tag{C.4}$$

and the corresponding uni-axial equivalent strain rate

$$\dot{\tilde{\varepsilon}} = \sqrt{\frac{2}{3} \dot{e}_{ij} \dot{e}_{ij}}\,. \tag{C.5}$$

The postulate is that the relation between stress and strain rate measured in a uni-axial experiment (see Figure 3.3) also gives a relation between the effective stress and effective strain, and hence also between Mises stress and corresponding strain rate (see Ranalli, 1995, p. 76):

$$\dot{\tilde{\varepsilon}} = A\tilde{q}^{n}\,. \tag{C.6}$$

To show that from this more general law the simpler experimental law follows, consider the case of the experiment of a tensile stress σ_T applied so that for an incompressible material: $\sigma_{11} = \frac{2}{3}\sigma_T$ and $\sigma_{22} = \sigma_{33} = -\frac{1}{3}\sigma_T$. For the mean stress (or hydrostatic pressure p) it follows that $p = \frac{1}{3}\left(\frac{2}{3}\sigma_T - \frac{1}{3}\sigma_T - \frac{1}{3}\sigma_T\right) = 0$, so that the Mises stress is $\tilde{q} = \sqrt{\frac{3}{2}S_{ij}S_{ij}} = \sqrt{\frac{3}{2}\left(\frac{4}{9}\sigma_T^2 + \frac{1}{9}\sigma_T^2 + \frac{1}{9}\sigma_T^2\right)} = \sigma_T$, and the strain rates are: $\dot{\varepsilon}_{11} = \dot{\varepsilon}_T$ and $\dot{\varepsilon}_{22} = \dot{\varepsilon}_{33} = -\frac{1}{2}\dot{\varepsilon}_T$. So clearly the mean stress is zero. The Mises equivalent strain rate is $\dot{\tilde{\varepsilon}} = \sqrt{\frac{2}{3}\dot{\varepsilon}_{ij}\dot{\varepsilon}_{ij}} = \sqrt{\frac{2}{3}\left(\dot{\varepsilon}_T + \frac{1}{4}\dot{\varepsilon}_T + \frac{1}{4}\dot{\varepsilon}_T\right)} = \dot{\varepsilon}_T$. Substituting the above expressions for the Mises stress and Mises equivalent strain rate in the invariant creep law, equation (C.6), we get the uni-axial law $\dot{\varepsilon}_T = A\sigma_T{}^n$.

To obtain a tensor form of the power-law creep equation, assume that the components of the strain rate at any point are proportional to the corresponding components of the stress deviator, as in Ranalli (1995) p. 76:

$$\dot{\varepsilon}_{ij} = \lambda S_{ij}. \tag{C.7}$$

Substituting this in the expression for the Mises equivalent strain rate (C.5) we get $\dot{\tilde{\varepsilon}} = \frac{2}{3}\lambda\tilde{q}$, so that: $\frac{2}{3}\lambda = A\tilde{q}^{n-1}$. And finally, the required tensor form of the power law creep

$$\dot{\varepsilon}_{ij} = \frac{3}{2}A\tilde{q}^{n-1}S_{ij}. \tag{C.8}$$

APPENDIX D: TIME-DEPENDENT LOADING IN ABAQUS

In ABAQUS a loading history is divided into steps each of which are treated as static loading situation in order to solve problems with a more complex loading history. For GIA modeling, the loading input is provided by an ice model. In that case, the increments in the ice model determine the steps denoted with subscript *j* in Figure 3.2. Within a step, strain is calculated in ABAQUS by integration of the stress-strain rate relation. Considerable deformation can take place within a time step of the ice model, therefore a step is further divided in increments.

There are two main types of algorithms for integrating the creep law in a FE program: implicit (backward Euler) and explicit (forward Euler). The explicit integration is simply written as

$$\Delta\tilde{\varepsilon} = \dot{\tilde{\varepsilon}}_t \cdot \Delta t \, , \tag{D.1}$$

where $\dot{\varepsilon}$ is given by the constitutive equation (3.25). The implicit integration is

$$\Delta\tilde{\varepsilon} = \dot{\tilde{\varepsilon}}_{t+\Delta t} \cdot \Delta t \, . \tag{D.2}$$

The accuracy of the integration scheme depends on the size of the increment. The length of these increments can be user-specified, or more conveniently, automatically decided in the software based on a given error tolerance. Naturally, the smaller the number of steps, the less computations are required, and the smaller the input and output files in the program. An extra reason to limit the number of steps is that at each step ABAQUS checks if the definition of the force is the same as that for the same node or node set in the previous step, which is a costly operation. By default, increment size is selected automatically based on the Creep Error Tolerance (CETOL) parameter. This parameter should be set so that stresses are computed with sufficient accuracy. CETOL is defined as: $\left(\dot{\tilde{\varepsilon}}_{t+\Delta t} - \dot{\tilde{\varepsilon}}_t\right)\Delta t$. In the ABAQUS Analysis User Manual, section 11.2.4, it is stated that the creep strain increment must be much smaller than the elastic strain increment. Here an empirical relation (determined by Dr. Patrick Wu) is used to determine the value of CETOL so that it is less than 0.5% of the maximum creep strain increment for a typical ice sheet and for a given step size length. A test was performed to see the effect on RSL curves of large CETOL values that were accidently left in the code (see Table D.1). The values in Table D.1 were used to plot the curves in Figure D.2. It can be seen that no visible difference arises from the difference in CETOL values. Since this is not conclusive evidence, the CETOL values determined according to the empirical rule described above were used for all results in Chapter 6.

Table D.1: CETOL values (unitless) used in a test for the effect of the CETOL parameter on relative sea level history.

increment	90 kyear	4 kyear	1 kyear
Large CETOL	1×10^{-1}	4×10^{-2}	1×10^{-2}
Small CETOL	2×10^{-5}	1×10^{-6}	3×10^{-7}

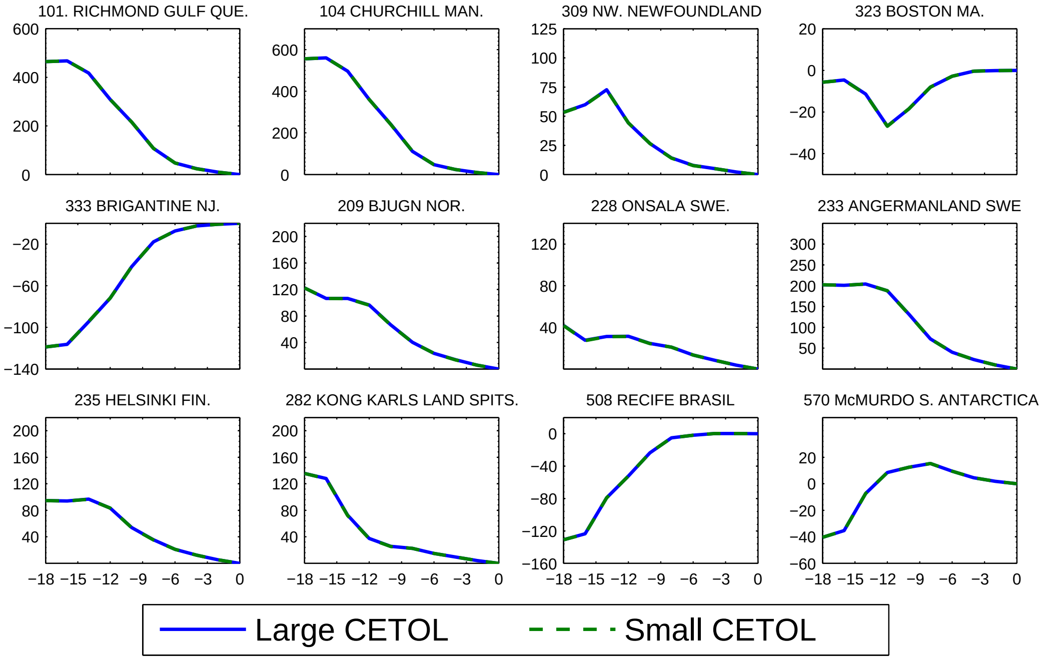

Figure D.1: RSL curve for non-linear GIA model with $n = 3$, $A = 3.3 \times 10^{-34}$ Pa^{-3}s^{-1} for the large and small CETOL values from Table D.1, after four iterations.

APPENDIX E: RSL SITES

ID	Lat	Lon	# obs	Name
101	57	-77	10	RICHMOND GULF QUE.
104	58	-94	7	CHURCHILL MAN.
106	59.8	-80.3	10	OTTAWA IS. NWT.
107	64.5	-84	7	SOUTHAMPTON IS. NWT.
113	62.8	-65.5	8	WARWICK SOUND BAF.
136	74	-93.7	9	N. SOMERSET IS.
147	80	-88	9	E. AXEL HEIBERG IS.
155	82.6	-72.8	10	THORES R. ELL.
202	70	29	8	VARANGER FJORD NOR.
209	63.7	9.6	11	BJUGN NOR.
228	57.3	12	9	ONSALA SWE.
233	63	18	7	ANGERMANLAND SWE.
235	60.2	24.9	10	HELSINKI FIN.
239	57.5	10.5	12	FREDERIKSHAVN DEN.
282	79	28	7	KONG KARLS LAND SPITS.
309	51.5	-56.5	12	NW. NEWFOUNDLAND
323	42.8	-70.8	8	BOSTON MA.
326	41.2	-72.5	7	CLINTON CT.
333	39.5	-74.5	6	BRIGANTINE NJ.
342	33	-80	7	CHARLESTON SC.
350	27.5	-96	8	NW. GULF OF MEXICO
358	32	-65	10	BERMUDA
508	-8	-35	7	RECIFE BRAZIL
512	-39.6	-62.1	9	BAHIA BLANCA ARGENTINA
570	-77.7	163.4	8	McMURDO SOUND ANTARCTICA
657	-35.9	150	10	MORUYA NSW.

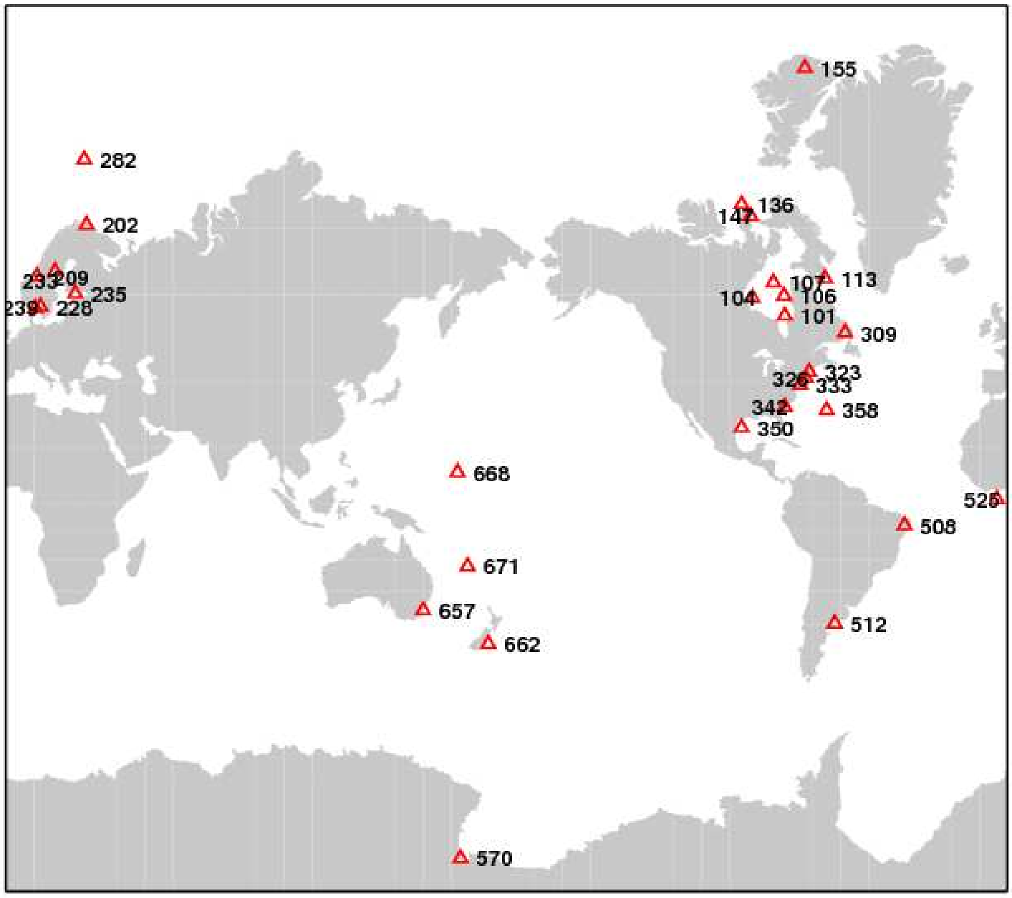

Figure E.1: Location of RSL sites.

References

ABAQUS Version 6.6 Documentation, Theory Manual. Simulia Inc.

Argus, D.F., W.R. Peltier, M.M. Watkins, (1999). Glacial isostatic adjustment observed using very long baseline interferometry and satellite laser ranging in geodesy, J. Geophys. Res. 104, pp. 29,077-29,093.

Barletta, V.A., A. Bordoni, (2009). Clearing observed PGR in GRACE data aimed at global viscosity inversion: weighted mass trends technique, Geophys. Res. Lett. 36, doi:10.1029/2008GL036429.

Becker, T.W., (2006). On the effect of temperature and strain-rate dependent viscosity on global mantle flow, net rotation, and plate-driving forces, Geophys. J. Int. 167, doi: 10.1111/j.1365-246X.2006.03172.x.

Berg, A.A., J. S. Famiglietti, M. Rodell, R. H. Reichle, U. Jambor, S. L. Holl, P. R. Houser, (2005). Development of a hydrometeorological forcing data set for global soil moisture estimation, International Journal of Climatology 25, 13, pp. 1697-1714.

Bettadpur, S. (2007a). Level-2 processing standards document – Rev. 3.0, Center Space Res., Univ. of Texas at Austin, Austin.

Bettadpur, S. (2007b), Level-2 Gravity Field Product User Handbook – Rev. 2.3, Center Space Res., Univ. of Texas at Austin, Austin.

Bettadpur, S., (2008). GRACE: Progress towards product improvement, and prospects for synergy with GOCE, 2008. Oral presentation, GGEO 2008 Symposium, June 23-27, 2008, Chania, Crete, Greece.

Bird, R.B., W.E. Stewart, E.N. Lightfoot, (1960). Transport Phenomena, Wiley, New York.

Braun, A., C.-Y. Kuo, C.K. Shum, P. Wu, W. van der Wal, G. Fotopoulos, (2008). Glacial isostatic adjustment at the Laurentide ice sheet margin: Models and observations in the Great Lakes region, J. Geodyn. 46, pp. 165-173.

Cathles, L.M., (1975). The Viscosity of the Earth's Mantle, Princeton University Press, Princeton, NJ.

Chambers, D.P., (2006). Evaluation of new GRACE time-variable gravity data over the ocean, Geophys. Res. Lett. 33, L17603, doi:10.1029/2006GL027296.

Chen, F., K. Mitchell, J. Schaake, Y. Xue, H.-L. Pan, V. Koren, Q. Y. Duan, M. Ek, A. Betts (1996). Modeling of land surface evaporation by four schemes and comparison with FIFE observations, J. Geophys. Res. 101, (D3), pp. 7251-7268.

Chen, J.L., M. Rodell, C.R. Wilson, J.S. Famiglietti, (2005a). Low degree spherical harmonic influences on Gravity Recovery and Climate Experiment (GRACE) water storage estimates, Geophys. Res. Lett. 32, L14405, doi:10.1029/2005GL022964.

Chen, J.L., C.R. Wilson, J.S. Famiglietti, M. Rodell (2005b). Spatial sensitivity of the Gravity Recovery and Climate Experiment (GRACE) time-variable gravity observations, J. Geophys. Res. 110, B08408, doi:10.1029/2004JB00353.

Chen, J.L., B.D. Tapley, C.R. Wilson, (2006). Alaskan mountain glacial melting observed by satellite gravimetry, Earth Planet. Sci. Lett. 248, pp. 368-378.

Chen, J.L., C.R. Wilson, (2008). Low degree gravity changes from GRACE, Earth rotation, geophysical models and satellite laser ranging, J. Geophys. Res. 113, doi:10.1029/2007JB005397

D'Agostino, G., G. Spada, R. Sabadini, (1997). Postglacial rebound and lateral viscosity variations: a semi-analytical approach based on a spherical model with Maxwell rheology, Geophys. J. Int. 129, 3, F9-F13, doi: 10.1111/j.1365-246X.1997.tb04487.x.

Dal Forno, G., P. Gasperini, E. Boschi, (2005). Linear or nonlinear rheology in the mantle: a 3D finite-element approach to postglacial rebound modeling, J. Geodyn. 38, pp. 183-195.

Dal Forno, G. and P. Gasperini, 2007. Modeling of mantle postglacial relaxation in axisymmetric geometry with a composite rheology and a glacial load interpolated by adjusted spherical harmonics analysis, Geophys. J. Int. 169, pp. 1301-1311.

Davis, J.L., J.X. Mitrovica (1996). Glacial isostatic adjustment and the anomalous tide gagues record of eastern North America, Nature 379, pp. 331-332.

Davis, J., M. Tamisiea, P. Elósegiu, J.X. Mitrovica, E.M. Hill, (2008). A statistical filtering approach for Gravity Recovery and Climate Experiment (GRACE) gravity data, J. Geophys. Res. 113, doi:10.1029/2007JB005043.

Davis, J., M.E. Tamisiea, E. Hill, (2006). Assimilation of GRACE and GPS data into models for glacial isostatic adjustment (GIA), AGU Fall Meeting, San Francisco.

De Bresser, J.H.P., C.J. Peach, J.P.J. Reijs, C.J. Spiers, (1998). On dynamic recrystallization during solid-state flow: Effects of stress and temperature, Geophys. Res. Lett. 25, 18, pp. 3457-3460.

Dickey, J.O., et al. (1997). Satellite Gravity and the Geosphere, National Academy Press, Washington, D.C.

Döll, P., F. Kaspar, B. Lehner (2003). A global hydrological model for deriving water availability indicators: model tuning and validation. Journal of Hydrology 270, pp. 105-134.

Déry, M. Steiglitz, E.C. McKenna, E.F. Wood, (2005). Characteristics and Trends of River Discharge into Hudson, James, and Ungava Bays, 1964–2000, J. Climate 18, 2540-2558.

Duan, X.J., J.Y. Guo, C. K. Shum, W. van der Wal, (2009). On the postprocessing removal of correlated errors in GRACE temporal gravity field solutions, accepted in Journal of Geodesy.

Dyke, A.S., V.K. Prest (1987). Late Wisconsian and Holocene History of the Laurentide Ice Sheet, Géographie physique et Quaternaire 41, pp. 237-263.

Dyke, A.S., J.T. Andrews, P.U. Clark, J.H. England, G.H. Miller, et al. (2002). The Laurentide and Innuitian ice sheets during the Last Glacial Maximum, Quat. Sci. Rev. 21, pp. 9-31.

Dziewonski, A.M., D.L. Anderson, (1981).Preliminary Reference Earth Model (PREM), Phys. Earth Planet. Inter. 25, pp. 297-356.

ETOPO5: Data Announcement 88-MGG-02, Digital relief of the Surface of the Earth. NOAA, National Geophysical Data Center, Boulder, Colorado, 1988.

Fairbanks, R.G., Mortlocka, R.A., Chiu, T.C., Cao, L., Kaplan, A., Guilderson, T.P., Fairbanks, T.W., Bloom, A.L., Grootes, P.M. & Nadeau, M.J, (2005). Radiocarbon calibration curve spanning 0 to 50,000 years BP based on paired ^{230}Th/ ^{234}U/ ^{238}U and ^{14}C dates on pristine corals, Quaternary Science Reviews 24, 1781--1796, doi:10.1016/ j.quascirev.2005.04.007.

Fan, Y., H. van den Dool (2004), The Climate Prediction Center global monthly soil moisture data set at a 0.5º resolution for 1948 to present, J. Geophys. Res. 109, D10102, doi:10.1029:2003JD004345.

Farrell, W.E., (1972). Deformation by surface loads, Rev. Geophys. Space Phys. 10, pp. 761-797.

Farrell, W.E., J.A. Clark, (1976). On postglacial sea level. Geophys. J. R. Astr. Soc. 46, pp. 647-667.

Flechtner, F., (2007). GFZ Level-2 Processing Standards Document – Rev 1.0, GeoForschungszentrum Potsdam.

Fleitout, L., (2007). GRACE data over Canada and postglacial rebound, Geophysical Research Abstracts, Vol.9, 10374, 2007, SRef-ID:1607-7962/gra/EGU2007-A-10374.

Gasperini, G., R. Sabadini, (1990). Finite element modeling of lateral viscosity heterogeneities and postglacial rebound, Tectonophysics 179, pp. 141-149.

Gasperini, P., D. Yuen, R. Sabadini, (1992). Postglacial rebound with a non-Newtonian upper mantle and a Newtonian lower mantle rheology, Geophys. Res. Lett. 19, pp. 1711-1714.

Gasperini, P., G. Dal Forno, E. Boschi, (2004). Linear or non-linear rheology in the Earth's mantle: the prevalence of power-law creep in the postglacial isostatic readjustment of Laurentia, Geophys. J. Int. 157, pp. 1297-1302.

Giunchi C., and G. Spada, (2000). Postglacial rebound in a non-Newtonian spherical Earth, Geophys. Res. Lett. 27, pp. 2065--2068.

GLSEA, (2008): http://coastwatch.glerl.noaa.gov/statistic/statistic.html, last accessed at: December 8, 2008.

Gough, W.A., C. Robinson, R. Hosseinian, (2005). The Influence of James Bay River Discharge on Churchill, Manitoba, Sea Level, Polar Geography 29, 3, pp. 213-223.

Gunter, B., J. Ries, S. Bettadpur, B. Tapley. (2006). A simulation study of the errors of omission and commission for GRACE RL01 gravity fields, Journal of Geodesy 80, pp. 341-351.

Haagmans, R.H.N., and M. van Gelderen, (1991). Error Variances-Covariances of GEM-T1: Their Characteristics and Implications in Geoid Computation, J. Geophys. Res. 96, B12, pp. 20,011-20,022.

Han, S., C. Jekeli, C.K. Shum, (2004). Time-variable aliasing effects of ocean tides, atmosphere, and continental water mass on monthly mean GRACE gravity field, J. Geophys. Res. 109, B04403, doi:10.1029/2003JB002501.

Han, S.-C., C.K. Shum, C. Jekeli, C.-Y. Kuo, C. Wilson, K.-W. Seo (2005). Non-isotropic filtering of GRACE temporal gravity for geophysical signal enhancement. Geophys. J. Int. 163, pp. 18-25.

Henton, J., M. Craymer, R. Ferland, H. Dragert, S. Mazzotti and D. Forbes (2006). Crustal motion and deformation monitoring of the Canadian landmass, Geomatica 60, pp. 173-191.

Heiskanen, W.A., H. Moritz, (1967). Physical Geodesy, W.H. Freeman and Company, San Francisco.

Hirth, G., D. Kohlstedt, (2003). Rheology of the upper mantle and the mantle wedge: a view from the experimentalists, in: Eiler, J. (Ed.), Inside the Subduction Factory, Geophysical Monograph Series 138, American Geophysical Union, Washington, DC, pp. 83-105.

Hughes, T., (1998). Ice Sheets. New York, Oxford University Press. 343 pp.

Hunger, M., P. Döll, (2008). Value of river discharge data for global-scale hydrological modeling. Hydrol. Earth Syst. Sci. 12, pp. 841-861.

Jekeli, C., (1981). Alternative Methods to smooth the Earth’s gravity field, Rep. 327, Dept. of Geodetic Science and Surveying, Ohio State University, Columbus, 1981.

Johnston, P., (1993). The effect of spatially non-uniform water loads on prediction of sea level change, Geophys. J. Int. 147, pp. 615-634.

Jolliffe I.T. (2002). Principal Component Analysis, Springer Series in Statistics, Springer, 2nd ed., New York, 487 pp.

Karato, S.-I., Wu, P. (1993). Rheology of the Upper Mantle: A Synthesis. Science 260, pp. 771-778.

Karato, S.-I, (1998). Micro-physics of post glacial rebound. In: P. Wu, Editor, Dynamics of the Ice Age Earth-A Modern Perspective, Trans Tech Publications, Zürich, pp. 351–364.

Karato, S.-I., (2003). The dynamic structure of the deep Earth, Princeton University Press, Princeton, New Jersey, USA.

Karato, S.-I, (2008). Deformation of Earth materials, Cambridge University Press, Cambridge, UK.

Kaufmann, G., D. Wolf (1999). Effects of lateral viscosity perturbations on postglacial rebound: an analytical approach, Geophys. J. Int. 137, pp. 489-500.

Kaufmann, G., (2000). Ice-ocean mass balance during the Late Pleistocene glacial cycles in view of CHAMP and GRACE satellite missions, Geophys. J. Int. 143, 142-156.

Kaufmann, G., K. Lambeck, (2002). Glacial isostatic adjustment and the radial viscosity profile form inverse modeling. J. Geophys. Res. 107, No. B11, doi:10.1029/2001JB000941.

Kendall, R.A., J.X. Mitrovica, G.A. Milne, (2005). On post-glacial sea level - II. Numerical formulation and comparative results on spherically symmetric models, Geophys. J. Int. 161, pp. 679-706.

Klees, R., E. Revtova, E., B. C. Gunter, P. Ditmar, E. Oudman, H. C. Winsemius and H. H. G. Savenije. (2008). The design of an optimal filter for monthly GRACE gravity models, Geophys. J. Int. 175, pp 417-432.

Klemann, V., P. Wu, D. Wolf, (2003). Compressible viscoelasticity: stability of solutions for homogeneous plane-Earth models, Geophys. J. Int. 153, pp. 56-585.

Korenaga, J., S.-I Karato, (2008). A new analysis of experimental data on olivine rheology, J. Geophys. Res., 113, B02403, doi:10.1029/2007JB005100.

Kuo, C.-Y., C.K. Shum, A. Braun, K.-C Cheng, Y. Yi, (2008). Vertical Motion Determined Using Satellite Altimetry and Tide Gauges, Terr. Atmos. Ocean. Sci. 19, No. 1-2. pp. 21-35.

Kusche, J., (2007). Approximate decorrelation and non-isotropic smoothing of time-variable GRACE-type gravity field models, J. Geod., doi: 10.1007/s00190-007-0143-3.

Lambert, A., N. Courtier, G.S. Sasagawa, F. Klopping, D. Winester, T.S. James, J.O. Liard (2001). New constraints on Laurentide postglacial rebound from absolute gravity measurements, Geophys. Res. Lett. 28, pp. 2109-2112.

Lambert, A., N. Courtier, T.S. James, (2006). Long-term monitoring by absolute gravimetry: tides to postglacial rebound, J. Geodyn. 41, pp. 307-317.

Latychev, K., J.X. Mitrovica, J. Tromp, M.E. Tamisiea, D. Komatitsch, C.C. Christara, (2005). Glacial isostatic adjustment on 3-D Earth models: a finite-volume formulation, Geophys. J. Int. 161, pp. 421-222.

Lee, H., C.K. Shum, Y. Yi, A. Braun., C.-Y. Kuo, (2008). Laurentide crustal motion observed using TOPEX/POSEIDON radar altimetry over land, J. Geodyn. 46, p. 182-193, doi: 10.1016/j.jog.2008.05.001.

Longman, I.M., (1962). A Green's function for determining the deformation of the Earth under surface mass loads, J. Geophys. Res. 67, 2, pp. 845-850.

Liu, X., (2008). Global gravity field recovery from satellite-to-satellite tracking data with the acceleration approach. PhD thesis, Delft University of Technology.

Luthcke, S.,B., A.A. Arendt, D.D. Rowlands, J.J. McCarthy, C.F. Larsen, (2008). J. of Glaciology 54, 188, pp. 767-777.

Mäkinen, J., V. Saaranen, (1998). Determination of postglacial land uplift from three precise levellings in Finland, J. Geod. 72, pp. 516-529.

Marshall, S., L. Tarasov., G.K.C. Clarke, W.R. Peltier, (2000). Glaciological reconstruction of the Laurentide Ice Sheet: physical processes and modelling, Canadian Journal of Earth Sciences 37, 5, pp. 769-793.

Martinec, Z., (2000). Spectral-finite element approach to three-dimensional viscoelastic relaxation in a spherical Earth. Geophys. J. Int. 142, pp. 117-141.

Meredith, D.D., (1975). Temperature Effects on Great Lakes Water Balance Studies, Water Resources Bulletin 11, 1, pp. 60-68.

Mayer-Gürr, T., A. Eicker, K.-H. Ilk (2007). ITG-Grace02s: A GRACE Gravity Field Derived from Short Arcs of the Satellites Orbit, Proceedings of the 1st International Symposium of the International Gravity Field Service "Gravity Field of the Earth", Istanbul.

Melosh, H.J. and A. Raefsky, (1980). The dynamical origin of subduction zone topography. Geophys. J. R. Astr. Soc. 60, 333-354.

Miller L., B.C. Douglas, (2006). On the rate and causes of twentieth century sea level rise, Phil. Trans. Roy. Soc. 364, 805-820, doi: 10.1098/rsta.2006.1738.

Milly, P. C. D., A. B. Shmakin (2002). Global modeling of land water and energy balances, part I: The land dynamics (LaD) model, J. Hydrometeorol. 3, 3, pp. 283--299.

Milne, G.A., J.X. Mitrovica (1998). Postglacial sea level change on a rotating Earth, Geophys. J. Int., 133**,** pp. 1-19.

Milne, G.A., (2002). Recent advances in predicting glaciation-induced sea level changes and their impact on model applications, in: Ice sheets, sea level and the dynamic Earth, pp. 157-176, eds. J.X. Mitrovica and L.L.A. Vermeersen, AGU Geodynamics Series 92.

Mitrovica, J.X., W.R. Peltier, (1989), Pleistocene deglaciation and the global gravity field, J. Geophys. Res. 94, No B10, 13,651-13,671.

Mitrovica, J.X. W.R. Peltier, (1991). On postglacial geoid subsidence over the equatorial oceans, J. Geophys. Res. 96, pp. 20,053-20,071.

Mitrovica, J.X., J.L. Davis, I. Shapiro, (1994), A spectral formalism for computing three-dimensional deformations due to surface loads 2. Present-day glacial isostatic adjustment J. Geophys. Res. 99, pp. 7075-710.

Mitrovica, J.X., (1996). Haskell [1935] revisited, J. Geophys. Res. 101, No. B1, pp 555-569.

National Snow and Ice Data Center, (1999). updated 2007. *World glacier inventory*. World Glacier Monitoring Service and National Snow and Ice Data Center/World Data Center for Glaciology. Boulder, CO. Digital media.

Pagiatakis, S.D., P. Salib (2003). Historical relative gravity observations and the time rate of change of gravity due to postglacial rebound and other tectonic movements in Canada. J. Geophys. Res. 108, B9, 2406, doi:10.1029/2001JB001676.

Parmentier, E.M., D.L. Turcotte, K.E. Torrance, (1976). Studies of finite amplitude non-Newtonian thermal convection, J. Geophys. Res. 81, pp. 1839-1846.

Paulson, A., S. Zhong, J. Wahr, (2005). Modelling post-glacial rebound with lateral viscosity variations, (2005). Geophys. J. Int. 163, pp. 357-371.

Paulson, A., S. Zhong, J. Wahr, (2007a). Limitations on the inversion for mantle viscosity from postglacial rebound. Geophys. J. Int. 168, pp. 1195-1209.

Paulson, A., S. Zhong, J. Wahr, (2007b). Inference of mantle viscosity from GRACE and relative sea level data. Geophys. J. Int. 171, pp. 497-508.

Paulson, A., (2006). Inference of the Earth’s mantle viscosity from post-glacial rebound, PhD Thesis, University of Colorado.

Peltier, W.R. (1974). The impulse response of a Maxwell Earth, Rev. of Geophys. Space Phys. 12, 4, pp. 649–669.

Peltier, W.R., D.A. Yuen, P. Wu, (1980). Postglacial rebound and transient rheology, Geophys. Res. Lett. 7, 10, pp. 733-736.

Peltier, W.R., A. Tushingham, (1989). Global sea level rise and the greenhouse-effect – might they be connected? Science 244, pp. 806-810.

Peltier, W.R. (1994). Ice age palaeotopography, Science 265, pp. 195-201.

Peltier, W.R. (1998). Postglacial variations in the level of the sea: implications for climate dynamics and solid-Earth geophysics, Rev. Geophys. 36, 4, pp. 603-689.

Peltier, W.R., R. Drummond, (2008). Rheological stratification of the lithosphere: A direct inference based upon the geodetically observed pattern of the glacial isostatic adjustment of the North American continent, Geophys. Res. Lett. 35, L16314, doi:10.1029/2008GL034586.

Peltier, W.R. (1999). Global sea level rise and glacial isostatic adjustment. Global and Planetary Change 20, pp. 93–123.

Peltier, W.R., (2004). Global Glacial Isostasy and the Surface of the Ice-Age Earth: ICE-5G (VM2) Model and GRACE, Annu. Rev. Earth Planet. Sci. 32, 111-149.

Podolefsky, N.S., S. Zhong, A.K. McNamara, (2004). The anisotropic and rheological structure of the oceanic upper mantle from a simple model of plate shear. Geophys. J. Int. 158, pp. 287-296.

Press, W.H., S. A. Teukolsky, W.T. Vetterling, B.P. Flannery, (1992). Numerical Recipes in Fortran 77, Vol. 1, 2nd edition, University of Cambridge.

Ranalli, G., (1995). Rheology of the Earth, 2nd edn, Chapman and Hall, London.

Ranalli, G., (2001). Mantle rheology: radial and lateral viscosity variations inferred from micro-physical creep laws, J. Geodyn. 32, pp. 425-444.

Rangelova, E. (2007). A dynamical geoid model for Canada, PhD thesis, University of Calgary.

Rangelova, E., W. van der Wal, A. Braun, M.G. Sideris, P. Wu, (2007). Analysis of Gravity Recovery and Climate Experiment time-variable mass redistribution signals over North America by means of principal component analysis, J. Geophys. Res. 112, F03002, doi:10.1029/2006JF000615.

Rangelova, E., W. van der Wal, M.G. Sideris, P. Wu, (2008). Spatiotemporal analysis of the GRACE-derived mass variations in North America by means of multi-channel singular spectrum analysis, IAG proceedings, GGEO symposium Chania, Crete, accepted.

Ray, R. D. and S. B. Luthcke (2006). Tide model errors and GRACE gravimetry: Towards a more realistic assessment, Geophys. J. Int. 167, 3, pp. 1055–1059.

Riva, R.E.M., R.S. Sabadini (2009). Compressible analytical Earth models: application to GIA, submitted to: Journal of Geodynamics.

Rodell, M., P. R. Houser, U. Jambor, J. Gottschalck, K. Mitchell, C.-J. Meng, K. Arsenault, B. Cosgrove, J. Radakovich, M. Bosilovich, J. K. Entin, J. P. Walker, D. Lohmann, D. Toll (2004), The global land data assimilation system, Bull. Am. Meteorol. Soc. 85, 3, pp. 381-394.

Sabadini, R., D.A. Yuen, E. Boschi, (1982). Polar wandering and the forced responses of a rotating, multilayered, viscoelastic planet, J. Geophys. Res. 87, pp. 2885-2903.

Sabadini, R., D. A. Yuen, M. Portney, (1986). The effects of upper-mantle lateral heterogeneities on post-glacial rebound, Geophys. Res. Lett. 13, 4, pp. 337-340.

Sabadini R., L.L.A. Vermeersen, (2004). Global dynamics of the Earth, Applications of normal mode relaxation theory to solid-Earth geophysics, Kluwer Academic Publishing, Dordrecht, the Netherlands.

Sasgen, I., Z. Martinec, K. Fleming, (2007). Wiener optimal combination and evaluation of the Gravity Recovery and Climate Experiment (GRACE) gravity fields over Antarctica, J. Geophys. Res. 112, doi:10.1029/2006JB004605.

Schertzer, W.M., J.H. Saylor, F.M. Boyce, D.G. Robertson, F. Rosa, (1987). Seasonal thermal cycle of Lake Erie, J. Great Lakes Res. 13, 4, pp. 468-486.

Schmeling, H., 1987. On the interaction between small- and large-scale convection and postglacial rebound flow in a power-law mantle, Earth Planet. Sci. Lett. 84, pp. 254-262.

Schmidt, R., F. Flechtner, U. Meyer, K.-H. Neumayer, C. Dahle, R. Konig, J. Kusche, (2008). Hydrological Signals Observed by the GRACE Satellites, Surv. Geophys., doi: 10.1007/s10712-008-9033-3.

Schotman, H.H.A., (2008). Shallow-Earth rheology from glacial isostasy and satellite gravity: a sensitivity analysis for GOCE, PhD thesis, Delft University of Technology.

Schrama, E.J.O, B. Wouters, D. Lavallee, (2007). Signal and noise in Gravity Recovery and Climate Experiment (GRACE) observed surface mass variations, J. Geophys. Res. 112, B08407, doi:10.1029/2006JB004882.

Sella, G.F., S. Stein, T.H. Dixon, M. Craymer, T.S. James, S. Mazzotti, R.K. Dokka, (2007). Observation of glacial isostatic adjustment in ‘‘stable’’ North America with GPS, Geophs. Res. Lett. 34, L02306, doi:10.1029/2006GL027081.

Shmakin, A.B., Milly, P.C.D., Dunne, K.A., (2002). Global Modeling of Land Water and Energy Balances. Part III: Interannual Variability. J. Hydrometeor. 3, pp. 311-321.

Simons, F., F. Dahlen, (2006). Spherical Slepian functions and the polar gap in geodesy, Geophys. J. Int. 166, pp. 1039-1061.

Sneeuw, N., (1994). Global spherical harmonic analysis by least-squares and numerical quadrature in historical perspective, Geophys. J. Int. 118-3, pp. 707-716

Spada, G., P. Stocchi, (2005). Solving the “sea level equation”: Part I – Theory, Samizdat Press.

Spada, G., A. Antonioli,S. Cianetti, C. Giunchi, (2006). Glacial isostatic adjustment and relative sea level changes: the role of lithospheric and upper mantle heterogeneities in a 3D spherical Earth, Geophys. J. Int. 165, pp. 692-702.

Steffen, H., G. Kaufmann, P. Wu, (2006). Three-dimensional finite-element modeling of the glacial isostatic adjustment in Fennoscandia, Earth Planet. Sci Lett. 250, 358-375.

Steffen, H., H. Denker, J. Müller, (2008). Glacial isostatic adjustment in Fennoscandia from GRACE data and comparison with geodynamical models, J. Geodyn. 146, pp. 155-164.

Steffen, H., O. Gitlein, H. Denker, J. Müller, L. Timmen, (2009). Present rate of uplift in Fennoscandia from GRACE and absolute gravimetry, accepted for Tectonophysics, doi: 10.1016/j.tecto.2009.01.012.

Steinberger, B., H. Schmeling, G. Marquart, (2001). Large-scale lithospheric stress field and topography induced by global mantle circulation. Earth Planet. Sci Lett. 186, p 75-91.

Strang van Hees, G.L., (1999). Some elementary relations between mass distributions inside the Earth and the geoid and gravity field, J. Geodyn. 29, pp. 111-123.

Swenson, S., Wahr, J., (2002). Methods for inferring regional surface-mass anomalies from Gravity Recovery and Climate Experiment (GRACE) measurements of time-variable gravity. J. Geophys. Res. 107, B9, doi: 10.1029/2001JB000576.

Swenson, S., J. Wahr, (2006). Post-processing removal of correlated errors in GRACE data, Geophys. Res. Lett. 33, L08402, doi:10.1029/2005GL025285.

Swenson, S., J. Wahr, (2007). Multi-sensor analysis of water storage variations of the Caspian Sea, Geophys. Res. Lett. 34, L16401, doi:10.1029/2007GL030733.

Tamisiea, M., J.X. Mitrovica, J. Tromp, J., G.A. Milne, (2002). Present-day secular variations in the low-degree harmonics of the geopotential: Sensitivity analysis on spherically symmetric Earth models, J. Geophys. Res. 107, B12, doi:10.1029/2001JB000696.

Tamisiea, M., E. Leuliette, J.L. Davis, J.X. Mitrovica, (2005). Constraining hydrological and cryospheric mass flux in eastern Alaska using space-based gravity measurements, Geophys, Res. Lett. 32, doi: 10.1029/GL023961.

Tamisiea, M.E, J.X. Mitrovica, J.L. Davis, (2007). GRACE gravity data constrain ancient ice geometries and continental dynamics over Laurentia. Science 316, pp. 881-883.

Tarasov, L., W.R. Peltier, (2004). A geophysically constrained large ensemble analysis of the deglacial history of the North American ice-sheet complex. Quat. Sci. Rev. 23, pp. 359-388.

Tarasov, L., W.R. Peltier, (2003). Greenland glacial history, borehole constraints, and Eemian extent. J. Geophys. Res. 108, B3, doi:10.1029/2001JB001731.

Tapley, B.D., S. Bettadpur, M.M. Watkins, C. Reigber, (2004). The gravity recovery and climate experiment: Mission overview and early results. Geophys. Res. Lett. 31, doi: 10.1029/2004GL019920.

Tromp, J., J.X. Mitrovica (2000). Surface loading of a viscoelastic planet: III. Aspherical models, Geophys. J. Int. 140, pp. 425-441.

Tushingham, A., W.R. Peltier, (1991). ICE-3G: A new global model of late Pleistocene deglacation based upon geophysical predictions of post-glacial relative sea level change, J. Geophys. Res. 96, pp. 4497-4523.

Turcotte, D. L., G. Schubert, (2002). Geodynamics, 2nd Edition, Cambridge University Press, New York.

Van den Berg, A., P.E. van Keken, D.A. Yuen, (1993). The effects of a composite non-Newtonian and Newtonian rheology on mantle convection, Geophys. J. Int. 115, pp. 62-78.

Valeo, C., W. van der Wal, S. Marshall, (2007). Validating gravimetry measurements in Canada with a continental scale hydrological database, International Association of Hydrological Sciences Publ. 316, pp. 169-177.

Van der Wal, W., H.H.A. Schotman, L.L.A Vermeersen, (2004). Geoid heights due to a crustal low viscosity zone in glacial isostatic adjustment modeling: a sensitivity study for GOCE, Geophys. Res. Lett. 31, doi:10.1029/2003GL019139.

Van der Wal, W., E. Rangelova, J.A.R. Blais, M.G. Sideris, P. Wu, (2006). Time Variable Gravity due to Seasonal Volume Changes in the Great Lakes derived from Satellite Altimetry and Tide Gauges, oral presentation, CGU Conference, Banff, May 14-17, 2006.

Van der Wal, W., P. Wu, M.G. Sideris, C.K. Shum, (2008a). Use of GRACE determined secular gravity rates for glacial isostatic adjustment studies in North America. J. Geodyn. 46, 144-155, doi:10.1016/j.jog.2008.03.007.

Van der Wal, W., E. Rangelova, M.G. Sideris, P. Wu (2008b). Secular Geoid Rate from GRACE for Vertical Datum Modernization, IAG proceedings, GGEO symposium Chania, Crete, accepted.

Van Hunen, J., S. Zhong, N.M. Shapiro, M.H. Ritzwoller, (2005). New evidence for dislocation creep from 3-D geodynamics modeling of the Pacific upper mantle structure. Earth Planet. Sci. Lett. 238, pp. 146-155.

Vaníček, P., E. Krakiwsky (1982). Geodesy, the concepts. Elsevier Science Publishers, Amsterdam.

Velicogna, I., J. Wahr, (2002). Postglacial rebound and Earth's viscosity structure from GRACE, J. Geophys. Res. 107, B12, doi: 10.1029/2001JB001735.

Velicogna, I., Wahr, J., (2006). Acceleration of Greenland ice mass loss in spring 2004, Nature 443, pp. 329-331.

Vermeersen, L.L.A, R. Sabadini, (1997). A new class of stratified viscoelastic models by analytical techniques, Geophys. J. Int. 129, pp. 531-570.

Wagner, C., D. McAdoo, J. Klokočník, J., Kostelecký, (2006). Degradation of geopotential recovery from short repeat-cycle orbits: application to GRACE monthly fields. J. Geod. 80, pp. 94–103.

Wahr, J., M. Molenaar, F. Bryan, (1998). Time variability of the Earth's gravity field: Hydrology and oceanic effects and their possible detection using GRACE, J. Geophys. Res. 103, B12, pp. 30,205-30,229.

Wahr, J., D. Wingham, C. Bentley, (2000). A method of combining ICESat and GRACE satellite data to constrain Antarctic mass balance, J. Geophys. Res. 105, B7, pp. 16279-16294.

Wahr, J., S. Swenson, V. Zlotnicki, I. Velicogna, (2004). Time variable gravity from GRACE: first results. Geophys. Res. Lett. 31, L11501, doi:10.1029/2004GL019779.

Wahr, J., S. Swenson, I. Velicogna, (2006). Accuracy of GRACE mass estimates, Geophys. Res. Lett., 33, L06401, doi:10.1029/2005GL025305.

Walcott, R. I., (1972). Late Quaternary vertical movements in Eastern North America: quantitative evidence of glacio-isostatic rebound, Rev. Geophys. 1, 0, pp. 849-884.

Wang, H., P. Wu, (2006). Effects of lateral variations in lithospheric thickness and mantle viscosity on glacially induced surface motion on a spherical, self-gravitating Maxwell Earth, Earth Planet. Sci. Lett. 244, pp. 576-589.

Wang, H., P. Wu, H.H.A. Schotman, Z. Wang, (2006). Validation of the coupled Laplace-Finite-element method for the loading problem of a laterally heterogeneous spherical Earth, Chin. J. Geophys. 49, 6, pp. 1515-1523.

Watkins, M., (2007). JPL Level-2 Processing Standards Document, Jet Propulsion Laboratory, Pasadena.

Wessel, P., W.H.F. Smith, (1991). Free software helps map and display data, Eos Trans., AGU, 72, 441.

Wiehl, M., Dietrich, R., Lehmann, A., (2005). How Baltic Sea water mass variations mask the postglacial rebound signal in CHAMP and GRACE gravity field solutions. In: Reigber, Ch., Lühr, H., Schwintzer, P., Wickert, J. (eds.) Earth observation with CHAMP. Springer-Verlag Berlin Heidelberg, 181–186.

Witze, A., (2008). Climate change: losing Greenland. Nature 452, 798-802 doi:10.1038/452798a.

Wolf, D., V. Klemann, J. Wunsch, F.P. Zhang, (2006). A reanalysis and reinterpretation of geodetic and geological evidence of glacial-isostatic adjustment in the Churchill region, Hudson Bay. Surv. Geophys. 27, pp. 19-61, doi:10.1007/s10712-005-0641-x.

Wouters, B., E.J.O. Schrama, (2007). Improved accuracy of GRACE gravity solutions through empirical orthogonal function filtering of spherical harmonics, Geophys. Res. Lett. 34, doi:10.1029/2007GL032098.

Wu, P., 1978. The response of a Maxwell earth to applied surface mass loads: glacial isostatic adjustment, MSc thesis, University of Toronto, Toronto, Ont..

Wu., P., W.R. Peltier, (1982). Viscous gravitational relaxation, Geophys. J. R. Astr. Soc. 70, pp. 435-485.

Wu, P., (1992). Deformation of an incompressible viscoelastic flat Earth with power-law creep: a finite element approach, Geophys. J. Int. 108, pp. 35-51.

Wu, P., (1995). Can observations of postglacial rebound tell whether the rheology of the mantle is linear or nonlinear?, Geophys. Res. Lett. 22, pp. 1645-1648.

Wu, P., Z. Ni, (1996). Some analytical solutions for the viscoelastic gravitational relaxation of a two-layer non-self-gravitating incompressible spherical Earth, Geophys. J. Int. 126, pp. 413-436.

Wu, P., (1998). Postglacial rebound Modeling with Power Law Rheology. In: Dynamics of the Ice Age Earth: A Modern Perspective, edited by Wu, P., Trans Tech Publ., Switzerland, pp. 365-382.

Wu, P., Z. Ni, G. Kaufmann, (1998), Postglacial rebound with lateral heterogeneities: from 2D to 3D modeling, In: Dynamics of the Ice Age Earth: A Modern Perspective, edited by Wu, P., Trans Tech Publ., Switzerland, pp. 557-582.

Wu, P., (1999). Modelling postglacial sea levels with power-law rheology and a realistic ice model in the absence of ambient tectonic stress, Geophys. J. Int. 139, pp. 691-702.

Wu, P., (2001). Postglacial induced surface motion and gravity in Laurentia for uniform mantle with power-law rheology and ambient tectonic stress, Earth Planet. Sci. Lett. 186, pp. 427-435.

Wu, P., (2002a). Effects of mantle flow law stress exponent on postglacial induced surface motion and gravity in Laurentia, Geophys. J. Int. 148, pp. 676-686.

Wu, P. (2002b), Mode coupling in a viscoelastic self-gravitatin spherical Earth induced by axisymmetric loads and lateral viscosity variations, Earth Planet. Sci. Lett. 202, pp. 49-60.

Wu, P., W. van der Wal, (2003). Postglacial Sealevels on a Spherical, Self-gravitating Viscoelastic Earth: Effects of lateral viscosity variations in the upper mantle on the inference of viscosity contrasts in the lower mantle, Earth Planet. Sci. Lett. 211, pp. 57-68.

Wu, P., (2004). Using commerical finite element packages for the study of Earth deformations, sea levels and the state of stress, Geophys. J. Int. 158, pp. 401-408.

Wu, P., H. Wang, (2008). Postglacial isostatic adjustment in a self-gravitating spherical Earth with power-law rheology, J. Geodyn. 46, pp. 118-130.

Yuen, D.A., G. Schubert, (1976). Mantle plumes - A boundary layer approach for Newtonian and non-Newtonian temperature-dependent rheologies, J. Geophys. Res. 81, pp. 2499-2510.

Zhong, S., A. Paulson, J. Wahr, (2003). Three-dimensional finite-element modeling of Earth's viscoelastic deformation: effects of lateral variations in lithospheric thickness, Geophys. J. Int. 155, pp. 679-695.

Zienkiewicz, O.C., R.L. Taylor, J.Z. Zhu (2005). The finite element method, its basis and fundamentals. Elsevier, Oxford